UNIVERSITY OF SOUTHAMPTON
FACULTY OF ENGINEERING, SCIENCE AND MATHEMATICS
SCHOOL OF PHYSICS AND ASTRONOMY

Spectral studies of small-scale auroral structure and plasma instability in the high-latitude ionosphere

Joanna Mary Sullivan

THESIS SUBMITTED FOR
THE DEGREE OF DOCTOR OF PHILOSOPHY
NOVEMBER 2008

UNIVERSITY OF SOUTHAMPTON

ABSTRACT

FACULTY OF ENGINEERING, SCIENCE AND MATHEMATICS
SCHOOL OF PHYSICS AND ASTRONOMY
Doctor of Philosophy

SPECTRAL STUDIES OF SMALL-SCALE AURORAL STRUCTURE AND PLASMA INSTABILITY IN THE HIGH-LATITUDE IONOSPHERE

by **Joanna Mary Sullivan**

Optical measurements of small-scale auroral structures are here combined with spectrographic data in order to study the relationship between auroral morphology and the energy characteristics of the precipitating population. It is shown that rayed auroral structures are associated with precipitating electrons with a broad range in energy, including a significant population at energies of around 100 eV. In comparison, observations of fast-moving auroral arc elements are shown to result from precipitation energy distributions peaking at several keV with a very small low-energy component.

This spectrographic information feeds directly into the study of naturally enhanced ion-acoustic lines, or NEIALs, which have been observed by incoherent-scatter radars at high-latitudes. It has been proposed that these radar enhancements result from natural plasma instability, causing the generation of ion-acoustic waves through the decay of unstable Langmuir waves, themselves driven by low-energy electron streams. Using multi-spectral imaging in combination with radar observations, a direct link is shown between ion-acoustic wave enhancements and precipitating electrons at 100 eV energies. Wave enhancements at the radar wavevector which are three orders of magnitude above the thermal level, are successfully modelled using the Langmuir decay interpretation for the time of observation.

Electron populations with a broad energy range are thought to result from Alfvénic acceleration mechanisms, which play an important role in the generation of small-scale auroral structure. With the recent advancements in multi-spectral imaging, it is now possible to resolve auroral filaments of a few hundred meters width. An interferometric imaging capability is under development for the EISCAT Svalbard Radar system, in order to resolve scattering wave structures on similar spatial scales within the radar beam. A technique is demonstrated by which to calibrate the position of coherent echoes detected by the interferometer. This will be of great use in clarifying the role of precipitating electron beams in turbulent plasma processes on small scales.

CONTENTS

LIST OF TABLES

LIST OF FIGURES

List of Acronyms

A full list of acronyms used in this thesis, and the page where they first appear in the text, is provided here to aid the reader.

AACGM	Altitude Adjusted Corrected Geomagnetic Coordinates	118
ACE	Advanced Composition Explorer	40
AMISR	Advanced Modular Incoherent Scatter Radar	156
ASK	Auroral Structure and Kinetics	28
DMSP	Defence Meteorological Satellite Programme	41
DV	Digital Video	34
EISCAT	European Incoherent Scatter	21
EMCCD	Electron Multiplying CCD	33
ESR	EISCAT Svalbard Radar	30
FWHM	Full Width Half Maximum	36
GLAT	Geographic Latitude	160
GLONG	Geographic Longitude	160
GPS	Global Positioning System	38
GSM	Geocentric Solar Magnetospheric	3
GUISDAP	Grand Unified Incoherent Scatter Data Analysis Programme	19
HiTIES	High Throughput Imaging Echelle Spectrograph	31
IGRF	International Geomagnetic Reference Field	30
IMAGE	International Monitor for Auroral Geomagnetic Effects	39
IMF	Interplanetary Magnetic Field	2
IS	Incoherent Scatter	17
KHO	Kjell Henriksen Observatory	31
MAG	Magnetic Field Experiment	41
MHD	Magnetohydrodynamics	7
MIC	Microchannel-plate Intensified CCD	33
MLAT	Magnetic Latitude	95
MLONG	Magnetic Longitude	161

MLT	Magnetic Local Time	95
MSIS	Mass Spectrometer-Incoherent Scatter	121
MSP	Meridian Scanning Photometer	97
NEIAL	Naturally Enhanced Ion Acoustic Line	20
NTP	Network Time Protocol	31
SAO	Smithsonian Astronomical Observatory	45
SIF	Spectrographic Imaging Facility	30
SSIES	Special Sensors-Ions, Electrons, and Scintillation	41
SWEPAM	Solar Wind Electron Proton Alpha Monitor	41
TLC	The Little Camera	33
UHF	Ultra High Frequency	17
UT	Universal Time	62
VHF	Very High Frequency	17

DECLARATION OF AUTHORSHIP

I, Joanna Sullivan, declare that the thesis entitled *Spectral studies of small-scale auroral structure and plasma instability in the high-latitude ionosphere* and the work presented in the thesis are both my own and have been generated by me as the result of my own original research. This work was done wholly while in candidature for a research degree at this University. No part of this thesis has previously been submitted for a degree or any other qualification at this or any other University.

I confirm that:

- where I have consulted the published work of others, this is clearly attributed;
- I have acknowledged all main sources of help;
- where the thesis is based on work done by myself jointly with others, I have made clear what was done by others and what I have contributed myself;
- where figures throughout the text are reproduced from the work of other authors, for illustration or discussion, such figures are always credited in the associated caption, and permission has been obtained from the copyright holder.

Those parts of this thesis which have been published are as follows.

- Chapter 4 was published as:

  Dahlgren, H., Ivchenko, N., Sullivan, J., Lanchester, B., Marklund, G., and Whiter, D.: Morphology and dynamics of aurora at fine scale: first results from the ASK instrument, Ann. Geophys., 26, 1041–1048, 2008b
- Parts of Chapter 5 were published as:

  Sullivan, J. M., Lockwood, M., Lanchester, B., Kontar, E. P., Ivchenko, N., Dahlgren, H., and Whiter, D.: An optical study of multiple NEIAL events driven by low energy electron precipitation, Ann. Geophys., 26, 2435–2447, 2008
- Chapter 6 was published as:

  Sullivan, J. M., Ivchenko, N., Lockwood, M., Grydeland, T., Blixt, E. M., and Lanchester, B. S.: Phase calibration of the EISCAT Svalbard interferometer using optical satellite signatures, Ann. Geophys., 24, 2419–2427, 2006

This thesis contains approximately 58,250 words, excluding references.

Signed:......................................
J. M. Sullivan, November 2008

ACKNOWLEDGEMENTS

There are many people that i'd like to offer my thanks to, for their help and support over the last few years. Firstly to my supervisors, Mike and Betty, for your ideas, guidance and words of encouragement over the course of this project. Thanks for all your time and effort, and for dragging me out of the occasional rut and pushing me onwards. Thanks also to Nickolay for your advice, helpful discussions and for patiently answering my endless IDL questions, and to Ian, Ivan, Paul, Vikki and Steve at RAL for all their help with managing and analysing the EISCAT radar data. EISCAT is an international association supported by China (CRIRP), Finland (SA), Germany (DFG), Japan (NIPR and STEL), Norway (NFR), Sweden (VR) and the United Kingdom (STFC).

Thanks to all the people that I've worked with on observing campaigns, for Friday gatherings, out-of-coffee errors, Norwegian pub quizzes, Kroa pizzas and campaign humour after three days of sleeping (or more accurately not sleeping) in a cupboard. To Tom and Anja for teaching me about radar technicalities and in Tom's case for teaching me how to juggle at 3 am in the ESR control room. Special thanks to Hanna, for her limitless enthusiasm ("Kalibrering är kul!"); Dan, for being able to fix anything with a length of duct tape, a screwdriver and a calculating expression; Olli, for his Finnish air of calm and tranquility; Molly, Elaina, Ian and Andy, for teaching me all about the instruments and answering my stupid questions, and Björn for his inimitable brand of sarcasm. Thanks also to Jeff, Fred and Margit for all your help over the campaign season; for lifts up the mountain, changing data tapes, having an infinite supply of screws and random tools for tinkering, and for letting us be the first squatters to camp out in your shiny new optical station.

To my office mates and the astro group, past and present, for random discussions over coffee, pub outings, Norwegian lessons, badminton and squash breaks, the game of thesis chicken and for generally making my time here an enjoyable one. Thanks also to my house mates, who have put up with me for the last year and a half, for evenings of guitar hero, heated monkey ball battles, house meals, supreme smut levels, Lizzie's baking extravaganzas, and especially for preserving my sanity and keeping me supplied with tea during the long dark hours of thesis writing madness.

I am also much indebted to the Southampton University Archery Club, for getting me down to the range after a long day at the office and providing some much needed de-stressing. To all the members, thanks for never failing to cheer me up, for fond memories of road trips and weekends away, and for becoming some of my closest friends at university. My time here would not have been the same without you. Rest assured that I'll be randomly turning up for shooting and reminiscing, as well as cheering madly when you beat EUAC for many years to come!

To my family, for their support throughout the course of this project and for being there for me in everything i do. And finally to Pete, for picking me up and keeping me going when the light at the end of the tunnel got really hard to see. Without your encouragement and understanding this thesis could not have been written. Apologies for being an absent stressed workaholic for the last few months, thankyou for always believing in me.

JMS
Southampton, November 2008

This thesis was typeset in LaTeX using MiKTeX 2.6, based on a style-file developed by Glenn Morris.

There is a theory which states that if ever anybody discovers exactly what the Universe is for and why it is here, it will instantly disappear and be replaced by something even more bizarre and inexplicable. There is another theory which states that this has already happened.

DOUGLAS ADAMS (1952–2001)

1

Introduction

1.1 Solar-terrestrial physics

Solar-terrestrial physics is the study of the interaction between solar activity and the Earth's environment. In addition to electromagnetic energy, the Sun emits a continuous stream of outflowing material with varying density and velocity. This 'solar wind' is a fully ionised gas (a 'plasma'), consisting mainly of protons and electrons but also with some He^{2+} and other heavy ions. The terrestrial magnetic field is shaped by the action of the solar wind forming a region known as the magnetosphere around the Earth. The magnetosphere has an almost hemispherical shape on the side facing the Sun, being compressed by the solar wind, and is then drawn out into a long tail on the side facing away from the Sun. At the magnetopause (the boundary where the dynamic pressure of the solar wind balances the pressure from the geomagnetic field) solar wind particles are deflected around the Earth. Despite this magnetic shielding effect, some solar wind plasma does enter into the high-latitude atmosphere through the process of reconnection, as described in Section 1.2.

The study of the solar-terrestrial system is key to understanding the nature of the plasma environment near Earth. The obvious practical applications include the prediction and tracking of dangerously energetic solar wind particle events and the protection of orbiting satellites and astronauts. Furthermore, the study of the magnetosphere and the coupling with atmospheric processes advances the understanding of many fundamental plasma phenomena. The interaction of magnetic fields, the propagation of plasma waves, acceleration mechanisms and the onset of instabilities are of great importance in the advancement of many physics applications such as plasma displays, particle accelerators and the practical realisation of fusion power. Plasma behaviour is frequently studied on small-scales under laboratory conditions, but the Earth's plasma environment provides a unique opportunity to study the processes occurring in a natural laboratory on planetary scales, reducing complications caused by edge effects and boundary conditions. An important characteristic of large-scale plasmas is described by the 'frozen-in-flux' theorem, which states that the plasma and the embedded magnetic field move together. This results in a weak magnetic field, the Interplanetary Magnetic Field (IMF) which is generated in the Sun, being carried to Earth by the solar wind. However on small spatial scales this frozen-in concept breaks down, resulting in the phenomenon of magnetic reconnection.

1.2 Magnetic reconnection

The variation of magnetic field over time in a plasma has convective and diffusive contributions. Under the high conductivity conditions in the large-scale interplanetary medium there is negligible diffusion; the magnetic field lines convect with the plasma motion (i.e. the frozen-in concept applies) and plasma trapped within different regions of field cannot blend together. Magnetic reconnection is the process by which particles associated with separate field lines can interact, and thereby allow solar wind particles to penetrate the magnetopause and enter the Earth's atmosphere. Figure 1.1 demonstrates the principles of magnetic reconnection. Separate field lines of opposite sense, when pushed towards each other by plasma flow until diffusion effects become significant (the hatched area represents the diffusion region), alter their topology to form two new field lines. The magnetic tension on the newly created field lines causes plasma outflow from the reconnection region, perpendicular to the direction of flow which brought the separate fields together. Each newly reconnected field line, shown in red in the figure, contains a mixture of plasma from both of the field lines in the original configuration.

This process can occur naturally in several regions of the magnetosphere, wherever field lines of opposite sense are brought into close proximity to each other. Reconnection is thought to be a continuous process in the tail region where geomagnetic

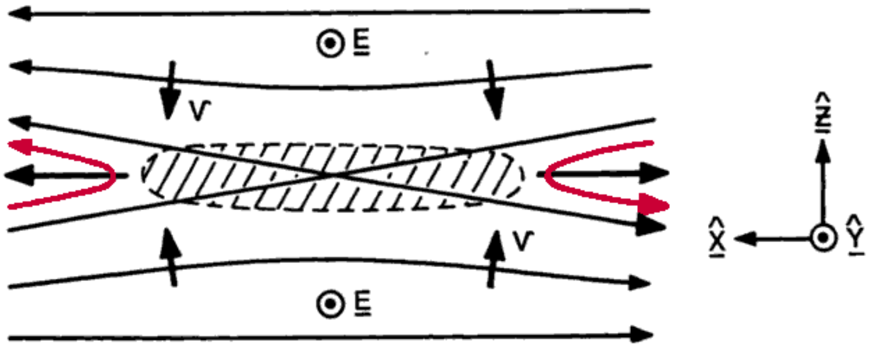

Figure 1.1: Schematic diagram of the field line configuration in magnetic reconnection, taken from Cowley (1985).

field lines originating from the northern and southern hemisphere are drawn out by the solar wind. Ions entering the tail reconnection region can be accelerated back towards the Earth generating nightside ion-induced auroral emissions. The electrons undergo additional acceleration closer to the Earth to give rise to electron-induced auroral emissions (See Section 1.6). On the dayside, reconnection occurs between the IMF and the geomagnetic field. This allows solar wind particles in the transitionary region of plasma just outside the magnetopause, known as the magnetosheath, to enter into the high-latitude atmosphere within a location known as the cusp. The configuration for reconnection on the dayside depends on the orientation of the IMF relative to the geomagnetic field. The Geocentric Solar Magnetospheric (GSM) coordinate system (defined in Appendix A) is aligned with the geomagnetic axis and is used in this thesis to describe the IMF. The IMF B_Z component in this frame best describes the degree to which the fields are anti-parallel and the resulting likelihood of reconnection to occur.

For the southward IMF B_Z (negative) situation, reconnection occurs at the dayside magnetopause. This increases the amount of open magnetic flux (field lines connected directly to the solar magnetic field) in the magnetosphere, expanding the auroral oval in both hemispheres. When the B_Z component is positive, the anti-parallel requirement means that reconnection can only occur when the IMF is draped over the geomagnetic field and interacts with the tail lobes. Although theoretically this can occur in both hemispheres simultaneously, it is far more likely that the draped field would favour reconnection in one hemisphere only. Unlike reconnection under southward IMF conditions, lobe reconnection in one hemisphere does not generate open flux but reconfigures already existing open field lines in the reconnecting hemisphere. Lobe reconnection of the same field line in both hemispheres actually reduces the amount of open flux (Lockwood and Moen, 1999).

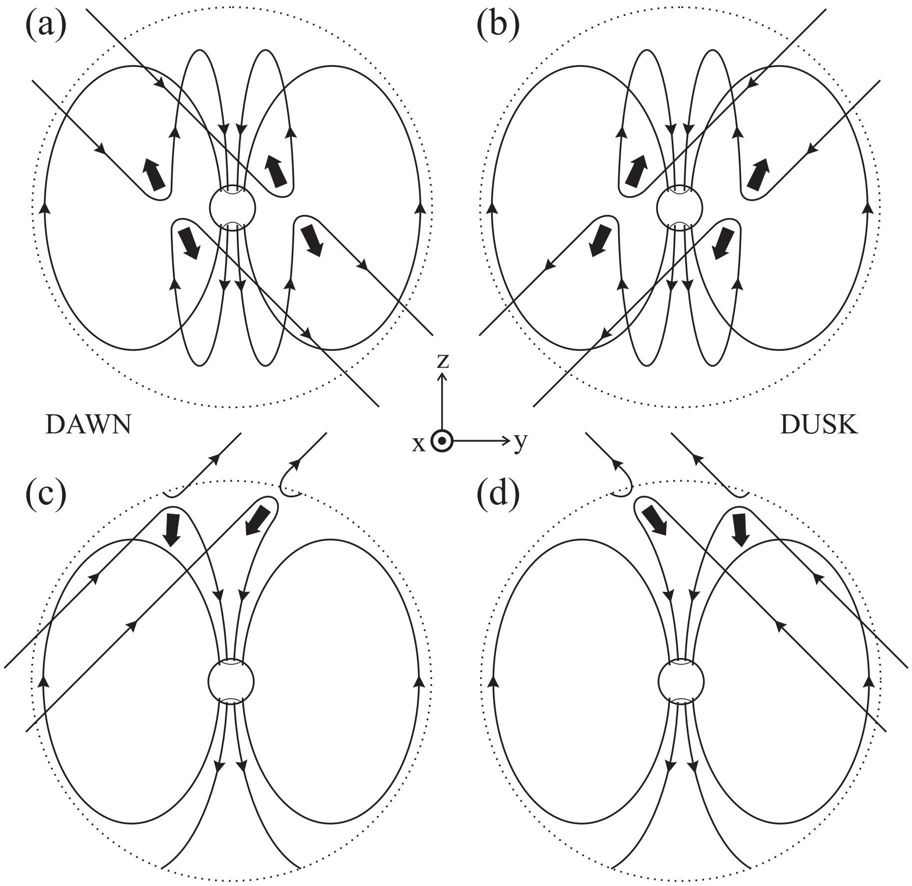

Figure 1.2: Typical reconnection configurations and the dependence on IMF B_Z and B_Y orientation, taken from Stubbs et al. (2001). Solid lines represent the magnetic field, dotted lines the magnetopause boundary and the large arrows show the direction of the resulting force due to the curvature of the newly reconnected field lines.

The detailed reconnection configuration and the resulting topology of the magnetosphere and the driving forces on the atmosphere also depend on the IMF B_X and B_Y components, as described further in Section 1.3. Figure 1.2 shows simplified reconnection configurations in the northern cusp for when the IMF B_Z component is negative (panels a and b) and positive (panels c and d). The additional effect of the orientation of the B_Y component (positive in panels a and c and negative in panels b and d) on the evolution of the reconnected flux is also shown.

1.3 Magnetosphere-Ionosphere coupling

The Earth's atmosphere is partially ionised by solar EUV and X-ray electromagnetic radiation and charged particle precipitation. The region of the atmosphere whose behaviour is influenced by significant ionisation levels is known as the ionosphere. The ionosphere varies in altitude according to solar activity but typically extends from around 80 km up to a few thousand kilometers, and is linked to the Earth's magnetosphere in a coupled system. Magnetospheric current systems close via currents flowing along the magnetic field direction and horizontal currents in the ionosphere. Large-scale regions of field-aligned current, specifically the region of up-going current (predominantly carried by down-going electrons) are associated with auroral activity. In addition to currents being mapped down into the ionosphere, magnetospheric activity also drives ionospheric plasma flows across the high-latitude region of open flux, known as the polar cap. Ongoing reconnection under negative IMF B_Z conditions sweeps newly opened field lines anti-sunward from the dayside. Field lines then reclose in the magneto-tail, causing a return flow sunward at lower latitudes. This flow system creates a two cell 'convection' pattern in the high-latitude ionosphere. During periods of positive IMF B_Z the situation is more complex, with reconfiguration of open magnetic field lines driving tail-lobe circulations and allowing sunward flows at high latitudes. Under positive IMF B_Z conditions multiple convection cells can form, with the sense of rotation and the relative dominance controlled by the orientation of the B_Y component (Cowley and Lockwood, 1992).

The magnetosphere and ionosphere form a complex interconnected system. Although this thesis concentrates on the study of auroral plasma on small spatial scales, small-scale behaviour is directly connected to and influenced by the behaviour of the Sun-Earth system as a whole. The placement of small-scale observations within the context of larger-scale events is essential in understanding the mechanisms responsible. Advancements in the theories of solar-terrestrial science must involve multiple spatial scales, i.e. from studies of solar wind and magnetosphere interaction on planetary spatial scales, to the filamentation of the auroral plasma on sub-kilometre scales as described in this thesis, and the relationships and feedback mechanisms between them.

1.4 Plasma oscillations

Any plasma exhibits collective behaviour, resulting from the electrostatic interactions between the charged particles. Electrons are attracted to form a cloud around positively charged particles, effectively screening their influence on the plasma. This screening occurs on a length scale known as the Debye length, λ_d. These conditions allow the existence of specific linear wave modes, rather than permitting a complete continuum as for electromagnetic waves. Allowed plasma waves are the means by which disturbances to the background plasma equilibrium can propagate, restoring quasi-neutrality and redistributing energy imbalances. Perturbations caused by the impact of the solar wind on the magnetopause can propagate through the magnetospheric plasma and down into the ionosphere. Plasma wave modes of particular relevance to this thesis are summarised here, using the simplified fluid approximation.

1.4.1 Electrostatic waves

The electrostatic attraction between ions and electrons causes natural oscillations when the plasma is disturbed from its equilibrium state. For high-frequency oscillations, ions are considered to be stationary with respect to the electrons because of their large inertia. Such oscillations occur at the electron plasma frequency, ω_{pe}, given by:

$$\omega_{pe} = (\frac{N_e e^2}{\varepsilon_0 m_e})^{\frac{1}{2}} \tag{1.1}$$

where N_e is the electron density, e is the charge of an electron, ε_0 is the permittivity of free space, and m_e is the electron mass. Although these oscillations are quickly damped in cold plasma, when thermal motions are taken into account they can propagate through the plasma as travelling electrostatic waves, known as electron-plasma or Langmuir waves. These waves satisfy the dispersion relation (describing the dependence of the frequency on wavenumber):

$$\begin{aligned} \omega &= (\omega_{pe}^2 + \gamma_e k^2 \frac{\kappa_B T_e}{m_e})^{\frac{1}{2}} \\ &= (\omega_{pe}^2 + 3k^2 V_{Te}^2)^{\frac{1}{2}} \end{aligned} \tag{1.2}$$

where γ_e is 3 for one-dimensional motion, being a statistical mechanics constant related to the number of degrees of freedom, k is the wavenumber, κ_B is Boltzmann's constant, T_e is the electron temperature and V_{Te} is defined as the electron thermal velocity.

For oscillations at lower frequencies the heavier ions are able to respond and can no longer be considered stationary in comparison to the electrons. Taking into account the equations of motion for the ions leads to the propagation of another class of waves known as ion-acoustic waves, satisfying the dispersion relation:

$$\omega = k(\frac{\gamma_e \kappa_B T_e + \gamma_i \kappa_B T_i}{m_i})^{\frac{1}{2}} = kC_s \tag{1.3}$$

where ions are assumed to be singly ionised, γ_i is the corresponding constant for ions, T_i is the ion temperature and C_s is defined as the ion-acoustic speed. These waves are effectively density fluctuations, similar to sound waves in an un-ionised gas. The electron-plasma and the ion-acoustic wave modes propagate parallel to the background magnetic field direction. In considering propagation oblique to the field-aligned direction, these waves are modified resulting in further electrostatic waves, namely the upper and lower hybrid oscillations and the electrostatic ion-cyclotron wave mode.

1.4.2 Electromagnetic waves

There is also a large collection of electro-magnetic waves which can exist in a magnetised plasma, in regimes of frequency much smaller and much greater than the gyro-frequencies for ions and electrons. The catalogue of possible wave modes is not described here, but a comprehensive discussion can be found in Baumjohann and Treumann (1996). Of particular importance in terms of acceleration processes and spatial structuring in the aurora are Alfvén waves, which are therefore explained here in further detail.

Alfvén waves are low frequency electro-magnetic waves, the existence of which was first predicted by Alfvén (1942) in conductive fluids. For a homogeneous background magnetic field, Alfvén waves propagate along the magnetic field direction, with the perturbation in both electric and magnetic field being perpendicular to the direction of propagation. The waves can be thought of as transverse waves, ‘shaking’ the lines of magnetic field in response to an initial disturbance. Under the fluid ideal approximations of Magnetohydrodynamics (MHD), Alfvén waves satisfy the dispersion relation:

$$\omega = k_{\|} V_A \tag{1.4}$$

where $\mathrm{k}_{\|}$ is the wavevector component parallel to the background magnetic field and the Alfvén velocity, V_A, is given by

$$V_A = \frac{B}{\sqrt{\mu_0 m_i N_i}} \tag{1.5}$$

where B is the magnetic field strength, μ_0 is the permeability of the plasma, m_i is the ion mass and N_i is the ion density. In this case the wave is dispersionless, i.e. the propagation velocity is identical at all wavelengths and is constrained to be purely along the magnetic field direction.

The inclusion of kinetic effects, such as thermal noise and finite ion gyroradius and electron mass, leads to the generation of an electric field with a component in the wave propagation direction, i.e. along the magnetic field. The waves are then said to be dispersive, where the propagation velocity is dependent on the wavenumber and can propagate at angles oblique to the magnetic field. These dispersive Alfvén waves commonly exist in two forms in the magnetosphere. At relatively low altitudes, just above the auroral ionosphere where the electron thermal speed is small, the waves are dominated by electron inertia effects and are known as inertial Alfvén waves. At higher altitudes of around 4 - 5 R_e the electron thermal speed is higher and thermal effects dominate, leading to waves known as kinetic Alfvén waves. The component of electric field parallel to the background magnetic field direction means that dispersive Alfvén waves can act to accelerate particles along the magnetic field lines towards the terrestrial ionosphere. The role of Alfvén waves in the acceleration processes associated with small-scale auroral structures is discussed further in Section 1.6.2.

1.5 Wave damping and growth

Although plasma waves can be well described by fluid approximations, the more thorough kinetic theory also includes terms quantifying the damping and growth of generated waves. Under kinetic theory, plasma species are described in terms of distribution functions, i.e. for a species, i, $f_i(r,v,t)$ gives the density of particles at position, r, with velocity, v, at a time, t. This approach leads to complex values of the angular wave frequency, ω:

$$\omega = \omega_R + i\omega_I \tag{1.6}$$

where the real part ω_R gives the wave frequency as predicted by the fluid approximations, and the imaginary part describes the damping or growth, for negative and positive ω_I respectively, due to wave-particle interactions inherent in the plasma. Plasma waves and particles can exchange energy under conditions where the velocity of the particles is similar to the phase velocity of the wave. If a particle is moving slightly slower than the wave, it will gain energy from the wave as it is caught up and pushed along. On the other hand if the particle is travelling faster than the wave it will be impeded, and will lose energy which is transferred to the wave. The overall effect of this exchange depends on the plasma distribution function.

1.5.1 Landau damping

The collisionless damping process within plasmas due to wave-particle interactions is known as Landau damping. The standard Maxwellian velocity distribution, describing a collection of particles in equilibrium at a particular temperature, is represented

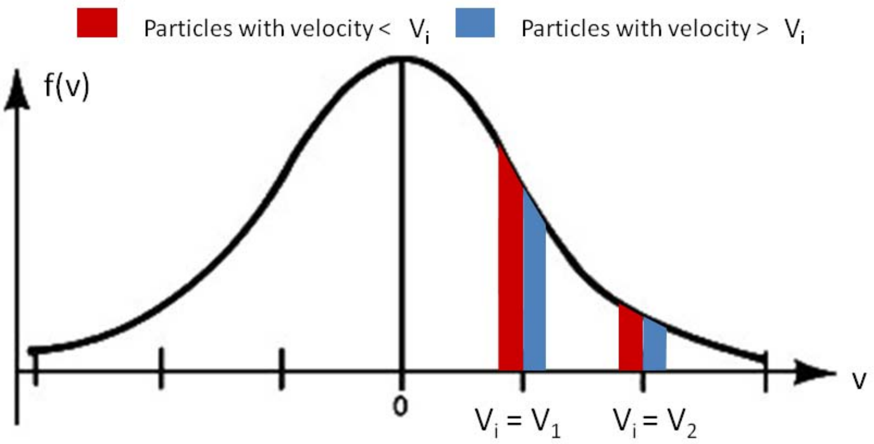

Figure 1.3: Demonstration of the Landau damping of waves through wave-particle interactions, for a Maxwellian velocity distribution of particles.

in Figure 1.3. The width of the spectrum gives a measure of the thermal velocity, a broader distribution meaning higher temperature. In distributions such as this where the particle density decreases with increasing velocity magnitude, for a wave of any phase velocity there are always more particles of similar velocity that are travelling slower than the wave than there are particles travelling faster than the wave. This results in a net exchange of energy from the plasma waves to the particles, effectively causing the wave to be damped.

This process acts on electron-plasma waves, through the interaction with electrons, and ion-acoustic waves, where there is Landau damping due to both electrons and ions. The damping contribution from interactions with ions is larger because of the larger slope of the distribution function, compared to the much broader function for the more mobile electrons. This dependence on the slope also results in the damping strength being related to the temperature ratio between ions and electrons. For large values of T_e / T_i, the phase velocity of the ion-acoustic wave increases, causing a resonance with particles of higher thermal velocity. At these velocities, the slope in the Maxwellian distribution function is smaller, resulting in weaker damping. This is demonstrated in Figure 1.3 where the slope at velocity V_2 is much smaller than at V_1. This relationship can be used in obtaining information about the temperature ratio in the ionosphere, as described further in Section 1.8.1.

1.5.2 Wave growth

Through equivalent arguments, a distribution function with a positive gradient at a particular thermal velocity, will act to drive the growth of plasma waves at the corre-

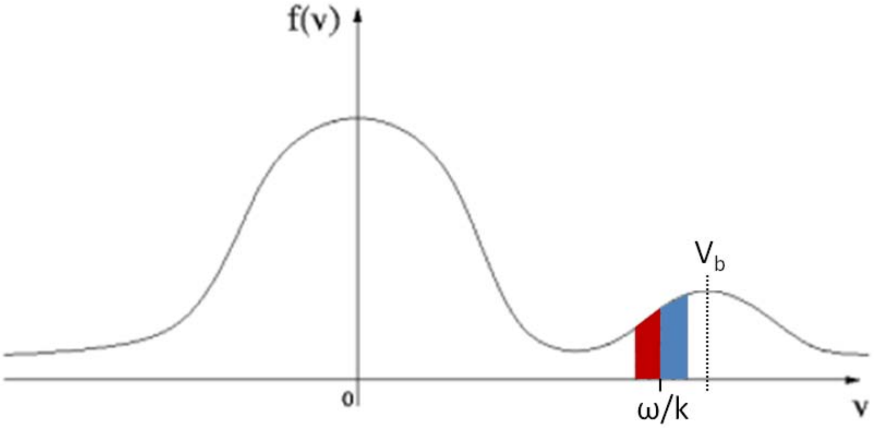

Figure 1.4: Representation of a bump-on-tail velocity distribution, as generated by a beam of particles streaming through a thermal plasma background.

sponding phase velocity. Such distributions can be set up for example by an electron beam streaming through a background plasma of lower density. The total distribution function is called a ‘bump-on-tail’ distribution and is unstable, acting to reduce the departure from equilibrium caused by the beam instability through the enhancement of wave modes. The growth of electron-plasma waves associated with bursts of electrons with corresponding energies (less than 300 eV to 3 keV) has been observed in auroral sounding rocket data (Ergun et al., 1991).

Figure 1.4 shows an example of a bump-on-tail distribution. Electrostatic waves with frequencies close to the resonant condition:

$$\omega = kV_b \tag{1.7}$$

where V_b is the mean field-aligned beam velocity, will be enhanced. The excited wave modes may also be unstable under certain beam streaming conditions and can decay into further wave modes as discussed further in Section 1.10.

1.6 Auroral physics

The aurora, seen within the polar regions of both hemispheres, has been a source of fascination for centuries, and was one of the key phenomena to lead to the emergence of the field of solar-terrestrial physics. The Aurora Borealis (northern hemisphere) and the Aurora Australis (southern hemisphere) are emissions of light, often forming complex and dynamic displays, in the polar regions. Aurora is the optical signature of particles, accelerated using energy extracted from the solar wind flow, precipitating into the ionosphere. Energetic particles collide with atmospheric constituents, exciting them into higher energy states. The excited atoms and molecules then relax back to lower states, emitting energy as light.

The study of aurora is key in answering many scientific questions. It can provide direct information about the particles entering the ionosphere from the Sun, through observations of resulting emissions. The guiding of charged particles by the Lorentz force means that auroral emission effectively acts as a tracer along the terrestrial magnetic field lines, allowing studies of wave distortions, motions and other processes acting on the magnetic field. The spatial scale of auroral features is several orders of magnitude smaller than corresponding processes mapped out into the magnetosphere. This means that in studying the near-Earth environment, ground-based auroral studies have a huge advantage compared to in-situ satellite measurements, in terms of the spatial and temporal resolution available. Auroral observations, in the form of temporal and spectral changes, can also provide insight into other related behaviour occurring in the ionospheric plasma such as plasma waves, heating effects and density fluctuations, as well as allowing active experimentation with recent studies of artificially generated aurora (see Kosch et al. (2007) for a review).

1.6.1 Large-scale auroral zones

As discussed in Section 1.3 the circuit between the ionosphere and magnetosphere is completed via large scale field-aligned current systems in the polar regions. Figure 1.5 gives a simplified representation of typical locations of these currents, known as Birkeland currents, looking at a cut through the magnetosphere system viewed from the magneto-tail. Regions of downward and upward current are associated with boundaries between different flow speeds, linked with regions of diverging and converging electric field respectively (Lyons, 1980). The anti-sunward flow direction and corresponding electric field from dawn to dusk at high latitudes as shown in the figure apply to negative IMF B_Z conditions. Field-aligned current systems are also generated during periods of positive B_Z, although with more complex and variable topology.

Downward current is readily supplied by ionospheric electrons flowing upwards from the atmosphere, usually without the need for any additional acceleration mechanism. However the increased mass of atmospheric ions means that they do not have enough energy to carry the required upward current. Instead upward current is predominantly carried by magnetospheric electrons. As there are less current carriers available in the magnetosphere, these electrons are accelerated down into the ionosphere in order to satisfy the current requirements. Electron acceleration via electro-

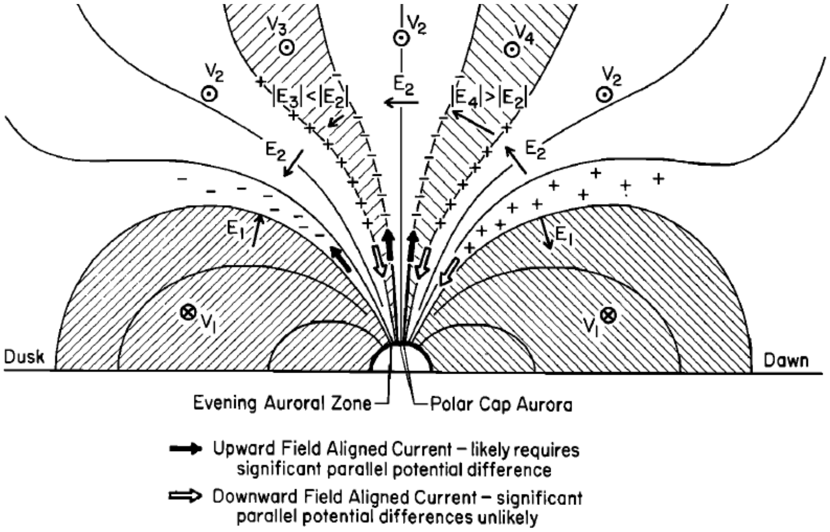

Figure 1.5: Typical locations of field-aligned Birkeland current systems for negative IMF B_z conditions, taken from Lyons (1980).

static potential drops along the magnetic field lines are thought to be responsible for large-scale auroral activity, although additional mechanisms are believed to play a role in the generation of small scale structure, as discussed further in Section 1.6.2. These accelerated electrons produce the visible aurora, forming a ring around the polar cap known as the auroral oval, corresponding to the region of upward Birkeland current.

There is a marked difference between the auroral signatures present on the dayside and nightside of the ionosphere. On the nightside, precipitating electrons are associated with newly closed field lines in the geomagnetic tail. The plasma is accelerated back towards the ionosphere in explosive high-energy events known as substorms. On the dayside, precipitating electrons are associated with open field lines connected to the IMF, and originate directly from the solar wind plasma. This leads to a precipitating population of high flux but relatively low energy compared to that within substorm events.

This thesis involves studies of the aurora in the dayside cusp region. The auroral oval on the nightside is generally located over the north of mainland Norway, whereas cusp aurora tends to occur at higher latitudes. The Norwegian island of Spitsbergen provides an ideal observing location, being frequently located under the dayside cusp and with its high latitude allowing observations during an extended period of 24-hour darkness around the winter solstice. The generation of large scale auroral zones is relatively well understood. However the mechanisms and plasma processes behind the production of the spatial structure on sub-kilometer scales, especially evident in the dayside cusp, are not yet clear.

1.6.2 Auroral acceleration mechanisms

Auroral populations have energies ranging from less than 100 eV up to several hundred keV. Some method of accelerating the thermal magnetospheric plasma (several eV) up to these energies is required. Large-scale auroral arcs can be well explained by the theory of electrons being accelerated to auroral energies via field-aligned potential drops above the topside ionosphere. The auroral electrons accelerated by potential drops tend to have a narrow peak in energy corresponding to the potential difference, and are known as inverted-V populations. Modelling work has shown that thin arcs can be produced by large fluxes of monoenergetic electrons embedded within a background of lower-energy particles (Lanchester et al., 1997). However the mechanisms that lead to small scale-arc distortions and dynamic filamentation in the aurora are not well understood.

It has been previously suggested that large-scale auroral features such as folds and spirals, and small-scale auroral curls are the result of electrostatic instabilities within the auroral acceleration region. Curls are often observed in regions of large velocity shears and are frequently thought to be associated with the Kelvin-Helmholtz instability (Wagner et al., 1983; Trondsen and Cogger, 1998). However recent studies have indicated that shear instabilities alone are not sufficient to explain observed curl systems, and that coupling with auroral acceleration processes must also be considered (Vogt et al., 1999). Small-scale filamentary structures have been linked to field-aligned bursts of electrons with a wide range of predominantly low energies, unlike the populations with a clear energy peak associated with acceleration by a potential drop. These electron bursts are thought to be accelerated by inertial Alfvén waves (Andersson et al., 2002). A review of the role of Alfvén waves in the small scale structuring of the aurora is given in Stasiewicz et al. (2000). In-situ rocket and satellite measurements have observed electric and magnetic field oscillations consistent with Alfvén waves in the topside ionosphere (Chaston et al., 1999; Hallinan et al., 2001), and evidence of Alfvén wave dispersion behaviour has been identified using high resolution auroral imagery (Semeter and Blixt, 2006). However, Alfvén wave accelerated electrons alone cannot easily produce the narrowest arc structures observed, at scale sizes down to 100 m (Chaston et al., 2003).

1.7 Auroral emissions

The auroral spectrum is composed of many individual emissions at different wavelengths. Each emission line corresponds to a particular transition between energy states within a particular excited atom or molecule in the ionosphere. Different emissions occur at different altitudes, predominantly due to the variation in chemical composition of the atmosphere with height. The variations in characteristic lifetime between different energy states also affect the height distribution of auroral emissions. Excited energy states which can exist for longer lifetimes before emitting auroral photons (metastable states) are more likely to lose energy through collisions than by emission, a process known as 'quenching'. This means that corresponding auroral emissions are only present at higher altitudes where the atmospheric density is lower.

In the following description of the key auroral emissions used in this thesis, ionospheric regions are often labelled in reference to distinct ionisation peaks (from solar radiation) in the altitude profile. 'E-region' refers to altitudes between around 90 and 150 km. The 'F-region' has an ionisation peak at 300 to 400 km altitude and extends up into the topside ionosphere, several thousand kilometres above the Earth's surface. Emission wavelengths in this thesis are referred to using the unit of Ångströms, commonly used in auroral spectroscopy, where 1 Å is equivalent to 10^{-10} m (0.1 nm).

1.7.1 $N_2$1PG band system

The first positive band system of molecular nitrogen ($N_2$1PG) lies between 6700 and 7500 Å, producing some of the strongest nitrogen emissions in the auroral spectrum (Gattinger and Vallance-Jones, 1974). The $N_2$1PG bands are produced by transitions from the vibrational states of the $B^3\pi_g$ electronic state to the vibrational states of the $A^3\Sigma_u^+$ electronic state. These are permitted transitions, causing the emissions to be 'prompt' (negligible radiative lifetime). Prompt $N_2$1PG emissions occur down to low E-region altitudes (below 100 km) before they become quenched. Figure 1.6 shows the dependence of the $N_2$1PG band system emission on precipitating electron energy and altitude, using the electron transport model of Lummerzheim and Lilensten (1994) with monoenergetic electron precipitation of total energy flux 1 mW m^{-2}. The peak emission altitude occurs at about 120 km, signifying production by high-energy precipitating electrons, i.e. energies of several keV.

1.7.2 O^+ ^{2}P - ^{2}D doublet

The oxygen emission doublet at 7320 and 7330 Å originates from transitions from the ^{2}P to ^{2}D state of O^+ (OII). These transitions are often referred to as 'forbidden', as they violate quantum mechanical selection rules assuming electric dipole radiation. Forbidden emissions have a small, but non-zero occurrence probability, but are

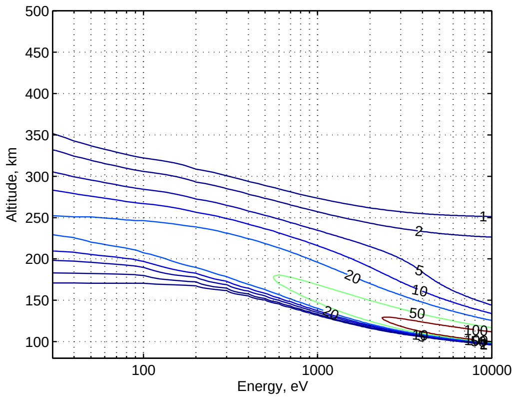

Figure 1.6: Modelled $N_2$1PG brightness in units of [photons/cm^3/sec], as a function of energy and altitude.

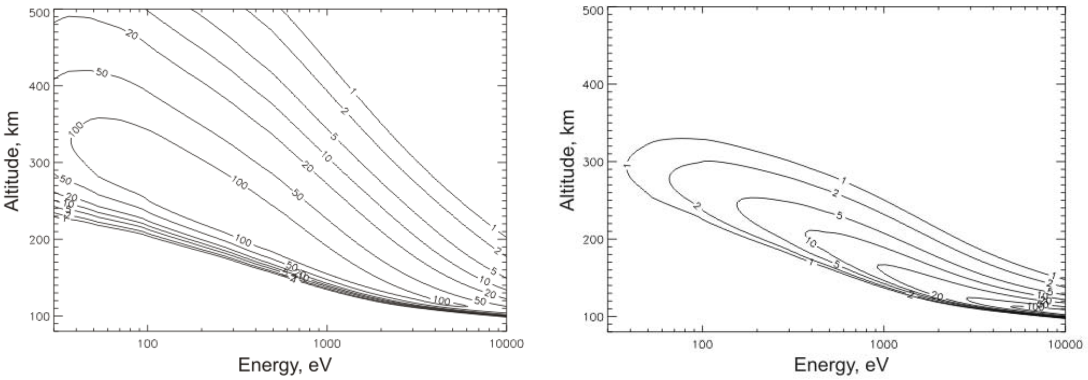

(a) O^+ ^2P - ^2D doublet **(b)** O_2^+ 1N band system

Figure 1.7: Modelled ionised oxygen emission rates in units of [photons/cm^3/sec], as a function of energy and altitude.

not seen in laboratory plasmas where states de-excite through collisional quenching first. In the low-density ionospheric plasma, forbidden emissions do occur, only at a lower rate compared with emissions from permitted transitions. As a result of this the O^+ ^2P state is meta-stable and the oxygen doublet emission has a radiative lifetime of around 5 seconds. The energy and altitude dependence of the forbidden oxygen doublet is shown in Figure 1.7a. The emission rates are again modelled using the electron transport model of Lummerzheim and Lilensten (1994) with monoenergetic electron precipitation. The emission peaks at altitudes of around 300 km and is most effectively excited by low energy (100 eV) electron precipitation. The long radiative lifetime causes the emission to be quenched at altitudes lower than around 250 km.

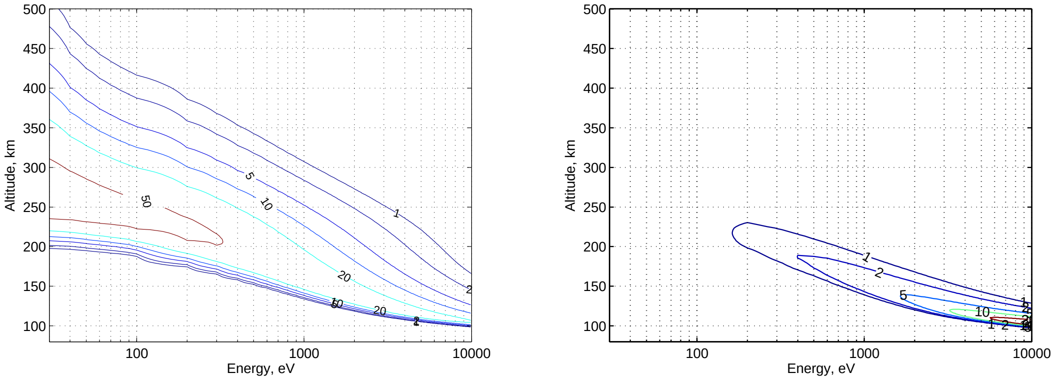

(a) Direct excitation

(b) Dissociation

Figure 1.8: Modelled atomic oxygen emission rates in units of [photons/cm^3/sec], as a function of energy and altitude.

1.7.3 O_2^+ band system

The first negative system of O_2^+, includes a strong emission peak at 5632 Å as well as other bands near 5250 and 6000 Å (Gattinger and Vallance-Jones, 1974), and produces some of the brightest prompt emission features in the auroral spectrum. The intensity of emission depends on both the energy of the precipitating particles and the atmospheric composition. The rapidly decreasing density of molecular oxygen with altitude results in the bands being most prominent at low E-region altitudes of around 110 km, i.e. produced by high-energy electron precipitation only. The modelled emission rate of the O_2^+ 1N band system is shown in Figure 1.7b.

1.7.4 O emission lines

The atomic oxygen lines at 7774 Å and 8446 Å have two main sources of production. In the F-region they result from the direct excitation of atomic oxygen (O + e^-) whereas in the E-region they are produced through dissociative excitation of molecular oxygen (O_2 + e^-). The O emission is suitable for characterising low energy precipitation at high time resolution, avoiding the problems with the long lifetime of the O^+ ^2P state. However, the emission must be used in combination with observations covering other oxygen spectral features in order to resolve the ambiguity of the source population. Figure 1.8 shows the modelled 7774 Å emission rates for the direct excitation process (panel a) and the dissociative process (panel b).

1.8 Incoherent scatter theory

Incoherent Scatter (IS) radars transmit a high power Ultra High Frequency (UHF) or Very High Frequency (VHF) electromagnetic wave into the ionosphere. Electrons in the path of the beam are accelerated by the incident wave and emit their own radiation as for any accelerating charged particle. If the electrons act in isolation this process is known as Thomson scattering. At the radar wavelengths, which are longer than the Debye length scale, electron behaviour is greatly influenced by the ion gas. In this case the scattered radiation is influenced by both electron and ion properties; this is known as incoherent scatter. The extremely weak scattered signal from the electrons (of order 10^{-17} W for a 1 MW transmitted beam) is detected by the radar receivers, and from it information about the ionospheric plasma in the radar beam can be deduced.

Power is received back from the ionosphere at frequencies other than the initial beam frequency, as a result of the Doppler broadening effect due to the motions of the scatterers. The collective behaviour of the plasma leads to the returned power being concentrated at particular frequencies, rather than being spread over a broad range corresponding to the large thermal velocity of individual electrons. The development of the expression for the incoherent scattering cross section is not repeated here, but leads to the result that most of the scattering is concentrated at natural electro-static wave modes within the plasma. A representation of a normal IS power density spectrum is shown in Figure 1.9. Increased scattering leads to peaks in power at frequencies where there is an ordered motion of the plasma, i.e. ion-acoustic waves at the ion-acoustic frequency KC_s and Langmuir waves near the electron plasma frequency. These spectral peaks are broadened by Landau and collisional damping to form the double humped ‘ion spectrum’ and the ‘electron plasma lines’ which occur at frequencies of around 5 kHz and several MHz respectively, relative to the central transmitter frequency. The symmetric nature of the radar power spectrum represents waves moving towards the radar receiver shifted to higher frequencies, while waves moving away from the radar are shifted to lower frequencies.

IS radar systems can only detect density fluctuations from waves which match the Bragg scattering condition. For any particular radar, the wave vector, or k-vector, for detectable waves, K_{IS} is related to the incident and scattered k-vectors, K_i and K_s, for the electrons:

$$K_{IS} = K_s - K_i \tag{1.8}$$

For a monostatic radar where the transmitter and receiver are at the same location, such as the system providing data for this thesis, K_s = -K_i, meaning that only waves

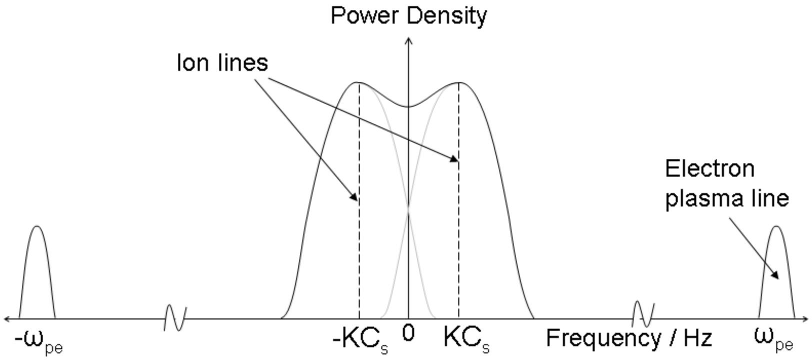

Figure 1.9: Schematic of a typical power density spectrum as measured by incoherent-scatter radar systems.

with a k-vector equal to twice the magnitude of the incident k-vector are detected. Excluding the case of bistatic radars where the illuminated scattering volume is at one specific altitude range, transmitting continuously with an IS radar would lead to backscattered signals from different altitude ranges arriving simultaneously at the receiver system. Pulse coding sequences, consisting of cycles of set transmission and reception intervals, are specially constructed in order to reduce the ambiguities in range. The altitude resolution is limited by the pulse scheme for all IS radar programmes, with the data being averaged over successive range gate intervals.

1.8.1 Deriving ionospheric parameters

When observing a weakly-scattering volume such as ionospheric plasma with IS radar, the statistical properties of the received signal are directly related to the statistical properties of the density fluctuations in the scattering volume. In the ionosphere most of the received power is due to scattering from electrons, having a much lighter mass than the ions. However, as the electrons are tied to the slower moving ions in the plasma, information about the ionospheric properties can be obtained, for the most part, by studying the ion-spectrum alone. This has advantages in that the ion-spectrum contains considerably more power than the electron-plasma lines and can be observed with less sensitive receiver systems. As a result of the larger ion mass, the ion-spectrum is also considerably narrower than the free electron spectrum in terms of frequency, meaning that it can be observed with a much smaller radar bandwidth.

A theoretical power density spectrum for the ion lines can be modelled using kinetic theory, for a thermal plasma with known properties. By comparing such theoretical spectra convolved with instrumental effects to the spectra recorded by incoherent scatter radar, the plasma properties of the sampled ionosphere can be deduced using an iterative least-squares fit procedure. As mentioned previously the temperature ratio determines the strength of Landau damping and therefore the broadening of the lines in the power density spectrum. Figure 1.10 demonstrates how the overall shape of the ion-spectrum alters depending on various ionospheric parameters. Low T_e / T_i ratios, high collision frequencies or high plasma temperatures all act to increase the level of damping, reducing the prominence of the separated ion-line peaks. In addition, the electron density is proportional to received power integrated over the ion-spectrum (almost equal to the total backscattered power as the plasma lines are comparably weak), and the ion drift velocity along the radar line of sight, V_i, is related to the displacement of the central valley between the ion-lines from the transmission frequency. The main parameters obtained directly through spectral fitting procedures, as employed in the Grand Unified Incoherent Scatter Data Analysis Programme (GUISDAP) and used in this thesis, are N_e, T_e, T_i and V_i. Other parameters, such as the ion composition and the ion-neutral collision frequency, can also be obtained.

It is important to note that derivation of ionospheric parameters in this way only applies for thermal plasma. When non-thermal effects alter the shape of the power density spectrum, i.e. asymmetric or enhanced ion-spectra or spectra including a peak at the central transmission frequency as observed by Winser et al. (1987); Lockwood et al. (1987), the fitting procedure can fail or produce spurious results. This effectively means there is no standard way of extracting ionospheric parameters from IS radar data during times of non-thermal plasma.

Non-thermal plasma spectra indicate instability associated with plasma turbulence, causing the growth of wave modes through positive gradients in the plasma distribution function. Linear and non-linear instabilities play an important role in redistributing accumulated energy and restoring the plasma to an equilibrium state. These instabilities are driven by free energy sources in the Earth's magnetosphere-ionosphere system and can act on a range of scales; from macroinstabilities resulting from plasma inhomogeneity, to smaller-scale microinstabilities caused by distortions to the distribution functions. Instability on small-spatial scales can lead to processes such as acceleration and heating which affect the large-scale structure and behaviour of the system as a whole. Turbulent processes are a common feature in all natural and laboratory plasmas, observed in astrophysical plasmas such as in accretion flows around stars and in the interplanetary medium, as well as in the solar wind and ionosphere. Understanding the complex nature of turbulent plasma processes remains an unsolved problem in fundamental physics and studies are essential in furthering knowledge of the behaviour of our plasma environment.

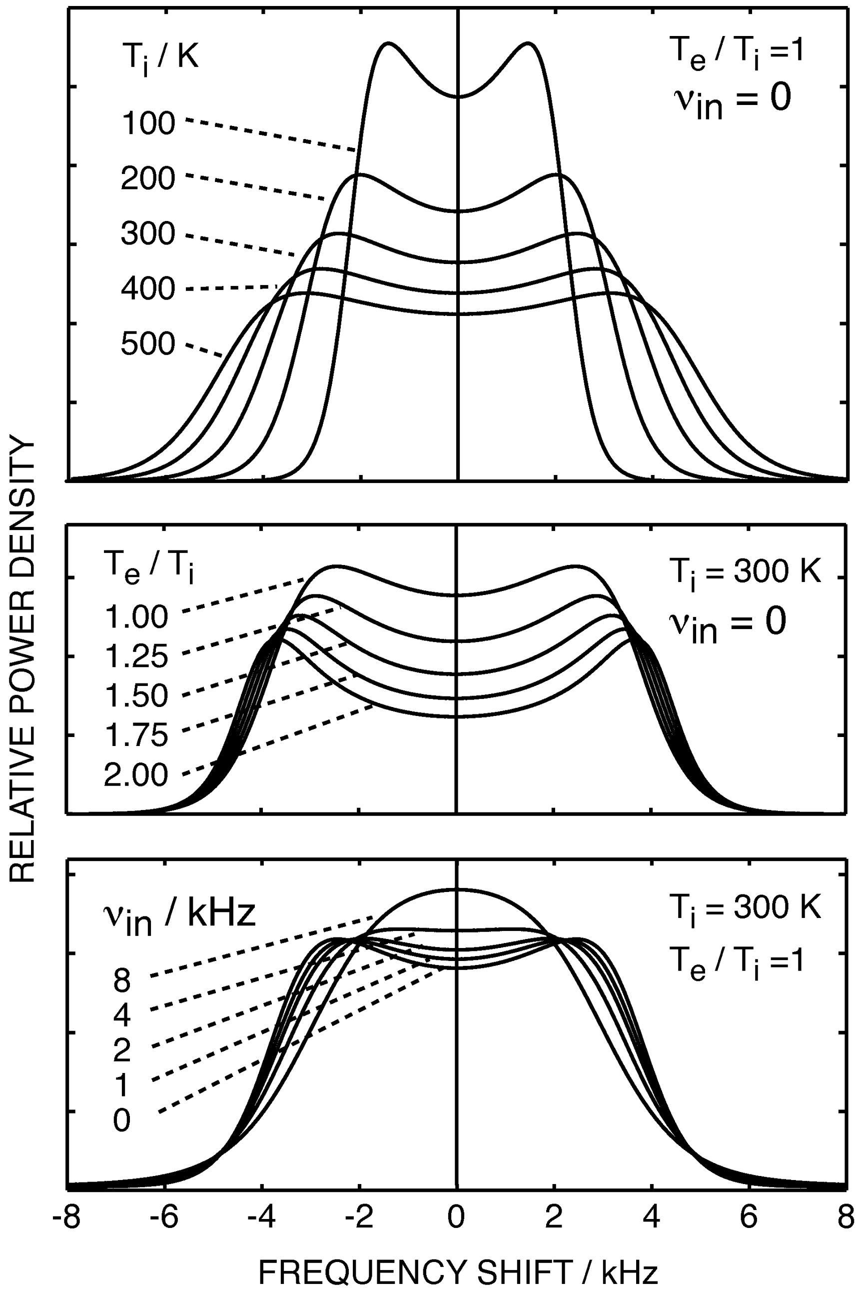

Figure 1.10: The effect of ion and electron temperature and collision frequency on the shape of the IS ion spectrum, taken from Nygrén (1996).

1.9 Observations of natural ion-acoustic enhancements

Received signals now commonly referred to as Naturally Enhanced Ion Acoustic Lines (NEIALs), have been reported in IS radar data sets over the last 20 years, representing the effect of a non-thermal plasma behaviour on the received power density spectrum. NEIALs appear as enhancements at the frequency of the ion-acoustic wave mode, increasing the strength of one or both or the up and downshifted ion-lines in the spec-

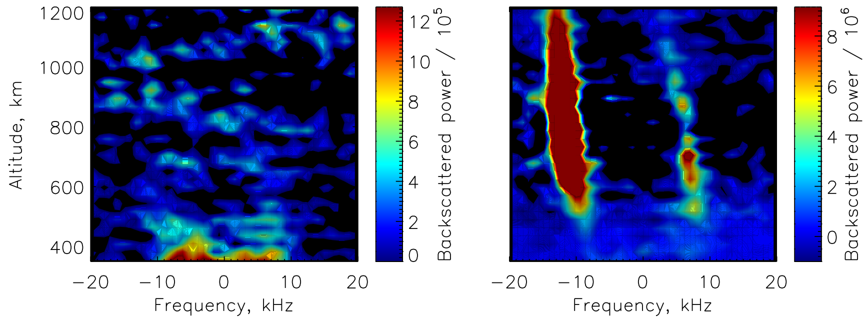

Figure 1.11: Examples of thermal (left) and naturally enhanced (right) ion-line spectra, measured by the EISCAT Svalbard radar on 22nd January 2004.

trum. Figure 1.11 gives examples of received power density spectra, demonstrating the difference between a normal thermal backscattered spectrum seen at the lowest altitudes in the left hand panel, and a NEIAL affected spectrum on the right. The NEIAL is over an order of magnitude stronger (note the difference in scale), suppressing the thermal spectrum and background noise in the right hand figure.

NEIAL signatures were first reported in the low-latitude night-side ionosphere with the Millstone Hill radar in North America (Foster et al., 1988), and have since been observed using the EISCAT radar systems (described in Chapter 2) in the high-latitude ionosphere, both on the nightside (Rietveld et al., 1991) and in the dayside cusp region (Buchert et al., 1999). The following section provides an overview of NEIAL characteristics, determined by previous observations using high-latitude IS radars and supporting instrumentation. This thesis is based on NEIAL observations in the dayside ionosphere, which exhibit some different characteristics from those recorded in nightside data.

1.9.1 Spatial and temporal characteristics

Many observations of NEIALs were originally discounted as enhanced scattering returns from satellites passing through the radar beam, rather than being of geophysical origin. However, by the early 1990s they were commonly accepted as natural plasma phenomena, with NEIAL spectra being typically observed over several hundred kilometer altitude ranges (as in the right hand panel of Figure 1.11), compared with satellites contaminating data within a single range gate (on the order of several kilometres).

A statistical survey of NEIAL occurrence altitudes has been given by Rietveld et al. (1996), using data from the European Incoherent Scatter (EISCAT) UHF radar in Tromsø, Norway, predominantly located within the nightside auroral oval. The occurrence rate was found to increase with altitude up to around 500 km, where the number of enhanced spectra peaked. Very few NEIALs were measured at altitudes below 250 km. A relationship between the altitude and the relative intensity of the up and down-shifted ion-lines was also evident. Above 300 km altitude, both lines showed enhancement to some degree, with the down-shifted line dominating in most cases. Below this, enhancement occurred in a single ion-line, with the up-shifted line becoming preferentially enhanced at lower altitudes below around 250 km. In data from the dayside cusp region, the same characteristics of changing line dominance with altitude are observed, although the height above which the downshifted line becomes dominant is higher at about 500 km. In addition, the peak occurrence altitude is higher at around 700 km (Grydeland et al., 2004). Observations of NEIALs from uncommonly large ranges were reported by Ogawa et al. (2006), who found enhancements between 1200 and 1900 km altitude.

A further spatial characteristic of NEIALs is their tendency to be predominantly observed in field-aligned data, i.e. where the radar is directed towards the local magnetic zenith. This indicates that NEIALs are related to field-aligned structures, and when they occur within a radar beam directed away from the magnetic zenith, they may well be misidentified as satellite signals or fail to produce the characteristic large increases in power. This interpretation was confirmed by recent interferometric studies, combining data from two separate IS radar receivers in order to resolve features within the commonly illuminated scattering volume (Grydeland et al., 2003). These studies have shown that NEIAL signatures originate from cylindrical structures aligned with the magnetic field, with field-perpendicular widths of the order 100 m, i.e. much smaller than radar beam widths.

NEIAL enhancements have been shown to vary between consecutive radar dumps at standard time integrations of 5 to 10 s (Rietveld et al., 1991), suggesting temporal behaviour of the instability on time scales shorter than this. Recent studies have employed radar data recorded at the raw voltage level at sub-second resolution, making it possible to follow the development of an individual NEIAL signature. Time series with 200 ms integrations show continuous evolution of power enhancements. Simultaneous enhancements in both ion-lines are frequently seen on these sub-second time scales, albeit with changes in relative intensity. Before the advent of sub-second resolution data, symmetrically enhanced spectra within a common volume were often thought to result from successive enhancements in each ion-line, summed through temporal averaging. Results from high temporal resolution radar data are not consistent with this interpretation (Grydeland et al., 2003).

1.9.2 Power and frequency dependence

The power level received during a NEIAL signature is increased by up to 3 orders of magnitude over the power for a normal thermal spectrum. The measurements of filament widths much smaller than the radar beam width (perpendicular to the magnetic field) indicates that the scattering cross section must be increased by up to 5 orders of magnitude above thermal level within the filament, in order to explain the observed levels of enhancement in data integrated over the entire beam width (Grydeland et al., 2003).

There are indications of instrumental selection effects associated with NEIALs, in that they are more commonly observed with some IS radar systems than others sampling the same ionospheric regions. In the case of two separate radars located at Tromsø, Norway, NEIALs are far more likely to be observed with the VHF radar (224 MHz) than the the UHF radar (933 MHz), for example in the event reported by Cabrit et al. (1996). The peak occurrence rate for NEIALs seen with the Tromsø VHF radar was also seen to occur higher in the ionosphere at around 800 km altitude, compared to at 500 km for the UHF data. This frequency dependence was later investigated in more detail in studies of power received across the narrow operating frequency range of an individual radar (Buchert et al., 1999; Ogawa et al., 2000; Forme et al., 2001). Indications were found of variations, in both the power received and the changes with altitude, as a function of wavelength, although conclusions are limited by the radar data integration times of several seconds. A further observation of note is the detection of enhanced Langmuir waves accompanying NEIAL signatures, both in the nightside ionosphere (Rietveld et al., 2002), and on the dayside (Strømme et al., 2005). The implications of such studies in terms of the generation mechanisms proposed to explain NEIALs are discussed in Section 1.10.

1.9.3 Links with auroral activity and other ionospheric parameters

In early studies using photometer and all-sky camera data, NEIALs, in both the dayside and nightside ionosphere were associated with the boundaries of auroral arc systems, specifically for red auroral activity (Collis et al., 1991; Rietveld et al., 1991). In more recent studies using cameras of narrower field of view and higher time resolution, NEIALs on the dayside have been associated with dynamic rayed auroral forms and coronal structures (i.e. tall rays in the magnetic zenith giving the perspective effect of a crown). Dynamic rayed aurora often has the appearance of ‘flaming aurora’, an effect caused by the differing times of flight for the precipitating population, suggesting a mixture of energies. Optical studies using white light cameras on the dayside have shown a link between NEIAL occurrence and rayed auroral filaments of similar scale size at sub-second resolution (Blixt et al., 2005; Grydeland et al., 2004).

However, NEIALs observed in the nightside ionosphere have recently been associated with the dark region immediately adjacent to an active auroral arc (Michell et al., 2008), rather than with rayed coronal forms. It is not yet clear whether smaller rayed filaments were present in the 'dark' region albeit with a much reduced intensity, or whether the links with aurora differ on the nightside, perhaps reflecting the different auroral morphology or even different generation mechanisms producing similar signatures in IS radars. With the NEIALs varying on such short time-scales, and the similarly active nature of the associated aurora, observations of high temporal and spatial resolutions are essential in clarifying the link between auroral intensity and NEIAL development.

NEIAL signatures are commonly associated with other ionospheric parameters, namely increased electron temperatures (Rietveld et al., 1991; Wahlund et al., 1993) of up to around 10,000 K (Forme and Fontaine, 1999) and 'Type 2' ion upflow events (Wahlund et al., 1992b). Type 2 upflows are caused by soft electron precipitation enhancing the electron temperature and pressure gradient, allowing electrons to flow upwards. This causes the generation of an enhanced parallel electric field, accelerating ions upwards in the ionosphere. These observations are therefore consistent with the relationship between NEIALs and auroral activity.

1.10 NEIAL generation mechanisms

A number of generation mechanisms have been invoked to try and explain NEIALs in IS radar data since they were first understood as signatures of geophysical plasma phenomena. These can be broadly categorised into two groups: those proposing direct destabilisation of the ion-acoustic mode by counter-streaming species, and those suggesting the generation of ion-acoustic waves through the parametric decay of unstable Langmuir waves. The mechanisms and their implications were reviewed in Sedgemore-Schulthess and St.-Maurice (2001), and are briefly summarised in the following section. None of the mechanisms can explain the detailed behaviour for all NEIALs detected in the ionosphere, although recent observations in the dayside cusp appear to be most easily modelled using the parametric decay theory.

1.10.1 Ion-ion or ion-electron streaming instabilities

Variations of this mechanism were proposed to interpret early reports of observed NEIALs, invoking flows of counter-streaming charged particles, either for two ion populations (Wahlund et al., 1992a) or for ions and electrons (Rietveld et al., 1991). However, in order to reproduce the enhanced power levels observed in NEIALs, extremely large flow densities are required.

In the case of ion-electron (current driven) streaming, with a cold background ion population and a heated electron population, a positive density gradient can be generated in the distribution function of the drifting electrons. Ion-acoustic wave growth will occur if the region of positive gradient lies near the phase velocity of ion-acoustic wave modes, as long as the ion distribution function remains at smaller velocities to negate the effect of Landau damping due to ions. In order to produce the necessary drift velocities requires current densities of several mA m^{-2} which are not directly observed in in-situ satellite data, but which are have been postulated to exist on short time scales in small current layers (Sedgemore-Schulthess et al., 1999). However the current driven mechanism will either act on down-going or up-going ion-acoustic waves depending on the current direction and cannot explain enhancements in both ion-lines simultaneously without temporal or spatial averaging in the radar data. High time resolution and interferometric studies in the dayside cusp do not support this interpretation, although some observations of asymmetric NEIALs in the night-side ionosphere show behaviour more consistent with a current driven interpretation, especially with enhancements occurring at low altitudes ($<$250 km).

Wahlund et al. (1992a) proposed an alternative approach using the ion-ion two stream instability, involving relative drifts between two ion species, e.g. H^+ and O^+ in the topside ionosphere. This mechanism does not require high current densities, but relies on densities of the minority species (i.e. H^+) that are higher than usually observed. This mechanism also requires ion drift velocities that are similar in magnitude to the ion thermal velocity. For large drift velocities (more than four times the thermal velocity), simultaneous enhancements in both ion-lines can be generated. However, such drifts are unlikely to be present in the lower F-region and below, where NEIALs are observed. Additionally not all NEIAL observations coincide with upflow activity and the ion-ion streaming mechanism also relies on some previous acceleration mechanism acting specifically on one population over the other, to cause the relative drifts.

1.10.2 Parametric decay of Langmuir waves

This mechanism relies on a large influx of electrons (auroral precipitation), causing wave growth at Langmuir wave mode frequencies, through the beam instability as described in 1.5.2. For specific beam conditions and ionospheric parameters, the generated Langmuir waves themselves are unstable, and undergo parametric decay. The pump Langmuir waves, $\omega^{l}(k^{l})$, decay into secondary Langmuir waves, $\omega^{l\prime}(k^{l\prime})$ at successively smaller wavenumber, and ion-acoustic waves, $\omega^{s}(k^{s})$, as part of a three wave interaction. It is the resulting ion-acoustic waves which are proposed to cause the ion-acoustic enhancements seen in IS radar data as NEIALs (Forme, 1993, 1999). The wave vector of the secondary Langmuir wave, which can also grow to exceed the instability threshold, is in the opposite direction to the pump Langmuir wave. Enhanced ion-acoustic waves travelling in either direction along the field line can therefore be generated in successive cascades of the decay process within the same volume. For the nth cascade the three-wave interaction conditions are:

$$\omega_{n}^{l\prime}+\omega_{n}^{s}=\omega_{n-1}^{l} \tag{1.9}$$

and

$$k_{n}^{l\prime}+k_{n}^{s}=k_{n-1}^{l} \tag{1.10}$$

Modelling results have shown that the relative amplitude of the two ion-lines can change on time scales of less than 100 ms, depending on when the three wave cascading process stops (Forme, 1999).

The ion-acoustic enhancement occurs over a restricted range of wave vectors, Δk, linked to the velocity spread of the electron beam, ΔV_b, by the relation:

$$\frac{\Delta k}{k}=\frac{\Delta V_b}{V_b} \tag{1.11}$$

where k and V_b are the average enhancement wave vector and beam velocity respectively. The received power depends very strongly on the wave vector for this mechanism, consistent with observations of dependence on radar transmission frequency for selected NEIAL events (Buchert et al., 1999). Beam electrons of low energy (10s - 100s of eV) are needed in order to generate ion-acoustic enhancements at the wave vectors of IS radars. This could explain the observed link between NEIALs and rayed coronal forms in dayside aurora, thought to contain a broad range of energies.

The parametric decay model has no requirement for current or ion densities significantly higher than have been observed. Beam densities of less than 10^{5} m^{-3} have been shown to produce multiple cascades for a beam energy of 30 eV. With a sufficient large spread in beam energy, the wave vector condition for detection by a radar can be satisfied by wave enhancements from the first and second cascade simultaneously. Changes in the beam parameters are analogous to a constant beam streaming through background plasma with changing parameters, i.e. changing atmospheric density and temperature altering the collision frequency with altitude. Consideration of the inhomogeneity of the ionospheric plasma has been shown to be a possible explanation for the changing dominance of one ion-acoustic line over the other with altitude, as observed in NEIALs (Forme et al., 2001). In more recent studies, the effects of plasma inhomogeneity and non-linear processes have been simulated numerically, in order to further understand the role of beam driven Langmuir turbulence in NEIAL generation (Kontar and Pécseli, 2005; Guio and Forme, 2006; Daldorff et al., 2007).

There have also been several reported observations of enhanced Langmuir waves accompanying NEIAL signatures, both in the nightside ionosphere using the EISCAT UHF and VHF receivers at Tromsø (Rietveld et al., 2002), and on the dayside using the EISCAT Svalbard Radar (Strømme et al., 2005). Streaming instabilities cannot generate high frequency plasma waves, whereas an electron beam with large energy spread ($\Delta V_b > 1/3V_b$) can trigger primary Langmuir waves over a sufficiently large bandwidth, such that the Bragg condition can be satisfied for both ion-acoustic and Langmuir waves in the same plasma volume (Strømme et al., 2005). The parametric decay mechanism can explain many of the features recently observed in NEIAL signatures, and has become the favoured theory for NEIALs in the dayside cusp, although other mechanisms can contribute to or even dominate the behaviour of some selected events, especially on the nightside.

1.11 Thesis summary

The principal aim of the work presented in this thesis is to advance our understanding of NEIAL echoes, which cause the backscattered power to increase by several orders of magnitude when recorded by incoherent scatter radar receivers. These signatures of plasma instability are not fully understood in terms of their generation and behaviour in the high-latitude ionosphere. Similar non-thermal plasma phenomena are likely to occur in both astrophysical and laboratory plasmas, leading to potential applications of this work to other disciplines in the future. This thesis concentrates on their relationship to small-scale structures in the auroral morphology and in the precipitation spectrum, along with what this implies for the proposed theories.

As with all solar-terrestrial research, the use of a wide selection of instrumentation is essential in order to understand the behaviour of the Sun-Earth system on large scales and to monitor coupled smaller-scale variations in detail. Chapter 2 gives a description of the instruments used in this thesis, including ground-based instruments used for remote-sensing of the ionosphere as well as in-situ satellites sampling particle populations directly. Many of the ground-based instruments are run directly by the University of Southampton, including the newly-built Auroral Structure and Kinetics (ASK) imager. All new techniques for the set-up of the instrumentation and the processing and analysis are described in Chapter 3.

Chapter 4 discusses the relationship between the morphology of small-scale auroral structures and the precipitating energy spectrum. A combined study of auroral behaviour is presented using multi-spectral imagers with extremely small fields of view and electron energy information from an optical spectrograph. The results demonstrate the role of a large component of low-energy electrons in the formation of rayed coronal structures at magnetic zenith. Multi-spectral imaging techniques are then used to provide information on auroral structures and energy during a period of multiple NEIAL observations, as described in Chapter 5. A direct link is shown between NEIAL signatures and low-energy emission intensity during the passage of coronal rayed structures. The implications of this relationship for the proposed NEIAL generation mechanism are discussed, and numerical simulations show the production of NEIALs for ionospheric conditions which match those observed.

Finally, Chapter 6 looks ahead to the next big advance in the study of NEIALs. Using multiple radar dishes together, NEIAL enhancements have been shown to originate in cylindrical filaments with scale sizes much smaller than the radar beam. Statistical studies can be used to investigate NEIAL behaviour and the relationship with auroral activity for cases where many NEIALs are observed within a short time period. However, in order to follow the evolution of a single NEIAL and its location with respect to auroral filaments (thereby resolving unknowns about NEIAL formation and development) requires spatial resolution within the normal radar beam width. The development of the interferometry technique and subsequent analysis is in its infancy. Chapter 6 describes a method to calibrate the spatial information obtained through interferometric phase products with respect to the location of small auroral features. This thesis concludes with a brief discussion in Chapter 7 of the advances made through work presented here and the questions that still remain to be answered in this field in the future. Appendix A defines the coordinate systems that apply to the data discussed.

2

Instrumentation

2.1 EISCAT Radars

The EISCAT (European Incoherent Scatter) scientific association runs three radar systems, applying the principles of incoherent scatter theory as described in Section 1.8. All of the EISCAT radars use a co-located transmitter and receiver. The intervals of transmission and reception are controlled using coded pulse sequences, which determine the range resolution of the received data. The EISCAT radar beams are generated by a collection of klystrons which accelerate electrons through a series of resonant cavities, modulating the electron stream density to produce amplified radio waves. The EISCAT mainland radar site just outside Tromsø in northern Norway, at $69^\circ 35'$ N, $19^\circ 14'$ E in geographic coordinates, has a VHF and a UHF radar running at 224 MHz and 931 MHz respectively. The VHF antenna consists of a 40 m by 120 m parabolic trough which can be run as two independent steerable arrays. The UHF radar is a 32 m steerable Cassegrain antenna, having a secondary reflector above the main dish for focussing. Additional passive receiver stations are located in Sodankylä, Finland, and Kiruna, Sweden to give a tri-static capability for the mainland system. In 1996 the EISCAT Svalbard Radar was added, to the north of the Norwegian mainland, as described further in Section 2.1.1.

Figure 2.1: The EISCAT Svalbard Radar (ESR) with (foreground) the 42 m fixed antenna and (background) the 32 m steerable antenna. (Photograph courtesy of Dan Whiter)

2.1.1 EISCAT Svalbard Radar

The EISCAT Svalbard Radar (ESR) is an incoherent scatter radar facility, just outside Longyearbyen at 78°9′ N, 16°2′ E, on the Norwegian island of Spitsbergen, part of the Svalbard archipelago. Its location means it is ideally situated to study dayside cusp phenomena. The ESR, shown in Figure 2.1, consists of one steerable 32 m antenna and one 42 m antenna, fixed in the field-aligned direction of 181.0°in azimuth and 81.6°in elevation. The exact pointing direction of the 42 m beam is adjusted to correspond to the International Geomagnetic Reference Field (IGRF) model value for the magnetic zenith direction, through use of a secondary reflector above the centre of the antenna which can be altered slightly in position. The ESR operates at a frequency of 500 MHz and has a transmitting power of up to 0.9 MW.

2.2 Spectrographic Imaging Facility

The Spectrographic Imaging Facility (SIF) is an optical instrument platform, operated by the University of Southampton and University College London, designed to study auroral emissions at high temporal and spatial resolution (McWhirter et al., 2003; Lanchester et al., 2003). From October 2000 until November 2007, SIF was located

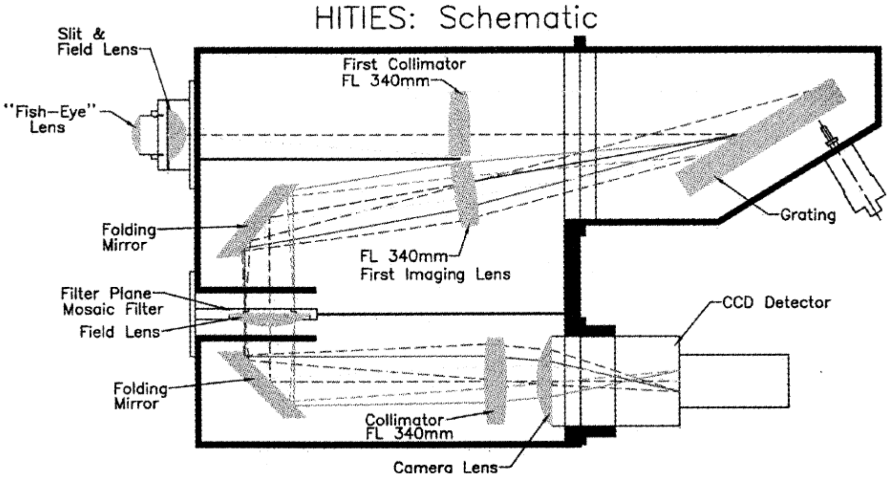

Figure 2.2: Schematic diagram of HiTIES, taken from Chakrabarti et al. (2001).

at the Auroral Station in Adventdalen (Sigernes et al., 2002), just outside Longyearbyen, Svalbard at 78°12′ N, 15°50′ E. This lies approximately 7 km north-west of the ESR. In November 2007, due to the increasing light pollution from Longyearbyen and the advantages of greater co-location between optical instrumentation and the EISCAT radar beam, the facility was moved to a new site at the Kjell Henriksen Observatory (KHO), a few hundred metres from the EISCAT radar.

The instrument platform consists of a narrow field intensified auroral imager, a High Throughput Imaging Echelle Spectrograph (HiTIES) and four supporting photometers with interchangeable narrow-band filters. All instruments are co-aligned and pointed towards the magnetic zenith according to the procedures outlined in Section 3.1. At the time of the move to the KHO, a new data storage array, with a capacity of 6 TB, was added to the instrument setup, allowing data for the majority of the observing season to be stored without need for on-site intervention. Timing accuracy between the instruments was also improved. A Network Time Protocol (NTP)-synchronised master clock was added, which feeds time signals through to the computers operating the photometers and HiTIES, and to the time stamp on the digital video feed for the auroral imager (see Section 2.2.2).

2.2.1 HiTIES :- High Throughput Imaging Echelle Spectrograph

The spectrograph on the SIF platform was originally designed and built at Boston University, by the Center for Space Physics (Chakrabarti et al., 2001). Light enters the instrument through a curved slit, 8 degrees in length when mapped onto the plane of the sky. The light is separated according to the wavelength using an echelle grat-

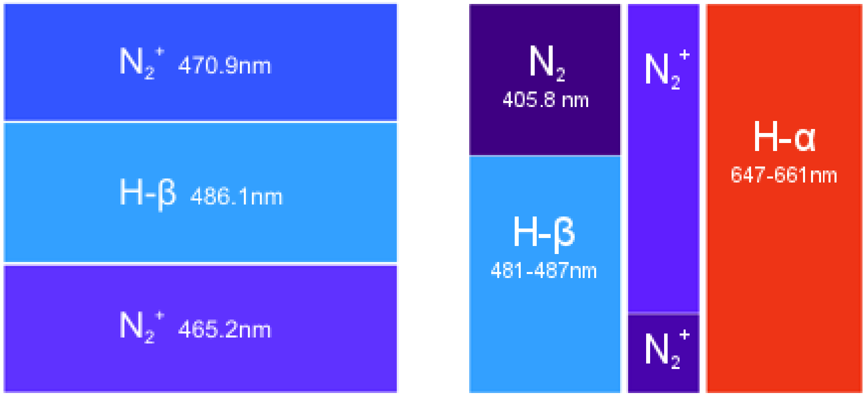

(a) H_β and N_2 emission filter

(b) Extended H_β and N_2 emission filter

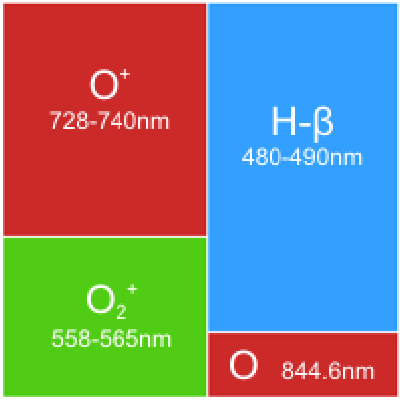

(c) ASK spectrographic support filter

Figure 2.3: The configurations of the HiTIES mosaic filters, showing the wavelength range and the spectral feature or region imaged by each panel.

ing, a specific type of diffraction grating optimised for higher orders, useful for high resolution spectrographic instruments. The optical layout of the HiTIES instrument is shown in Figure 2.2.

In the resulting diffracted image, having a spectral resolution of around 1 Å per pixel, successive orders are overlaid on top of each other, making spectral signatures of emission lines impossible to separate without the use of filtering. A filter mosaic is used to select different spectral regions of interest for different parts of the detector area. Since the initial installation of HiTIES on Svalbard, three different filter mosaics have been used to image in several different spectral bands of interest. Diagrams showing the wavelength regions of the filter panels and their configuration are given in Figure 2.3, for each of the mosaics. This thesis involves data from the four panel mosaic filter (Figure 2.3c), which was designed to support the ASK instrument (see Section 2.3), covering similar spectral ranges as the filters used on the ASK cameras.

The HiTIES detector technology has evolved throughout the lifetime of the SIF instrumentation. In November 2005 the current CCD detector was installed on HiTIES. This consists of an Andor iXon Electron Multiplying CCD (EMCCD) with 512 by 512 pixels. With the EMCCD the low-light signal is amplified on the chip itself before the readout amplifier. This is in contrast to a conventional intensified CCD where the readout noise is amplified along with the signal, giving a poorer signal to noise ratio. The Andor EMCCD used on HiTIES uses water cooling to reduce the operating temperature down to -80°. This results in very low levels of dark noise, and means that high quality data can be obtained with integration times as short as to 5 seconds. Prior to October 2005, HiTIES was running with a CCD detector supplied by PixelVision, which again used water cooling, and had a resolution of 1100 by 1050 pixels. A Microchannel-plate Intensified CCD (MIC) was also in use for selected time intervals, namely during the winter 2001/2002 observing season and in January 2004. With a higher noise level present in both and a problem with MIC in particular of low sensitivity at the red end of the light spectrum, these detectors were retired after the installation of the Andor EMCCD.

2.2.2 Narrow field imager, ‘TLC’

The narrow field auroral imager, known as The Little Camera (TLC), is based on a commercially available video CCD camera, provided by Photonic Science Ltd, with an added intensifier to increase sensitivity in low light. TLC is fitted with a long-pass filter, which eliminates the long-lived auroral emissions at wavelengths shorter than 6450 Å (specifically at 5577 and 6300 Å) which would smear the image. This results in the TLC imager being primarily sensitive to the $N_2$1PG emissions in the passband as described in Section 1.7.1, but also including the OII doublet, and a number of atomic oxygen transitions.

From the original installation of SIF on Svalbard up until November 2007, TLC was equipped with an f1.2 lens, focal length of 50 mm, giving a field of view of 16 degrees by 12 degrees. When SIF was moved to the new auroral station, TLC became ideal as a supporting wider angle camera, to place small scale images from the ASK instrument (see Section 2.3) in context within larger auroral features. The camera was then fitted with a 15 mm Sigma fisheye lens, which gives a larger field of view with a 68 degree diagonal (assuming a linear projection) intersected by the TLC sensor diameter of 18 mm. For all TLC imager data referred to in this thesis, the original narrow field lens configuration was in use.

The change in instrument site also prompted a change in the way video camera data was stored. At the Auroral Station in Adventdalen, video was recorded on a

SVHS recorder in time lapse mode which provided imaging data at a resolution of 5 frames per second. For particular short intervals, scheduled to coincide with EISCAT radar operations or during active conditions, data were recorded onto Digital Video (DV) tapes at full resolution at 25 frames per second. This system of manually recording data meant that TLC data were only stored when someone was available at the Auroral Station. It also required the digital capture and conversion of the recorded video into digital image frames before it could be analysed. The increased SIF data storage after the move to the KHO meant that video camera data could instead be captured directly to computer in real time, and saved as raw digital video streams on the data server. The resolution of the saved data streams can be remotely controlled via software, leading to TLC data being available at any required resolution for the entire observing season, from November 2007 onwards. As mentioned at the beginning of this Section, time stamping on the video stream was done via an NTP-synchronised master clock from this point onwards. Prior to the move to the KHO, the timing for TLC was set manually to the nearest second, and then fine-tuned to a much higher degree of accuracy by comparing satellite passages, seen in both TLC and a second time-synchronised imager. This procedure is explained in detail in Section 3.3.1.

2.2.3 Photometers

On initial installation, SIF was equipped with two supporting photometers, based on Hamamatsu photomultiplier detectors, with low noise photocathodes. The sensitivity has been calculated at 20 counts per second per Rayleigh (McWhirter et al., 2003). In November 2004 two additional photometers, identical in specification, were installed to complete the current configuration. The time resolution is adjustable up to 16 Hz, with the current software setup. Each photometer is fitted with an interference filter of 10 Å bandwidth. From the initial setup to the current configuration, many different filter combinations have been used. Photometer data was used to identify times of auroral activity, but was not used in further detail for the work presented in this thesis.

2.3 ASK - Auroral Structure and Kinetics

The Auroral Structure and Kinetics (ASK) instrument (Ivchenko et al., 2008) was designed to study small scale auroral features at very high temporal and spatial resolution. It was originally designed and built at the University of Southampton in 2005,

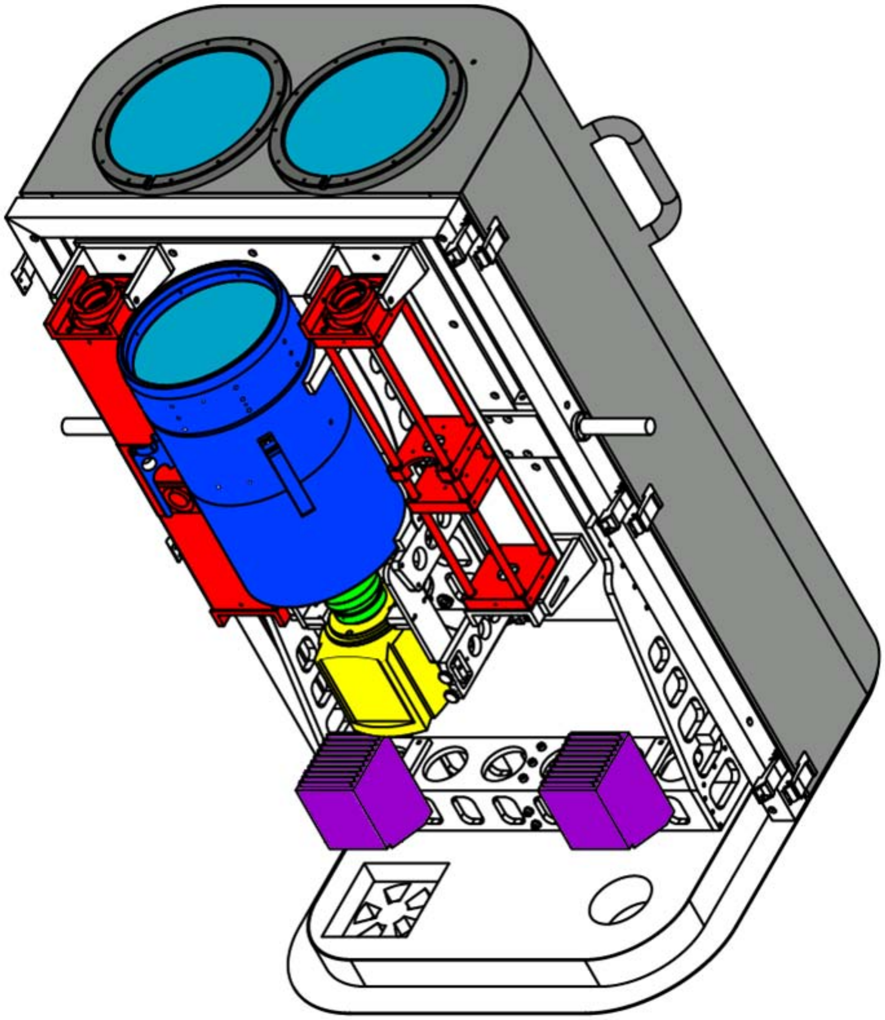

Figure 2.4: Schematic diagram showing the components of the Auroral Structure and Kinetics (ASK) instrument.

and is now run as a joint collaboration with the Alfvén Laboratory KTH, Stockholm. ASK consists of three separate auroral cameras, each fitted with a narrow-band interference filter to image in different wavelength regions, and two supporting photometers.

A schematic diagram of the instrument is shown in Figure 2.4. Mounted inside the bottom half of the optical housing are the two photometers (shown in red) and one of the Andor EMCCD detectors (yellow) with Kowa lens (green) and telescopic converter (blue). The top half of the housing, shown with the external cover on, contains the other two identical cameras. At the base of the optical casing, two heating systems with circulatory fans can also be seen (purple). Conventional multi-spectral auroral imaging uses a filter wheel to cycle consecutively through different wavelength regions. With the three separate cameras on ASK, imaging in different spectral bands is truly simultaneous. ASK can therefore be used to study the relationship between fine-

Table 2.1: ASK filter characteristics for the 2005/2006 campaign season.

Camera	Central wavelength, Å	Spectral width, Å
ASK 1	5620	26
ASK 2	7319	10
ASK 3	7774	15

scale auroral features and characteristic energy at much higher temporal resolution.

The interference filters fitted on the ASK cameras are interchangeable, and a variety of different filter combinations have been used for different observing locations and science priorities. This thesis concentrates on ASK data during the instrument's first season of operation at the EISCAT site on Svalbard. The filters in use during that season are therefore described in full here. An overview of the central wavelengths and the spectral Full Width Half Maximum (FWHM) is given in Table 2.1

The ASK filters are designed to cover the key auroral emission features, as described in Section 1.7. The ASK 1 filter covers the wavelength range of two emission bands of the O_2^+1N system present in the E-region of the ionosphere: $O_2^+1N(1,0)$ and $O_2^+1N(2,0)$. This spectral range is also covered by the O_2^+ panel on the HiTIES four panel mosaic filter (Figure 2.3c), for comparison. The filter on ASK 2 detects emission from the forbidden oxygen line at 7320 Å, occurring higher up in the ionosphere at F-region altitudes. Other contaminating emissions are also present. Hydroxyl airflow emission lines and emission from $N_2$1PG bands lower down in the E-region act as contaminants within the wavelength range covered by the ASK 2 filter. The same spectral features are again present in the corresponding wavelength range of the O^+ panel on HiTIES. Finally, the ASK 3 filter is centred on the atomic oxygen emission line at 7774 Å. In this case the relevant panel on the HiTIES spectrograph does not cover a similar wavelength range, but is centred on another atomic oxygen emission line, produced through equivalent processes, at 8446 Å.

Each of the cameras uses an Andor iXon EMCCD 512 by 512 pixel detector, identical to the one used currently on the HiTIES instrument on SIF. The CCD temperature is reduced to -49° thermoelectrically using air cooling within the detector housing itself. The detectors are each equipped with a Kowa 75 mm lens giving a field of view of 6.1° by 6.1°. The low-noise EMCCD detectors mean that the ASK instrument can be run at time resolutions of up to 20 frames per second without any pixel binning, or up to 50 frames per second with pixel binning i.e. applying 2 by 2 binning to give an effective detector area of 256 by 256 pixels. In October 2006, telescopic converters were added to each of the cameras, doubling the angular magnification i.e. giving a smaller 3°wide field of view. ASK data presented in this thesis use the origi-

Figure 2.5: Photograph of the ASK instrument, mounted on the side of the ESR transmitter hall.

nal pre-telescope configuration.

ASK has been run at both of the EISCAT transmitter sites, i.e. at Tromsø in the north of mainland Norway and on Svalbard. At Svalbard the ASK instrument was installed on a platform attached to the outside of the main transmitter hall, as shown in Figure 2.5. The ASK instrument was designed to be run outdoors for reasons of portability and to increase the number of possible observing sites. There were also no inside observation facilities available at the EISCAT radar site on Svalbard at the time of its manufacture. Three computers, one to control each of the cameras, are also located outside in a container at the base of the main optical housing. A heating and circulation fan system is therefore employed to try and keep the computers and instruments at a stable temperature, and also to keep the optical windows for the cameras and photometers free of ice and snow.

Data are passed continuously to the ASK master computer, which is kept indoors, via the network. For normal running, ASK generates approximately 40 Gb per hour (at 20 Hz with 2 by 2 pixel binning). Data therefore need to be written onto LTO-2 storage tapes daily via the ASK master computer, throughout the campaign season. Online keograms, giving a summary of auroral activity in the cameras, are automatically generated in real time. High resolution data for cloudy or quiet periods can then be deleted before writing to tape.

2.4 Andor imager

The Andor imager was provided by Andor Inc. on loan for January 2004, and was located at the Auroral Station in Adventdalen beside the SIF platform. It was used as a test camera in the feasibility study for the Auroral Structure and Kinetics (ASK) project. The imager used an Andor iXon EMCCD detector, identical to those fitted on the completed ASK instrument and the current configuration of HiTIES. For the data shown in this thesis the Andor imager was running with 2 by 2 pixel binning at a time resolution of 2 frames per second, although these settings were variable and software-controlled. The detector was fitted with a 50 mm lens providing a 9°square field of view and a narrow interference filter of central wavelength 7325 Å and FWHM 30 Å. The filter is centred on the forbidden oxygen (OII) ^{2}P - ^{2}D doublet at 7320 and 7330 Å as described in Section 1.7.2. However, the oxygen doublet is embedded in the first positive band of molecular nitrogen, meaning that some $N_2$1PG emission is also detected within the Andor passband.

2.5 Odin imager

The Odin camera, shown in Figure 2.6, is run by the University of Tromsø. Odin records data onto DV tapes during specific events or timed instrument collaborations, rather than continuously through the winter season. Odin, described fully in Blixt et al. (2005) is a white light, intensified auroral imager with field of view 14.3°by 10.9°. The hardware produces a standard video signal at 25 frames per second, which is then converted to DV format in real time. The time code is synched to Global Positioning System (GPS) satellite time signals, which allows the recorded video data to be synchronised with other instruments, and can be stamped directly onto the saved image frames. The portable nature of Odin has led to its use at both of the EISCAT radar transmitter sites, in Tromsø and on Svalbard. In both cases the imager was located close to the EISCAT antennas, and is pointed towards magnetic zenith, i.e. with a look direction co-aligned with the EISCAT radar beam.

Figure 2.6: Photograph of the University of Tromsø Odin imager, mounted at the EISCAT radar site in Tromsø. (Photograph courtesy of Dan Whiter)

2.6 IMAGE magnetometer chain

The International Monitor for Auroral Geomagnetic Effects (IMAGE) network (Viljanen and Häkkinen, 1997) consists of 30 ground-based magnetometer stations across Scandinavia, northern Russia and Estonia, as shown in Figure 2.7. The IMAGE network uses fluxgate magnetometers to monitor geomagnetic activity, in the form of current systems and wave motions in the coupled magnetosphere-ionosphere system, across large areas of the globe. The IMAGE magnetometer network is predominantly used in combined studies with other instruments which take measurements at a single point i.e. the EISCAT radars. The large-scale coverage of the magnetometer network can help to solve the temporal-spatial ambiguity problem during times of moving current systems. Each magnetometer station consists of a three-axis fluxgate magnetometer measuring three components of the terrestrial magnetic field, X (north), Y (east) and Z (downwards), using a local geographic coordinate system (Appendix A).

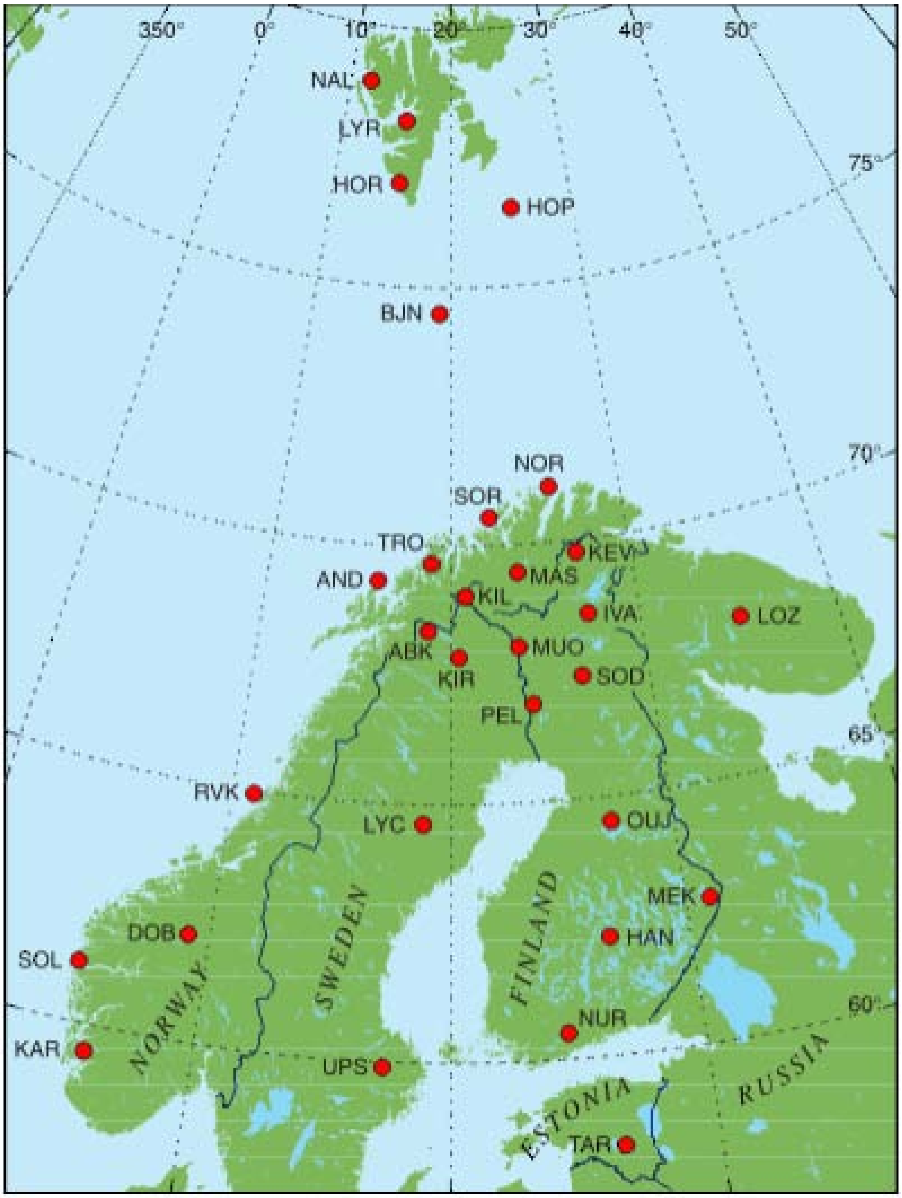

Figure 2.7: Map showing the location of the IMAGE magnetometer stations, as of November 2007. (Modified from original map drawn by Lasse Häkkinen)

2.7 Satellite Instrumentation

2.7.1 Advanced Composition Explorer (ACE) satellite

The Advanced Composition Explorer (ACE) is a satellite currently in orbit around the L1 Lagrange point (a gravitational equilibrium point between the sun and the earth), approximately 1.5 million kilometres from the earth, upstream in the solar wind. It carries a suite of instruments designed to provide near-continuous coverage of solar wind parameters and to measure particle intensities both from the sun and from galactic sources. This thesis uses data from two instruments on board the ACE satellite:

the Solar Wind Electron Proton Alpha Monitor (SWEPAM) and the Magnetic Field Experiment (MAG).

The SWEPAM instrument (McComas et al., 1998) provides information on the solar wind particle flux (densities, velocities and temperatures) for ions and electrons simultaneously. Electrostatic analysers are used to measure the energy per unit charge based on the curved path of charged particles as they pass through the detector systems. The SWEPAM instrument is sensitive to ion energies between 0.26 keV and 36 keV and electron energies between 1.6 eV and 1350 eV. The spin of the ACE spacecraft means that the instruments can make full 3D plasma measurements, giving 64 second averages of solar wind parameters.

The MAG instrument on ACE (Smith et al., 1998) gives near-continuous measurements of the three components of local magnetic field, using a pair of triaxial fluxgate sensors, similar to those used in the ground-based IMAGE magnetometer chain. The sensors are mounted on booms about 4 metres away from the main spacecraft. The instrument has a very large range in sensitivity, measuring fields of between 0.0001 and 65,536 nT per axis. The MAG instrument provides measurements of the IMF using a standard integration time of 16 seconds, with 1 second data available for selected intervals.

2.7.2 Defence Meteorological Satellite Programme (DMSP)

The Defence Meteorological Satellite Programme (DMSP) group of satellites orbit the earth at an altitude of approximately 850 km, covering the polar regions at least twice per day. A collection of instruments provide data for both solar-terrestrial, meteorological and oceanographic applications. The DMSP satellites can provide snapshots of the precipitation in regions sampled by ground-based instruments, during times of closely co-located crossings. This thesis uses data from several onboard instruments. The SSJ/4 sensor, a precipitating electron and ion spectrometer, measures downward fluxes of ions and electrons from 30 eV to 30 keV in 19 energy channels. A complete energy spectrum is measured once every second. The Special Sensors-Ions, Electrons, and Scintillation (SSIES) instrument measures the parameters of the bulk plasma, including the three components of plasma velocity, electron and ion temperatures, electron and ion densities and plasma composition, using a combination of several Faraday cups (conducting chamber used to detect charged particles) and an electron probe.

3

Instrumental and Analysis Techniques

Many of the optical instruments providing the data shown in this thesis are run by the University of Southampton. As well as the resulting scientific studies, experimental work, in the form of instrument installation and operation, advancing data extraction methods and developing calibration techniques, has therefore formed a significant part of this PhD project. This chapter presents instrumental procedures and data processing techniques developed and applied by the author, in collaboration with Dan Whiter of the University of Southampton and Nickolay Ivchenko and Hanna Dahlgren of the Alfvén Laboratory KTH in Stockholm.

3.1 SIF Instrumentation Set-up

For most of the PhD research period, the author was responsible for setting up the SIF instrument platform at the beginning of each campaign season and after hardware changes. In order to study small-scale auroral forms at high temporal resolution, it is essential to have all instruments on the SIF platform co-aligned and pointed towards magnetic zenith to a high degree of accuracy. It is also necessary to have accurate time stamping in order to combine data with measurements from other instruments such as the ESR, as discussed further in Section 3.3.1.

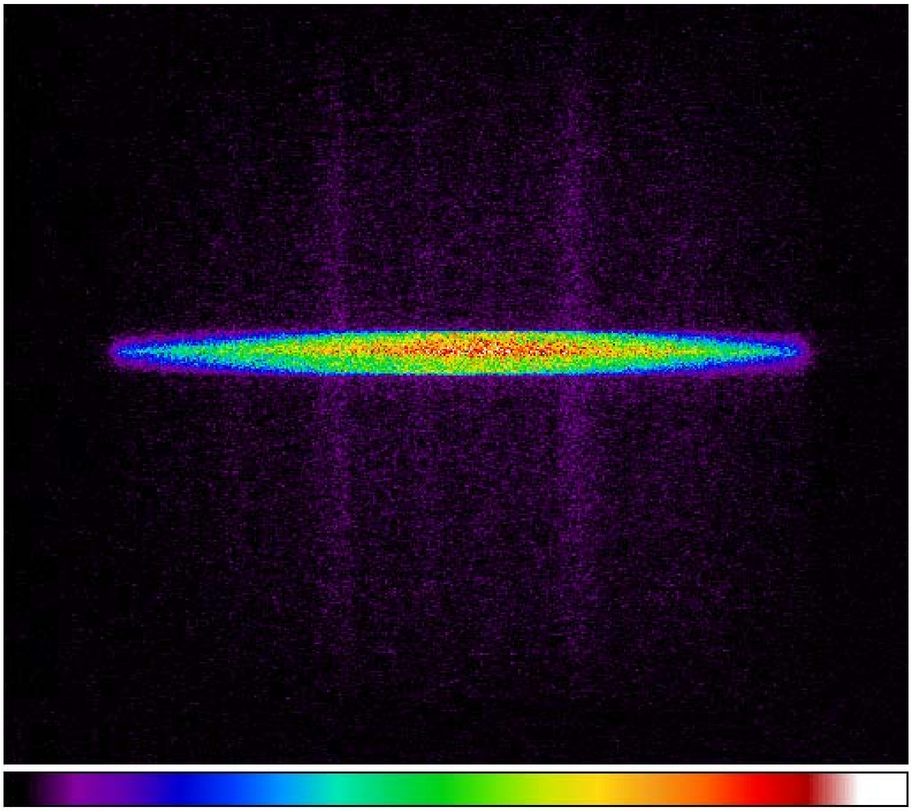

Figure 3.1: False colour CCD image (uncalibrated) taken during the aligning of the SIF instrumentation at the KHO site in November 2007. Polaris can be seen as a strong enhancement at all wavelengths in the centre of the HiTIES slit. The spatial direction, along the length of the slit, is shown by the vertical y-axis and the wavelength direction is shown by the horizontal x-axis. The faint enhancements at particular wavelengths are the result of all the overlapping orders from airglow and weak auroral emissions present in the background night sky.

3.1.1 Co-alignment

In order to combine data from the TLC, HiTIES and each of the four photometers, all must be accurately co-located to look at the same region of sky. The attachment of each of the instruments to the SIF platform is done in such a way that all should be pointing roughly in the same direction when firmly fastened to the main optical plate. To fine-tune the alignment, adjustable screws are fitted which control the orientation, both along the magnetic meridian and in the east-west direction, for each of the photometers and the TLC. Fine-tuning is done using observations of the pole star, Polaris, which has a relatively constant position in the sky. The entire SIF platform is manually moved to locate Polaris in the centre of the HiTIES slit. The HiTIES filter mosaic is first removed so that Polaris is seen as a large increase in intensity across all wavelengths in the centre of the CCD detector (central along the side representing the spatial length of the slit), as shown in Figure 3.1.

The position of the TLC is then adjusted so that Polaris appears in the centre of the camera field of view. Prior to the digitisation of the TLC data, this was done by matching Polaris to the position of a cross-hair marked on the centre of a monitor displaying the TLC feed. In November 2007, this was improved by the addition of a cross-hair onto the central pixel of the digital image stream itself, updated and displayed in near-real time for the purposes of aligning. All aligning of the TLC was done using the narrow field of view lens (field of view 16° by 12°) for greater accuracy.

To fine-tune the alignment of the photometers, each is slowly moved through the whole range of movement using the adjustment screws, in the north-south and the east-west direction. With Polaris still in the centre of the HiTIES slit, the photometers are adjusted in turn and fixed at the centre of the intensity peak where the highest intensity is recorded in each direction of freedom. Even though the motion of Polaris around the sky is small, with it being so near to the Earth's axis of rotation, it may still drift out of the HiTIES slit before all four photometers can be adjusted. The SIF platform is adjusted as required to keep Polaris central within the slit, until all instruments are accurately co-aligned.

3.1.2 Aligning SIF on the magnetic zenith

Once all the instruments are co-aligned, the look direction for the SIF platform must be aligned with the local magnetic field, i.e. pointing towards magnetic zenith. This is done using theoretical star maps showing the star field as it should appear when the camera look direction is field-aligned, and comparing this with what is actually seen in the field of view. This technique was again improved with the digitisation of TLC, when the theoretical positions of zenith stars could be overlaid on the frames of the image stream, rather than having to compare star maps and TLC images by eye. Once all individual instruments have been adjusted and fixed to preserve their co-alignment, the entire SIF platform is manually adjusted in both azimuth and elevation until the observed and mapped stars appear identically in TLC.

3.1.3 HiTIES focusing and grating settings

Focusing of the spectrograph is most easily achieved if there is aurora present during the equipment setup. For the three panel and the five panel nitrogen mosaic filters, this is really the only viable option to achieve the best possible focus. The collimating lens between the filter mosaic and the detector lens is adjusted until the nitrogen auroral emission lines are at their minimum thickness on the CCD images. For the four panel mosaic, airglow emission lines and a hydrogen lamp can also be used as an alternative for focusing. It was found that it was not possible to have emission lines at opposite ends of the visible spectrum both at the best possible focus i.e. the hydrogen line at blue wavelengths and the airglow lines at the red end of the spectrum. A compromise was reached, adjusting the collimating lens to achieve reasonable focus on both. This was checked and varied as necessary at the beginning of each observing season, depending on changing science priorities and collaborations with other instruments. The grating setting, controlling the tilt angle of the diffraction grating, determines where the spectral lines fall on the CCD image. This is also checked and varied as necessary at the start of each season, according to which filter mosaic is being used. The grating setting is adjusted in order to get all emission features of interest centred within the appropriate panel on the mosaic.

3.2 Camera field of view mapping

The research described here uses images from multiple cameras, all with different field of view sizes and potentially slightly different look directions. To combine data from separate cameras, or to use optical images together with data from the ESR, requires a method of relating pixels on the camera image to the area of sky actually being viewed. Small scale auroral structures such as thin auroral rays can be as narrow as 100 m across at an altitude of around 300 km. This corresponds to a desired accuracy in the camera pointing angle of roughly 0.01°in order to work with images at this spatial scale. The author has worked, in collaboration with Nickolay Ivchenko, on the creation and refinement of automated software to establish the conversion factors from the pixel coordinates on the CCD to local azimuth and elevation. This was done through observing where known catalogued stars appear on the images. This technique was then applied to all camera data presented in this thesis.

For the first image frame in a camera data sequence, the predicted positions of known stars from the Smithsonian Astronomical Observatory (SAO) catalogue which should appear in the field of view are mapped onto the camera image, using an approximate pointing direction. An area around the predicted location is selected and a double gaussian fit used to pinpoint the actual star position in both the x and y directions. The star central point position in pixel coordinates is saved. SAO stars which are isolated in the sky and of significant intensity are used to avoid the possibility

Table 3.1: Coefficients describing the conversion from pixel number to celestial coordinates, for an example Odin data sequence.

Coefficient	Description
0.360000	Centre of image array along x axis
0.288000	Centre of image array along y axis
0.344077	Measure of ratio between x and y axis scaling
0.309765	Measure of distortion due to optics
-0.517207	Measure of pixel distortion due to image digitisation
4.63420	Rotation angle of image (between vertical and meridian)
3.40101	Azimuth of camera look direction (radians)
1.42512	Elevation of camera look direction (radians)

of misidentification. Software was developed to run automatically through all subsequent frames for the event sequence, tracking and saving the positions of the stars. Recording the pixel coordinates of stars throughout the data sequence allows any camera shifts to be noted, discounting the possibility of outliers giving false readings, and reduces the statistical uncertainty of the final fit by having many samples.

For each image frame, the predicted star locations were fitted to the corresponding pixel positions for an identified star. The relation between the celestial coordinates and the rectangular pixel grid of the camera is calculated using standard coordinates, based on equations of spherical geometry described in Smart and Green (1977). The conversion coefficients for the best fit, including any distortions inherent in the optics or in the image processing, are returned. The coefficients from throughout each image sequence were then averaged, excluding any noted outliers, to obtain the pixel-to-celestial coordinate conversion factors. These coefficients should remain constant as long as there are no shifts in camera position or changes in the imaging hardware, but they are checked for each image data sequence. Table 3.1 shows an example of a set of these average conversion coefficients from a ten minute Odin sequence of images, along with a brief description of what each coefficient represents.

With an automated system for mapping fields of view, an approximate camera pointing position is needed, close enough to the true position to locate an identified star within the search area on the image. However the benefits of such a system over manual star locating and identification, as previously employed for camera data, is the reduced uncertainty in the final mapping parameters. For example, in a 20 minute data sequence, with 5 frames per second resolution, if 5 clear isolated stars can be identified in each frame, this gives 30,000 reference points for the fitting procedure.

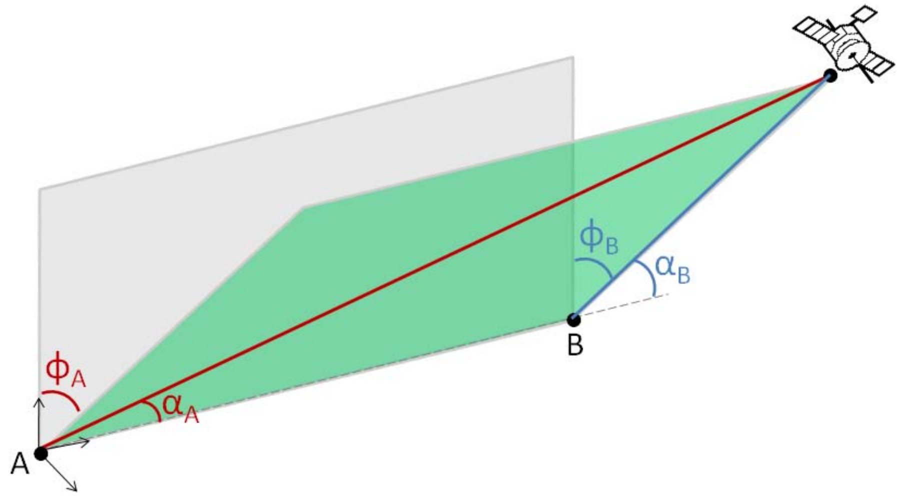

Figure 3.2: The optical coordinate system in α and ϕ. The two observing points labelled A and B represent the Adventdalen auroral station and the EISCAT site respectively. The plane containing the optical baseline and the magnetic zenith position is shown in grey. The plane intersecting the optical baseline and an observed satellite at a particular time is shown in green.

The look direction parameters are then accurate to well within the 0.01°needed to work with the images in terms of sub-kilometer spatial structures. An example set of around 30,000 star positions gives the standard deviation of the calculated elevation and azimuth angles to be less than 1×10^{-4} degrees, theoretically corresponding to a spatial uncertainty of less than 1 m at an altitude of 300 km, i.e. less than the pixel resolution of all of the imagers used here. For camera data at lower temporal resolution or during times where few stars are visible, the mapping procedure is run for longer intervals of time to maintain the accuracy of the look direction parameters.

3.3 The optical α and ϕ coordinate system

For observation from separated locations, i.e. from the ESR site and from the Adventdalen auroral station, optical positions can be described using a standard coordinate system in α and ϕ, at any given time. α is the elevation angle of a satellite signal from the observing location. ϕ is the angle between the field aligned plane containing the optical baseline (between the two observing sites) and the satellite signal. A representation of the optical coordinate system used is shown in Figure 3.2. The geometry of the coordinate system and the effect of parallax between the different viewing locations allows firstly the data timing to be synchronised for the two stations, and secondly the altitude of the satellite to be calculated.

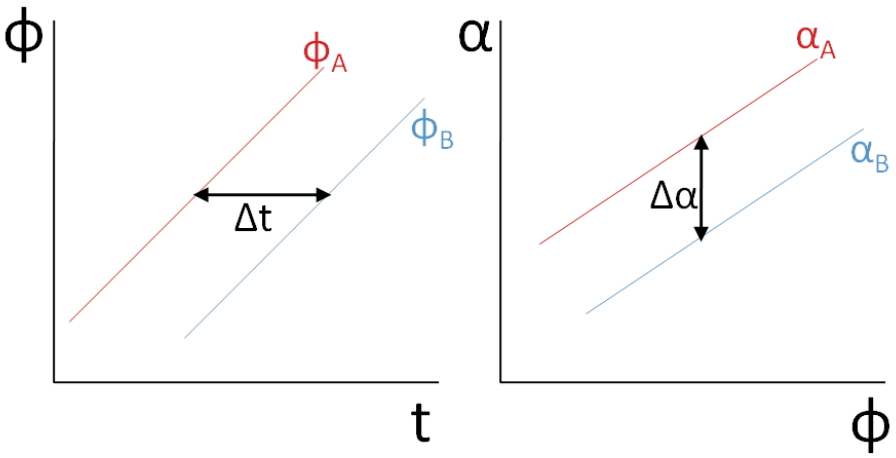

Figure 3.3: Demonstration of the use of satellite tracks, mapped in the α,ϕ coordinate system, to correct for timing differences between two camera data sequences and to estimate the altitude of satellite signals. A theoretical satellite passage as seen by the TLC camera is shown in blue. The same satellite as seen by a camera at the EISCAT site is shown in red. Δt gives directly the timing difference to be corrected for between the two sequences. $\Delta\alpha$ can be used to estimate the satellite altitude.

3.3.1 Timing correction

As mentioned briefly in Section 2.2.2, the timing accuracy of the TLC camera and other SIF instrumentation was improved in November 2007, with the addition of an ntp-synchronised master clock. This research uses camera data from earlier campaigns at the old observatory in Adventdalen, where the video time stamp was set manually and is therefore only accurate to the nearest second at best. In order to use this TLC data at the full 25 frames per second in collaboration with other instruments, a new technique was developed by the author to correct for this timing inaccuracy. The corrected data revealed that the automated time stamp was prone to drifting by up to a few seconds each day meaning that during periods of remote running and during campaigns if the timing was not reset regularly, the time stamp could be out by a considerable margin. The correction method relies on having another narrow field auroral imager with a GPS or NTP-synchronised time stamp at the EISCAT radar site, running at the same time as the TLC data sequence, i.e. ASK or Odin. Tracks of passing satellites can then be compared in order to match the TLC time stamp to that of the other imager.

For any particular time the α coordinate of a passing satellite signal will be different for each observing site, due to their lateral separation and also the difference in altitude, i.e. α_A for the EISCAT site camera and α_B for TLC at the Adventdalen station. However, the ϕ coordinate should be identical for the satellite signal as seen from either observing site at any given time. The time stamp on the TLC image can

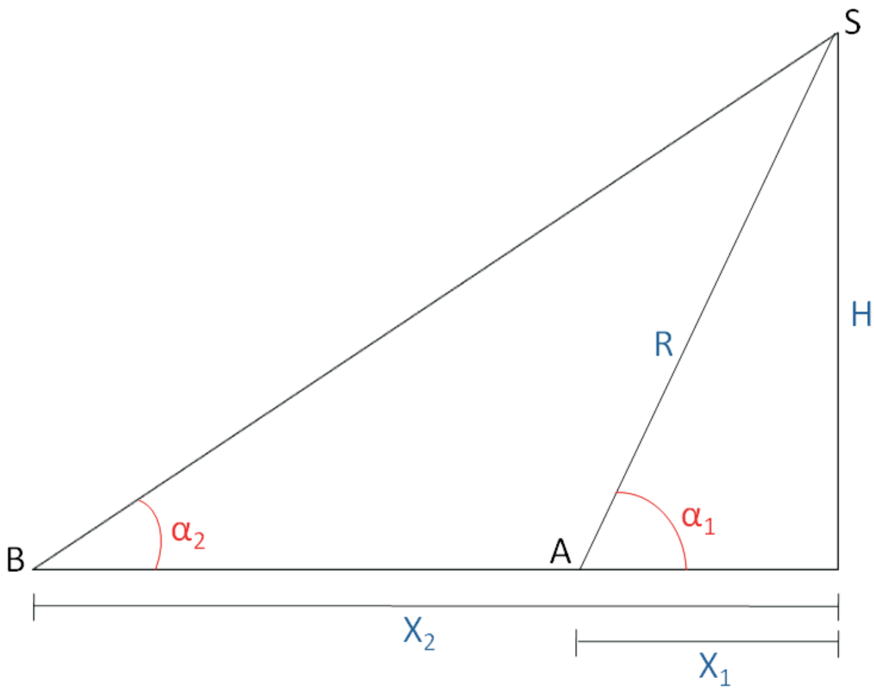

Figure 3.4: The geometry of range triangulation for observations using the optical co-ordinate system.

therefore be corrected in order to match the ϕ_B values (TLC view) to the ϕ_A values (EISCAT view) for every time frame, as shown in the left panel of Figure 3.3.

3.3.2 Range triangulation

As well as correcting for timeshift, the technique of tracking a satellite in α and ϕ coordinates from separated locations can also be used to estimate its altitude. This is useful for identifying signatures in the EISCAT radar beam which correspond to satellites tracked optically as discussed in Chapter 6. Once the timing between the two observing sites has been synchronised, the separation in α coordinate at any fixed ϕ can be used to estimate the satellite altitude through triangulation, as shown in the right panel of Figure 3.3. The geometry of the observing system for use in range estimation is shown in Figure 3.4 (exaggerated scale for demonstration purposes), assuming the difference in altitude between site A (ESR) and site B (Auroral station) is negligible compared to the altitude of the satellite.

Using the trigonometric relations,

$$X_1 = \frac{H}{\tan \alpha_1} \quad \text{and} \quad \mathrm{X}_2 = \frac{\mathrm{H}}{\tan \alpha_2} \tag{3.1}$$

and given that X_2 - X_1 is equivalent to the optical baseline, it can be found that

$$H = \frac{B_{opt}}{(\cot\alpha_2 - \cot\alpha_1)} \tag{3.2}$$

and

$$R = \frac{H}{\sin\alpha_1} \tag{3.3}$$

where B_{opt} is the length of the optical baseline, H is the vertical altitude of the satellite, and R is the range to the satellite from the ESR site.

3.4 Camera calibration

3.4.1 Flats and darks

To calibrate the intensity of all camera data, it is important to take into account the flat field:- the array describing the relative response of all the pixels on the CCD to a uniform light source, and the dark signal:- the current due to thermal electrons accumulating during the exposure and the read out noise. For most optical instruments, flat fields are measured by means of shining a standard white light source lamp onto the sensing area and recording the pixel response. However with the intensifiers employed on all of the auroral imagers used in this thesis to increase the sensitivity to weak emissions, there is a danger of saturating the optics and this method could not be used. Instead data from periods of uniform cloud are averaged over several minutes to produce a flat field for each camera. For the ASK cameras, dark CCD captures are recorded at the beginning of each 20 minute data sequence. For the other imagers dark images are recorded separately at regular intervals throughout the observing season, by manually closing the shutter in the case of the Andor imager, or putting on the lens cap for the TLC imager. These dark values are then subsequently removed from the main data sequences. For all of the cameras, a corrected image is then calculated where:

$$correctedimage = \frac{(rawimage - dark)}{(flatimage - dark)} \tag{3.4}$$

3.4.2 Intensity calibration

The corrected image can then be calibrated into units of intensity. A common method of intensity calibration would be to use a laboratory lamp of known brightness and record the measured enhancement on the imager sensor. However with the available standard flat lamp being too bright for the intensified imagers, an alternative technique was developed using the brightness of known stars seen in the imager fields of view, also avoiding the need to transport the cameras to a special calibration lab. Calibration using star brightness has the advantages of inherently taking into account the effect of the observation domes, the possibility of changing atmospheric extinction levels if specifically done near the time of auroral events, and is automatically available for clear sky periods at any point during the observing season. For ASK in particular, star calibration accounts for the transmission through the cover windows, which would be difficult to reproduce accurately in an optical calibration lab. Star calibration can also be adapted to take into account changing background conditions, i.e. for a period of aurora recorded during increasing sunlight contamination. Intensity calibration using stars has been applied to camera data used in this thesis.

The software for star calibration of camera data was developed originally for ASK data by Hanna Dahlgren (Alfvén Laboratory KTH, Stockholm) and the author, and then modified by the author for use with data from other auroral imagers. Bright isolated stars, identified in the SAO star catalogue and visible in the camera field of view, are located in pixel coordinates on the images, using identical techniques as described in Section 3.2. With the celestial to pixel coordinate conversion done previously, the star can be tracked across the images by mapping its theoretical motion. For every frame in a sequence of images with no aurora, the pixel intensity values for each identified star is recorded. A box of 11 by 11 pixels is selected around the location of the star in the imager, and the measured intensity is summed for all pixels within the box area. Four identical selected areas, adjacent to each side of the star window are averaged to provide a background intensity value. The background is subtracted to provide a reading of the intensity enhancement in the imager due to the star only. The count values are then divided by the integration time of one camera frame, i.e. 0.04 seconds for full resolution (25 frames per second) data, in order to get the measured intensity in counts per second. To obtain a calibration for auroral intensity during times of hazy cloud, star brightnesses are recorded during similar atmospheric conditions, i.e. as near to the observation data as possible. Intensity calibrations done during times of thin cloud rely on the assumption that the cover has no spatial structure and is constant over the time used for the calibration. The process of recording star brightnesses is done for as many identifiable isolated stars, and as many frames as possible, in order to obtain a reliable intensity calibration.

The theoretical spectral fluxes of the stars are found from the Allen star classification tables (Allen, 1973). Stars are categorised into 7 groups, O, B, A, F, G, K and M, each with a typical emission spectrum. The emission intensity versus wavelength

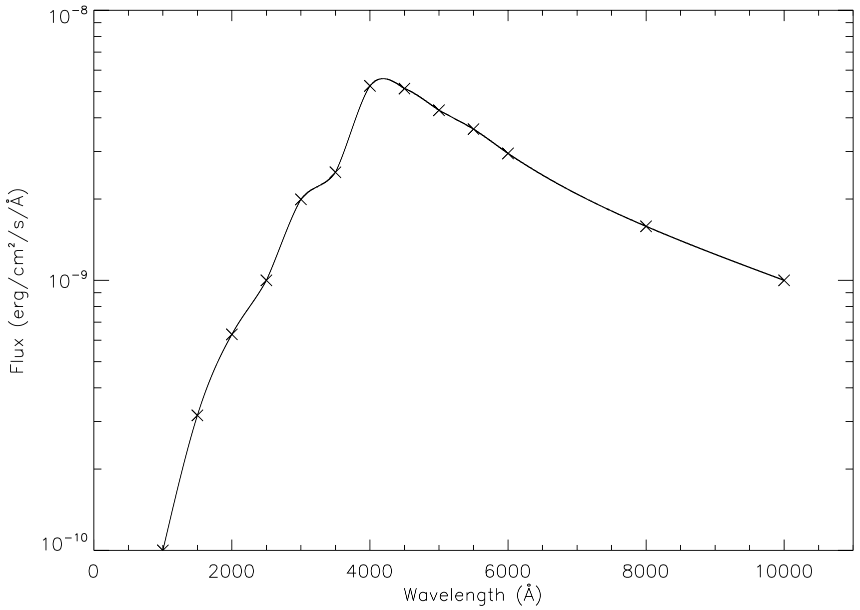

Figure 3.5: Emission spectrum for the G class of stars, using the Allen spectral classification system.

spectrum for the G class of stars is shown in Figure 3.5. The star intensity calibration procedure uses 6 of these classes (the O spectral class is not used). The Allen star flux is given in erg cm^{-2} s^{-1} $\mathrm{Å}^{-1}$ which corresponds to $5.035 \times 10^7 \times \lambda$ photons cm^{-2} s^{-1} $\mathrm{Å}^{-1}$.

With only 6 classes and 5 Å wavelength resolution, the use of Allen tables can mean that the deviation of actual star behaviour from the typical emission spectrum is significant. This method therefore needs as large a sample of stars used in each image frame as possible, in order to improve the statistics and thus the accuracy of the calibrations. For the Svalbard data used in this thesis, the number of stars observed in the direction of magnetic zenith proved large enough to obtain intensity calibrations which were stable over time and agreed with other instrumentation. During the season in which ASK was operated at Tromsø, it was found that the reduced number of visible stars led to significant variations in the calibration when stars with anomalous spectra moved into the field of view. This technique is therefore currently being modified to use more detailed star spectrum libraries with greater wavelength resolution. The Pulkovo Spectrophotometric catalogue and the Pickles Stellar Spectral Flux Library can be used in conjunction to get measured spectra for hundreds of stars visible in the field of view at Tromsø. This technique will be applied to future camera intensity calibrations for both Tromsø and Svalbard data, but is not discussed further in this thesis.

The star fluxes $F(\lambda)$ for each star are obtained by scaling the appropriate Allen curve according to the star's magnitude. This is then integrated over the filter width and convolved with the filter transmission curve $T(\lambda)$ of the appropriate imager. The observed enhancement for each star in counts per second can then be plotted against the theoretical star brightness as seen through the filter, in units of photons cm^{-2} s^{-1}, for each imager. The slope of the best fit represents the intensity calibration factor, $K1$, i.e. for $K1$ = 100, 1 count/s is equivalent to 1/100 photons cm^{-2} s^{-1}. The intercept should ideally be zero as the instrumental dark current has already been removed, but this may not always be the case, i.e. during times of thin uniform cloud when the intercept may become negative. This can also be taken into account when calibrating auroral data, to adjust the emission brightness accordingly.

For auroral optical measurements the Rayleigh, a standard unit of surface brightness is commonly used, where 1 Rayleigh, corresponds to $\frac{10^6}{4\pi}$ photons cm^{-2} s^{-1} sr^{-1}. The ASK images presented in Chapter 4 are displayed using intensities in Rayleighs as seen through the filter. The solid angle field of view of one pixel in steradians, $\Delta\Omega$ is given by:

$$\Delta\Omega = \frac{A}{f^2} \tag{3.5}$$

where A is the physical area of one pixel on the CCD (obtained by dividing the sensor area by the number of pixels) and f is the focal length of the camera. For the ASK cameras, the pixel area is 16 $\times$ 16 μm^2 and the focal length is 75 mm. This gives a calculated pixel field of view of 4.6 $\times$ 10^{-8} sr. The proportionality constant to convert the star flux from photons cm^{-2} s^{-1} into Rayleighs, $K2$, is then given by:

$$K2 = \frac{4\pi}{10^6\Delta\Omega} = 276/sr \tag{3.6}$$

The final conversion factor, $K3$, from measured intensity in counts per second to brightness in Rayleigh is then $K1/K2$, i.e. 1 count/s is equivalent to $K2/K1$ Rayleigh. The ASK data in this thesis takes place during a clear sky period with no visible thin cloud cover to take into account. The final Allen star calibration values used were therefore averaged over clear intervals during the period 4 December to 12 December at the start of the 2005/2006 observing season, and are shown in Table 3.2. The calibration was re-checked at the end of the season and found not to have changed significantly, There is, however, an inherent uncertainty in the calibration factor $K3$, associated with averaging over clear sky periods in which some variation is visible, which is estimated here to be of the order 10%.

Table 3.2: ASK Intensity calibration factors for the 2005/2006 observing season.

Camera	$K1$	$K3$ ($K2/K1$)
ASK 1	500	0.5
ASK 2	250	1.1
ASK 3	200	1.4

3.5 Extracting spectrographic data from HiTIES

The software packages to extract emission line information from the raw HiTIES CCD data were initially written by Nickolay Ivchenko, but have been added to and developed by the author, in conjunction with Hanna Dahlgren and Daniel Whiter. The locations of the different panels of the filter mosaic have to first be mapped onto the CCD pixel area. The appropriate part of the image for each wavelength region of interest can then be selected. Rather than extracting the whole area for each panel, a smaller region with width 0.2 times that of one panel is used as standard. This region is positioned close to the middle of the filter mosaic, i.e. near the centre of the slit, to reduce the influence of increased noise from the less illuminated regions at the edges of the CCD. For the HiTIES four panel mosaic used in this thesis, as shown previously in Figure 2.3c, data from the O^+ and O_2^+ panels on the left hand side of the filter are extracted from the right-most edge, and for the H_β and O panels data are extracted from the left-most edge.

3.5.1 Wavelength calibration

After the panel region has been selected, the pixel numbers across the panel in the wavelength direction have to be converted into a true wavelength scale, so that the wavelength of features in real data can be determined. This is done by comparing reference spectra at known wavelengths to measured spectra observed in HiTIES during clear sky periods. The reference spectra used come in two forms. For a daylight period used for wavelength calibration, the solar Fraunhofer absorption spectrum within the appropriate wavelength region is produced for each panel. For night-time periods, theoretical hydroxyl emission lines are used. Because of the finite spectral resolution of the spectrograph, the emission and absorption lines appear smeared in real data. The reference spectra in either case are therefore convolved with the HiTIES instrument function (a gaussian of set width) to enable easy comparison with the measured spectra in HiTIES data.

The pixel to wavelength fit is described by the cubic polynomial:

$$\lambda(p) = \lambda_0 + \lambda_1(p - p_0) + \lambda_2(p - p_0)^2 + \lambda_3(p - p_0)^3 \tag{3.7}$$

where p is the pixel number, p_0 is the reference pixel number corresponding to wavelength and λ_i are the polynomial coefficients. The best set of coefficients describing the fit for each mosaic panel are found by matching identifiable features in both the reference and the measured spectra.

3.6 SIF slit location

In order to use HiTIES spectrograph data in conjunction with data from auroral imagers, a technique was developed to map the position of the spectrograph slit onto the plane of the sky using the passage of stars. The method is very similar to that used to locate the camera fields of view. However, unlike in image frames, the narrow width of the slit and the short time that stars are visible in slit images means that the tracking of the stars cannot be automated using a rough initial pointing direction. If the initial value is out by more than the angular width of the slit, then predicted star crossings will not appear at all in the slit, and the mapping parameters cannot be adjusted in the direction perpendicular to the slit length.

Instead keograms collapsed in wavelength (i.e. extracted data slices of intensity along the length of the slit stacked across in time) are used to view the positions of stars passing through the slit, as they appear on each particular panel. Spectrograph data at high temporal resolution, generally with a 5 s integration period, are used to obtain clear signatures of the short-lived crossings for accurate comparison with the predicted star motions. The positions of bright stars in the keogram, seen in one or two consecutive time slices and over several pixels along the slit, are selected manually. The predicted positions of SAO stars in the keogram can then be calculated using a set of rough initial pointing coordinates. The initial discrepancy between the predicted and observed positions of stars in the keograms, in the direction perpendicular to the slit length, is dependent on the time resolution of the data. For high resolution data the large potential separation means that it is impractical to try and match up the SAO stars and corresponding enhancements using automated search windows. The star crossings are therefore manually identified by comparing patterns in the star field. The coefficients for a polynomial fit describing the azimuth and elevation points along the curve of the slit can then be found. Where different panels on the filter mosaic occupy different regions along the length of the slit, i.e. for the four panel mosaic, this

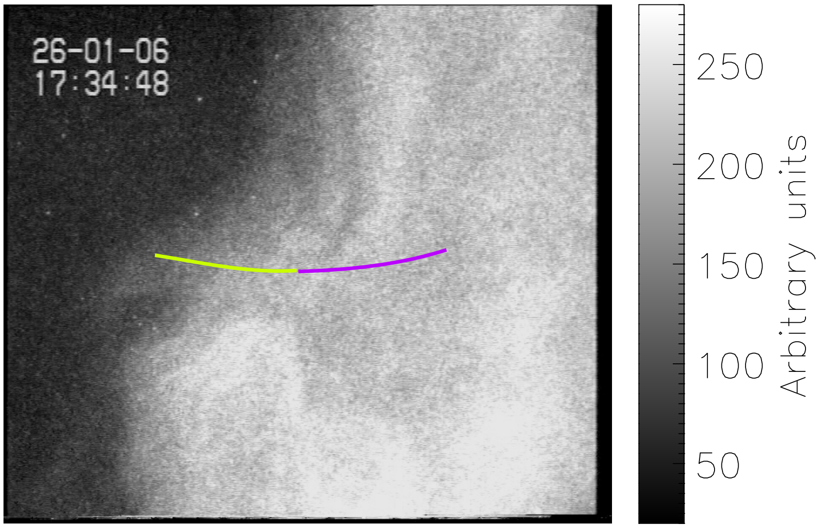

Figure 3.6: Video frame from the SIF camera showing the position of the HiTIES spectrograph slit mapped onto the image coordinates. The four panel mosaic filter was in use at this time, with two panels on either side of the central point, along the slit length. Stars visible in panels on either side were used to plot the positions of the panel regions separately in green and purple.

fitting procedure is done for each panel, and then combined to map the position of the entire slit. Figure 3.6 demonstrates the use of the slit locating routines, showing the panels on either side of the slit for the four panel mosaic, mapped onto a camera image from the TLC.

3.7 Spectrograph intensity calibration

3.7.1 Flats, darks and bias

As with the camera images, the raw spectrograph data also need to be processed to take into account the flat and dark readings for the CCD images. As briefly mentioned in Section 3.4.1, the dark signal contains two contributions; the thermal electrons collected in each pixel during the exposure, and the electrical noise added during the image readout, known as the bias voltage. The corrected data image, S_{cal}, is obtained by:

$$S_{cal} = \frac{M_{data} - (B+T)}{M_{flat} - (B+T)} \tag{3.8}$$

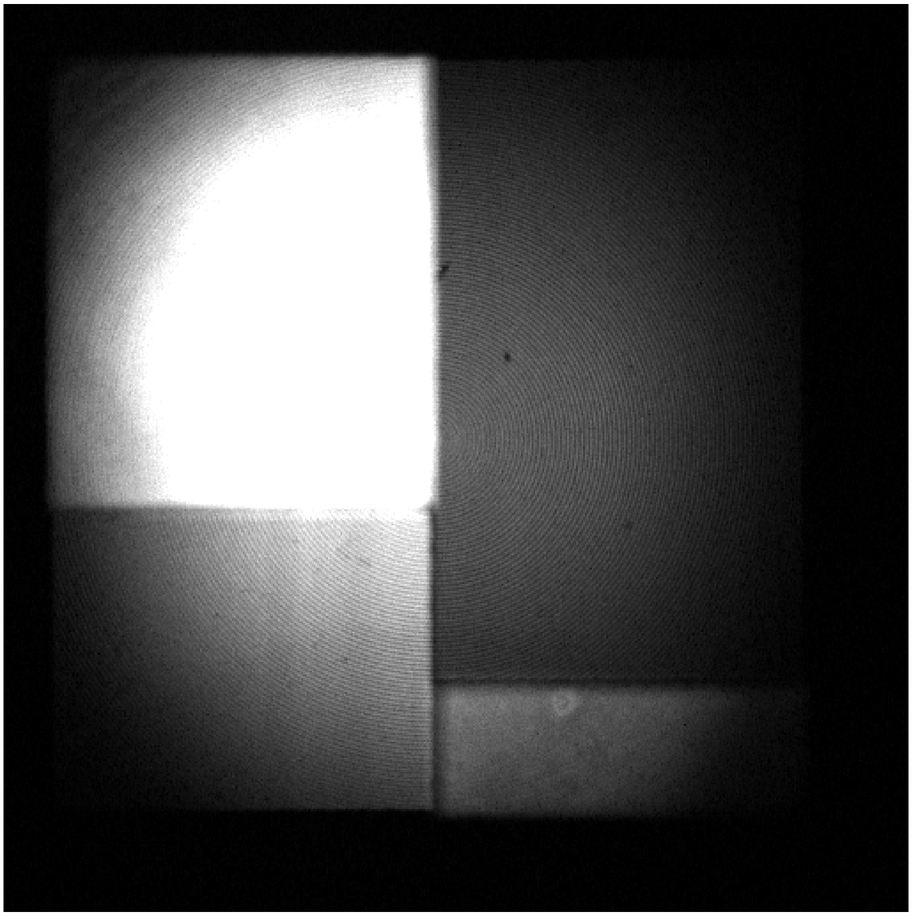

Figure 3.7: Averaged flat image using 30 s exposures from 01/12/2005, showing the response of the HiTIES Andor CCD to the flat field lamp. The difference in flat lamp intensity transmitted for each panel can clearly be seen, as well as the Fresnel diffraction pattern due to light passing through the aperture lens.

where M_{data} is the measured auroral image, B is the bias voltage, T is the thermal noise and M_{flat} is the flat image.

The flat field for the spectrograph, correcting for any pixel to pixel variation in illumination or in response on the CCD, is obtained using a standard flat lamp held over the HiTIES lens. Flat signal levels are proportional to the integration time of the spectrograph image, and are therefore recorded for 5 s, 10 s, 30 s etc., and applied to the data of corresponding exposure time. The flat field used to calibrate the HiTIES data from January 2006 shown in this thesis is shown in Figure 3.7. This flat field was created by averaging 40 flat images each of 30 s exposure time, taken between 10:25 and 10:45 UT on 1 December 2005.

Dark images are produced by capturing CCD exposures with the shutter closed in the case of the Andor detector, or with the HiTIES lens covered by a lens cap for the previous PixelVision and MIC detectors. For the spectrograph data shown in this thesis, 10 minute average dark exposures were recorded separately at various times throughout the observing season, and scaled for different exposure lengths. Each data image is then corrected using the dark file closest in time, scaled to the appropriate exposure. Dark captures were taken every few days during manned campaign periods, but were not updated as often for intervals of remote running. Although the bias voltage should be constant, data revealed slow (time scale of hours to days) variations over time. With the potentially long time between dark HiTIES exposures this variation needs to be taken into account.

In order to correct for the bias changes on the spectrograph, data was integrated within a region outside of the illuminated area of the CCD frame, for each HiTIES image. The difference is calculated between this and the corresponding value integrated over an identical region of the dark file being used for that image. This offset should be zero if there is no temporal variation of the bias. If there is a discrepancy, then the average difference per pixel is additionally subtracted from each pixel in the image. For ASK, using the same Andor detector as the current spectrograph setup, dark captures are recorded at the start of each 20 minute data sequence. There is therefore very little variation in the bias between dark images. From the 2007 / 2008 season onwards, data sequences were separated into approximately 30 minute intervals, similar to for the ASK cameras. A series of 3 dark captures are now recorded automatically at the beginning of each sequence. Although this leads to greater noise than in a 10 minute dark exposure, the problems with bias variation are greatly reduced.

3.7.2 Absolute intensity calibration

As the camera data are normalised according to the flat fields, obtained using a standard flat lamp, it is effectively the brightness of the flat lamp which needs to be intensity calibrated. The spectrograph flat fields can be calibrated into units of absolute brightness either directly, using a lamp of known spectral emission, or by using the brightness of stars as they appear in each panel of the filter mosaic. As with camera data, star calibration automatically takes into account the effect of the observing dome and atmospheric extinction levels, and can be done for every flat field taken over the observing season. It is therefore the predominant method used to calibrate HiTIES data presented in this thesis.

The theoretical flux of SAO stars identified in the HiTIES keograms are found using the Allen tables, scaled according to the magnitude of the star. The theoretical enhancement that a star would produce as it passes through the slit can be calculated, taking into account the aperture area of the lens (i.e. the slit area) and the length of

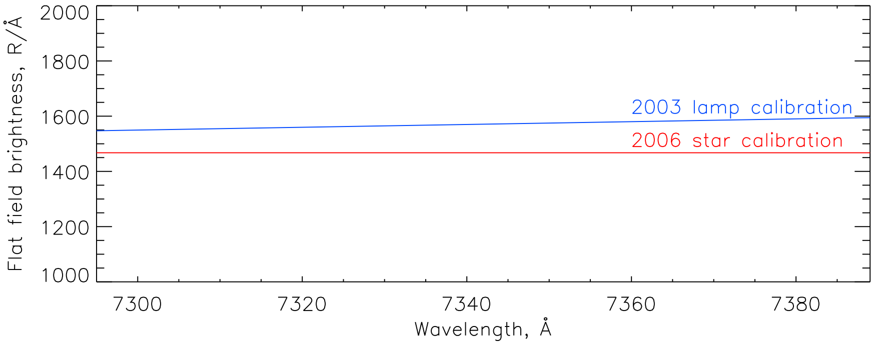

Figure 3.8: Comparison between absolute intensity calibrations of the HiTIES spectrograph flat field for the O^+ panel of the filter mosaic. Wavelength dependent values obtained using a direct measurement of the flat lamp in a calibration lab are shown by the blue line. The average intensity for the panel as obtained using observations of identified stars is shown by the red line.

time that the star is visible in the slit, t_{star}, given that:

$$t_{star} = \frac{W}{\omega_{star}} \tag{3.9}$$

where W is the slit width in radians and ω_{star} is the angular velocity of the star as it crosses the slit in rad s^{-1}. The comparison of this with the measured enhancement of a star (subtracting a background level) in the keogram can then be used to obtain an absolute calibration factor. The full details of the star calibration procedure for HiTIES are not discussed further here, but can be found in Whiter (2008). The main source of uncertainty in this procedure is again the possibility of discrepancies between the actual star spectrum and the scaled spectrum assigned for the star class according to Allen (1973). With the large number of stars visible from Svalbard and discounting outliers in the final fit, the uncertainty is estimated to be less than 10%.

Star calibration can be applied for all of the HiTIES panels except for the 0 panel. Very few stars are visible at the wavelength range of this panel, at the near infra-red end of the electromagnetic spectrum. The flat lamp has been calibrated directly, using the method described in Sigernes et al. (2007), twice in the past ten years of operation. The most recent calibration was in 2003, which is why lamp calibration is not the first choice for data from 2006 onwards. Measuring the flat lamp directly does have some advantages in that it is possible to obtain a wavelength dependent calibration. For star calibration, the keogram brightnesses are averaged over wavelength, meaning that it is only possible to get an averaged calibration for each HiTIES panel.

For the O panel, the 2003 lamp calibration values were used to calibrate the flat field, instead of the star calibration technique. Figure 3.8 shows the comparison between the 2003 lamp calibration and the values obtained using star calibration for the January 2006 period. It can be seen that there is a good agreement between the two, although the lamp calibration gives brightnesses of approximately 5-10% higher. This is within the bounds of uncertainty estimated for the star calibration process but could also indicate some change in the flat lamp output over time.

4

Morphology and dynamics of aurora

In this chapter some of the first results from the Auroral Structure and Kinetics (ASK) instrument are presented, combined with data from the Spectrographic Imaging Facility (SIF), to study the morphology and spectrographic signatures of auroral features at fine scale. The events shown here indicate that dynamic aurora with small scale arc structures are coupled to predominantly high energy electron precipitation, while coronal rayed aurora has a significant component of low energy precipitation. This work was done as a collaboration between the author and Hanna Dahlgren, building on software and techniques developed by Nickolay Ivchenko. In addition to the interpretation of the results, the author's specific contribution was in the analysis and presentation of the HiTIES spectrograph and TLC camera data, while the ASK images were processed by Hanna Dahlgren. The work presented here has been published as part of Dahlgren et al. (2008b). Further results and information about the quantitative separation of emissions in the ASK 2 filter can be found in the companion paper, Dahlgren et al. (2008a), although this is not discussed further in this thesis.

4.1 ASK and HiTIES observations

This study uses data recorded during the first season of ASK operation, after its initial installation at the EISCAT radar site on Svalbard. The three ASK cameras were run with the filter configuration as listed in Table 2.1. The ASK intensities were calibrated using stars, as explained in Section 3.4. For this winter campaign, the HiTIES spectrograph on SIF was set up with the four panel mosaic filter, as described in Section 2.2.1, designed to complement the ASK measurements by covering similar spectral ranges. The HiTIES spectrograph data was calibrated with respect to wavelength and intensity, using the methods described in Section 3.5.

Events of auroral activity in ASK were surveyed for the winter campaign season of 2005 / 2006. Three events are presented in detail in this chapter, chosen to represent different types of auroral structure. The time resolution of the ASK cameras was varied between the intervals studied here, and is described for each event. The HiTIES spectrograph was running with an integration time of 30 seconds throughout all the events. The lower temporal resolution of HiTIES limits its ability to analyse rapid changes in the precipitation spectrum for these events, but it does provide important information on how to interpret the emissions in the ASK cameras.

4.2 HiTIES emission spectra

Aurora is the sum of many emissions of different wavelength contributing to the total observed intensity. Each auroral emission has its own characteristic spectral shape, which can be detected by spectrographic instruments such as the HiTIES spectrograph. Where multiple emissions are present in the same wavelength region, the measured spectrum will be a combination of different spectral shapes added together. In particular the O^+ HiTIES panel (corresponding to the ASK 2 filter) covers several groups of spectral lines each with very different source populations. In order to interpret the measured O^+ spectra for the following events, reference spectra for each of the auroral emissions are shown in Figure 4.1. These reference spectra are taken at times where the relevant emission dominates, found by surveying long intervals of SIF data, with no other spectral features observed in the passband. Figure 4.1a, taken at 18:06:56 Universal Time (UT) on 26 Jan 2006, shows the molecular $N_2$1PG bands, while Figure 4.1b, taken at 17:28:02 UT on the same day, shows the forbidden doublet emission lines from O^+. It can be seen that although the oxygen doublet feature dominates, there is some underlying emission from the nitrogen bands. Figure 4.1c,

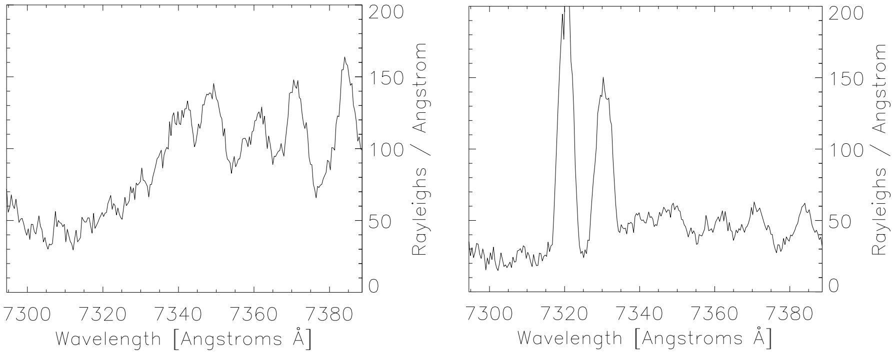

(a) $N_2$1PG reference spectrum **(b)** O^+ reference spectrum

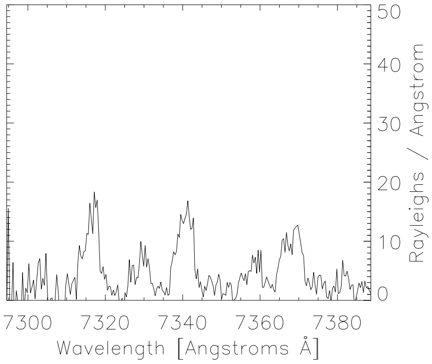

(c) Airglow reference spectrum

Figure 4.1: HiTIES spectra during times of different emissions dominating in the O^+ panel.

taken at a time later on the same day, with no auroral activity, shows the background sky spectrum including emission lines from the OH band (airglow). The background spectrum has been integrated between 19:22:14 UT and 20:12:48 UT, to view the spectrographic features above the noise level. The other HiTIES panels, although only having one main emission feature in the passband (molecular oxygen bands in the O_2^+ panel and the atomic oxygen line at 7774 Å in the O panel), also have some contribution from hydroxyl airglow emission.

4.3 Event 1: 2 January 2006, 16:28 UT

4.3.1 Camera observations

A summary keogram showing a 20 minute sequence of data (one ASK ‘megablock’) covering the first event, is shown in Figure 4.2. From top to bottom, the panels show data from the ASK 1, ASK 2 and ASK 3 imagers respectively. Each keogram shows a

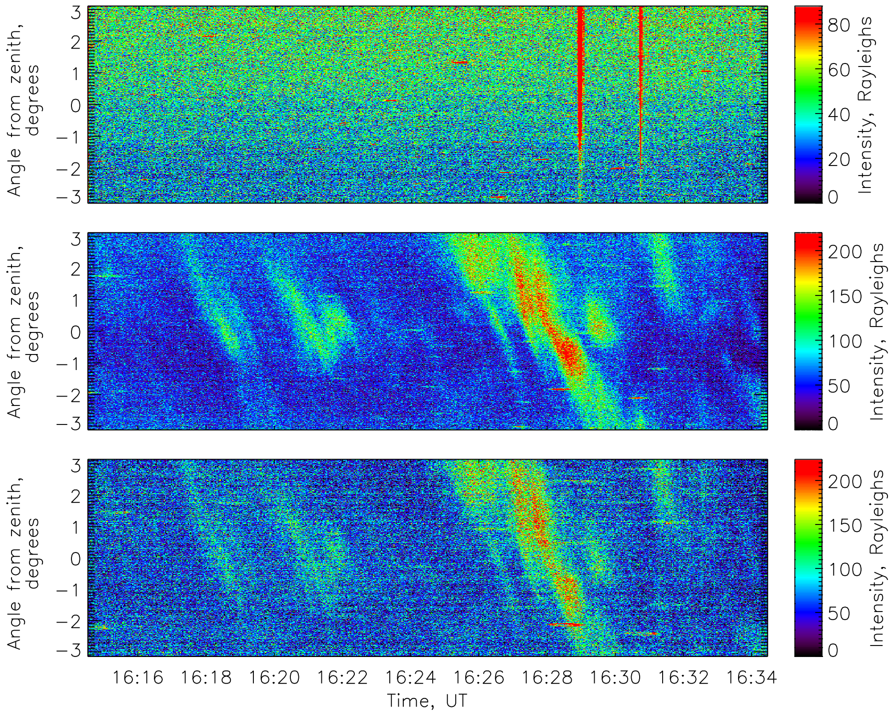

Figure 4.2: Keograms of ASK 1 (top), ASK 2 (middle) and ASK 3 (bottom) camera data, for a 20 minute interval starting at 16:14:32 UT. Image cuts are taken along the North-South meridian line.

time series of slices of the camera image, taken along the magnetic north-south meridian line. The vertical axis is the angle from the centre of the field of view (at magnetic zenith), with north positive. These plots were constructed using mean (2 second) ASK images to show the general characteristics and evolution of the auroral event. The main period of auroral activity is between 16:26 and 16:30 UT. However, the aurora is only present in the ASK 2 and ASK 3 imagers. Emissions in ASK 1 are at the noise level. The two strong enhancements appearing across nearly the entire image slice of ASK 1, at 16:29 UT and just before 16:31 UT, may be due to contaminating light at wavelengths specific to the ASK 1 filter. The ASK 2 and ASK 3 data sequences show that the other cameras were not affected.

Figure 4.3 shows calibrated images from the ASK 2 and ASK 3 cameras, in which the detailed evolution of the aurora can be seen. The full temporal resolution available for ASK was 4 frames per second. The direction of north for each camera is shown by the red arrow. It can be seen that although the co-alignment is not perfect, the difference in position of the cameras is small compared to the size of visible structures and is not a factor in the description of the auroral morphology. Images are presented from within the interval 16:27 UT to just after 16:29 UT. The images show a quiet unstructured auroral arc with intensity of less than 250 Rayleigh at both the ASK2

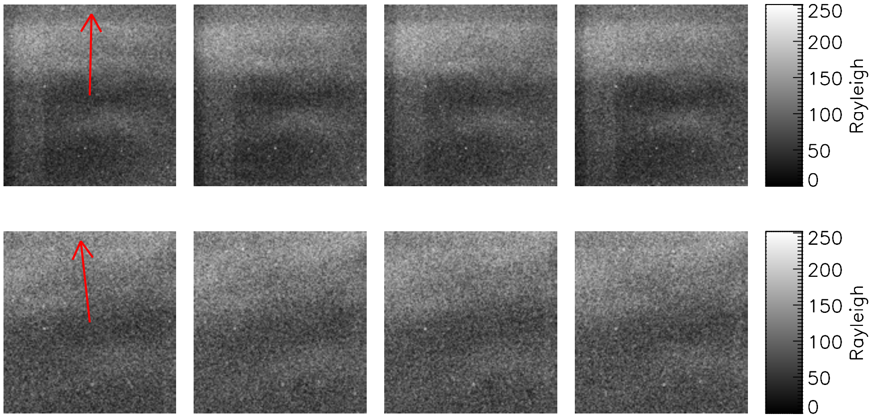

(a) ASK image frames, 16:27:00 UT onwards

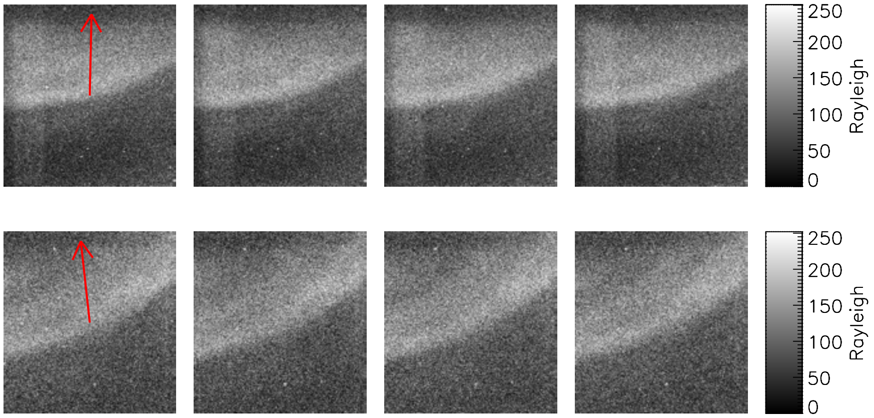

(b) ASK image frames, 16:28:00 UT onwards

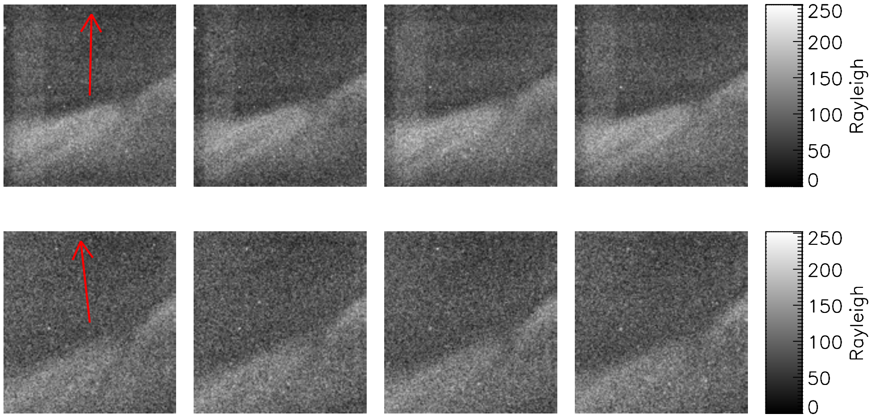

(c) ASK image frames, 16:29:00 UT onwards

Figure 4.3: Time series of consecutive ASK images covering 1 second in total, with the initial images at times spanning the auroral event. ASK 2 images are shown on the top row and ASK 3 images on the bottom row, for each time sequence.

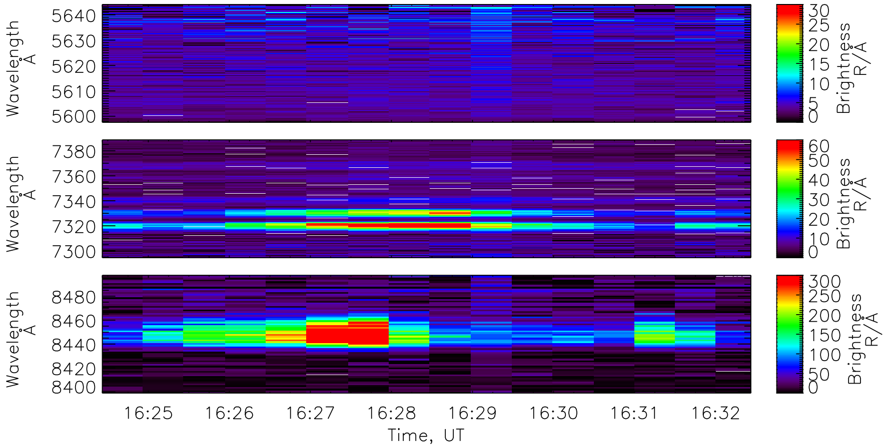

Figure 4.4: HiTIES spectrogram plots showing emission data in R/Å, from the O_2^+ (top), O^+ (middle) and O (bottom) panels. Calibrated wavelengths for the emissions are shown on the vertical axis.

and ASK 3 wavelengths. The arc first appeared in the north of the ASK field of view, shown in Figure 4.3a, approached magnetic zenith (Figure 4.3b) and then drifted away to the south (Figure 4.3c).

4.3.2 Spectrographic analysis

The characteristics of the emissions caused by the incoming precipitation are shown by the HiTIES spectrographic data (30 second integration time) in Figure 4.4. The interval between 16:24 and 16:32 UT is shown, covering the time of the arc passage. The panel data are shown in brightness units of Rayleighs per Ångström (R/Å), using star calibration for the O_2^+ (top) and O^+ (middle) panels, and lamp calibration for the O (bottom) panel, as described in Section 3.7. Emission line features are only evident in the O^+ and O panels. The O^+ (middle) panel shows emission lines at 7320 and 7330 Å, coinciding with the time the arc passes through the centre of the ASK field of view. The O (bottom) panel shows intense emission from atomic oxygen, strongest when the arc approaches magnetic zenith.

Figure 4.5 shows the line spectra at consecutive 30 second integration periods. Data is shown from three HiTIES panels: O_2^+, O^+ and O from left to right. For each integration period, an ASK frame, showing the typical auroral morphology present within the interval, is given for easy comparison, aligned below the HiTIES panel covering corresponding spectral features. As described earlier, the arc is not visible at all in the ASK 1 filter, which is sensitive to emission from O_2^+1N bands in the ionospheric E-region. The line spectra extracted from the O_2^+ HiTIES panel confirm that the molecular oxygen emissions are at or below the noise level, i.e. there are no

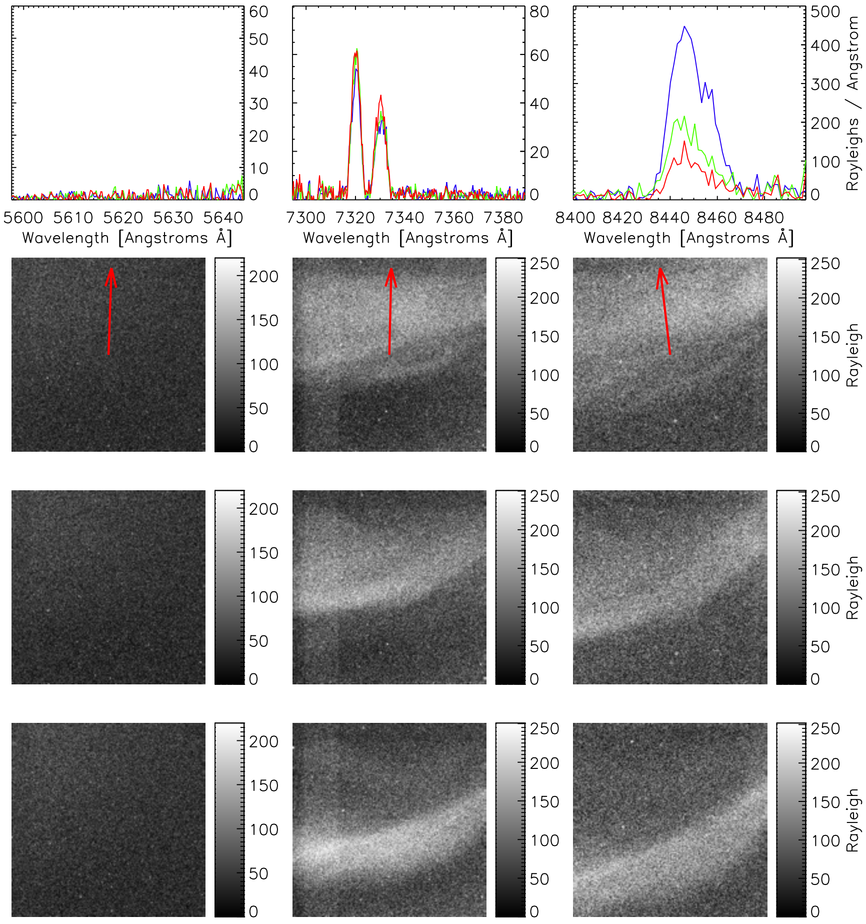

Figure 4.5: Top row: HiTIES spectra for three consecutive integration periods beginning at 16:27:28, 16:27:58 and 16:28:28 UT, shown in blue, green and red respectively. The ASK images below are aligned with time increasing down the page, with ASK 1, ASK 2 and ASK 3 data in order across from left to right.

E-region emissions detected at this wavelength range throughout the arc's passage. The O^+ HiTIES panel data shows that the O^+ doublet is the main emission within the wavelength range. There is no visible contaminating emission from $N_2$1PG bands or OH airglow above the noise level. This indicates that the arc intensity as seen in ASK 2 is predominantly caused by O^+ emission in the F-region. Of the two possible emission sources in ASK 3, the F-region emission at 7774 Å has a similar excitation process to that of the emission line seen in the O panel at 8446 Å. This, along with the fact that E-region ionisation is not seen to be present in either ASK 1 or ASK 2 implies that the emission intensity of around 200 Rayleigh seen in ASK 3 is also predominantly originating from the F-region of the ionosphere.

The combination of ASK camera data and HiTIES spectral data indicate that this auroral event is caused by purely low-energy precipitation. The O panel shows a second enhancement in 8446 Å emission at 16:31 UT, after the passage of the discrete arc shown in detail here. This feature does not correspond to a clear auroral structure seen in the ASK cameras. Instead, it appears to be related to a patch of diffuse aurora to the north of the ASK field of view. Although not specifically shown here, the survey of auroral events from the 2005/2006 season indicated that a diffuse background of weak auroral intensity with no distinguishable structure visible is also common during similar ionospheric conditions, i.e. purely low energy precipitation.

4.3.3 Temporal and spatial scales

The auroral arc is present in the ASK field of view for over 2 minutes, moving slowly across the sky. Changes in the structure and position of the arc are seen to occur on time scales of tens of seconds, much longer than the temporal resolution of the ASK imager with no variation visible between consecutive frames. The spectrographic information on the nature of the incoming precipitation allows the altitude of the auroral structures to be estimated. Images of auroral features as seen in the magnetic zenith can then be used to estimate the spatial scale of structures perpendicular to the magnetic field line. ASK 3 images are used because of the inclusion of long-lived emissions in the ASK 2 passband, which would lead to some smearing out of auroral structures. Figure 4.6 shows an ASK 3 image taken at 16:28:15 UT when the arc structure is observed at its narrowest, appearing near the centre of the field of view at magnetic zenith. The overlaid white line represents a north-south cut across the image, that was used in estimating the width of the auroral arc.

Figure 4.7 shows the variation in emission brightness along this line cut. The data have been smoothed by applying a boxcar average of width 20 to reduce noise and reveal the underlying forms. This was found to be the least smoothing necessary to pick out the arc above the pixel to pixel noise level, but measured widths will consequently be an upper estimate. In this case the arc is superimposed on a background of diffuse auroral emissions and a baseline level for the discrete arc structure is set as shown by the white horizontal line. The maximum intensity level is set as shown by the red line. The angular width of the arc, with the edges defined to be where the intensity falls to half of the maximum value is measured as 1.7°, shown by the green lines. With the high level of noise in this intensity plot, the exact width measurement is very dependent on where the background level is set. The width therefore has an uncertainty estimate of $\pm\ 0.5^\circ$. The arc width is overlaid in red on the previous ASK 3 image (Figure 4.6). The width found using the intensities along the line cut does correspond to the approximate width as it appears to the human eye, indicating that the smoothing factor is not increasing the measured width significantly.

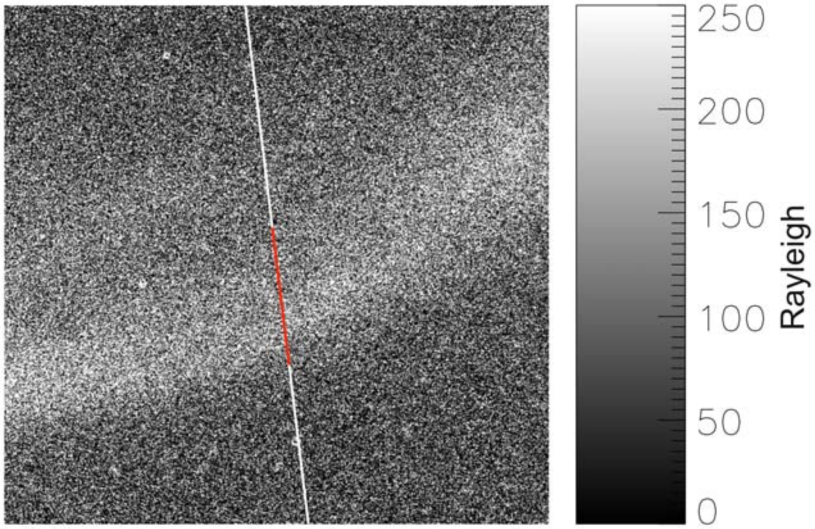

Figure 4.6: Calibrated ASK 3 image taken at 16:28:15 UT, showing the auroral arc passing through magnetic zenith. The north-south cut used for estimating the width of discrete structures is shown in white. The defined width, found using the intensities across the line cut as shown in Figure 4.7 is overlaid in red.

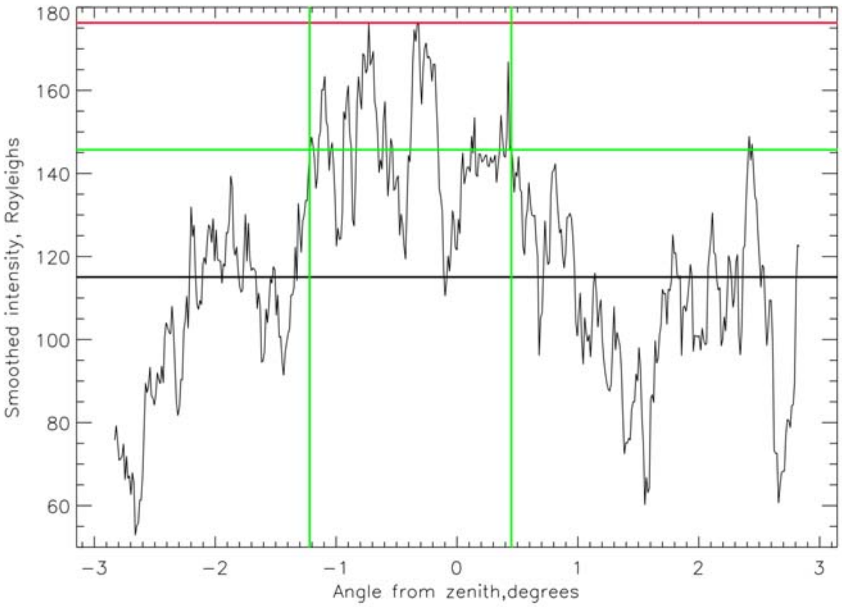

Figure 4.7: Calibrated intensities along a north-south cut across the image shown in Figure 4.6. The red line shows the maximum intensity measured within the arc, the black line shows the level taken to be the background on either side of the discrete structure and the green lines shows the calculated width at half the maximum intensity.

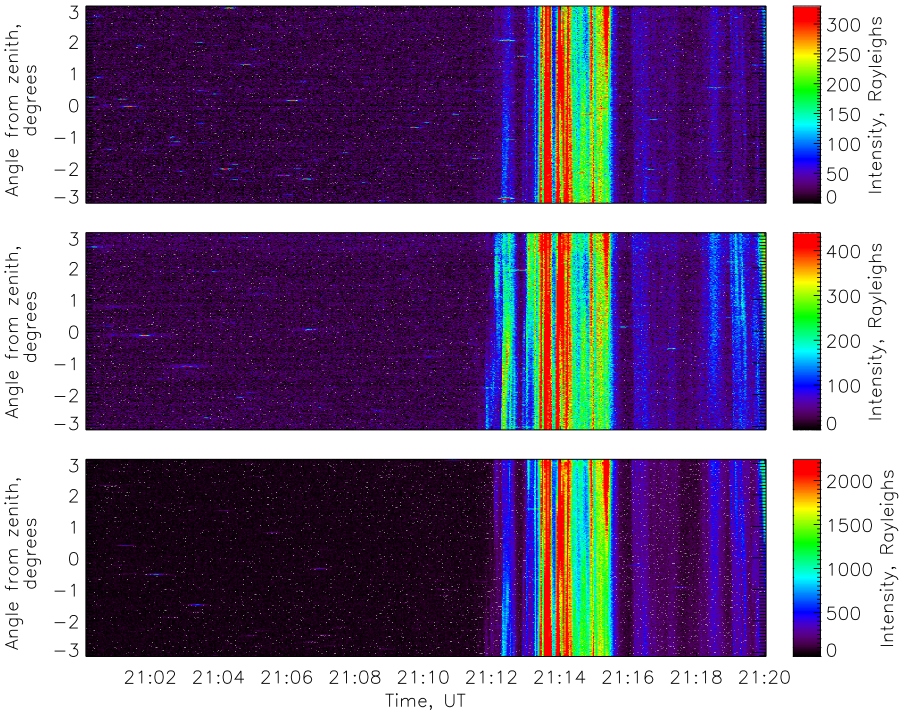

Figure 4.8: Keograms of ASK 1, ASK 2 and ASK 3 camera data, for a 20 minute interval starting at 21:00:06 UT. Image cuts are taken along the North-South meridian line.

Combined optical and spectrographic information indicate that the intensity in the ASK 3 camera is predominantly due to the excitation of atomic oxygen in the F-region. Using an emission altitude of 250 km in ASK 3, shown to be the peak altitude for the F-region O excitation in Section 1.7.4, the arc width, x, can be estimated as 7.4 km $\pm$ 2.2 km, applying the approximation $x = h\sin\theta$, where h is the altitude in km and θ is the angular width of the structure.

4.4 Event 2: 2 January 21:14 UT

4.4.1 Camera observations

The summary keogram for this event is shown in Figure 4.8. Auroral activity is evident between 21:12 and 21:16 UT and has a similar appearance in all three of the ASK imagers. Rather than a single structure moving across the field of view, the aurora in this case fills the image and varies on short time scales.

Calibrated ASK images at the full temporal resolution (4 frames per second) are shown in Figure 4.9. The north direction is shown by the red arrows on the initial im-

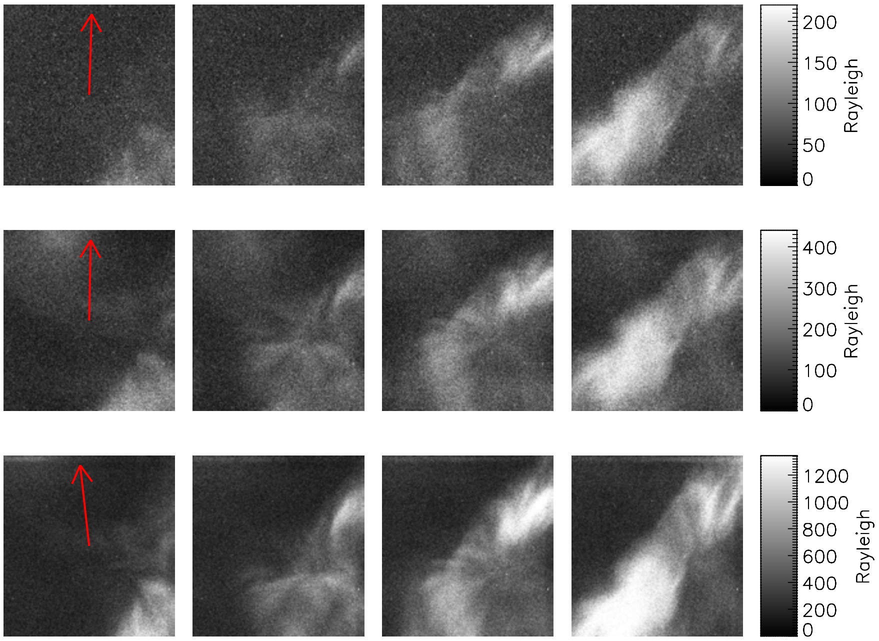

(a) ASK image frames, 21:13:00 UT onwards

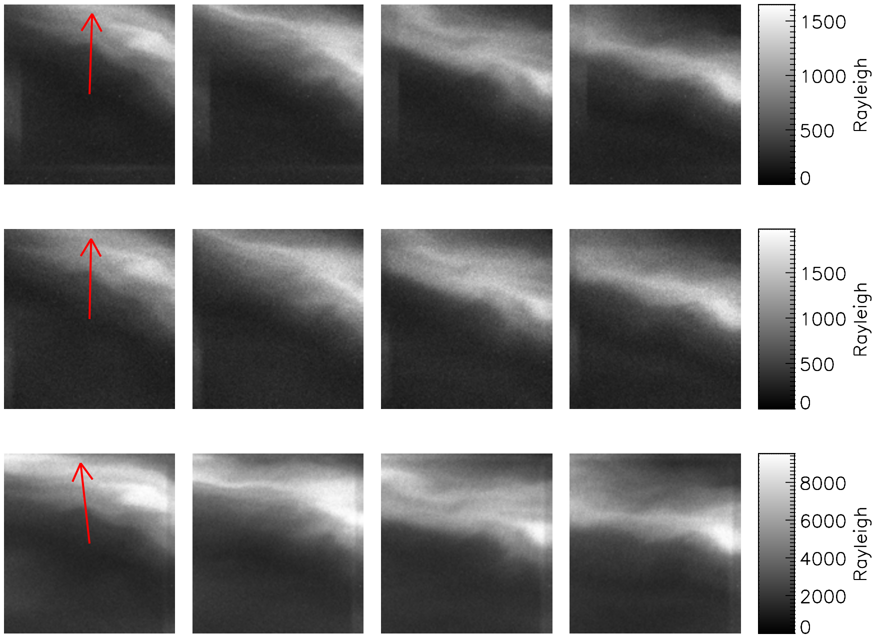

(b) ASK image frames, 21:14:00 UT onwards

Figure 4.9: Series of consecutive ASK images covering 1 second in total, with the initial images at times spanning the period of auroral activity. Images are presented in the order ASK1, ASK2, ASK3 vertically for each time sequence.

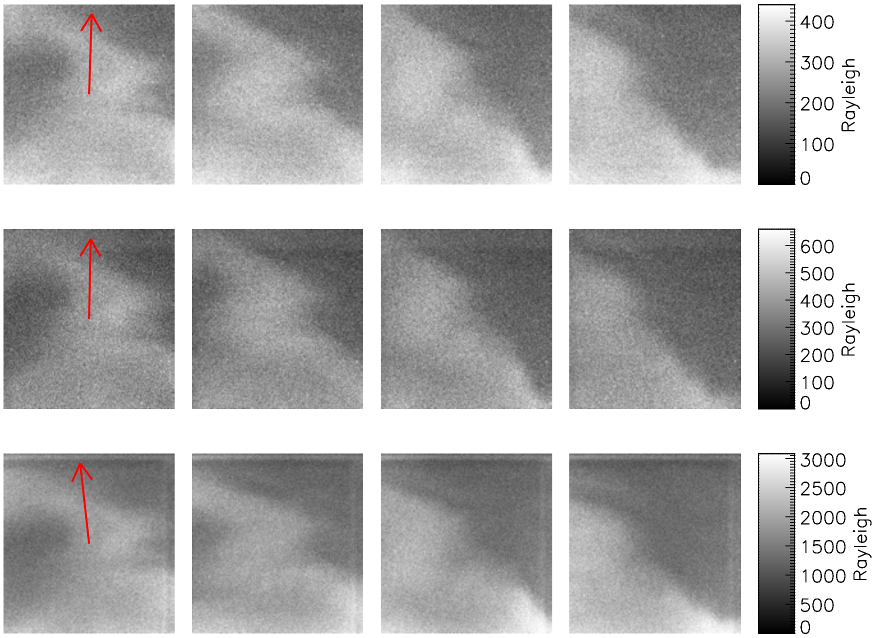

(c) ASK image frames, 21:15:00 UT onwards

Figure 4.9: Continued from previous page.

ages. Images are shown for three time periods during the event, in order to display the evolution of the auroral structures on both short time scales and over the entire interval. The images of the aurora are almost identical at the three different wavelengths of the ASK cameras. The auroral features are complex in form, with thin filaments present within larger scale auroral structures, which can fill most of the field of view. Variation in both the small scale filaments and the larger scale forms is observed on short time scales.

4.4.2 Spectrographic analysis

Figure 4.10 gives the HiTIES data for this event from 21:11 UT until 21:18 UT, and shows a very different series of emissions than for the low-energy event. Enhancements are present in the HiTIES panels shown here (O_2^+, O^+ and O), from 21:13 UT until just after 21:15 UT. The O_2^+ panel also shows some emission from the oxygen doublet at 7320 and 7330 Å, but it is weak in comparison to the molecular nitrogen bands.

Figure 4.11 shows the HiTIES line spectra plots in comparison with ASK images for this event. The O_2^+ HiTIES panel and the bright auroral structures present in the ASK 1 images, confirm the presence of strong O_2^+ emissions. The line spectra plots show intensities of up to 140 R/Å in the O_2^+ panel, where only noise was detected

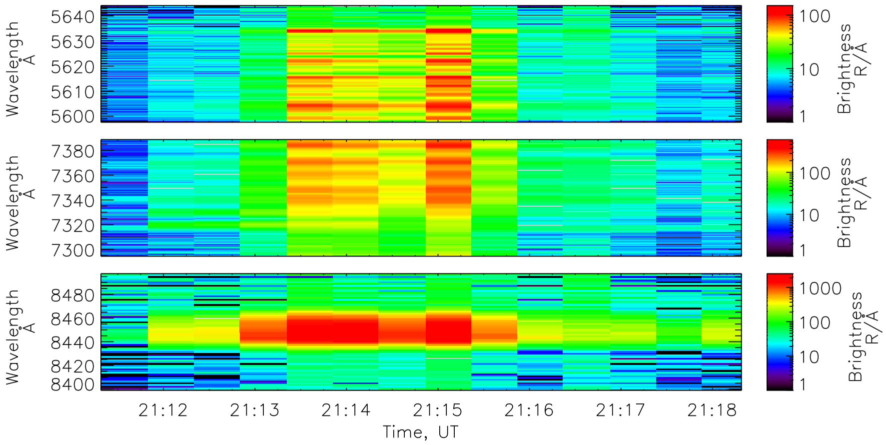

Figure 4.10: HiTIES spectrogram plots showing emission data in R/Å, from the O_2^+ (top), O^+ (middle) and O (bottom) panels. Calibrated wavelengths for the emissions are shown on the vertical axis.

in the previous event. The O^+ HiTIES panel shows oxygen doublet emission lines at 7320 and 7330 Å (intensity of around 120 R/Å) at the times shown in black and blue, but in this case they are embedded within the much stronger emission bands of $N_2$1PG. At the later time intervals, shown in green and red, the N_2 bands increasingly dominate in comparison to the O^+ doublet. The HiTIES spectral information here shows that the predominant emission contributing to the auroral intensity seen in the ASK 2 camera, is from the $N_2$1PG band in the E-region. Strong atomic oxygen emissions, with intensities of around 2000 R/Å are observed, both in the ASK 3 images and in the O panel of the HiTIES data. The presence of strong O_2^+ bands as described previously indicate that the dissociation of molecular oxygen in the E-region is the main source of excited atomic oxygen states. The HiTIES spectral information indicates that the auroral activity for this event is the result of higher energy electron precipitation.

4.4.3 Temporal and spatial scales

The auroral activity in this event changes on far shorter time scales than the auroral arc shown in Event 1. The frames shown in Figure 4.9 demonstrate that the auroral forms are changing, either in location or in internal structure, on sub-second time scales, with variations visible between successive image frames. The auroral forms are also far more complex in structure. Generally the aurora has the appearance of fast-moving loops, curls and patches with relatively large scale size, regularly filling the entire 6°field of view. Thin filaments of increased brightness are often seen within or on the edge of larger auroral features.

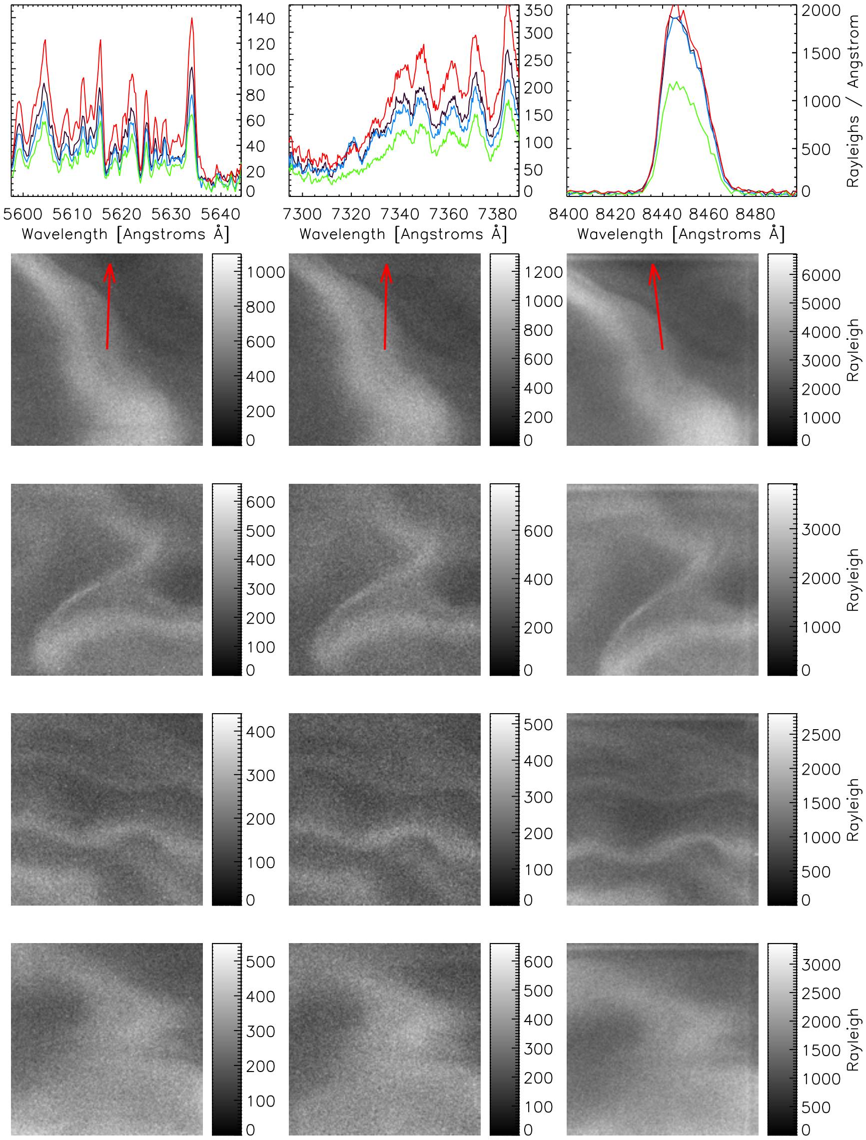

Figure 4.11: Top row: HiTIES spectra for four consecutive integration periods beginning at 21:13:21, 21:13:51, 21:14:21 and 21:14:52 UT, shown in black, blue, green and red respectively. The ASK images below are aligned with time increasing down the page, with ASK 1, ASK 2 and ASK 3 data in order across from left to right. The direction of north is shown by the red arrows.

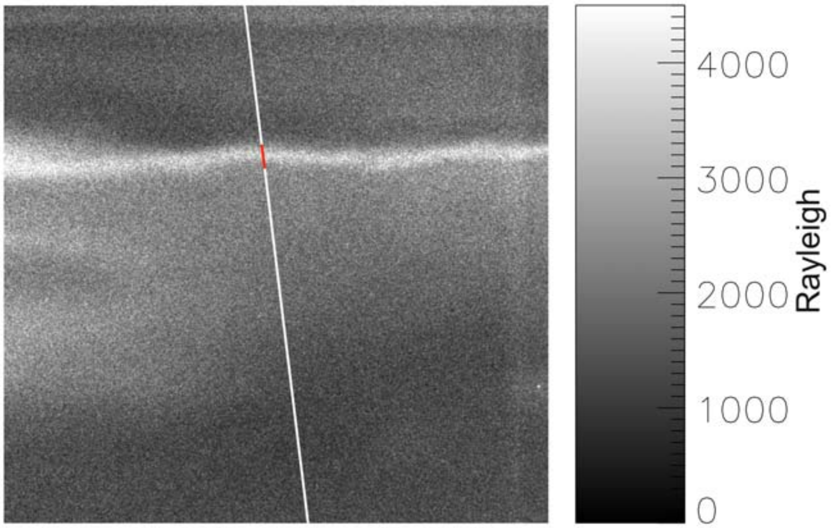

Figure 4.12: Calibrated ASK 3 image taken at 21:14:03 UT, showing a bright arc element on the edge of a larger arc system. The north-south cut used for estimating the width is shown in white. The measured width is overlaid in red.

Figure 4.12 shows an image from the ASK 3 camera, taken at 21:14:03 UT. A bright thin arc is visible near magnetic zenith, on the edge of a larger diffuse arc structure. The variations in intensity along the north-south cut, marked in white, are shown in Figure 4.13. With the higher intensities measured in this event, a lower smoothing factor of width 10 was needed to reveal the structures above the noise level. The arc angular width, measured using a cut-off at 50% of the peak intensity minus background, is found to be just under 0.3°with an uncertainty of plus or minus 0.1°. The main bright arc element appears on the northern edge of a larger region of aurora, with a much sharper boundary visible to the north than to the south. The intensity to the south of the arc element was used as the background level in order to differentiate between the element and the larger arc, which do appear to be separate features with a discontinuity in intensity.

For this event, emission was found to be predominantly at E-region altitudes, indicating that dissociation of molecular oxygen is the main source of intensity in ASK 3. Using the peak emission altitude of 110 km, shown by modelling in Section 1.7.4 for the E-region source of atomic oxygen emission, the filament width can be estimated as 0.6 km ± 0.2 km.

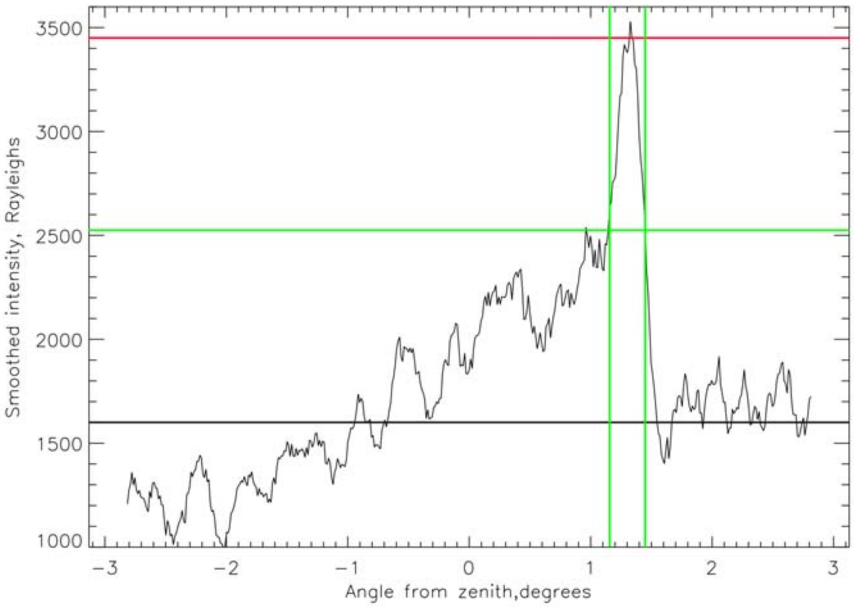

Figure 4.13: Calibrated intensities along a north-south cut across the image shown in Figure 4.12. The red line shows the maximum intensity measured within the arc element, the black line shows the level taken to be the background, separating the discrete structure from the auroral background and the green lines show the calculated width at half the maximum intensity.

4.5 Event 3: 26 January, 17:36 UT

The third event analysed here exhibits combined characteristics from the previous two studies, and demonstrates the short time scales on which auroral morphology and the characteristics of incoming precipitation can change.

4.5.1 Camera observations

The 20 minute keogram sequence of ASK 2 and ASK 3 camera data from the evening of 26 January 2006, is shown in Figure 4.14, beginning at 17:30:17 UT. Data from the ASK 1 camera was unavailable for this time interval, due to a failure of the ASK 1 control computer disk. The TLC imager is primarily sensitive to $N_2$1PG bands in the E-region and was used to confirm the presence of high-energy auroral features, which would normally be detected in ASK 1. The TLC camera is fitted with a 6450 Å cut-off filter, and so does not provide the same narrow wavelength band information as ASK, but with the larger field of view (16 degrees by 12 degrees) it does help to locate the ASK images within the context of larger scale auroral features.

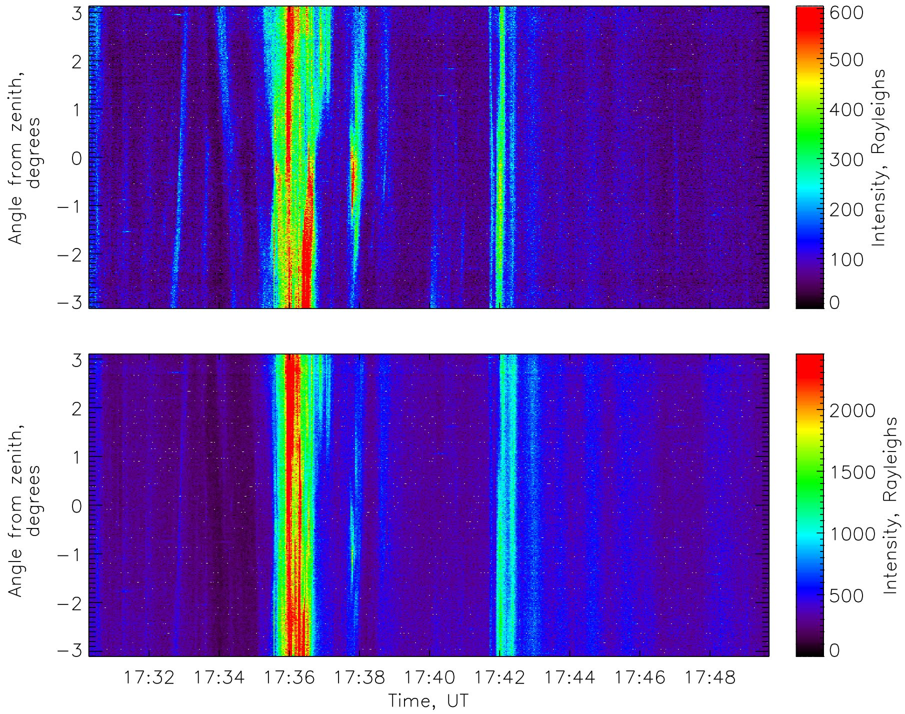

Figure 4.14: Keograms of ASK 2 and ASK 3 camera data, for a 20 minute interval starting at 17:30:17 UT. Image cuts are taken along the North-South meridian line.

Figure 4.15 shows the TLC keogram for this event, covering the corresponding 20 minute ASK megablock. The TLC was operating in time lapse mode for this interval, during remote running hours after the manned campaign season had ended. This gives a calculated time resolution for the images of 2.8 frames per second. For the keogram plot, mean values of 10 successive frames are used for each image cut, giving an effective temporal resolution of 3.6 seconds. The top and bottom 5% of the data values have been discarded to remove outliers. For this time interval, TLC images were used for purely diagnostic purposes in locating large scale auroral features, and were therefore not calibrated into units of absolute intensity. The colour scale used here is a direct representation of detector counts. The third event shown in this section is based on the auroral intensification around 17:36 UT, which appears in both the ASK cameras and the centre of the TLC field of view.

The evolution of the auroral structures present during this interval are shown in image frame sequences approximately 30 seconds apart in Figure 4.16. The time resolution of the images is 5 frames per second for the ASK data, and 2.8 frames per second for the TLC data. The direction of north is shown by the red arrows. The images show a clear variation in the auroral morphology present throughout the interval. At the beginning of the event, the aurora is characterised by rayed filamented features.

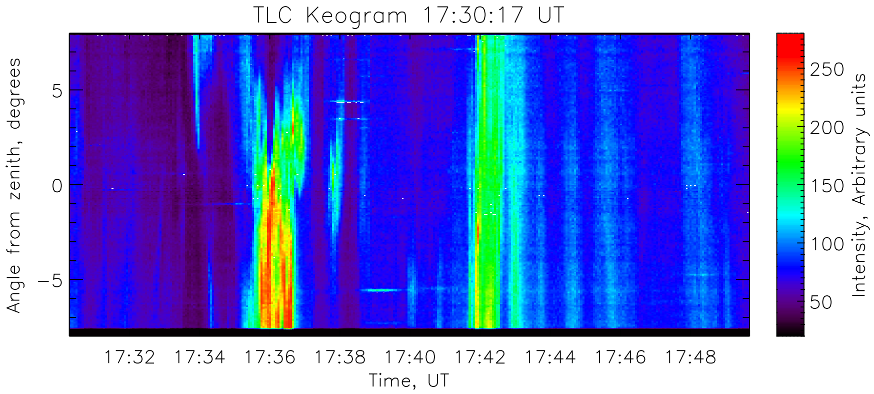

Figure 4.15: Keogram of TLC data, for a 20 minute interval beginning at 17:30:17 UT. Image cuts are taken along the North-South meridian, centred on the middle of the image frame (directed towards local magnetic zenith).

The TLC camera shows that the rays observed in ASK form part of a large coronal rayed structure around magnetic zenith. Within 30 seconds the aurora has changed completely in nature. The ASK images show intense wave forms and dynamic curls with well defined edges in brightness. Finely structured filaments and black lanes can be seen extending away from the main bright regions. The TLC images show that these features are part of an extensive wave pattern seen almost filling the TLC field of view across magnetic zenith. After a further 30 seconds the aurora returns to having the appearance of ray-like structures, similar in form and brightness to that at the beginning of the event, extending around magnetic zenith.

4.5.2 Spectrographic analysis

Figure 4.17 shows the HiTIES data for this interval. The second panel (O^+ shows strong emissions of similar intensity for both the O^+ doublet and the $N_2$1PG bands, at around 17:36 UT, with the O^+ doublet dominating immediately before and after. Enhanced O_2^+ and O emissions, in the first and third panels respectively, are observed at the same time.

Figure 4.18 is as described for the previous events, except that camera frames from the TLC imager on SIF are shown in place of ASK 1 data. The position of the HiTIES spectrograph slit is shown mapped onto the images from the TLC camera. The H_β and the O panels (on the right of the filter mosaic in the orientation of Figure 2.3c) are represented by the yellow section of the curve, and the O^+ and the O_2^+ panels (on the left of the filter mosaic) are represented by the purple section of the curve. The O^+ panel (middle column) in Figure 4.18 shows that the oxygen doublet

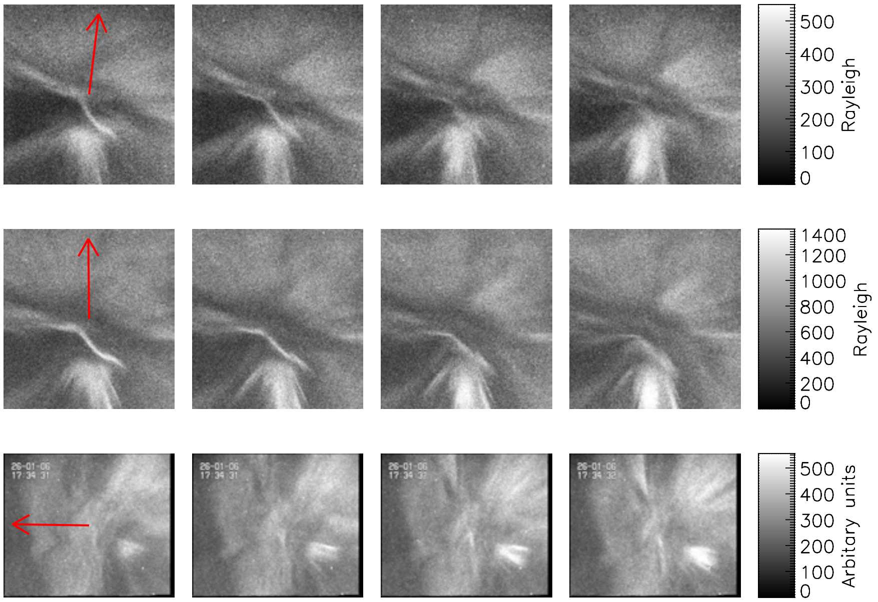

(a) ASK and TLC image frames, 17:35:33 UT onwards

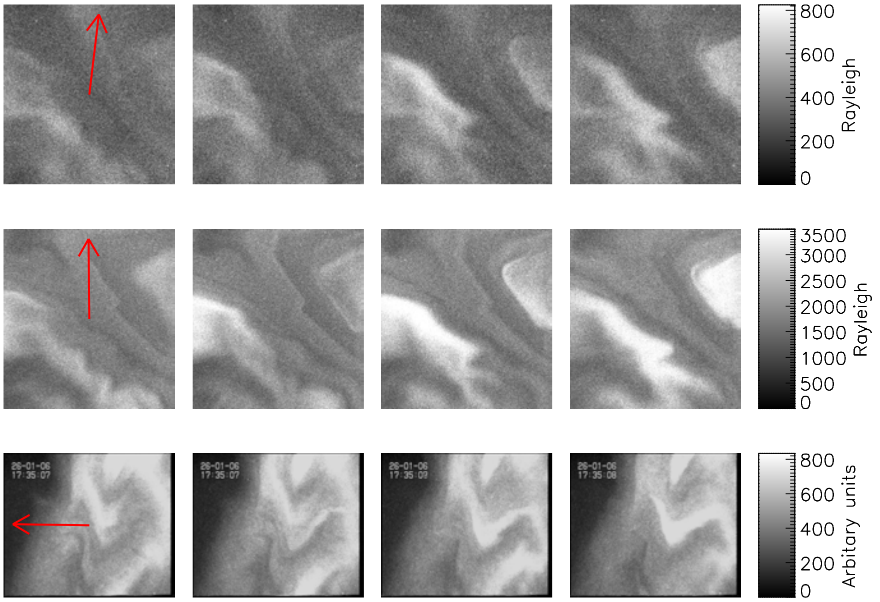

(b) ASK and TLC image frames, 17:36:09 UT onwards

Figure 4.16: Series of consecutive 0.2 s integration ASK images and corresponding TLC images, with the initial images at times spanning the auroral enhancement. Images are presented in the order ASK2, ASK3, TLC vertically for each time sequence. Note that the time stamp imprinted on the TLC images was inaccurate for this interval; the TLC timing was manually synchronised to the ASK data.

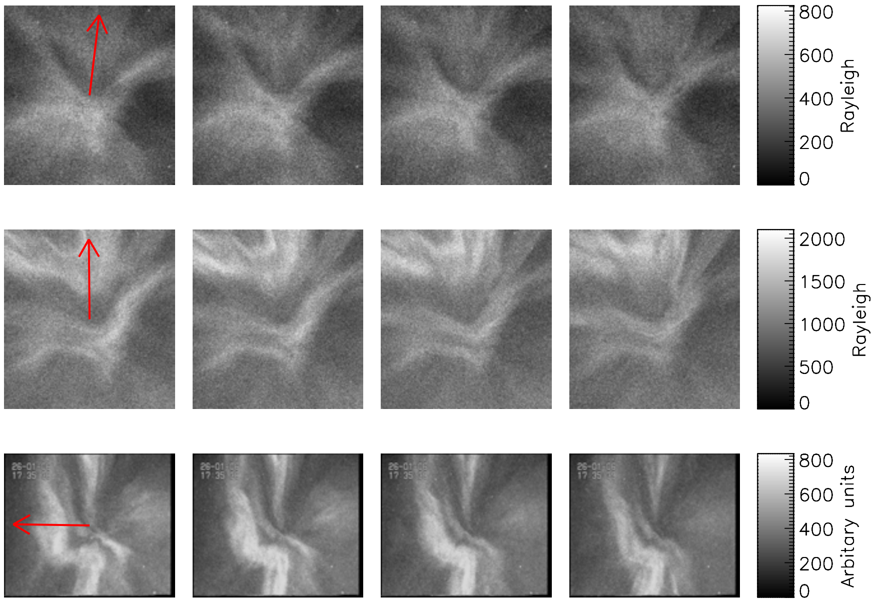

(c) ASK and TLC image frames, 17:36:40 UT onwards

Figure 4.16: Continued from previous page.

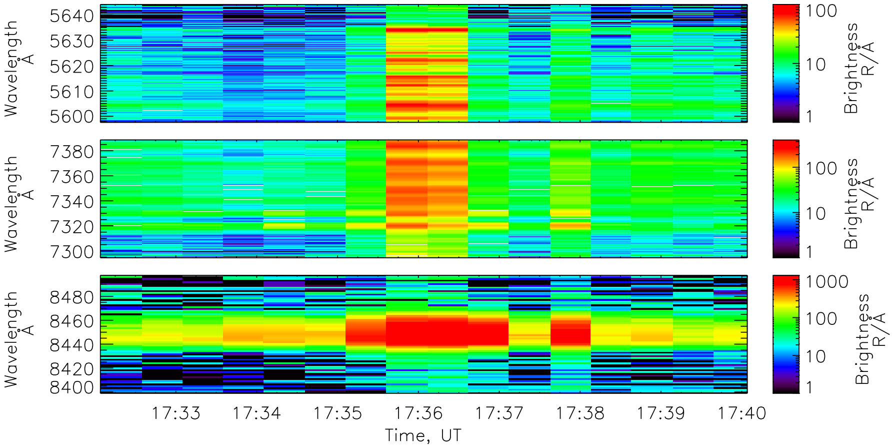

Figure 4.17: HiTIES spectrogram plots showing emission data in R/Å, from the O_2^+ (top), O^+ (middle) and O (bottom) panels. Calibrated wavelengths for the emissions are shown on the vertical axis.

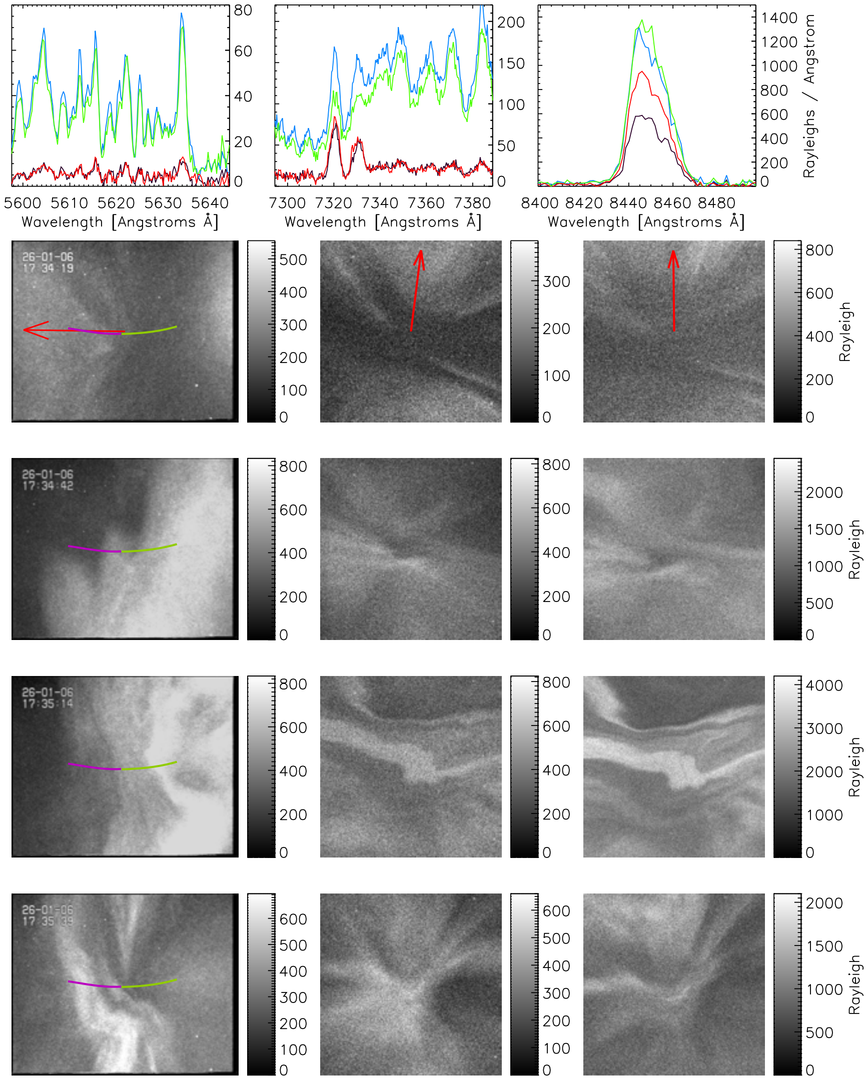

Figure 4.18: Top row: HiTIES spectra for four consecutive integration periods beginning at 17:35:06, 17:35:36, 17:36:07 and 17:36:37 UT, shown in red, blue, green and black respectively. The TLC and ASK images below are aligned with time increasing down the page, with TLC, ASK 2 and ASK 3 data in order across from left to right. The direction of north is shown by the red arrows.

emission lines at 7320 Å and 7330 Å are enhanced throughout the interval. For the first and last HiTIES integration periods (red and black), emission from the O^+ doublet dominates the O^+ panel passband. The O_2^+ panel (left column) shows that emission from the molecular oxygen bands in the E-region is also present but weak (less than 20 R/Å). This confirms that emissions resulting from low energy precipitation are dominating. The ASK images taken from within the red and black intervals show slowly evolving auroral rays.

In the middle HiTIES time intervals (blue and green), there is a burst of enhanced molecular emissions. The O_2^+ panel shows strong molecular oxygen bands caused

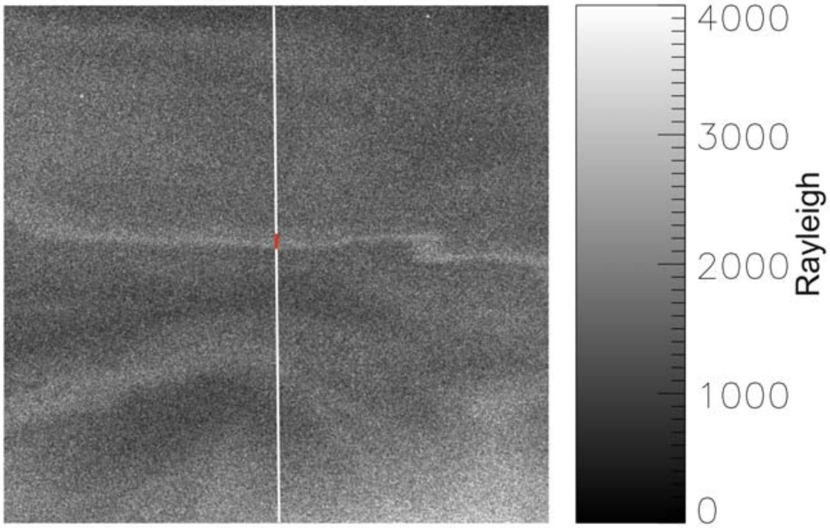

Figure 4.19: ASK 3 image taken at 17:36:22 UT, showing a thin arc structure in the magnetic zenith. The north-south cut used for estimating the width is shown in white. The measured width is overlaid in red.

by higher energy precipitation. Molecular nitrogen bands are seen to be contributing strongly to the emission in the O^+ panel, at over 200 R/Å. However unlike for Event 2, the oxygen doublet emission in the O^+ panel also increases in intensity up to around 170 R/Å, remaining at a comparable level with the enhanced nitrogen bands, rather than becoming swamped by them. During the blue and green intervals intense auroral waveforms and thin arc elements with fluid-like motions are seen in the ASK images.

4.5.3 Temporal and spatial scales

The time scales of auroral evolution vary throughout the course of this event. For the low energy rayed aurora intervals, there is no sub-second variation. Small scale filamentary features within the coronal pattern vary on a time scale of about a second. This behaviour changes drastically with the burst of higher energy precipitation observed in the second and third intervals. Well defined patches of bright auroral emission are seen to evolve on time scales comparable to the ASK time step length of 0.2 seconds for this event.

Spatially, the aurora was seen to include structures with narrower filaments than in either of the two previous events. Figure 4.19 shows an ASK 3 image frame taken at 17:36:22 UT when the thinnest arc structures were observed across the magnetic field line direction at zenith. Figure 4.20 shows the intensities across the marked line-cut, with a 10 point smoothing factor applied. The angular size of the arc elements is

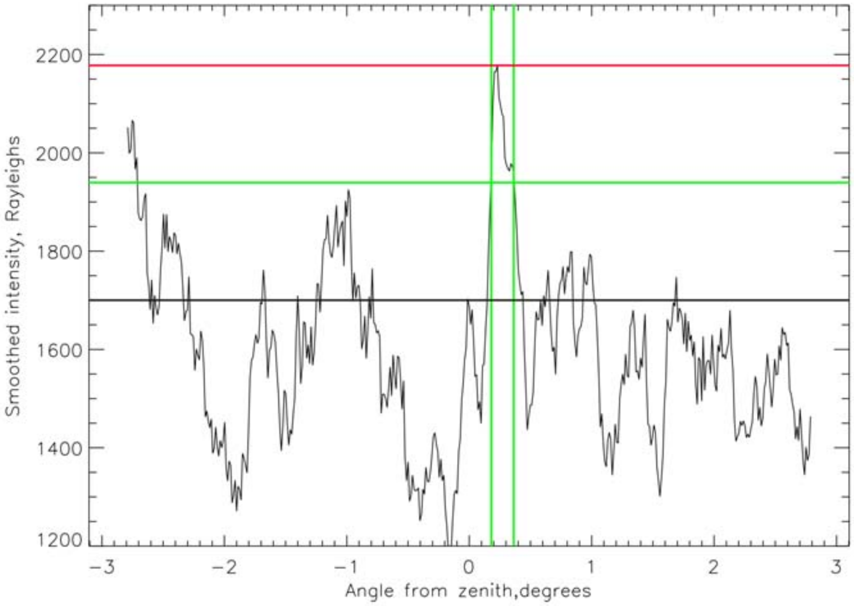

Figure 4.20: Calibrated intensities along the north-south cut shown in Figure 4.19. As before, the red line shows the maximum intensity measured within the arc element, the black line shows the level taken to be the background, and the green lines show the calculated width at half the maximum intensity.

found to be 0.2°± 0.1°.

The times of thin fluid arc elements in the ASK camera data are characterised by strong emissions in the O^+ oxygen doublet as well as in the O_2^+ and $N_2$1PG molecular bands, indicating incoming precipitation with a mix of both high and low energies. This results in emission at different altitudes in the ionosphere, leading to difficulty in assigning a typical peak emission altitude for estimating the spatial scale. Figure 4.21 shows a TLC image taken at 17:36:18 UT, displayed in red, and an overlaid image from ASK 3 at the same time, displayed in blue. Both images are shown mapped onto a common coordinate system, fixed with respect to the distant stars. Any structure at a finite altitude will appear to shift position between the two observing points, due to the effect of parallax. This parallax displacement will be parallel to the orientation of the baseline between the ASK and TLC cameras, shown as vertical in Figure 4.21. The white line shows the parallax between the edges of an auroral feature identifiable in both cameras. This gives the altitude of the emission for this feature as around 100 km, as shown by the scale to the right. The same peak emission altitude of 110 km as used for Event 2 in the ASK 3 camera was therefore used here, which gives an estimated spatial scale of around 400 ± 200 m.

Figure 4.21 also shows that the images of the auroral elements appear the same when viewed stereoscopically, although with some displacement along the optical

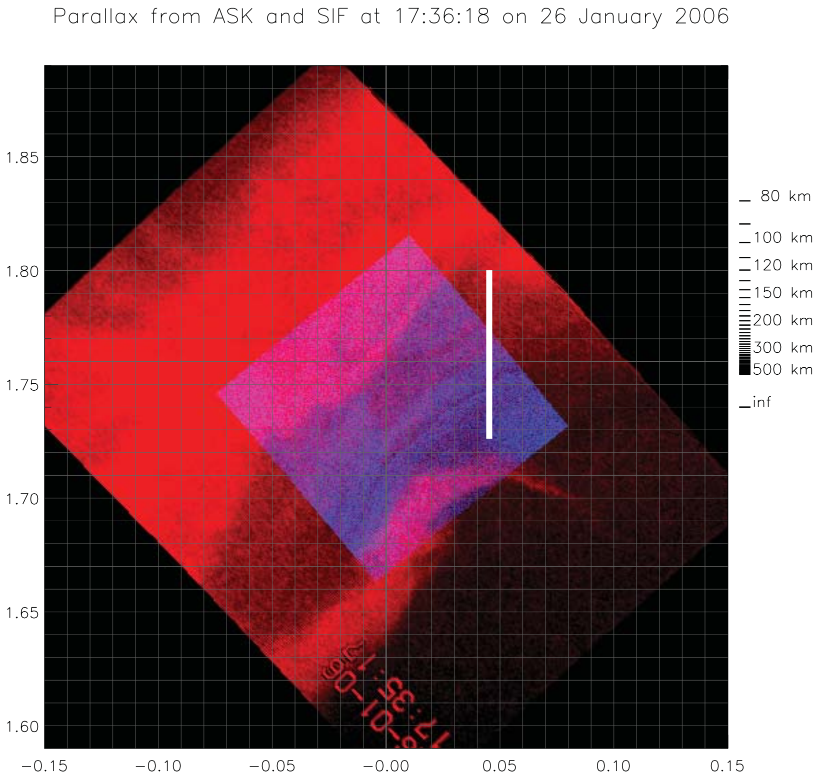

Figure 4.21: Overlaid ASK (blue) and TLC (red) images demonstrating the difference in field of view and the parallax shift (white line) caused by the 7 km separation between the imagers. The grid step is 0.01 rad.

baseline. This implies that the auroral features must come from a rather narrow altitude region. If the structures had a large extent in altitude, features at large range would exhibit smaller parallax shift, distorting the appearance of the overall auroral image.

4.6 Data considerations

4.6.1 Arc width measurements

The most important consideration in measuring the width of an auroral arc is its elevation angle. The apparent width observed will only corresponding to the actual arc width when viewing in the magnetic zenith. The apparent width broadens rapidly at only a few degrees off zenith (Lanchester, 1980). Clear structures as close as possible to the magnetic zenith were used for width estimation. For Events 1 and 3 the arc structure was within 0.5°of zenith at the time of arc estimation. For Event 2, the complex nature of the aurora led to single arc elements being rare. The only clear feature suitable was at 1.5°away from magnetic zenith, meaning that the true arc width is likely to be smaller than the apparent width.

Previous descriptive studies of auroral arcs have not always used absolute criteria to define the widths (Maggs and Davis, 1968). An arc that appears thin in a narrow view camera can suddenly change to fill most of the field of view on a higher gain setting. For uncalibrated instruments where the gain is unknown, such as for some all-sky cameras, an absolute measure of arc scale size cannot be made. There is also the question of where the edge of an auroral arc is defined to be. The intensity of an auroral arc does not instantly fall to zero at a certain point, but instead decreases gradually to some background level. The apparent width of an auroral feature is sometimes simply stated, presumably judged by eye, and is not always defined objectively.

The use of calibrated ASK intensities here, given in units of Rayleighs, allows an absolute width scale to be obtained, comparable with data from other independent instruments. The measured width has here been defined as the distance, perpendicular to the arc, between points where the intensity falls off to half the maximum intensity of the structure. This definition has been used in previous statistical studies of arc widths, such as by Knudsen et al. (2001), and although it cannot be said to represent an absolute width any better than other criteria, a common definition does allow meaningful comparisons between different studies. However, in the estimation of half widths, a background level must be subtracted. For the data shown here, it is not always clear where the background level should be defined, and the measured arc widths are very sensitive to this. Even with the resulting uncertainties in the widths, there is a very clear difference between the large-scale arc and the narrow filaments and arc elements when high energy precipitation is present. However, the difference between the purely high energy forms and the thin structures during a mixture of precipitation energy may in part due to the background uncertainty.

A further consideration is the difference between what is seen as an individual structure and what appears as intensity modulations of only 5 to 10% within a larger band of luminosity. This depends greatly on the imaging contrast of the camera system as discussed by Davis (1978) and Haerendel (1999). For Event 2, where the arc scale size was observed at 600 m across, the imaging contrast of the main defined filament (defined as 100 times the amplitude of the arc, 1850 Rayleighs, divided by the sum of the arc intensity plus the background, 3450 Rayleighs) is 54%. For Event 3, where the thinnest arc structures were observed at 400 m across, the contrast is weaker, although the intensity peak at 2175 Rayleighs and the background level at

1700 Rayleighs still gives a modulation of 22%. This structure could be considered as a small-scale modulation feature within a larger auroral structure.

The exposure time of an individual frame also needs to be taken into consideration, as discussed by Lanchester et al. (1997). In their event, an arc moving rapidly across the camera field of view only appeared at its narrowest when the exposure time was reduced to 2.5 ms. For the events presented here the ASK exposure time is 0.2 s or more, meaning that fast moving features will be smeared out across the image during this time, and will appear to have a larger than true width. For this reason, combined with other factors discussed, the arc widths given here are upper bound estimates.

4.6.2 HiTIES slit location

With the combination of spectrographic data and optical imaging it is possible to identify the small-scale auroral structures that contribute to the spectrographic measurements. The centre 4°of the 8°long HiTIES slit is used to sample the aurora over the 30 second integration period. For Event 1, a single auroral arc, stable on long time scales, moved slowly across the centre of the optical image. The gradual increase and decrease in O^+ emission seen in the spectrograph is clearly linked with the auroral arc moving through the centre of the image and the HiTIES slit. For Event 2, with the auroral features moving on time scales much faster than the integration time of the spectrograph, this one to one relationship cannot be established. However, a general link between spectrographic emissions and auroral morphology can still be obtained, with the overall behaviour of the aurora being constant over several HiTIES integration periods. The fact that the features predominantly fill the entire ASK field of view, together with the speed at which the structures move, implies that the centre of the slit will be filled by the aurora for most, if not all, of the 30 second integration period. Temporal averaging over an integration interval where the aurora moves out of the slit for a time would result in the spectral emission intensities given here being an underestimate.

For Event 3, the situation is more complicated as the aurora does not fill the entire HiTIES slit throughout the interval. This is demonstrated clearly in Figure 4.22, which displays a keogram from the TLC imager, similar to Figure 4.15, except that the image cuts are taken along the length of the HiTIES slit as it is mapped onto the TLC field of view. The white vertical lines show the four consecutive intervals corresponding to the 30 second integration periods of the HiTIES spectrograph. It can be seen that during the periods of predominantly low-energy precipitation (first (red) and last (black) intervals) the rayed aurora is seen mainly to the north of magnetic zenith

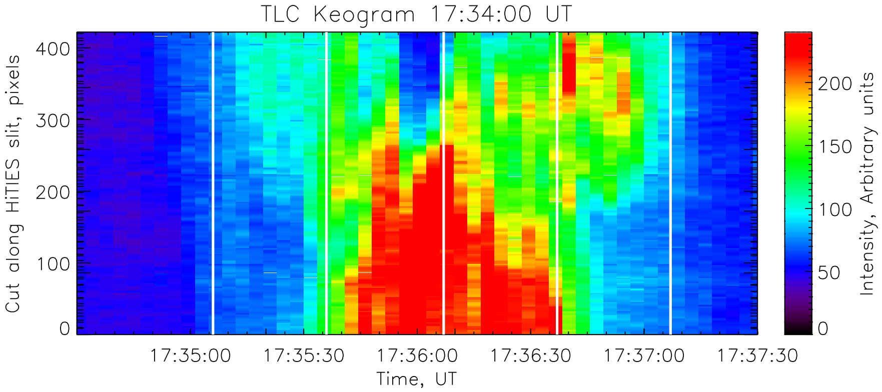

Figure 4.22: TLC Keogram showing image cuts taken along the HiTIES slit position. The white vertical lines at 17:35:06, 17:35:36, 17:36:07, 17:36:37 and 17:37:07 UT represent the four HiTIES integration periods as described previously.

for some of the integration period, i.e. at the very beginning and end of the event. This means that the brightest aurora is not always central in the spectrograph field of view, and not necessarily covering the section of the HiTIES slit marked in purple on the images, representing the O_2^+ and O^+ panels. At these time the reduction in high energy signatures accompanying the oxygen doublet emission in the O^+ panel may, in part, be a result of only sampling the tops of the rays, nearer the centre of the image.

However, as shown in the image sequences in Figure 4.16, the rayed emissions do extend to cover the centre of the field of view, towards the end of the first interval after 17:35:30 UT and at the beginning of the last interval until 17:36:50 UT. The emissions appear centrally in the slit for a significant fraction of the integration time, especially for the last interval where emissions are present centrally for almost half of the period. This implies that the higher energy emission from $N_2$1PG bands should still show a strong signature if it were present although reduced due to the temporal averaging. The O^+ panel data for Event 3 in Figure 4.18 shows that although some peaks related to the $N_2$1PG bands can be identified, the intensities are only marginally above the background noise level. Although the location of the aurora may be having some influence, the relative increase of the low-energy oxygen doublet emission during times of auroral rays is interpreted to be physical and not simply a spatial effect.

Furthermore, for the two higher energy (blue and green) intervals in Event 2, comparing both the ASK images and the O^+ panel, it can be seen that the system of arcs contains more visible ray-like structures within in it during the blue interval. This interval shows the oxygen doublet emission is at the highest intensity measured over the course of the entire event, comparable with the intensity of the $N_2$1PG bands. For the interval marked in green, the oxygen doublet, although still a strong feature in the emission spectrum, has weakened in intensity compared to the $N_2$1PG bands. The ASK images here show aurora which is purely in the form of thin dynamic arc structures. For these two intervals the auroral activity does cover the centre of the spectrograph at magnetic zenith, which confirms the link between rayed aurora and precipitation with a relatively large contribution from low-energy electrons.

4.7 Discussion

4.7.1 Multi-spectral imaging

Instrument developments in spatial and temporal resolution available for auroral imaging in recent years have led to more studies concentrating on small-scale thin arcs and filamentary structures within larger auroral forms (Trondsen and Cogger, 1998; Semeter and Blixt, 2006). Small-scale measurements are essential in order to understand the complexity in auroral structure, which theoretical generation mechanisms must be able to reproduce. High-resolution imaging can provide a detailed picture of the spatial structure and temporal changes in auroral, but gives little or no information about the energy of the precipitating particles. Spectrographic data can be used to estimate the energy distribution from the auroral emissions. Kaila (1989) showed how the energy of auroral electrons in discrete arcs can be determined by the intensity ratio of the 6300 Å and 4278 Å emission lines, as observed by photometers. Imaging spectrographs, providing simultaneous measurements in a number of different wavelength regions have also been used to investigate auroral emissions (Pallamraju and Chakrabarti, 2005; Ivchenko et al., 2004). However, spectrographic instruments cannot match the sub-second temporal resolution of intensified optical imagers and, with measurements from a single narrow slit, they do not differentiate between spatial and temporal changes.

The use of combined spectrographic and optical camera data, as shown here, can be used to investigate the relationship between the incoming electron flux and the observed auroral morphology, and unravel temporal and spatial changes. Although the ASK imager already provides some spectral information through the use of narrow pass-band filters, the spectrographic information allows the additional separation of different emissions that appear within the wavelength range of each camera. Detailed knowledge of the energy distribution is crucial in understanding the acceleration processes operating above the ionosphere, which are responsible for creating the dynamics and spatial structures observed (Semeter et al., 2001).

4.7.2 Acceleration mechanisms

The variation in precipitating electron energies between different auroral structures, is an essential indicator of the Alfvénic and inverted-V acceleration mechanisms. The results presented here agree with previous multi-spectral imaging case studies. Ivchenko et al. (2004) showed that the presence of rayed arcs was related to enhancement in emission from the O^+ doublet and low energy precipitation. In Ivchenko et al. (2005) an auroral curl was shown to lack any significant low energy component, while rayed structures were associated with a mixture of both low and high energy precipitation. Furthermore, in an optical camera study Blixt et al. (2005) showed that aurora of the type termed 'dynamic rayed aurora', appeared to be linked to precipitating electrons with a broad range of energies. Dynamic rayed formations often had the appearance of 'flaming aurora', due to the variations in time of flight of incoming electrons with different energies. The necessary broad-energy range spectrum with a significant low energy tail, is suggested to be of the type produced by Alfvénic acceleration.

The results from combined ASK and HiTIES spectrograph measurements show purely high energy precipitation during times of auroral waves and loops, while a mixture of precipitation energies is observed during times of rayed aurora. This supports the theory that rays are signatures of Alfvénic acceleration. Although not shown here, Dahlgren et al. (2008b) also presents O_2^+ / O intensity ratios over the ASK field of view during the purely high energy event (Event 2), where the images of the aurora appear identical in each camera. The results show that a thin auroral filament can be identified in the ratio plots, implying an increase in energy within the filament compared to the surroundings. On the other hand, an auroral fold has no associated difference in energy, being purely the result of an increased electron flux compared to the background. This agrees with the interpretation that, even for high-energy aurora, models to explain the generation of small-scale features and arc distortions must take acceleration mechanisms into account, as well as electrostatic instabilities within the acceleration region.

4.8 Summary

This chapter presents some of the first results from the ASK (Auroral Structure and Kinetics) instrument, a new multi-spectral imager developed to observe small scale auroral structures in several wavebands simultaneously. The results shown here are from three very different periods of auroral activity, comparing the auroral morphology with changes in the characteristic energy of the precipitating particles. Supporting information from the HiTIES spectrograph, as part of the Spectrographic Imaging Facility (SIF), is used to identify spectral lines within the passband of each of the ASK cameras and determine the source of the emissions.

The first event shows a slow-moving faint auroral arc associated with purely low energy electron precipitation. The second event has incoming electrons of primarily high energy and very little low energy component. In this case the aurora is in the form of bright dynamic patches and filaments, varying on short sub-second time scales. The spectral information for the third event shows the prevalence of both low-energy and high-energy precipitation, with associated rayed aurora and thin streaming arcs respectively.

In summary these events suggest that aurora during primarily high-energy precipitation tends to be more dynamic, varying on shorter time scales, than aurora during low-energy precipitation. Rays are seen to be associated with a mix of precipitation energies including a strong low-energy component, whereas thin fluid-like arcs are a signature of predominantly high-energy precipitation. The characteristic scale sizes of auroral features also seems to have a dependence on the energy of the precipitation. For the low energy event, the arc width was measured to be 7.4 km, whereas arc elements in the purely high-energy event, and in the high-energy dominant interval within the final event, were measured at around 600 m and 400 m respectively. This suggests that some high-energy component in the precipitation population is necessary for the generation of small scale structures.

5

A study of multiple NEIAL events

In this chapter, optical data are compared with EISCAT radar observations of multiple Naturally Enhanced Ion-Acoustic Line (NEIAL) events in the dayside cusp. This study uses narrow field of view cameras to observe small-scale, short-lived auroral features. Using multiple-wavelength optical observations, a direct link between NEIAL occurrences and low energy (about 100 eV) optical emissions is shown. This is consistent with the Langmuir wave decay interpretation of NEIALs being driven by streams of low-energy electrons. Modelling work connected with this study shows that, for the measured ionospheric conditions and precipitation characteristics, growth of unstable Langmuir (electron plasma) wave modes can occur, which decay into ion-acoustic waves. The link with low energy optical emissions shown here, will enable future studies of the shape, extent, lifetime, grouping and motions of NEIALs. This work has been published by the author in Sullivan et al. (2008), and was carried out in collaboration with Eduard Kontar of the University of Glasgow. The author's contribution was the analysis and interpretation of the optical and radar data and the processing of data for input to the Langmuir turbulence model, while the model itself was devised and run by Eduard Kontar.

5.1 Motivation

Recent spectrographic imaging studies, presented in this thesis and in Ivchenko et al. (2005) and Dahlgren et al. (2008b), have shown that rayed aurora is associated with precipitating auroral electrons of mixed energy, with a large contribution to the total energy flux from low-energy electrons. Combined radar and optical studies have identified a link between NEIALs occurring in the dayside cusp and thin rayed auroral structure of similar scale size (Blixt et al., 2005; Grydeland et al., 2004). From a number of proposed theories, ‘parametric decay’ has emerged in recent studies as the most likely candidate for the mechanism responsible for NEIAL observations in the dayside cusp. As described in Section 1.10, low-energy electron beams cause the growth of unstable Langmuir (electron-plasma) waves through the bump-on-tail instability; these waves decay to ion-acoustic wave modes at IS radar wavelengths (Forme, 1993, 1999; Kontar and Pécseli, 2005), giving radar echoes which are much stronger than those from thermal vibrations. The requirement of the parametric decay mechanism for low-energy electron beams may account for the observed link with rayed aurora, now known to contain a significant population of low-energy electrons.

Multi-spectral imaging of the aurora during times of NEIALs can be used for the direct study of emissions from low-energy electrons. The low-energy component of auroral precipitation can be imaged using the forbidden oxygen (OII) ^{2}P - ^{2}D emissions at 7320 and 7330 Å, which are predominantly produced by auroral electrons with energies of around 100 eV, as described in Section 1.7.2. Previous optical camera studies of the aurora during dayside NEIALs have used imaging either in white-light or with a long-pass cut-off filter applied to concentrate on the prompt $N_2$1PG band at 6700 to 7500 Å. Few studies have compared the variation of auroral emissions present within the radar beam with the occurrence of NEIALs. Where multi-spectral studies have been made, the parallax effects of using instruments at locations separated from the radar have not been taken into account. Geometry considerations become very important at the small-scale level needed to study NEIAL behaviour. Previous studies have suggested that high-energy particles may also have an important part to play in the generation of NEIALs (Lunde et al., 2007). It may be possible to differentiate between different NEIAL generation mechanisms by determining whether the presence of high-energy precipitation directly drives the instability itself or provides more favourable conditions for NEIALs to be observed at ISR wavelengths.

Auroral emissions are generated at lower altitudes than where NEIAL signatures are generally observed in the cusp ionosphere. In order to understand the processes driving NEIALs, it is important to investigate directly the conditions at NEIAL altitudes. Orbiting spacecraft, such as the DMSP satellites, can provide information on large-scale precipitation characteristics. However with the inaccuracies inherent in mapping the magnetic field line topography in altitude, satellite data cannot be linked to individual NEIAL and auroral filaments on sub-kilometer scales. The use of ionospheric modelling with satellite data inputs to try and replicate NEIAL behaviour may help to advance our understanding of NEIAL generation.

5.2 Event Context

This study concerns the interval from 08:50 UT to 10:00 UT on 22 January 2004, in which multiple NEIAL signatures were recorded by the ESR. Using a range of instrumentation, it is possible to infer information about the plasma conditions and field configurations over the course of the event, to aid in interpretation and discussion of the results. All coordinates systems referred to in the following section are defined in Appendix A.

5.2.1 Solar wind

The observations took place during a period of active solar wind conditions measured by the ACE spacecraft, following a coronal mass ejection a few days earlier. The ACE solar wind plasma data is shown in Figure 5.1 and the IMF (interplanetary magnetic field) data in Figure 5.2.

A marked depression in the solar wind number density and dynamic pressure occurred at ACE between 08:10 UT and 09:20 UT. The solar wind speed was extremely high at this time. The component of velocity towards the Earth (V_x in the GSM coordinate system) averaged 640 km s^{-1}, within the interval corresponding to the density drop. Using the ACE spacecraft coordinates, with an average distance from Earth of 1.4606×10^6 km over the corresponding interval, a first estimate of the delay time between solar wind signatures at ACE and their arrival at the Earth is calculated at 38 minutes. The interval of interest occurred after a northward turning of the IMF B_Z component, detected at the ACE spacecraft at 07:44 UT. IMF B_Z then remained weakly positive until 09:20 UT in the ACE time frame. IMF B_Y was strongly negative throughout the interval.

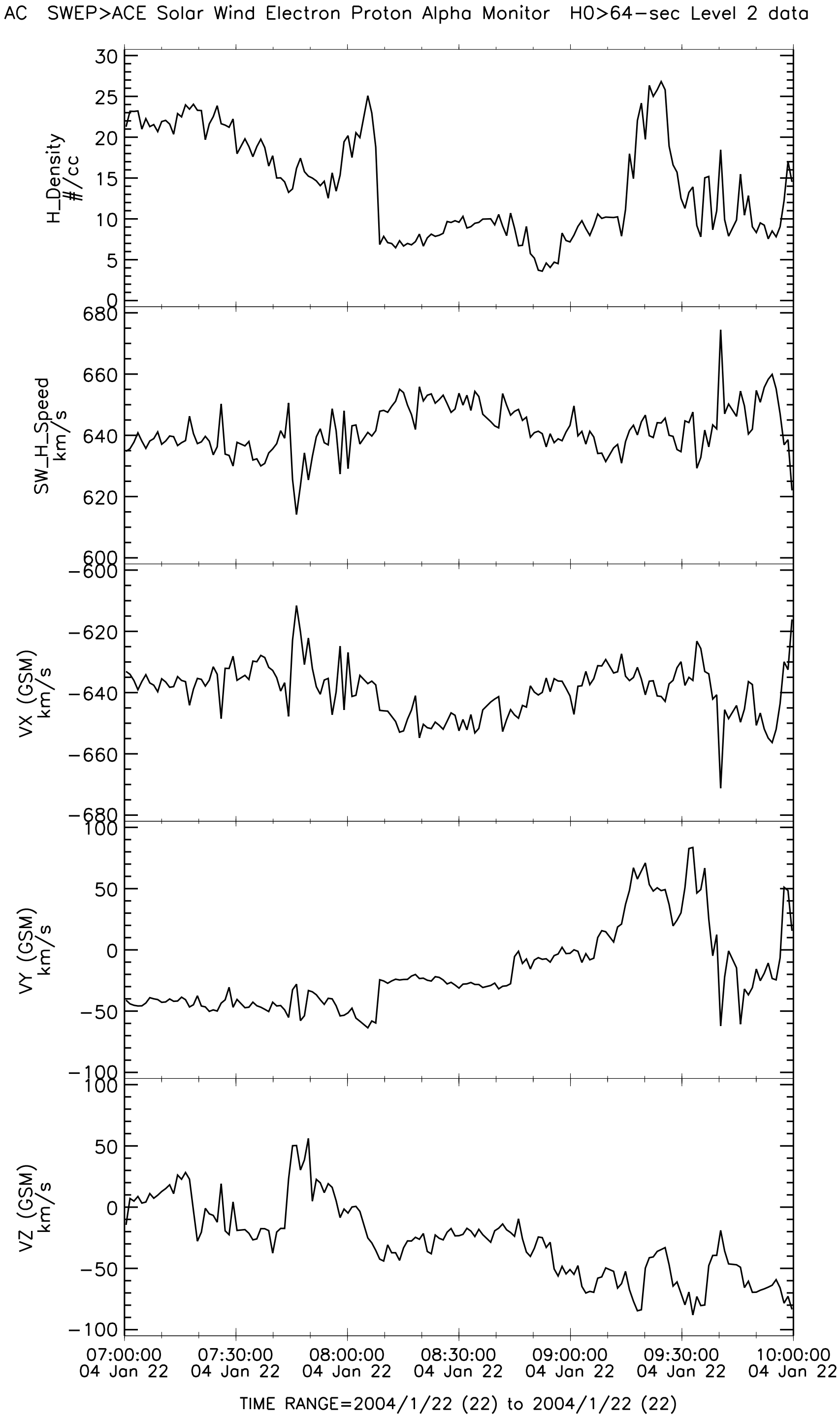

Figure 5.1: Solar wind plasma data from the ACE spacecraft, with thanks to the ACE SWEPAM instrument team and the ACE Science Center.

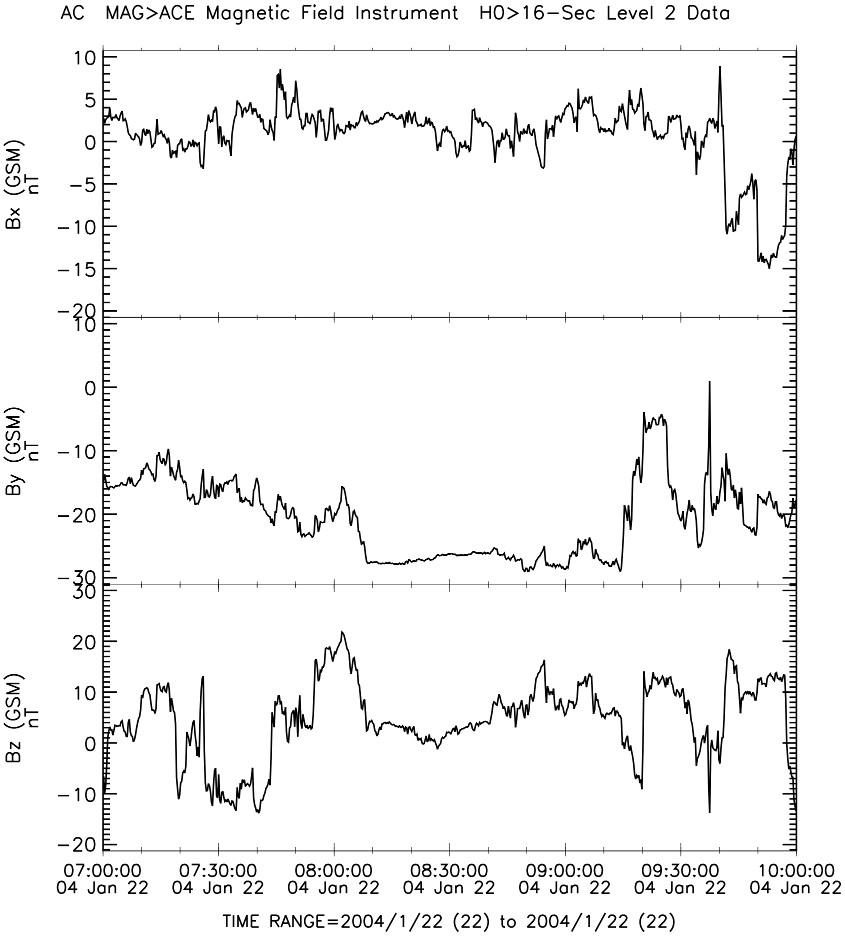

Figure 5.2: IMF data from the ACE spacecraft, with thanks to the ACE MAG instrument team and the ACE Science Center.

5.2.2 Magnetic topology

The passage of a DMSP satellite over the northern polar cap allowed the reconnection topology and the resulting convection pattern to be inferred in the region of our observations, using the measured flow velocities. Figure 5.3 gives a representation of the convection pattern in Magnetic Local Time (MLT) and Magnetic Latitude (MLAT) coordinates, based on the DMSP satellite cross-track (perpendicular to the direction of motion) velocities, shown in green and blue. Although the data quality for the highest latitude section of the pass is often ‘undetermined’, the velocities indicate the presence of one main polar cap convection cell with anti-clockwise rotation, marked in pink, on the dusk side. Embedded within the undetermined vectors are some of highest confidence (in green) which are consistent with the other data. At lower latitudes a conventional dusk cell can be seen (with anti-sunward flow in the polar cap) but there are only very weak flows on the dawn side. The topology of the velocities indicate

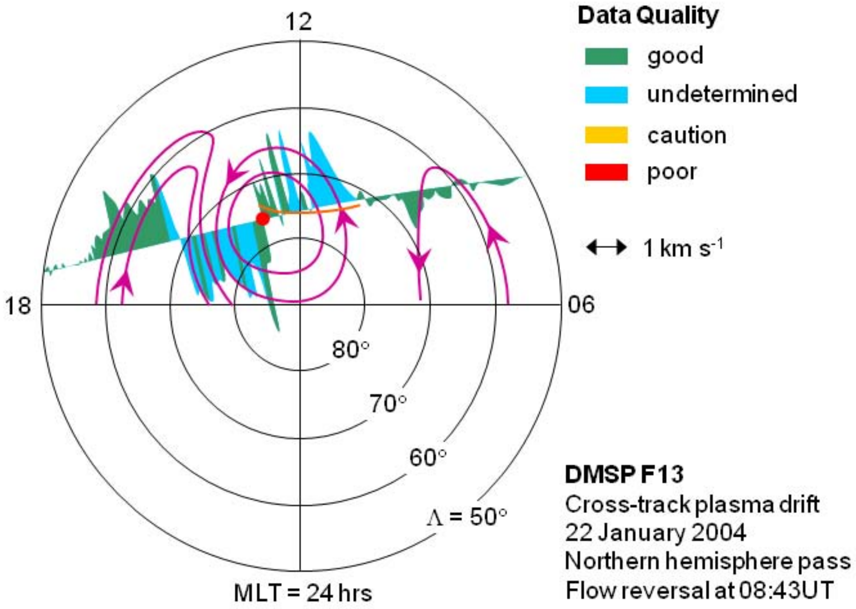

Figure 5.3: Schematic representation of the convection configuration, using DMSP cross-track plasma velocities from 08:34 to 08:54 UT provided by the Center for Space Sciences at the University of Texas at Dallas.

a lobe reconnection configuration in the northern hemisphere (Sections 1.3 and 1.2). One polar cap convection cell has been shown to dominate for large $|B_Y|$ (Reiff and Burch, 1985; Ruohoniemi and Greenwald, 1996) under $B_z > 0$ conditions. Sunward flows from lobe reconnection all return tailward with the same sense of rotation, due to the strong east-west component of the magnetic tension force (anti-clockwise for negative IMF B_Y as shown in Figure 1.2).

For such a 'lobe stirring cell', the reversal between sunward and anti-sunward flow in the central polar cap is associated with the eastward edge of the reconnection X-line which is driving the flow. This reversal intersects the spacecraft track at the point marked with a red dot in Figure 5.3, encountered at 08:43 UT, at 76.0 MLAT and 13.2 MLT (81.0° N, 43.0° E in geographic coordinates), i.e. to the east and slightly to the north of Svalbard (ESR coordinates 78.2° N and 16.0° E) at this time. This point will be close to the east end of the X-line but could be slightly sunward or anti-sunward of it. If the X-line is at or anti-sunward of the red dot, a distinct change in the particle precipitation would be observed at the reversal, as the satellite passes onto newly opened field lines. If the X-line were sunward of the pass, the satellite would instead cross onto open field lines that were reconnected previously and have since been swept tailwards. These 'old-open' field lines are associated with greatly reduced electron densities precipitating in the Earth's reference frame and such a clear change would not be observed.

Particle data from this DMSP satellite pass is presented and studied in further detail in a later section of this chapter, but is briefly referred to here to aid in understanding the reconnection topology. In Section 5.9, Figure 5.20 shows that the precipitation seen by DMSP F-13 changed dramatically at around 08:44:10 UT. Almost no ion precipitation was seen before this time whereas after it a dispersed arrival of sheath-like ions is seen. This is after the satellite crossed the flow reversal boundary, indicating that the lobe reconnection site was anti-sunward of the satellite pass after 08:44:20 UT. The existence of a strong lobe reconnection cell in the DMSP velocity data and the onset of soft precipitation over Svalbard (described in the next section) at 08:43 UT, occur over a minute before the dispersed arrival of ions seen in the DMSP particle data. Thus the failure of F-13 to observe lobe reconnection soft precipitation between 08:43 and 08:44:20 UT indicate that it passed directly through the lobe reconnection X-line footprint (from the anti-sunward to the sunward side) shortly before 08:44:20 UT. The proposed location of the X-line consistent with observations is shown by the orange line in Figure 5.3.

5.2.3 Ground-based observations of activity

Figure 5.4 shows data from the Meridian Scanning Photometer (MSP) instrument at the auroral station in Adventdalen. Each photometer makes a complete scan along the magnetic meridian in 16 seconds. Data is shown for the five MSP wavelengths: 6300, 4278, 5577, 4861 and 8446 Å in order from top to bottom. The auroral activity expanded over the magnetic zenith at 08:43 UT, with an arc previously present on the southern horizon. The presence of intense soft particle precipitation is shown by the strong pulsed intensities in the 6300 Å filter channel (top panel), which continue throughout the entire interval. The sudden onset of auroral activity over all latitudes indicates that the event is triggered by a temporal change, i.e. the onset of reconnection over Svalbard, rather than an already established spatial feature moving into the field of view of the Longyearbyen instruments, although motions in the purely east-west direction cannot be ruled out using meridian scanning instruments. The meridian profiles of intensity from the 5577 and 8446 Å photometers give some suggestion of the aurora brightening fractionally sooner to the north of magnetic zenith. This can be interpreted as field lines to the north of Longyearbyen filling up first, after the onset of reconnection.

Figure 5.5 shows magnetic field data from the Svalbard stations of the IMAGE magnetometer network. The B_x component (northwards in the local geographic coordinate system) shows a negative bay with an amplitude of around 200 nT, represent-

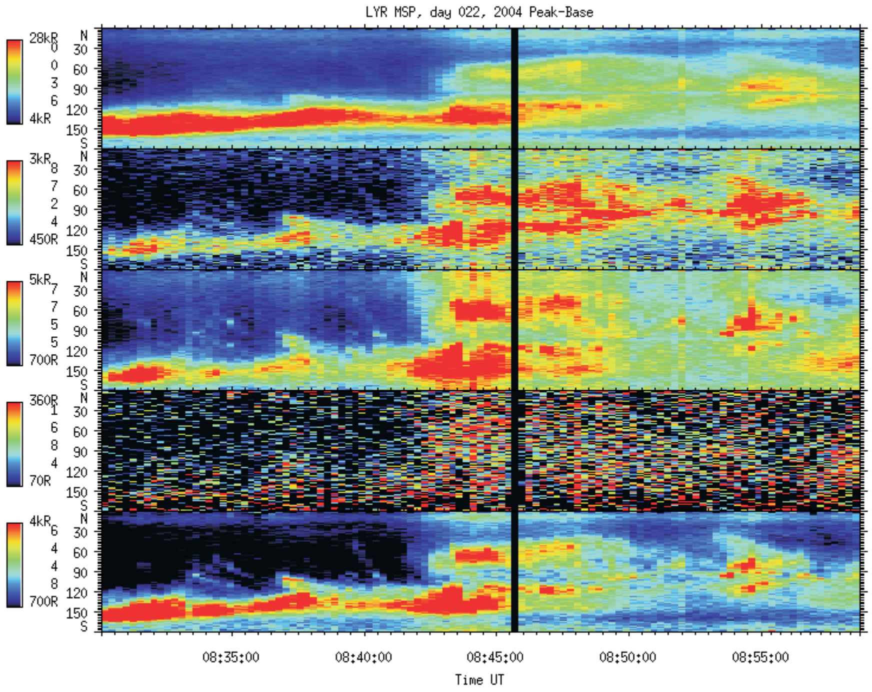

Figure 5.4: Data from the Meridian Scanning Photometer (MSP) instrument at Longyearbyen, for the wavelength channels 6300, 4278, 5577, 4861 and 8446Å in order from top to bottom. Note that the 4861 Å panel observes the H_β emission, a signature of proton precipitation, which is seen to be very weak for this interval.

ing large-scale current activity. The interval studied here takes place during disturbed magnetic activity directly following this feature. Quasi-periodic oscillations, with amplitudes of approximately 50 nT, are seen in the B_x component until 10:00 UT. The negative bay peaks at around 08:43 UT, corresponding to the onset of auroral activity over Svalbard.

5.2.4 Analysed ESR data

Figure 5.6 shows an overview of analysed ESR data, from the 42 m field-aligned antenna, at 2 minute resolution for the radar run between 04:04 and 12:00 UT. The ESR data for this interval contained many NEIAL signatures which as discussed in Section 1.8.1 makes the analysis of radar data fail. However, thermal data dumps can be used for analysis of the background ionospheric parameters before and after NEIALs, if not for during the NEIAL signatures themselves. In the interval when NEIAL observations occurred, from around 08:45 to 10:00 UT, the ESR analysis shows enhanced electron densities, extremely high electron and ion temperatures, and strong ion upflow at altitudes above 400 km. It should be noted that in 2 minute resolution data the fitted ionospheric values may be affected by a NEIAL spectrum recorded

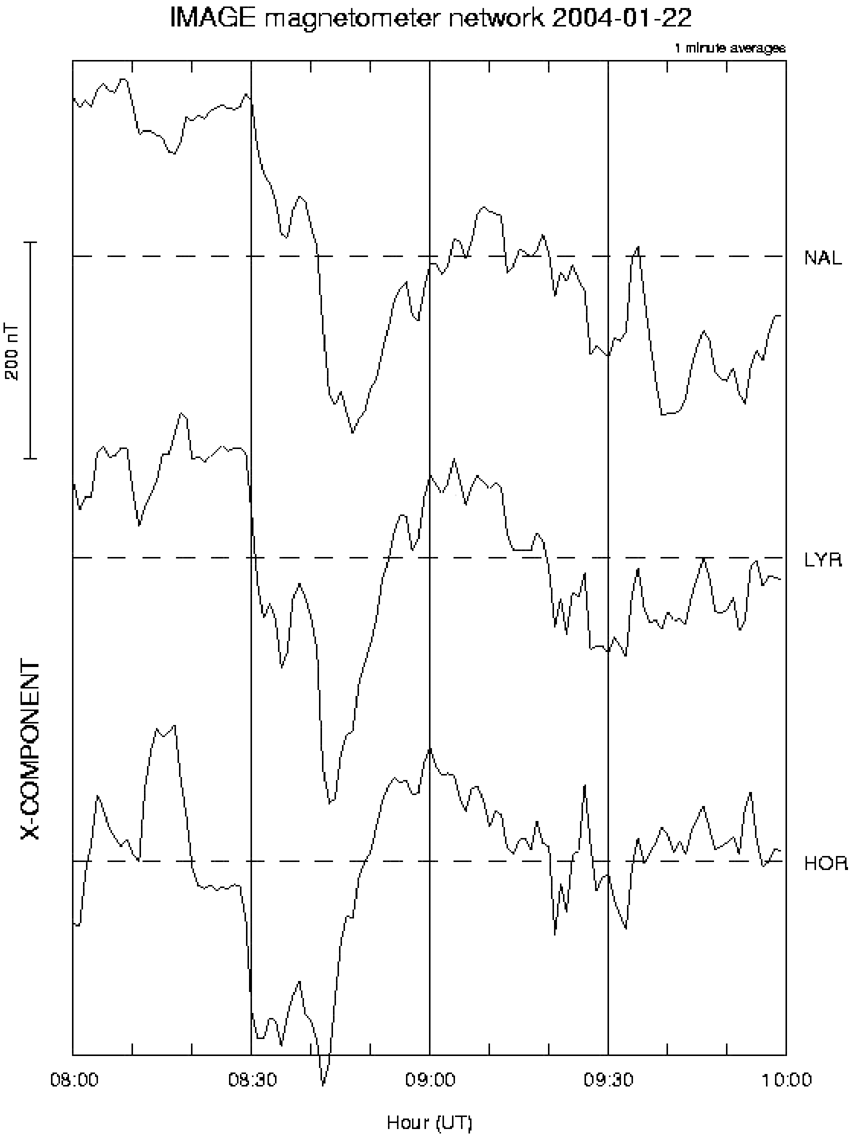

Figure 5.5: IMAGE magnetometer X-component data from 06:00 to 10:00 UT, averaged over 1 minute intervals.

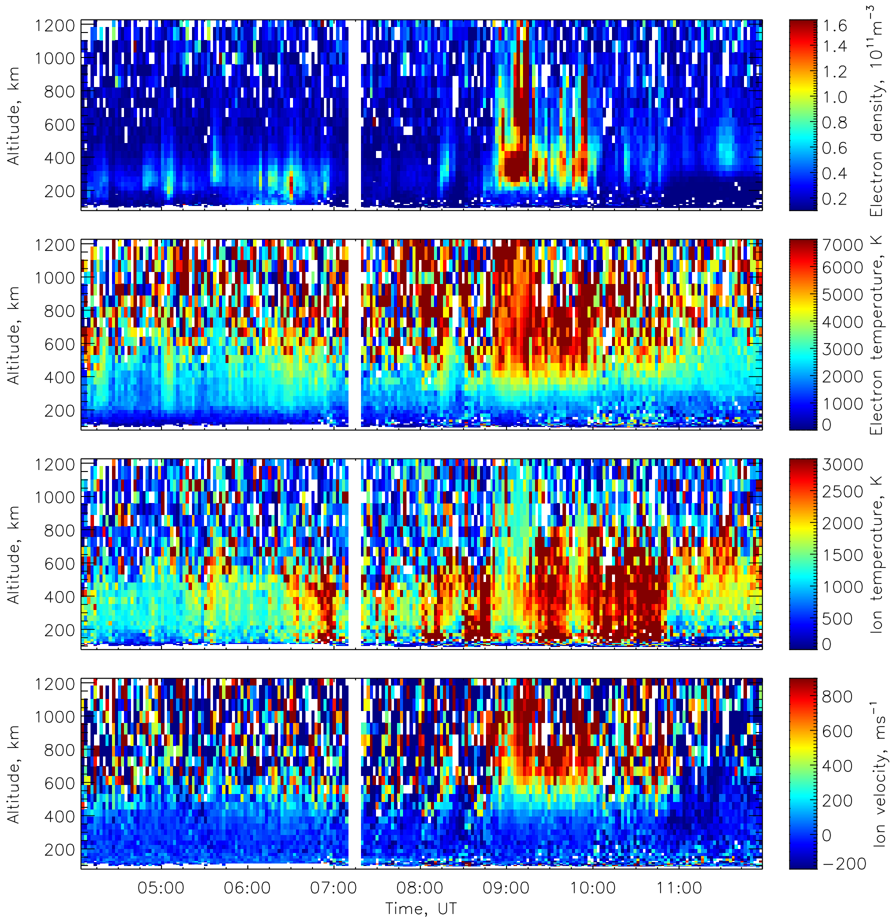

Figure 5.6: Analysed ionospheric parameters from the ESR radar on 22nd January, at 2 minute resolution.

during the integration period. In order to verify and use the analysed parameters, the NEIAL affected dumps must be filtered out. This is discussed further in Section 5.9. However, Frederick-Frost et al. (2007) compared the ESR electron and ion temperatures with the in-situ thermal electron and ion temperatures as measured by the ‘SERSIO’ sounding rocket, launched into the active cusp region on the same day, and found them to be in close agreement. The analysed data also show ion temperature enhancements and ion upflow outside the time interval in which NEIALs were observed, indicating that the ionospheric parameters shown here are physical and not affected greatly by the NEIAL spectra.

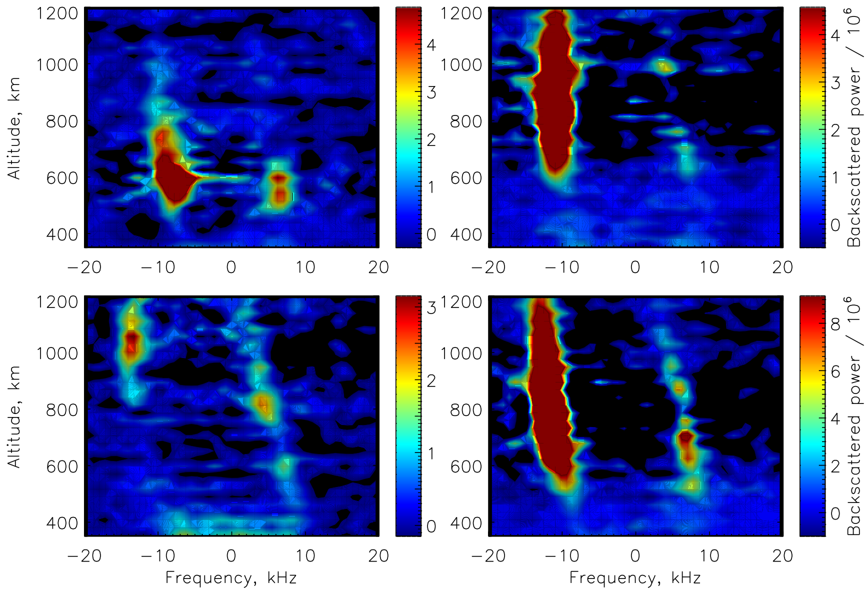

Figure 5.7: Examples of range corrected NEIAL spectra recorded by the ESR (Alternating code 1 only) on 22nd January 2004. The spectra shown in order from left to right and top to bottom are from 08:53:00, 09:15:11, 09:38:14 and 09:54:14 UT (end time of the 42 m antenna data dumps).

5.3 NEIAL observations in EISCAT Svalbard Radar

For the period studied here the ESR programme ‘tau0’ was used, an alternating code experiment covering all altitudes from 120 km to 1200 km, analysed with 3 km range resolution. Data were received from the 32 m and 42 m dishes alternately. At the time of the observations presented, the 32 m antenna was deployed at a low elevation and therefore only the 42 m measurements are used here. The integration time is 6.4 seconds but followed by a gap of 6.4 seconds for each data point. The collection of raw voltage level data at millisecond resolution was unfortunately not implemented at the radar for this campaign season, but will now be in operation whenever possible for future ESR runs.

This study compares the level of the emissions present in both of the narrow-view imagers with the times of NEIAL power enhancements detected by the ESR. The time resolution of the radar data available for this study is not high enough to follow the behaviour and evolution of an individual NEIAL, which varies on a sub-second time scale. However, this interval contains an unprecedented number of NEIALs occurring in a relatively short period, which allows us to make a statistical study of the relationship between NEIALs and the aurora present in the radar beam.

Figure 5.7 show four examples of typical NEIAL spectra recorded between 08:45

and 10:00 UT. The spectra have been individually scaled in order to demonstrate the possible problems with contouring in the description of NEIALs. For the majority of the NEIALs in this period the enhancement at the frequency of the up-going (down-shifted frequency) ion-acoustic wave dominates. However, when the scale is adjusted to saturate the dominant shoulder, the down-going (upshifted frequency) wave also appears enhanced, although at a weaker level, which may not be evident in auto-scaled spectral plots as produced by the standard EISCAT software. For the NEIALs observed in this time interval, all displayed some enhancement at both the up-going and down-going wave frequencies, although the up-going enhancement is generally stronger and extends to a higher altitude. For some spectra there is a shift of the zero frequency towards negative values with increasing altitude (as, for example, in the bottom two panels of Figure 5.7) which can be a signature of ionospheric upflow increasing in velocity with altitude.

5.4 Optical analysis

In previous studies, wide-angle optical instruments have been used to investigate the auroral precipitation characteristics over Svalbard during times of NEIALs. However, the filamentary NEIALs, and the dynamic structured aurora seen to be associated with them, are small-scale in nature. This means it is important to use optical measurements of higher spatial resolution. The previous chapter showed the value of using the HiTIES spectrograph to provide information about the precipitating energy spectrum, in combination with spatial measurements from the ASK cameras.

5.4.1 HiTIES spectral data

HiTIES was operating with the 3 panel filter mosaic (Figure 2.3a) for this interval, using an integration time of 15 s for each exposure. Although, this mosaic was primarily designed to study N_2^+ and H_β emission, the N_2^+ 1N(1,3) panel also contains emission from the O^+ $^4P -^4 D^0$ multiplet at 4639 - 4696 Å. The contribution from the O^+ multiplet has been shown to increase during times of low-energy precipitation, increasing the ratio of the N_2^+ 1N(1,3) to the N_2^+ 1N(0,2) intensities seen by the spectrograph (Ivchenko et al., 2004). In this case, the twilight conditions during the interval in which NEIALs were observed led to difficulties in using this technique. An attempt was made to remove the contaminating sunlight, which swamped the spectra making any O^+ emissions impossible to discern, using a solar spectrum normalised to the data, as described in Robertson et al. (2006). In the resulting sunlight-subtracted HiTIES spectra, the H_β line which is present over several integration periods is recovered, demonstrating the effectiveness of this technique for long-lived emissions. However, intensities at the wavelengths of the O^+ multiplet were not above the noise level.

The intensities of the O^+ lines are too weak (for the event studied by Ivchenko et al. (2004) the multiplet was at most 20% of the total N_2^+ 1N(0,2) intensity) compared to the noise introduced in correcting the spectra for sunlight contamination. This may, in part, be due to the emissions not being present for the entire HiTIES integration interval. NEIAL signatures in the radar vary on sub-second time scales and are only visible in integrated data due to the enhanced power received being several orders of magnitude greater than the thermal spectra. If low-energy spectral precipitation features were linked to NEIALs, a similar variation on sub-second scales would be expected, leading to the low-energy emission lines appearing to be at a very weak level in 15 s integrated spectra. Hence, sunlight-subtracted HiTIES data could not be used to identify any transient precipitation features for this interval.

5.4.2 Multi-spectral imaging

Spectral information is essential in obtaining information about the precipitation characteristics linked with the generation of NEIALs in the radar. Two auroral imagers with different filter wavelengths, the TLC and the Andor imager, were therefore used to study the variation of emissions present in the radar beam to provide information about the precipitating energy spectrum. As described in Chapter 2 the Andor imager filter is centred on the OII doublet with some background emission from $N_2$1PG also in the passband, while the TLC imager is primarily sensitive to the $N_2$1PG bands but also includes some contribution from the oxygen emissions.

Imager sunlight subtraction

The event presented here took place in the morning hours of 22 January 2004, ending near local noon. There is therefore a slowly-varying contribution to the recorded intensities in the auroral imagers used in this study, due to varying levels of scattered sunlight. This extra ‘dark’ signal had to be subtracted before calibration, as well as the instrumental dark noise level. Ideally this would be quantified by using camera data from a nearby day with no auroral activity at the corresponding time. However, with common changes in camera gain settings, prolonged periods of cloud cover, and

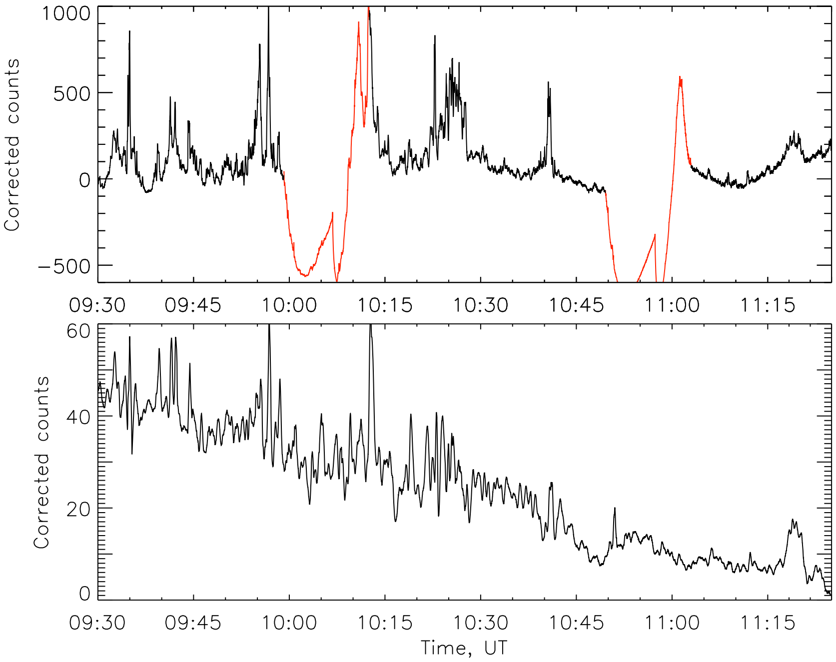

Figure 5.8: Gain variations in the Andor data set (top panel) and the corresponding TLC data for comparison. The data counts were integrated within a circular area representing the radar beam (0.6°angular radius) for each camera. Sections of data shown in red were treated as missing data.

auroral activity visible on most clear sky days, it was not possible to find a suitable interval near enough in time to give identical sunlight levels. Instead, the sunlight contribution was estimated by a linear fit to brief periods of clear sky before and after the main auroral event in the cameras used. The resulting intensity calibration $K1$-values (see Section 3.4.2) were calculated using stars observed in two ten-minute intervals before and after the event, and found to agree within the uncertainty of the $K1$-value fluctuations. This indicates that the majority of the sunlight contamination was correctly removed from the data, although the calibrated intensities may still have some small sunlight component. The long time scales of scattered sunlight variation mean that it is not a factor in the analysis of short-lived discrete auroral features, as described in this study.

Andor imager data gain

The lack of full thermal control for the testing setup of Andor had some implications for the data. Although temperature control systems are now employed on the final ASK instrument, for the initial implementation available on this day, overheating led to regular dropouts in the gain for the Andor imager. Figure 5.8 shows a period of

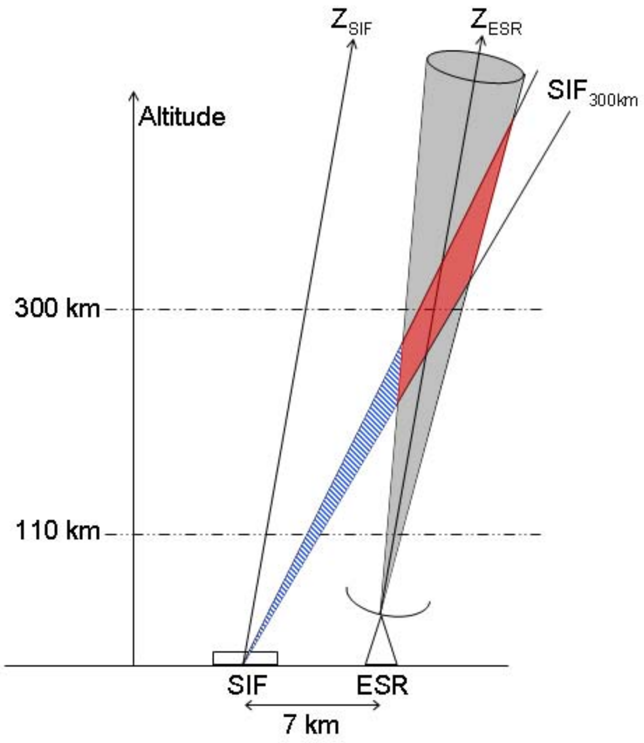

Figure 5.9: Representation of the viewing geometry used in this study. The emission volumes observed by the two imagers at the Auroral Station site are compared to the scattering volume illuminated by the ESR beam.

Andor data counts, integrated within a circular area on the image, in the top panel, showing the regular pattern in intensity variation due to overheating (in red). For comparison the corresponding time series from the TLC camera is shown in the bottom panel. Some auroral intensity variation can still be seen in the Andor dropouts, although at a much reduced level, confirming a problem with the gain at these times. Attempts were made to recover the complete Andor data sequence, by using a high-pass filtering method and by comparison with stars and auroral brightnesses in the TLC data sequence. However, with the aurora varying on a similar time scale as the gain oscillations and commonly filling the entire field of view, and also the ratio between emissions in Andor and ASK not remaining constant, these were unsuccessful. Measurements during the gain oscillation periods, identified later in the event when the auroral activity was minimal, were therefore removed, leading to a non-continuous Andor data set. The sections of data plotted in red in Figure 5.8 were treated as missing data for the analysis in this chapter. Careful analysis, comparing intensities in different cameras, confirmed that the gain was uniform and stable in the remaining data.

5.4.3 Viewing Geometry

A schematic view of the instrumentation geometry is shown in Figure 5.9. On sub-kilometer scales, the spatial separation between the imagers and the ESR becomes important; cross sections of the radar beam at different heights map to different locations in the image frames as seen from the Auroral Station. If the Andor and SIF imagers had been co-located with the radar beam, then the intensity recorded would be a combination of oxygen doublet and nitrogen emissions all located within the main beam. The separation of the optical instrumentation and the ESR therefore helps in this respect, in that the two main emissions in the beam are separated by altitude, and are therefore also separated in the images. The area on the Andor images representing the ESR beam at 300 km will contain only the oxygen contribution of the in-beam emission. The use of observations slightly oblique to the field line, separating emissions by altitude, was shown to be possible by Semeter (2003).

However, the separation causes a new source of the nitrogen contaminant in the Andor imager. Figure 5.9 shows a representation of the source of this possible contamination, with an exaggerated view of the observation geometry used here. The area on the Andor image representing the position of the ESR beam at 300 km will mainly consist of the contribution from low-energy emission within the beam, shown by the red shaded region. However there may also be some emission from higher energy precipitation outside the beam at lower altitudes, shaded in blue, contributing to the total line of sight intensity. By comparing the Andor (OII) intensity with the intensity in the wider filter of the SIF imager at the same look direction, this contamination can be quantified.

Figure 5.9 also demonstrates that when observing from a site separated from the radar, aurora from high-energy particles seen in the direction of magnetic zenith, will not be located in the main radar beam, due to the low altitude of emission. Previous studies looking at the relationship between high energy particles and NEIALs have not always accounted for this, e.g. Lunde et al. (2007). Since the filaments associated with NEIALs have been shown to have scale sizes much smaller than the width of the radar beam, this is an important consideration.

5.5 Relationship between NEIALs and optical emissions

The intensities recorded in the TLC camera gradually decreased over time during the interval 08:45 to 10:00 UT, while the intensities in the Andor remained constant on

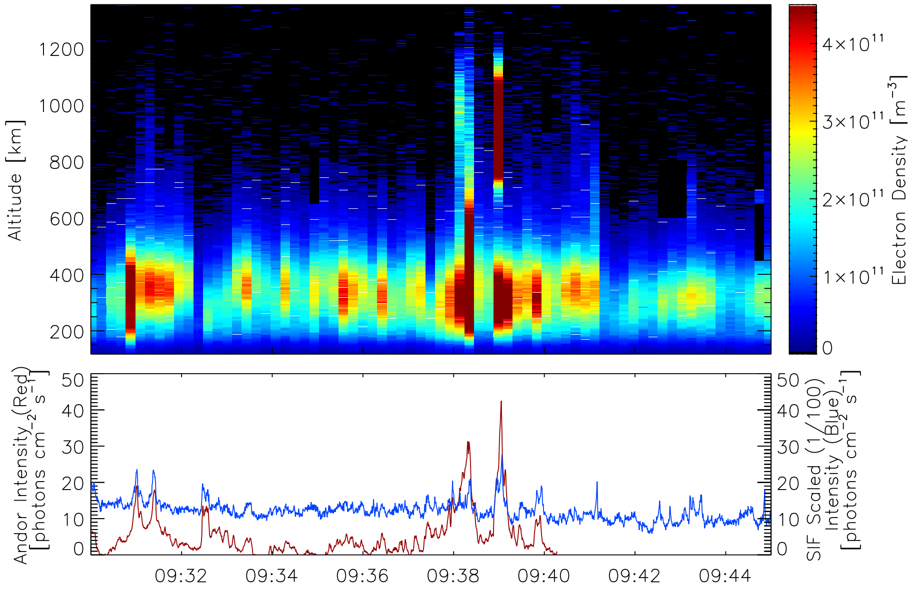

Figure 5.10: Data for the interval 09:30 - 09:45 UT. Top panel: ESR raw electron density (scaled Debye-corrected backscattered power) as a function of altitude and time. Bottom panel: Intensity of the optical emission within the solid angle corresponding to the radar beam at 300 km altitude for the Andor imager (in red) and the SIF imager (in blue).

long time scales. With the TLC being primarily sensitive to $N_2$1PG emission, this indicates that the level of high-energy precipitation present in the ionosphere decreases throughout the course of the event. The general decrease also verifies that the majority of sunlight contamination has been successfully removed from the TLC, since this would be increasing approaching local noon. As the general precipitation conditions were therefore seen to be changing, the entire interval was split up into 15-minute sections, in order to separate the small-scale variations from the underlying long-term trends. Using this approach it was also possible to study if the behaviour of small-scale changes and the relationship with NEIAL signatures had any dependence on the large-scale precipitation environment.

The results for two of the 15 minute sections are given in Figures 5.10 and 5.11, which show the relationship between enhancements in ESR backscattered power and the intensity of the optical emissions for periods beginning at 09:30 and 09:45 UT. The top panels show the altitude profiles of temperature-corrected backscattered power from the ESR, scaled to represent units of electron density (but note that this scaling applies only for thermal plasma). The bottom panels show the calibrated intensity integrated over the solid angle corresponding to the cross section of the radar beam at 300 km on the Andor and SIF images, in red and blue respectively. There is a clear correlation between discrete NEIAL signatures and times of increased emission seen

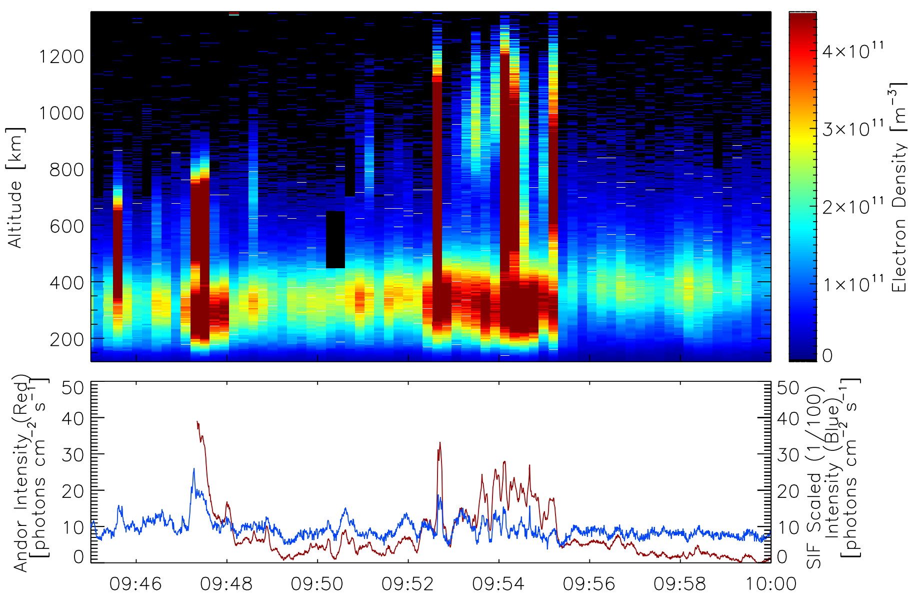

Figure 5.11: As for Figure 5.10, for the interval 09:45 -10:00 UT.

by Andor in the radar beam.

Although the ESR experiment 'tau0' does not have a separately recorded power profile in the coding, the representation of power shown in the top panels was formed by extracting the zero lag measurements from the alternating codes. However, zero lag values, while giving the best signal-to-noise ratio, are not fully decoded in range, leading to NEIAL features appearing from a larger than true altitude range. Despite this, Figures 5.10 and 5.11 are adequate for NEIALs to be identified clearly in the ESR spectra by the increase in scattered power received over an extended altitude range, compared to the normal thermal level. Satellite signals in fully range-decoded data appear as similar enhancements in power, but are only present in a restricted altitude range, i.e. in one or two radar range gates. Power enhancements due to satellites were identified by looking directly at the range extent in the raw spectra (spectra are composed by combining several short lags and are therefore fully decoded in range) and also by noting visible satellite crossings in the imager frames. Power measurements corresponding to identified satellite enhancements have been reset to zero, and can be seen as black features appearing with an altitude range of about 200 km (resulting from the break-down in range decoding) in the profiles.

There is some evidence for enhancements in electron density at or below about 400 km, corresponding to NEIAL events at higher altitudes, for example at 09:39 UT in Fig. 5.10. In cases where the low-altitude enhancement is separate from the NEIAL at higher altitude, with a clear distinction between maxima as in the example noted, these are likely to be real density enhancements. The radar data alone therefore show direct evidence for soft electron precipitation accompanying NEIALs. Electrons of 100 eV energy cause an ionisation peak at around 250 km altitude, as has been modelled using the electron transport model of Lummerzheim and Lilensten (1994) and shown in Whiter (2008). However, because of the use of the zero-lag profile and the associated large range ambiguity, care must be taken where there is no clear distinction. There is the possibility of NEIAL enhancements affecting range gates at lower altitudes.

The intensities integrated within the radar beam location (bottom panels) were calculated assuming an ESR beam width (full width at half power) of 0.6 degrees. With a much larger filter passband than Andor, the intensity levels in the SIF camera are in general much larger, and have been scaled by a factor of 0.01 in order to show them on the same axis. There is also some slowly varying offset in the SIF intensity, that is predominantly due to continuous emission excited by the high-energy precipitation but may also contain some residual continuum and solar scattering background. As discussed in detail above, the Andor imager is predominantly responding to the low-energy oxygen doublet (OII) emission, with some contamination from the background nitrogen bands, while the SIF imager is primarily sensitive to the $N_2$1PG emissions in the passband, with some contamination from OII and other nitrogen emission. The relative brightness of OII and $N_2$1PG emissions therefore depends on the energy of the precipitating particles.

The two time intervals shown previously in Figures 5.10 and 5.11 are taken from the end of the period of NEIAL activity when the emission from high energy precipitation is low. It can be seen that the main peaks in Andor, corresponding to the times of NEIALs are characterised by an increase in the Andor to SIF ratio, i.e. the Andor intensity is predominantly enhanced. This confirms that at these times Andor is responding specifically to an increase in low energy precipitation enhancing the OII emission, rather than an increase in the $N_2$1PG background. The increased Andor to SIF ratio at times of NEIALs therefore implies that the related auroral structures are the direct result of low energy electron fluxes, entering the topside ionosphere i.e. ‘primary precipitation’, and not due to secondaries resulting from successive collisions of higher energy precipitating particles as they pass through the ionosphere.

Two 15 minute sections of data from earlier in the interval, beginning at 08:45 and 09:00 UT are shown in Figures 5.12 and 5.13 respectively. Here the relationship between NEIAL signatures and intensity enhancements in Andor is not one-to-one as seen later on, although a relationship can still be seen in some cases, i.e. at 08:53:00, 08:57:42, 09:05:10 and 09:10:43 UT (integration end times). Additionally, the Andor

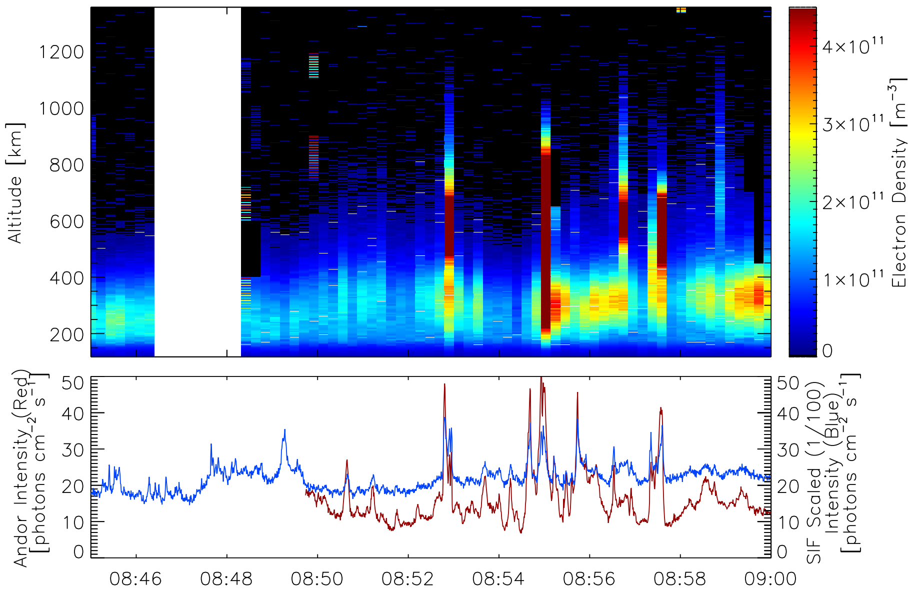

Figure 5.12: As for Figure 5.12, for the interval 08:45 - 09:00 UT

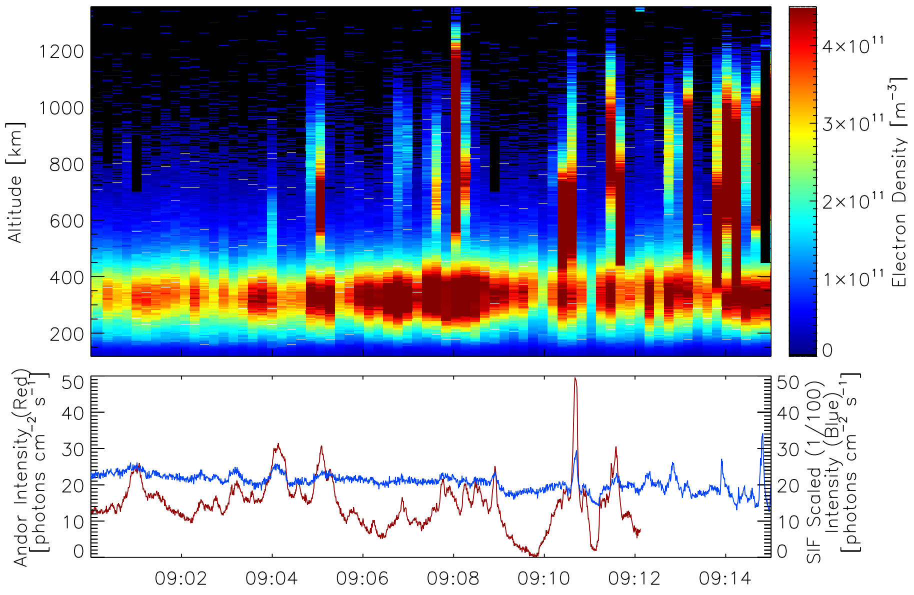

Figure 5.13: As for Figure 5.13, for the interval 09:00 - 09:15 UT.

enhancements are often accompanied by strong enhancements in the corresponding intensity in the TLC camera. This implies that the Andor camera is also responding to the large amount of contaminating $N_2$1PG at these earlier times. This distinction is discussed in further detail in Section 5.7.

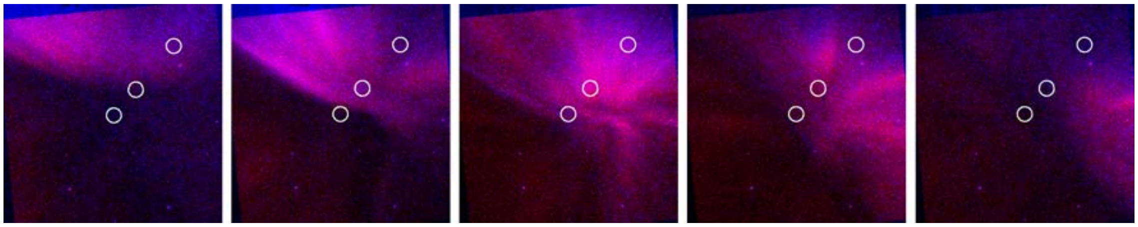

Figure 5.14: Multi-wavelength composite image showing the enhancement in OII emission associated with the NEIAL signature at 09:39:03 UT. The frames shown were taken at 09:38:53, 09:38:58, 09:39:03, 09:39:08 and 09:39:13 UT from left to right. The direction of north is vertically downwards and the east direction is to the right for the image orientation as shown here. The white circles shown progressively further out from the centre of the image, represent the position of the ESR beam (FWHM 0.6 degrees) at altitudes of infinity, 300 km and 110 km respectively. The result of not taking into account the parallax effect, i.e. effectively assuming infinite altitude, can clearly be seen.

5.6 Imaging an individual NEIAL

NEIALs occur at the same time as short-lived auroral structures pass through the radar beam. These have been shown to be predominantly low-energy emission features. Overlaid images from both Andor and SIF, as shown in Figure 5.14, can provide an image of the optical evolution of a NEIAL signature, both spatially and in energy. In the composite images Andor data are shown in red, SIF data in blue. The overlaid frames shown are taken at 5 second intervals, with the central (third) image at 09:39:03 UT. The images show the optical intensification related to the discrete NEIAL signature at 09:39:03 UT, as shown in Figure 5.11.

The three white circles marked on the images represent the position of the radar beam, again using the nominal angular diameter of 0.6°, at different altitudes mapped onto the image coordinate frame. The circle nearest the centre of the image frames shows the position of the ESR if no parallax considerations are taken into account, i.e. assuming the camera and radar are at the same location, effectively mapping the radar beam at an infinite altitude. The circles positioned progressively further away from the centre of the image represent the location of the radar beam at 300 km and 110 km respectively, i.e. the peak-emission altitudes for OII and $N_2$1PG emission respectively. It can be seen that the feature responsible for the discrete enhancement in the OII emission at 300 km altitude is a spatial structure, with a rayed arc passing through the ESR beam. The auroral structure in this case moved from the south-west of the field of view to the north-east. This large-scale drift motion was seen for all the rayed auroral events in this interval.

5.7 Statistical Analysis

A statistical analysis of the interval 08:45 UT to 10:00 UT was made to compare the incidence of fine-scale aurora with NEIAL signatures present in the ESR beam. A sampling length of 15 mins was chosen as optimum for the changing ionospheric conditions. In order to identify ESR data dumps affected by NEIALs using a fixed criteria, the backscattered power profile was created from the zero lags as described in 5.5. The power profiles for the interval between 09:45 and 10:00 UT are shown in the top panel of Figure 5.15. As mentioned previously, power enhancements due to satellites have been removed from the data set. The data was integrated over all altitudes between 500 km and 1200 km, shown by the white dashed lines in the figure, i.e. well above normal F-region ionisation altitudes. The bottom panel shows the integrated 'apparent' electron densities. Data dumps with associated densities over a threshold level of 2×10^{13} m^{-3}, as shown by the red dashed line, were classed as NEIAL events; the measured densities are not valid as a result of the non-thermal spectra. The majority of NEIAL signatures stand out distinctly, although this classification threshold does remove some profiles which appear weakly enhanced at high F-region altitudes, for example at 09:48:41 and 09:51:15 UT (integration end times). Having a stricter criterion reduces the risk of including false positives in statistical studies, e.g. a strong thermal spectra or satellite signals ringing outside the standard range removed for an identified satellite (such as at 08:50:01 in Figure 5.12) could be wrongly identified as a NEIAL. However, it also means that some weak NEIALs accompanying auroral enhancements are discounted.

The Andor imager intensity values were separated according to whether or not they occurred within a time ($T \pm \tau$) where T is the time of the nearest NEIAL event recorded in the radar, and τ is 6.4 seconds, the temporal uncertainty due to the resolution of the radar data points. The time series of auroral intensity from the SIF imager was interpolated to the lower temporal resolution (2 frames per second) of the Andor imager. This allows the calculation of ratios for each time step and therefore separates OII emission events from $N_2$1PG contamination features.

Figure 5.16 shows the resulting histograms for the three consecutive 15 minute intervals from 08:45 UT until 09:30 UT, progressing from left to right. The top panels show the intensity values recorded by the Andor camera (again integrated within the beam location at 300 km as in Figures 5.10 and 5.11), separated into those associated with a NEIAL event (shown in red) and those with no associated NEIAL (shown in black). It can be seen that in the first two time intervals the difference between the two is negligible, but in the third plot, starting at 09:15 UT, the separation between

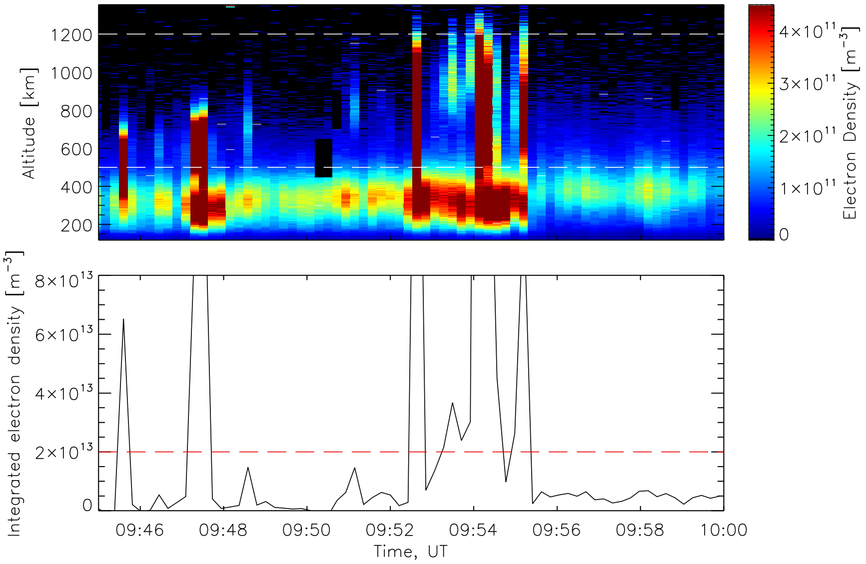

Figure 5.15: Power profiles for the interval between 09:45 and 10:00 UT, showing the integrated power threshold used to classify NEIAL events.

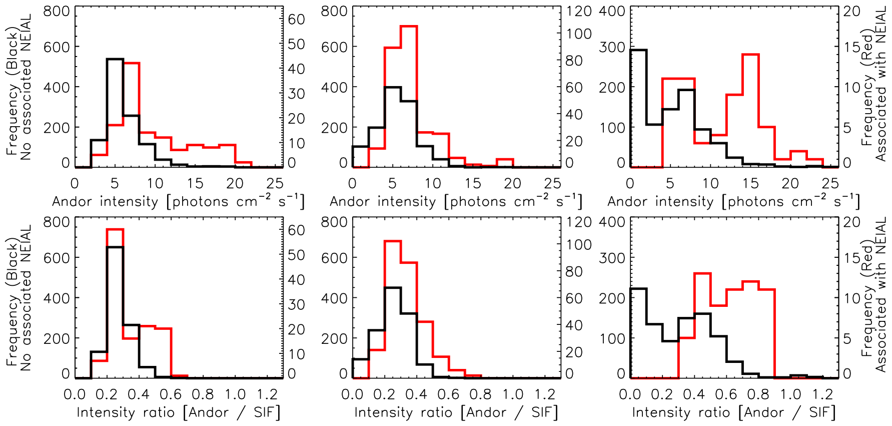

Figure 5.16: Andor intensities and Andor / SIF ratios separated into data points associated with a NEIAL (shown in red), and those where no NEIAL was recorded (shown in black). The histograms shown are for 15 minute intervals of data, starting, from left to right at 08:45 UT, 09:00 UT and 09:15 UT respectively.

the populations becomes significant, with NEIAL events associated with increased emission in the Andor. This distinction is also seen in the plot of camera ratios (bottom panel) for this time section, confirming that it is increased levels of OII emission that are associated with NEIAL signatures.

Figure 5.17 shows similar histograms for the later intervals starting at 09:30 UT and 09:45 UT (data shown in Figures 5.10 and 5.11). Here, two clear populations are evident, both in the Andor intensity alone and in the Andor/SIF ratio (which may be somewhat affected by the background level in the SIF intensity). Even though

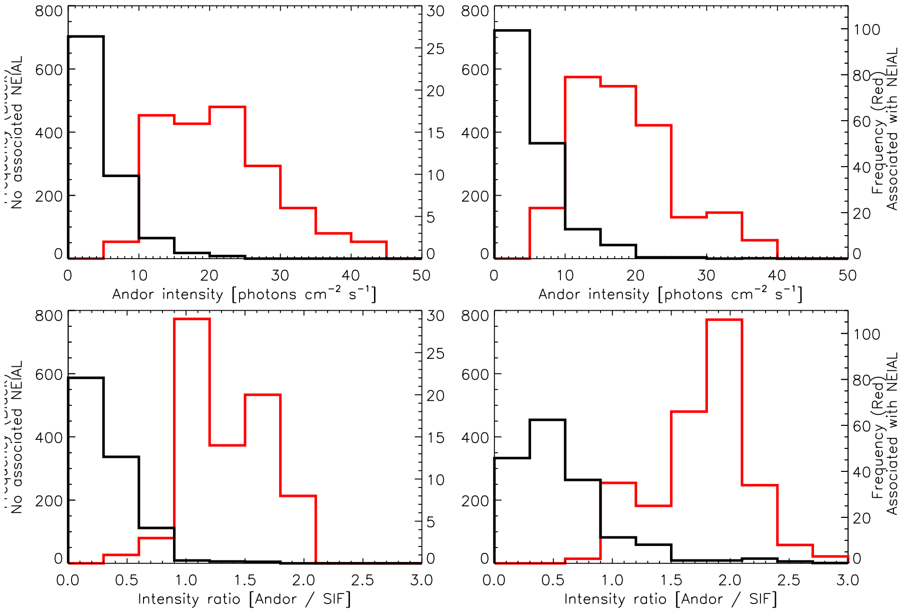

Figure 5.17: As Figure 5.16 for the 15 minute intervals starting at 09:30 UT (left column) and 09:45 UT (right column).

the separation is distinct, it is not exclusive, with a third population of precipitation which may or may not cause NEIALs to be generated, i.e. an auroral population near the triggering criteria. This implies that the critical threshold for the generation of NEIALs is not fixed, and may depend on other factors in the ionosphere.

The high occurrence frequencies shown in these histograms reflect, in part, the high temporal resolution of the optical data, in comparison with the integration time for each radar data dump, and also a degree of binning applied to clarify trends. Using the chosen threshold criteria to identify NEIALs, the numbers of affected radar data dumps in each successive 15 minute interval, starting at 08:45 UT through to 09:45 UT, are 5, 20, 4, 3 and 13 respectively.

5.8 The role of high-energy precipitation

The long-term trends in the intensities measured by the TLC camera suggested a large influx of high energy precipitation at the beginning of the interval, which gradually diminishes over time. The electron density profiles measured by the ESR confirm this. Figure 5.18 shows the radar E-region raw electron densities, representing the effect of ionisation, averaged over each 15 minute interval between 08:45 UT and 10:00 UT. Radar data dumps identified as NEIALs have been treated as missing data in the averaging. E-region ionisation is caused directly by the precipitation of high (> 1 keV)

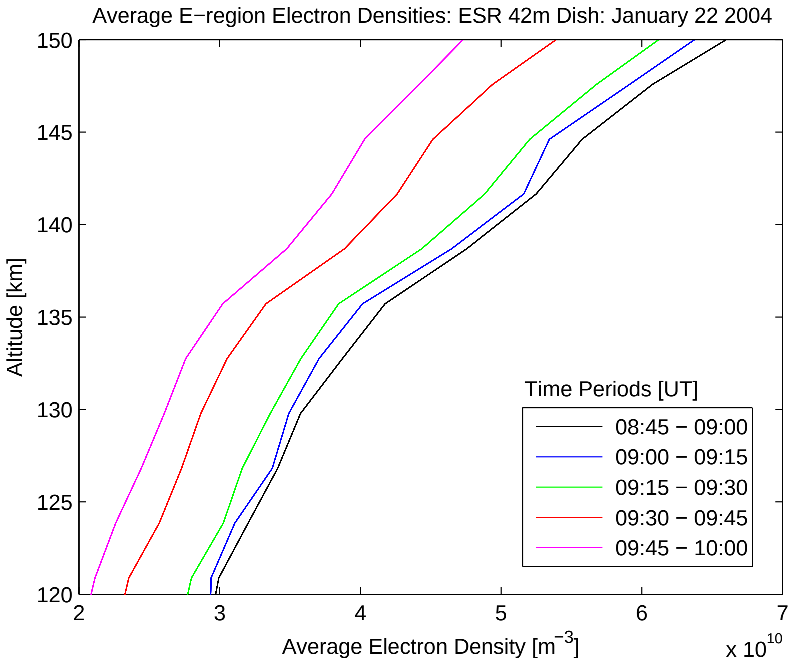

Figure 5.18: Average ESR raw electron densities (Debye-corrected) for consecutive 15 minute intervals between 08:45 UT and 10:00 UT.

energy electrons (Rees, 1989). It is apparent that there is a much larger population of high-energy electrons precipitating at the beginning of the period. Over time the precipitation becomes more dominated by low-energy precipitation. Energy-time spectrograms (not shown here) from the SWEPAM instrument on the ACE satellite show a gradual softening (reduction of high energies) in the solar wind electron population over the interval, which explains this progression.

Figures 5.16 and 5.17 show there is a relationship between times of increased OII emission and NEIAL signatures. However, the difference between the population associated with a NEIAL and that which is not, becomes more distinct progressing through the interval 08:45 to 10:00 UT, and only becomes significant after 09:15 UT. An almost unambiguous relationship between NEIALs and auroral intensity is clear when the high-energy precipitation is at its lowest. This implies it is the low-energy precipitation that is the direct driver for the NEIAL events, and that the relationship between NEIALs and auroral activity becomes harder to discern when the Andor imager is responding more to contaminating emission in the passband from high-energy precipitation. During times of strong $N_2$1PG aurora, the relatively weak contributions from the OII doublet to the Andor bandpass are overpowered by the molecular emissions. This may explain why there is no significant relationship between the aurora and NEIAL occurrence, even in the ratio plot, for the data between 08:45 UT and 09:15 UT.

These results suggest that the high-energy precipitation, while present to some extent throughout the entire interval, is not related to the NEIALs directly. Instead it appears to mask the true link between the aurora and the NEIALs by contaminating the wavelength ranges at which the OII emission is present. The implications of this are discussed further in Section 5.10.4.

5.9 Langmuir turbulence modelling

An important question to ask in order to justify the interpretation of enhanced ion-acoustic waves driven by decaying electron plasma waves, is whether theoretical models for these processes can replicate the observed events using the ionospheric parameters recorded at the time. An existing model describing the behaviour of Langmuir turbulence in the ionosphere is here modified to accept measured atmospheric and precipitation parameters. Any ion-acoustic wave enhancements generated by the simulations can then be compared with the NEIAL signatures observed by the ESR and reported in this chapter.

The Langmuir turbulence model used is based on that described in Kontar and Pécseli (2002) and Kontar and Pécseli (2005). The full mathematical details are beyond the scope of this thesis, and only a brief summary is given here. The model self-consistently describes the interaction of electrons, Langmuir waves, and ion-acoustic waves in F-region ionospheric plasma using the approximation of weak turbulence theory. Weak turbulence kinetic equations are solved in time and k-space with time-dependent injection of electrons. Using the assumptions described in detail by Kontar and Pécseli (2002), the kinetic equation for the resonant interaction $\omega_{pe} = kv$ of electrons and Langmuir waves (Vedenov et al., 1962), can be written as:

$$\frac{\partial f}{\partial t} = \frac{4\pi^2 e^2}{m^2} \frac{\partial}{\partial v} \frac{W_k^l}{v} \frac{\partial f}{\partial v} - v \left(\frac{\partial f_0}{\partial x} \right) \bigg|_{x=x_S} (v,t), \tag{5.1}$$

where $f(v,t)$ is the electron distribution function and $W_k^l(k,t)$ is the spectral energy density of Langmuir waves, playing the same role for waves as the electron distribution function does for particles. The last term introduced in Equation (5.1) is a source/sink of electrons, mimicking free downward precipitating electrons along the magnetic field lines.

The precipitation of electrons is modelled by scatter-free one-dimensional streaming from the satellite location $x = 0$ (where electrons were measured at approximately

850 km) to the depth of the point of simulation x_S, described by

$$f_0(v,x,t) = g(v)\exp(-(x-vt)^2/d^2), \tag{5.2}$$

where d is an estimate of the spatial size of the electron cloud along the magnetic field line direction, and $g(v) = Av^{-\delta}$ is the initial distribution function from satellite data.

Equation (5.1) is solved simultaneously with the corresponding equations for Langmuir waves W_k^l

$$\frac{\partial W_k^l}{\partial t} = \frac{\pi\omega_{pe}^3}{nk^2} W_k^l \frac{\partial f}{\partial v} - 2\gamma_c W_k^l + St_{decay}(W_k^l, W_k^s) + St_{ion}(W_k^l), \tag{5.3}$$

and ion-acoustic waves W_k^s

$$\frac{\partial W_k^s}{\partial t} = -2\gamma_k^s W_k^s + St_{decay}(W_k^s, W_k^l), \tag{5.4}$$

where

$$\gamma_k^s = \sqrt{\frac{\pi}{8}}\,\omega_k^s \left[\frac{C_s}{v_{Te}} + \left(\frac{\omega_k^s}{kv_{Ti}}\right)^3 \exp\left[-\left(\frac{\omega_k^s}{kv_{Ti}}\right)^2\right]\right], \tag{5.5}$$

is the Landau damping rate of ion-sound waves, containing both electron and ion components. $C_s = \sqrt{\kappa_B T_e(1+3T_i/T_e)/m_i}$ is the ion-acoustic speed.

The first term on the right hand side of Equation (5.3) accounts for the wave generation/absorption by electrons. The damping term, γ_c, is included to take into account the collisional damping of Langmuir waves with $\gamma_c = \nu_{ei} + \nu_{en}$, where $\nu_{ei} = (34 + 4.18\ln(T_e^3/n_e))n_e T_e^{-3/2}$ and $\nu_{en} = 5.4 \times 10^{-10} n_{gas} T_e^{1/2}$ are electron-ion and electron neutral collisional frequencies respectively. The last two terms on the right hand side of Equation (5.3) and the last term in Equation (5.4) describe nonlinear wave-wave interactions. Specifically, the term, St_{decay}, describes the decay $l \leftrightarrows l' + s$ of a Langmuir wave $\omega^l(k^l)$ into a ion-acoustic wave $\omega^s(k^s)$ and a 'daughter' Langmuir wave $\omega^{l\prime}(k^{l\prime})$, while the term St_{ion} denotes Langmuir wave scattering from ions, $l + i \rightarrow l' + i'$ which is also known as nonlinear Landau damping (see Kontar and Pécseli (2005) for details). The initial level of Langmuir and ion-sound waves was taken to be thermal $W_k^l(t=0) = W_T^l$ and $W_k^s(t=0) = W_T^s$.

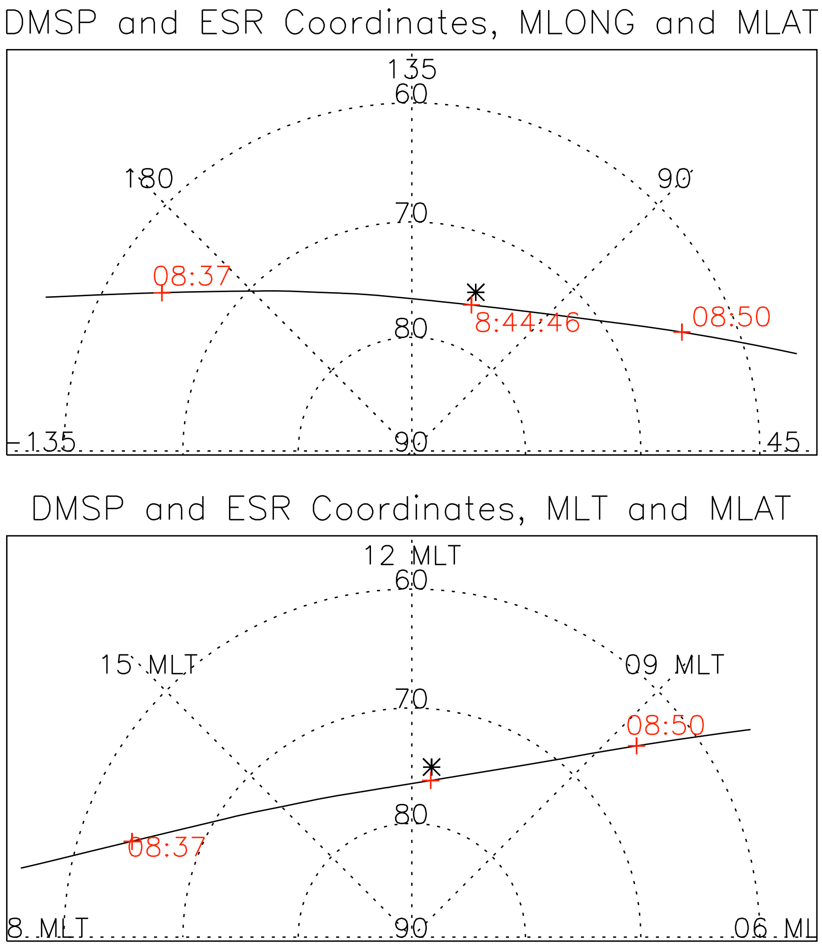

Figure 5.19: Geomagnetic map projections of the F-13 satellite coordinates during the pass over Svalbard.

5.9.1 Satellite measurements

For this study, a pass of the DMSP satellite F-13, at approximately 850 km altitude, provides a snapshot of the downward precipitation in the region being sampled by the instruments at Longyearbyen. Figure 5.19 shows map projections of the positions of the satellite as it passes over Svalbard, with the location of the ESR marked by a star. The geographic coordinates of both the satellite and the ESR were converted identically into magnetic longitude and latitude using the Altitude Adjusted Corrected Geomagnetic Coordinates (AACGM) system, to avoid the possibility of errors resulting from using coordinates applying different magnetic field models. The time of closest approach was calculated to be at 08:44:46 UT, just before the onset of the NEIALs studied here, when the satellite passes within approximately 30 km in longitude, and 150 km to the north, of the ESR beam at 850 km altitude.

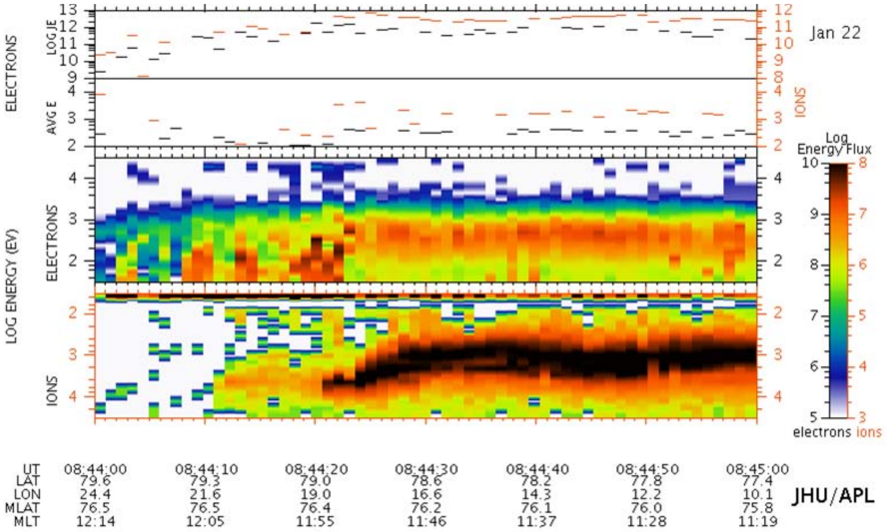

Figure 5.20: DMSP spectrogram from the F-13 satellite, for the interval 08:44 UT to 08:45 UT.

Figure 5.20 shows the DMSP F-13 spectrogram for ions and electrons for the interval 08:44 UT to 08:45 UT. Strong bursts of low-energy (around 100 eV) electrons are observed at 08:44:09, 08:44:14 and 08:44:20 UT. The bursts of low-energy electrons can be seen before the main bulk of the more energetic sheath-like population, which precipitated along the (reconfigured) open field lines after 08:44:23 UT. This also coincides with the dispersed sheath-like ion signature (lower panel).

The top panel of Figure 5.21 shows the electron precipitation in units of differential number flux (electrons s^{-1} keV^{-1} cm^{-2}) for one steradian, measured by four of the energy channels on the DMSP detector. The dashed vertical lines mark times for which the spectrum is shown in the panels below, being representative of the spectra observed during this interval. The spectra indicate a high-energy accelerated population above 0.5 keV and a low-energy population, fitted here by two power laws. The individual spectra are extremely variable and the observed shapes are influenced by detector noise and low count rates to varying degrees. However, the spectra taken at times within the observed low-energy bursts, as shown by the top two spectra examples, suggest a plateau, or even a positive gradient in the case of the spectra at 08:44:17 UT, at energies less than 100 eV. For comparison, the spectra within the main region of cusp precipitation, such as the spectrum shown in the bottom panel, exhibit no features indicative of wave growth at low-energies.

For use as an input to the model, the initial distribution function of energetic electrons, $g(v) = Av^{-\delta}$, was obtained using the DMSP F-13 measurements at 08:44:20 UT, at the peak density of the low-energy bursts. In converting the differential number flux into a distribution function, a solid angle of 1 steradian was assumed for the elec-

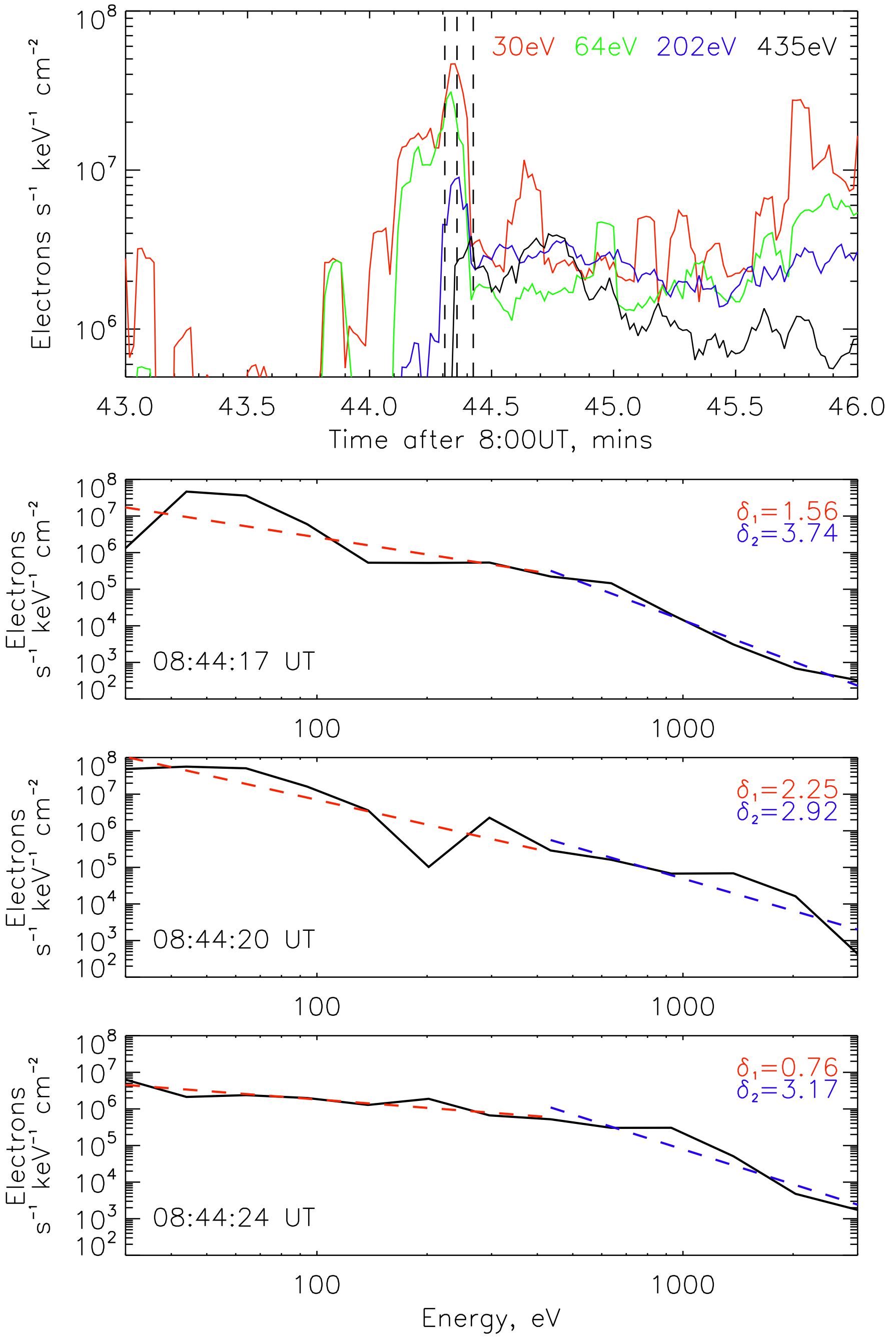

Figure 5.21: Density and spectral characteristics for electrons observed by the DMSP F-13 satellite.

Table 5.1: Plasma parameters for the Langmuir turbulence simulations.

Altitude, km	T_e, K	T_i, K	N_e, m^{-3}	f_{pe}, MHz	n_{gas},cm^{-3}
700	6000	1400	4.7×10^{10}	2.0	5×10^5

tron beams. The power-law index $\delta \approx 4$ gave a good fit for the energetic population above 500 eV, for the majority of the spectra within the strongest low-energy burst from 08:44:17 to 08:44:21 UT. The peak number density of energetic electrons above velocity $v = v_0$, $n(v = v_0)$, given by $n(v = v_0) = \int_{v=v_0}^{\infty} g(v)dv$, was calculated to be approximately 10 cm^{-3}.

The characteristic spatial scale of the electron beam along the magnetic field line direction, d in Equation 5.1, was taken to be 30 km for the model run. The vertical scale size is expected to be similar to the horizontal extent of the electron burst which can be estimated from the DMSP data. The orbital velocity of the satellite at 850 km altitude is 7.5 km sec^{-1}. The strongest low-energy burst had a duration of around 4 seconds which implies a horizontal extent of 30 km, assuming that the observed changes in the data are purely spatial and not temporal.

5.9.2 Ionospheric parameters

The Langmuir turbulence model was run for an altitude of 700 km, which was found to be the average height of peak power in the raw spectra for all NEIAL data dumps. Background ionospheric parameters were taken from GUISDAP ESR analysis results, at a time resolution of 64 seconds. Parameter results were integrated between 600 km and 800 km to increase signal to noise levels, collected over the interval 08:45 UT to 10:00 UT.

Appropriately binned histograms of the analysed ionospheric parameters were used to find a clear modal value for electron density, electron temperature and ion temperature. It is important to note that using data from the entire interval means that dumps containing NEIALs, where the analysed values are unreliable, will also be included. However, despite the large numbers of NEIALs in this period, there are still more thermal dumps than enhanced, meaning that the modal value should be a good representation of the true ionospheric parameters. Realistic neutral density n_{gas} values at 700 km are taken from from the Mass Spectrometer-Incoherent Scatter (MSIS) atmospheric model. The plasma parameters and the associated electron plasma frequency used in the simulations are given in Table. 5.1.

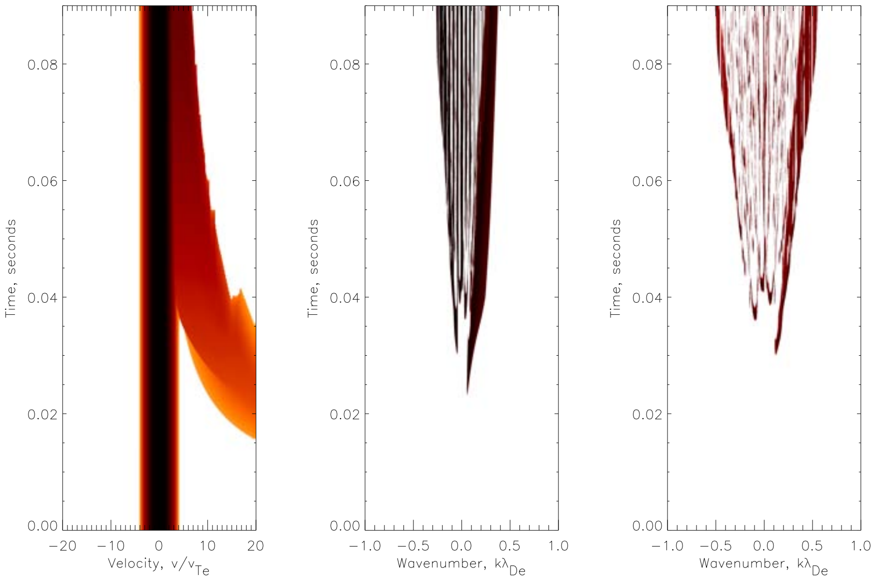

Figure 5.22: The modelled evolution of electron distribution function (left panel), Langmuir waves (middle panel) and ion-acoustic waves (right panel), in time and velocity/wavenumber space, at 700 km altitude.

5.9.3 Modelling results

The evolving electron distribution function $f(v)$ and the spectral energy densities of generated Langmuir W_k and ion-acoustic W_k^s waves from our simulations are presented in Figures 5.22 and 5.23. The wave characteristics are shown in terms of the wave vector multiplied by the electron Debye length. At time $t = 0$, only the thermal ionospheric electron population can be seen (left panel in Figure 5.22 and the black solid line in Figure 5.23). The initial distribution function, obtained from DMSP satellite data is shown by the dashed line in Figure 5.23. The first non-maxwellian electrons with velocity $v \sim 20\ v_{Te}$ appear at the altitude of 700 km approximately 20 ms after the start of the simulations (left panel in Figure 5.22). After $\sim$ 25 ms the number density of the precipitating electrons becomes high enough to generate Langmuir waves (Figures 5.22,5.23). As a result the electron distribution function starts to relax towards a flatter distribution (red line in Figure 5.23). The generation of Langmuir waves continues and the first non-thermal ion-acoustic waves appear at $k\lambda_{De} \sim 0.1$ after approximately 30 ms. After this time, Langmuir waves with higher wave vector k_L start to decay and produce ion-acoustic waves with larger k_S. The normalised scattering k-vector ($k_{Bragg}\lambda_{De}$) of ion-acoustic waves detected with the ESR is approximately 0.5, with $\lambda_{De} = 2.4$ cm for the values of electron density and temperature used here. Generated ion-acoustic waves at this k-vector, should be observed as NEIALs in ESR data. The simulation results in Figure 5.22 show that the radar should first detect downward propagating (upshifted) ion-acoustic waves approximately 75 ms

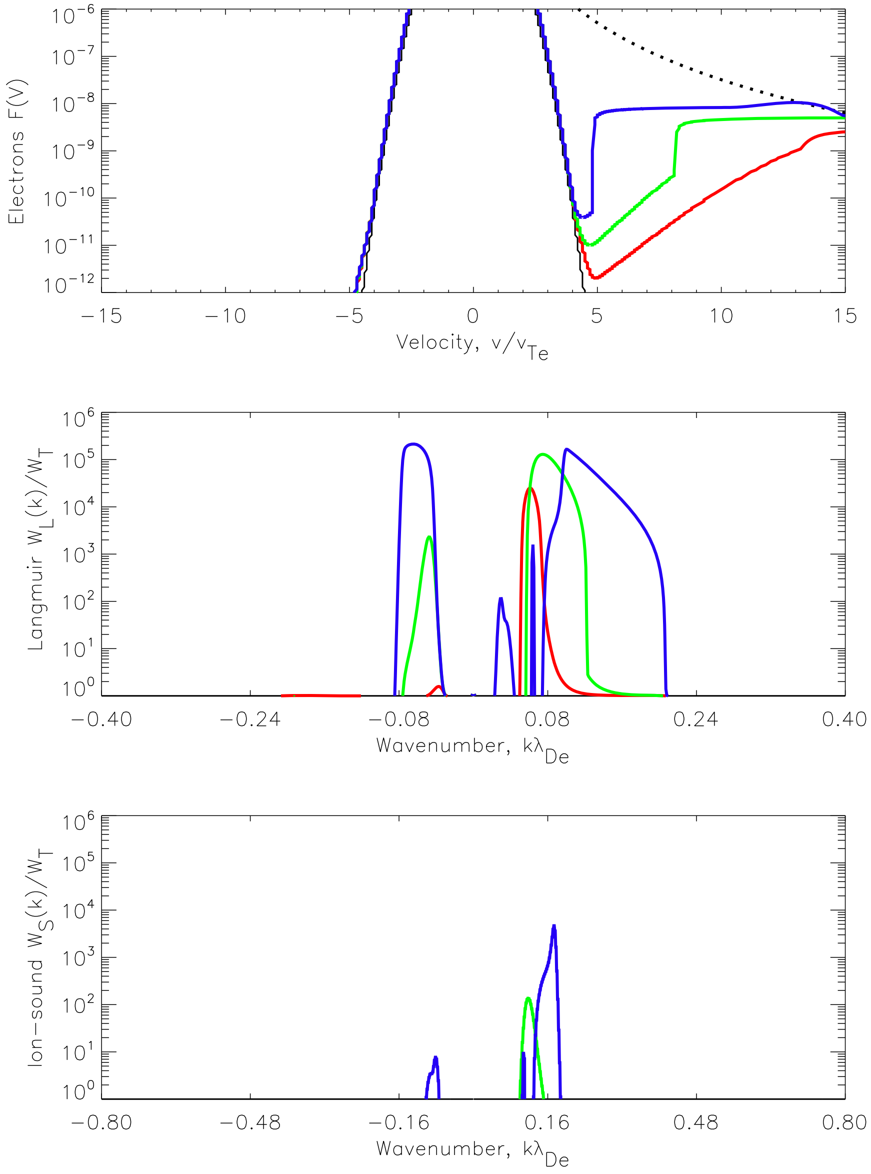

Figure 5.23: Plots showing the evolution of the electron distribution function $f(v)$ [cm^{-4}s] (top), Langmuir waves $W_k(k)/W_T$ (middle), and ion-acoustic waves W_k^s/W_T^s (bottom) for the plasma parameters at 700 km at simulation times of 25, 30, and 35 ms (red, green, and blue lines, respectively). The dotted line in the electron distribution panel gives the initial electron distribution $g_0(v)$ (the power-law fit to the satellite data at 8:44:20 UT).

after the start of simulations. Upward propagating (downshifted) ion-acoustic waves with the same intensity at $k_{Bragg}\lambda_{De} \sim -0.5$ only appear later in the simulations at approximately 90 ms (Figure 5.22). The level of ion-acoustic turbulence is around three orders of magnitude above the thermal level, as shown in Figure 5.23.

It should be noted that Figure 5.23 only shows the simulation results up to 35 ms and does not include the later time steps corresponding to when waves are present at ESR k-vectors. After 40 ms since the start of simulations, ion-acoustic wave activity remains similar in magnitude, with a maximum spectral energy density three orders above the thermal level, seen at $k_{Bragg}\lambda_{De} \sim 0.5$ after 80 ms. However at these later times wave activity becomes present at a large range of discrete k-vectors, completely swamping the earlier features. Time steps later than 35 ms have therefore been omitted from this figure, so that the temporal evolution of the wave growth can still be seen. These simulations demonstrate clearly that the electron distribution, seen by DMSP immediately before the onset of the northward IMF sheath-like cusp precipitation, is expected to drive NEIALs via the parametric decay of Langmuir waves.

5.10 Discussion

The properties of the NEIALs recorded in this radar data set agree with previous observations. NEIAL enhancements are present over several hundred kilometres in altitude range, with an average maxima in the NEIAL power at around 700 km for the events here. The peak altitude agrees with a previous report of NEIAL observations in the cusp by Grydeland et al. (2004) who found a peak occurrence at 700 km. Past studies of the distribution in power between the up and down-shifted ion-acoustic lines, found that the downshifted enhancements dominate at altitudes above 500 km (See Section 1.9). For the spectra observed here, the dominance of the down-shifted ion-line therefore agrees with results from previous surveys, although NEIALs at lower altitudes are not seen in this interval.

NEIAL signatures are generally only present in one radar dump, although some extended periods of NEIAL activity, affecting two consecutive data dumps are also observed in this data set. This agrees with the results from a survey of EISCAT UHF data by Rietveld et al. (1996) who found that lifetimes were predominantly shorter than a 10 second data dump, although NEIALs lasting for 3 or 4 consecutive dumps were also observed. However, recent studies of sub-second variations imply that a single enhanced radar dump could actually be the result of several individual NEIALs. Such time averaging cannot be discounted with the available resolution of this data set. NEIALs have also been previously observed to have links with ion upflow driven by electron temperature enhancements (Type 2 ion upflow). The analysed ESR parameters show that this is also the case for this interval. The large number of NEIAL signatures in the ESR for this interval, together with supporting multi-spectral optical observations and monitoring of solar and geomagnetic activity, give new insights about the nature and location of the source population responsible for their generation.

5.10.1 Onset of electron precipitation and instability

The sharp drop in the solar wind density occurred at ACE between 08:10 UT and 09:20 UT. The IMF B_Z component also returned to being negative at 09:20 UT. Using a 40-minute lag time, the interval of low solar wind density and northward IMF corresponds exactly to the interval in which NEIALs are seen in main interval of activity in the radar data. Although the lag time, inferred from the earthward velocity measured at ACE was calculated to be 38 minutes, this does not take into account any response time of the magnetosphere-ionosphere system, which can readily account for the extra 2 minutes. It is therefore reasonable to infer that the times of observed activity in the ionosphere are linked to the magnetic topology and the solar wind environment, either by directly causing the onset of lobe reconnection or by locating the region of precipitating flux within the ESR field of view, or a combination of both.

It should be noted that Lorentzen et al. (2007), who discuss the IMF and ionospheric conditions for the same time period as presented here, state a delay time between ACE signatures and the ionospheric response of 59 minutes. This much longer time lag is obtained by comparing the time of the northward turning in the IMF B_x component with the time that the aurora extends over magnetic zenith. The time of the IMF B_x reversal will be associated with the cessation of reconnection at the subsolar point, i.e. at around 15 R_e. As the IMF B_x component is small and the ACE satellite orbit is always close to sun-earth line (the distance of separation between ACE and the sun-earth line is an order of magnitude less than the distance of ACE from earth for this interval), a standard delay time based on solar wind propagation is unlikely to give this large an error. This indicates that the northward turning is not the direct trigger for the onset of lobe reconnection over Svalbard. A different interpretation is therefore suggested here in which the drop in solar wind density, occurring approximately 20 minutes after the reversal of IMF B_z, causes the onset of the ionospheric activity over the ESR.

During an interval of northward IMF B_Z, a large B_X component is usually necessary to drape the solar wind magnetic field over the magnetosphere, where it can reconnect to field lines on the tail-side of the polar cap. In this case the B_X component is within 5 nT of zero, meaning that the topology does not naturally favour lobe reconnection in the winter hemisphere (Crooker and Rich, 1993; Lockwood and Moen, 1999). However, this may be overcome by the high solar wind speed measured during this interval (around 640 km s^{-1}), which would increase the extent of magnetic field line draping. A further restriction to northern lobe reconnection is the requirement that the reconnection outflow speed must exceed the sheath velocity, directly related to the solar wind velocity. The high solar wind velocity here may cause the impedance of the sunward outflow which leaves the reconnection site at the Alfvén velocity. The Alfvén velocity is proportional to the magnetic field and inversely proportional to the plasma density as described in Section 1.4.2. The solar wind data in this case show a reduction in density, with an accompanying increase in the magnetic field strength due to the IMF B_Y component becoming more negative. A rough calculation using the ACE values gives an increase in V_A by a factor of 2 after the density drop, which may be sufficient to make V_A exceed the sheath flow speed and allow the onset of lobe reconnection. The combination of high solar wind speed and a sharp drop in density is therefore likely to be the cause of the sudden onset of auroral precipitation over Svalbard. A second drop in density is measured by ACE after 09:30 UT (lagged time 10:10 UT), although very little precipitation is observed by the ESR after 10:00 UT (see Figure 5.6). However, by 09:20 UT the IMF B_Y component becomes less negative, which would alter the convection topology in the polar cap. Cowley and Lockwood (1992) estimated a time scale of 15 mins for changes in convection configuration. Using this assumption, the convection pattern may have altered so that the ESR field of view was on old open field lines and failed to see any repeat onset of lobe reconnection at the time of the second solar wind density drop.

The magnetic configuration during periods where IMF $B_Z > 0$ can be extremely complex; observations suggest that reconnection can involve a single quasi-stationary X-line or can cause the formation and tailward retreat of a sequence of multiple X-lines (Hasegawa et al., 2008). As mentioned briefly in Section 5.6, there is a drift of auroral features predominantly to the east, but also with some northward motion, during the interval 08:45 to 09:00 UT. The strongly negative IMF B_Y configuration results in an eastward component to the flow of the plasma on newly reconnected field lines in the lobe. Intermittent pulses of aurora moving across the sky may therefore be signatures of successive X-lines pulled tailward throughout the course of the event.

5.10.2 NEIAL source population

The cross-track velocity and precipitation data from the F-13 DMSP satellite pass located the reconnection X-line in the vicinity of Svalbard, just before the onset of the event (Figure 5.3). From the plots representing ESR backscattered power, there is a tendency for NEIALs to occur at sharp boundaries in the F-region density, ie. on the edges of dropouts in the cusp electron enhancement. Clear examples of this are seen at 09:55:18 UT in Figure 5.11 and 08:57:42 UT in Figure 5.12. Sharp density dropouts of this nature cannot be purely temporal variations; the ionisation levels have a long response time to changes in precipitation, i.e. up to several minutes (Roble and Rees, 1977). Instead they are interpreted as being the result of changes in the location of the nearby X-line, i.e. the ESR beam changes from viewing strong electron densities caused by precipitation on newly opened field lines, to viewing the much lower densities on old-open field lines.

The convective motion of the reconnection X-line with respect to the background plasma leads to a spatially dispersed arrival of particles gaining access to the ionosphere after the magnetic topology change in reconnection; this dispersal being according to their time of flight. This leads to the the concept of the ‘ion-edge’ and the ‘electron-edge’, being the location with respect to the X-line at which ions and electrons respectively are first observed (the electron edge being closer to the X-line due to the greater velocity of electrons). The density dropouts could therefore be caused by the ion-edge, where the majority of cusp precipitation arrives, moving back and forth over the ESR. It is therefore suggested that the low-energy electrons driving NEIAL signatures here, could originate from very near the lobe reconnection X-line itself, arriving between the X-line footprint and the ion-edge, before the main cusp population arrives. This picture is consistent with the data shown by the DMSP particle spectrum (Figure 5.21) with the low-energy electron bursts appearing before the main cusp population, with a clearly ion-dispersed boundary after 08:44:23 UT.

Streams of low-energy electrons, thought to originate from the magnetopause reconnection region, have been previously observed in magnetospheric spacecraft data during periods of both southward (Fuselier et al., 1995; Lockwood and Hapgood, 1998) and northward (Lavraud et al., 2006) IMF B_Z. It should be noted that these studies discuss observations of counter-streaming electron populations, formed of both down-going and mirrored electrons. For the lower DMSP altitudes of observations presented here, the majority of electrons would be those down-going within the loss cone, i.e. forming a downward electron beam such as is used in the Langmuir modelling study. This interpretation is fully consistent with the flow reversal and ion precipitation seen by DMSP F-13 and the ground-based observations from Svalbard, as discussed earlier in this chapter.

It should be noted however, that not all sharp density boundaries are accompanied by a NEIAL, e.g. at 09:11:09 UT in Figure 5.13, but several complicating factors mean that a one-to-one relationship is unlikely to be obtained, even if NEIALs were directly caused by reconnection populations. Firstly, the reconnection could be turning on and off so that the electron streams are not always present. Indeed, the sequence of auroral events moving north-east over Svalbard indicates that this is the case, suggesting a continual sequence of X-lines forming, moving over the ESR and then fading. Secondly, short-term changes in the local magnetic zenith direction may lead to complications with the observations of NEIAL signatures in the fixed ESR 42 m dish. Changes to the local field-aligned direction, caused by strong horizontal currents over Svalbard, may cause NEIAL signatures to appear spatially disjointed from associated boundaries in cusp precipitation, or even to be not detected at all, if generated at high altitudes outside of the ESR field of view. A change in the combined horizontal component of local magnetic field, ΔH, of 250 nT, gives a change in the zenith direction of the order 0.3°. Oscillations in the IMAGE magnetometer data (X-component shown in Figure 5.5) do reach amplitudes of over 200 nT, altering the field-aligned direction on the same scale as the ESR beam width. These complications mean that the link between NEIAL generation and reconnection electron streams is not always straightforward, but is significant for the high numbers of northward-IMF cusp NEIALs in the data presented here.

5.10.3 Turbulence modelling

The Langmuir turbulence model presented in this chapter uses kinetic equations in the regime of weak turbulence, which does have some implications for the validity of this study. For the weak turbulence approach to be valid, the plasma parameters must satisfy the condition:

$$\frac{W}{N_0 \kappa_B T} \ll (K\lambda_{De})^2 \tag{5.6}$$

where W represents the spectral energy in the beam, $N_0 \kappa_B T$ the thermal energy in the plasma, K is the wave number for the peak of generated Langmuir waves and λ_{De} is the Debye length for electrons. Using expressions for characteristic energy this can be written as:

$$\frac{N_{beam} {V_{beam}}^2}{N_0 {V_{th}}^2} \ll (K\lambda_{De})^2 \tag{5.7}$$

where N_{beam} is the beam density, V_{beam} is the beam velocity, N_0 is the background electron number density, V_{th} is the thermal velocity of the plasma. This simplifies to:

$$\frac{N_{beam}}{N_0} \ll \frac{{V_{th}}^4}{{V_{beam}}^4} \tag{5.8}$$

for the Langmuir wave peak. From the modelling results shown in Figures 5.22, the central wavenumber of Langmuir growth appears around 0.2 $K\lambda_{De}$. Using the relation

$$\frac{V_{beam}}{V_{th}} = \frac{1}{K\lambda_{de}} = 5 \tag{5.9}$$

this leads to a value of 2×10^{-3} for the right hand side of Equation 5.8. The ratio of peak beam density to background density is an order of magnitude lower than this, meaning that the conditions for weak turbulence are satisfied.

There is also the question of the growth time of Langmuir waves from positive gradients in the electron distribution function. The characteristic time scale for wave growth, τ, is given by

$$\tau = \frac{N_0}{N_{beam}\, f_{pe}} \tag{5.10}$$

For the parameters used here, this is calculated to be on the order of 1×10^{-3} seconds, i.e. far less than the time resolution of the DMSP data. In comparison, the collisional time scale, τ_c, given by

$$\tau_c = \frac{4\pi V}{\Omega f_{pe}} \tag{5.11}$$

is of the order of seconds and is therefore not a significant factor here compared to the growth time. As a result of this, the spectra obtained from 1 second resolution DMSP data is unlikely to exhibit any signs of positive gradients, i.e. bump-on-tail populations, in the distribution function. Only the ‘relaxed’ distribution would be observed; for example a flattened plateau at low energies may be the signature of a previously unstable distribution after wave growth has occurred. Frederick-Frost et al. (2007) suggested that the lack of bump-on-tail distributions observed directly in SERSIO rocket data for the same interval as studied here, was evidence that Langmuir turbulence was not a factor in the generation of the observed NEIALs. However the short time scale determined here for unstable distributions mean that this argument cannot be used. The SERSIO rocket was also 500 km away from the ESR beam at closest approach. Frederick-Frost et al. (2007) state that the rocket trajectory was still in the same region of large scale precipitation as the ESR, but the results here show that the electron distribution functions can vary on spatial scales of tens of kilometres, with spatially narrow bursts of low energy electrons being observed very near to the reconnection X-line, separate to the main region of incoming precipitation.

5.10.4 High-energy precipitation

High-energy particle precipitation is present to some extent throughout the period in which NEIAL signatures are observed by the ESR. However, statistical analysis indicates that energetic precipitation is not directly linked to NEIAL occurrence. In this case it is masking the relationship with lower energy precipitation. NEIALs in the dayside cusp region are predominantly recorded during times of dynamic rayed aurora (Blixt et al., 2005), and are not observed at times of low-energy quiet arcs which have no high energy component. This suggests that the presence of some energetic particles is favourable for NEIALs to be seen in ESR data.

One possible explanation for this is that a broad mix of precipitating electron energies, shown to be present in dynamic rayed auroral forms, has a larger spread of electron beam velocities than a purely low-energy population. Using the ‘parametric decay’ interpretation, this therefore increases the bandwidth of the unstable electron population causing the growth of Langmuir waves, which directly increases the range of wavelengths over which ion-acoustic waves are enhanced (Forme, 1999). A wider range of precipitating energies therefore increases the chance of enhancement at the fixed wave vector of an IS radar. A greater beam energy spread also increases the chance of satisfying the Bragg conditions for enhanced down-shifted and up-shifted lines to be observed simultaneously. The vast majority of raw spectra identified as NEIALs in this study show clear enhancements in both lines, although with the time resolution available in this experiment, temporal averaging cannot be ruled out.

Another effect of energetic precipitation may be its role in enhancing the electron temperature in the surrounding ionosphere. The analysed radar parameters show that the interval of NEIAL activity is associated with strongly elevated electron temperatures compared to ion temperatures, a feature common in previous NEIAL studies. A higher ratio of electron temperature to ion temperature, as well as increasing the bandwidth of ion-acoustic enhancements, reduces the Landau damping of ion-acoustic waves. The criteria for instability is that the generation of ion-acoustic waves should be faster than their absorption, which is only possible where $T_e \gg T_i$. This is consistent with studies that have shown the occurrence of NEIALs to be rarer during times of high ion temperature (Ogawa et al., 2006).

Studies of NEIALs in the night-side ionosphere have reported that radar enhancements are often seen near the edges of structured auroral arcs (Collis et al., 1991).

This is contrary to the observed link between NEIALs and filamentary rays on the dayside, indicating a relationship with different precipitation characteristics. Michell et al. (2008) presented observations of NEIALs originating from the dark region immediately adjacent to an active auroral arc. Observations of NEIALs in the night-side ionosphere can often exhibit behaviour more consistent with a current driven (i.e. ion-electron streaming instability) interpretation, especially with enhancements occurring at low altitudes ($<$250 km) (Rietveld et al., 1991). This suggests the possibility that dayside and nightside echoes may be the result of different generation processes, but with similar signatures in the radars.

5.11 Summary

In this chapter, a clear link has been shown for the first time, between NEIALs in the dayside cusp and emission from low-energy (100 eV or less) electrons, using auroral imaging in the forbidden (OII) emission doublet. The results from cameras at two different wavelengths imply that this emission is due to low-energy primary electron precipitation, and not secondaries linked to incoming particles of higher energy. It is proposed that the presence of some energetic particles is favourable for NEIALs to be seen in ESR data, but may not be directly related to the generation of the enhancements themselves. Incoming bursts of low-energy electrons, ‘supra-thermal electron bursts’ have been shown to be related to dispersive Alfvén wave activity and acceleration processes (Chaston et al., 2007). For these observations of NEIALs in the northward-IMF cusp, a link is suggested between the causal low-energy electrons and the footprint of a lobe reconnection site.

One NEIAL event shown in detail here reveals the drift of a small long-lived feature (seen in the imager field of view for over 20 seconds), briefly intersecting the radar beam. This is interpreted as the NEIAL being a spatially distinct feature, as opposed to a purely temporal change within the radar scattering volume. The results here suggest that filaments associated with ion-acoustic enhancements can be persistent within a larger region of precipitation, and are only detected as they pass through the main radar beam.

Using theoretical modelling, the soft precipitation spectrum present at the time of these observations, as recorded by a DMSP pass at 850 km altitude, has been shown to be sufficient to drive the generation of NEIALs through the mechanism of parametric decay of Langmuir waves. Simulation results reveal the generation of ion-acoustic wave activity at ESR wavelengths, first in the upshifted line and then in the down-shifted line, three orders of magnitude above the thermal level. The ability to drive the model using the observed spectrum of precipitation at NEIAL altitudes, as well as observing the effects in terms of auroral emissions lower down in the ionosphere, is of great importance in understanding NEIALs.

6

Phase calibration for ESR interferometry

Studies of the link between natural ion-line enhancements in radar spectra and auroral activity have been limited by the spatial and temporal resolution available for radar observations. The next challenge is to use shorter sub-second integration times in combination with interferometric programmes to resolve spatial structure within the main radar beam, and so relate enhanced radar echo filaments to individual auroral rays.

This chapter presents initial studies of a novel technique to calibrate the received phase of a coherent signal, observed using the two antennas of the ESR as an interferometer, with the position of the scattering source along the interferometric baseline. This technique uses satellite signatures, observed in optical imagers and in ESR power density spectra. It is shown that a consistent relationship can be found only if the satellite passage through the phase fringes is adjusted from the passage predicted by optical tracking. This required adjustment is interpreted as being due to the vector between the theoretical focusing points of the two antennae, i.e. the true radar baseline, differing from the baseline obtained by survey between the antenna foot points. This work has been published by the author in full, in Sullivan et al. (2006), using optical satellite tracking software developed by Nickolay Ivchenko, and the interferometric radar data products provided by Tom Grydeland.

6.1 Motivation

The temporal variability and fine structure of NEIAL events leads to problems with temporal and spatial resolution when investigating the link with auroral structures in further detail. Standard ESR coding schemes have a temporal resolution of the order of 10 s, whereas ion-acoustic enhancements have been shown to vary on the subsecond time scale (Grydeland et al., 2003). At 300 km altitude, a region of common NEIAL enhancement at the ESR, the width of the 42 m radar antenna beam is around 6.75 km (Grydeland et al., 2003), making 100 m-wide filaments impossible to resolve individually.

NEIALs are observed to have a very strong backscattering effect, with scattering cross sections 4 to 5 orders of magnitude above thermal levels (Grydeland et al., 2004). The high signal-to-noise ratio of these signatures mean that shorter integration times can be used to record them. By sampling raw (voltage-level) data, time series with resolution limited only by the interpulse period of the transmission code can be obtained for each radar antenna. For the experiment discussed here the limiting resolution is 10 ms, whereas 200 ms radar data has been shown to be sufficient to follow the temporal resolution of NEIALs (Grydeland et al., 2004). Increased spatial resolution can be achieved by the use of new interferometry techniques. These employ the voltage time series from the two antennae of the ESR, which are approximately 130 m apart. The challenge now is to get radar observations down to the spatial scale of these enhancements and compare their location within the radar beam with the positions of auroral ray structures, in order to investigate previously found correlations in further detail.

For the interferometric technique, raw (voltage-level) samples are recorded. The resulting difference between phase received at each of the antennae can then be computed for the total scattered signal received in each integration period. In an ideal system, this phase difference would occur solely due to the difference in path length from the source of scattering to the focus of each receive antenna. This could then be used to derive the location of a coherent scattering structure along the radar baseline within the main beam.

However, as for all interferometric receiver systems, the ESR has sources of additional phase which contribute to the final phase value recorded, as the raw signal is transferred between different components and changed in frequency by mixing with the output of various local oscillators. This unknown system phase offset depends on factors such as signal path length (e.g. cable lengths, component group delays) and it can also vary slowly with environmental changes (e.g. changes in temperature). In addition, to quantify the phase shifts induced by the path difference alone requires precise knowledge of the interferometric baseline. Although the distances between the footpoints of the antenna have been accurately measured by survey, the true interferometric baseline depends on the actual focusing points within each dish, which are in effect theoretical, rather than physically measurable. It should be noted here that for the frequency of the radar (500 MHz), the wavelength is 60 cm and hence errors in the baseline of just a few centimeters will cause large errors in phase that will change as the angular coordinates of the echo source change.

6.2 Method

It has been seen in previous studies that satellites passing through the main ESR beam cause strong coherent echoes similar in strength to natural NEIAL enhancements. Indeed, many early observations of NEIALs were originally discounted as being due to satellite crossings (Foster et al., 1988). This chapter presents a possible technique to use passing satellites, seen both optically and in radar spectra, to calibrate the values of phase recorded with the position of the scattering structures along the baseline. The satellite traces in the imagers, both remote-site and co-located (with the ESR), enable the theoretical phase values during the crossing through the radar beam to be predicted and compared with the recorded values. The system phase offset, representing the effect of the ESR receiver hardware on the phase of the outputted signal can therefore be found. The technique of tracing optical signatures to calibrate radar phase has been employed previously for stratospheric radars (looking at lower altitudes below 50 km) using aircraft signals (Chen et al., 2002), but this is the first study of its applicability to satellite signals and the ESR. This chapter looks at the feasibility of the phase calibration technique using satellite signals seen optically and by the ESR in the morning hours of 26 January 2003, an interval during which some NEIALs were present in the radar data and structured rayed aurora were measured with optical instruments.

6.2.1 ESR Interferometry

In the interferometric set up, both ESR antennas are aligned along the magnetic field line, with look direction 181.0°in azimuth and 81.6°in elevation. Throughout the radar run, transmission is through the 32 m antenna only, while both antennae are set to receive. The radar programme ‘LT1HL’ used here is a long-pulse experiment using two long pulses per interpulse period. For the 2002-03 campaign season the ESR system recorded integrated lag profile matrices at 2 s resolution from each of the two antennae at various frequencies. In order to access raw (voltage-level) data, the 11.25 MHz intermediate frequency signal was split off and sampled independently in a MIDAS-W type receiver system (Holt et al., 2000), assembled by the University of Tromsø.

6.2.2 Optical Instrumentation

Two optical imagers were running throughout this campaign season, the University of Tromsø digital imager, ‘Odin’, mounted at the ESR site, and the SIF ‘TLC’ imager at the Auroral Station in Adventdalen, 7 km away from the radar site. Both imagers were fitted with a short-wavelength cut-off filter at 6450 Å, eliminating the long-lived emissions from atomic oxygen. The imager fields of view were located onto the plane of the sky as described in Section 3.2. For the 2002-03 campaign season, the Odin imager was fitted with a GPS time feed, whereas the SIF platform clock was running independently. In order to compare the results using satellites tracked from both optical stations, the SIF timing was synchronised to the Odin time clock using observed satellite passes on 26 January 2003 as described in Section 3.3.1.

6.3 Data collection

6.3.1 Interferometric data products

The voltage level data, obtained at sub-second resolution from each of the ESR antennae, were used to calculate the power received in each antenna and the interferometric data products of phase difference and coherence (normalized cross spectrum). These procedures are documented in full in Grydeland et al. (2004). Figure 6.1 shows example range-frequency plots of the data products that are obtained.

The two panels on the top row show the received power spectra, obtained in the same way as in the normal ESR receiver system by fourier transforming the autocorrelation functions for each antenna. The left-hand plot is for the 42 m antenna, the right-hand plot for the 32 m antenna. The signal received from a satellite can be clearly seen as an increased backscatter of several orders of magnitude at a range near 500 km in the data from both antennae. The bottom left panel shows the coherence value. The interferometric coherence is defined as the normalised cross-correlation between two complex signals, in this case the signals received at the 32 m and 42 m

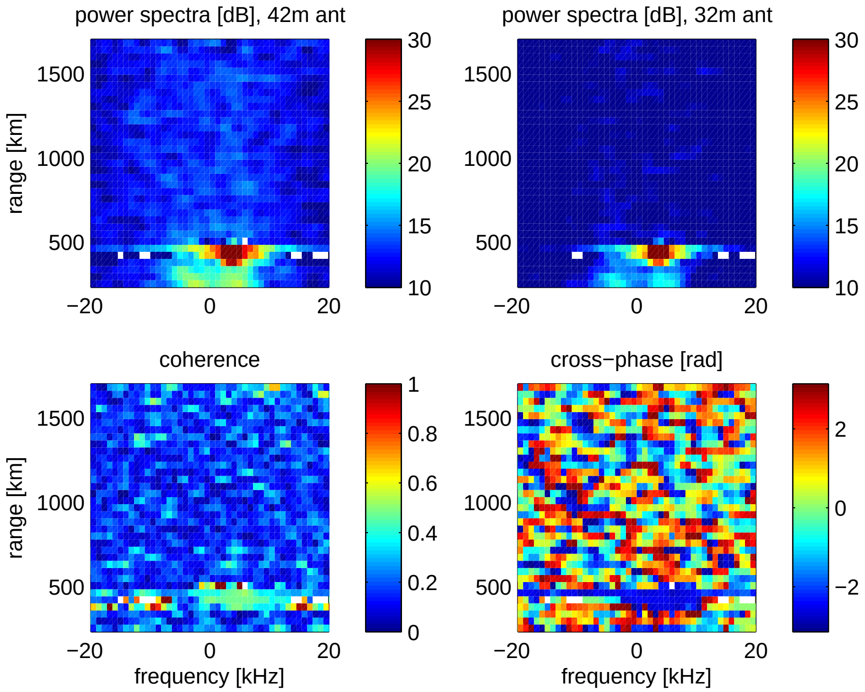

Figure 6.1: Example plots of received power in the 32 m and 42 m ESR antennae and the interferometric data products of phase difference and coherence, as a function of frequency and altitude.

antennae, described by:

$$\zeta = \frac{< S_1 S_2* >}{\sqrt{< S_1 S_1* >< S_2 S_2* >}} \tag{6.1}$$

where ζ is the coherence value, S_1 and S_2 are the signals received by the 32 m and 42 m antennae, $< S_1 S_2 >$ denotes the expectation value of the signal products and $*$ denotes the complex conjugate. The coherence value gives a measure of how similar the two signals are, with a maximum value of 1 if the signals are identical. For normal incoherent scatter, where the scattered signal is altered by the random thermal motions of electrons, the coherence should be zero. As the scatter becomes more like that from a hard target, i.e. from a satellite, where structures can be considered stationary within the time it takes to transmit and receive the radar code, the coherence increases. Figure 6.1 shows that coherence values significantly above zero only occur within the satellite echo. The bottom right panel shows the difference in phase between the two complex signals received at the 32 m and 42 m antenna. With no other sources of additional phase, this phase difference is directly proportional to the difference in path length of the two signals according to:

$$\phi = \frac{2\pi}{\lambda}\Delta x \tag{6.2}$$

where ϕ is the phase difference in radians, λ is the wavelength (0.6 m in the case of the ESR) and Δx is the path difference. The path difference depends on the position of the satellite signal in the direction parallel to the radar baseline, as described in Section 6.3.2.

Satellite signals are observed in the power spectra as an increase in power received in one or two range gates for several data dumps at a particular frequency. One such satellite signature is shown in Figure 6.1 at 06:36:58 UT. The central range and frequency for several identified satellites were manually selected by cursor using power density spectra recorded at 0.2 s integration with a range resolution of 42 km from 232 to 1702 km. The recorded values of power in each antenna, coherence and phase (used now and in all future references to mean the difference between the phases received at the 32 m and 42 m antennas) at the corresponding range and frequency were then extracted. The satellite was located within the power spectrum arrays for every 0.2 s integration during the satellite pass because there is the possibility of some shift in frequency over the course of the satellite pass, due to the ESR look direction not being vertical. The angular width of the main radar beam, even though small compared with the altitude of satellites, does cause the doppler frequencies of some satellite signals to shift towards negative values as the satellite passes through the main beam. The difference in range is not noticeable at the range resolution of the radar program.

6.3.2 Optical satellite tracking

The optical paths for satellites which passed through the radar beam were tracked by the Odin imager. Its co-location with the ESR avoided complications due to parallax effects. Software was developed to trace automatically the path of a satellite in the Odin field of view (after its approximate position in one frame has been selected manually) using a double gaussian fit within a square search region of size 5 pixels. The central coordinates, accurate to the nearest pixel, were then converted into the azimuth and elevation coordinate system.

The phase values due only to path differences were then predicted for each satellite location using approximate values for the antennae geometry. These phase values were then compared to those produced as ESR interferometric data products, in order to quantify differences in the assumed geometry and any sources of extra phase inherent in the receiver system. Assuming that the length of the radar baseline is negligible compared to the range to the satellite signatures, the look direction to the signal can be taken to be identical for each antenna. This means that the path difference, Δx, is given by:

$$\Delta x = B\cos\alpha \tag{6.3}$$

where B is the length of the baseline between the two radar antennae and α is the elevation of the radar beams. A path difference equal to the ESR wavelength of 0.6 m equates to a phase difference of 2π. Within the common volume of the 32 m and 42 m beams, parallel contour lines of equal phase difference (fringes) are located perpendicular to the radar baseline. In the first instance, a nominal baseline $\overline{N}$ was used. $\overline{N}$ was taken to be horizontal with a length of 132.5 m, as measured by 2D survey between the footpoints of the two antennae. This baseline produced phase fringes where points differing in phase by 2π have an angular separation of 0.26° spatially. It was then possible to map satellite paths through the radar phase fringes and produce a series of theoretical phase values over time.

The 7 km separation between the two narrow imagers used here means that for periods where Odin is completely obscured by cloud, the SIF camera may be relatively clear with satellite signals visible throughout the period of observation. Part of this study was to investigate the feasibility of using SIF to confirm indirectly the track of a satellite though the radar beam, making the appropriate corrections for parallax effects. This will maximise the usable satellite passes for times of localised cloud, such as occurred during the event described here, or where data from an imager co-located with the ESR is unavailable.

6.4 Results and Analysis

It was found that not all satellites gave a long-lived coherent signal or clear patterns in phase behaviour. Satellites that passed close to the centre of the radar beam and travelled at a low enough velocity that the aliasing effects of the phase variation at 0.2 s resolution were manageable, were needed to produce reliable phase calibration results. For this particular event, Odin is obscured by cloud soon into the observation period, leading to only one suitable satellite passing near enough to the radar beam being found for this analysis. This passed through the radar sidelobes with closest approach to the main beam at 06:38:07 UT. Although this means that full phase calibration is unlikely to be possible for the times of observed NEIALs, this satellite can be used to demonstrate the phase calibration technique. The satellite track is shown traced onto the Odin field of view (720 by 576 pixels) in Figure 6.2. The satellite was observed for 15.96 s in the Odin field of view, with an average angular velocity 0.774 degrees per second. With the ESR radars able to detect small pieces of space debris

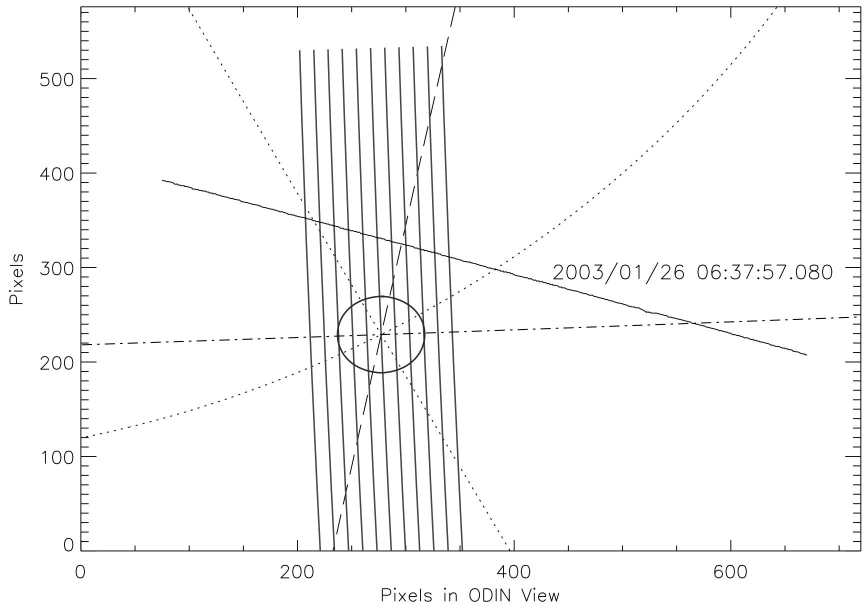

Figure 6.2: Odin field of view; dash-dot line marks the cut of the sky by the plane containing the ESR interferometric baseline and the magnetic zenith direction, dashed line marks the cut of the sky by the plane containing the optical baseline and magnetic zenith direction, dotted line shows the meridian passing through the magnetic zenith, dotted arc shows the east-west line through the magnetic zenith, the solid circle of radius 0.8° marks the half power level of the radar beam, solid thin lines mark the location of the ESR phase fringes and the thin black line shows the trace of the satellite from its position in each Odin frame.

(Lehtinen et al., 2001) as well as orbiting satellites, it was important to confirm that the satellite tracked optically was correctly associated with a satellite signature seen at the corresponding time in the radar power spectra. Time-synchronised optical tracks taken from the two separated camera sites were used to find an approximate range by triangulation, estimated at 530 km.

As a secondary check, the theoretical variations of intensities were also produced. These describe the effect of the antenna function on the intensity received for the satellite as it passes through the beam, based on its optical location. The predicted intensity variations were produced using the formula for the gain pattern of a parabolic antenna given by:

$$G \propto [\frac{\lambda r_0}{\sin\theta} J_1(\frac{2\pi r_0 \sin\theta}{\lambda})]^2 \tag{6.4}$$

where λ is the transmitted wavelength, θ is the angle of observation away from the central axis of the beam, r_0 is the radius of the antenna and J_1 is a first order Bessel function. As the transmission is on the 32 m antenna only, the receiver pattern for the 42 m dish is proportional to the product of the 32 m and 42 m beam patterns $G_{32}G_{42}$, while the 32 m dish intensity is proportional to the 32 m beam pattern squared $(G_{32})^2$.

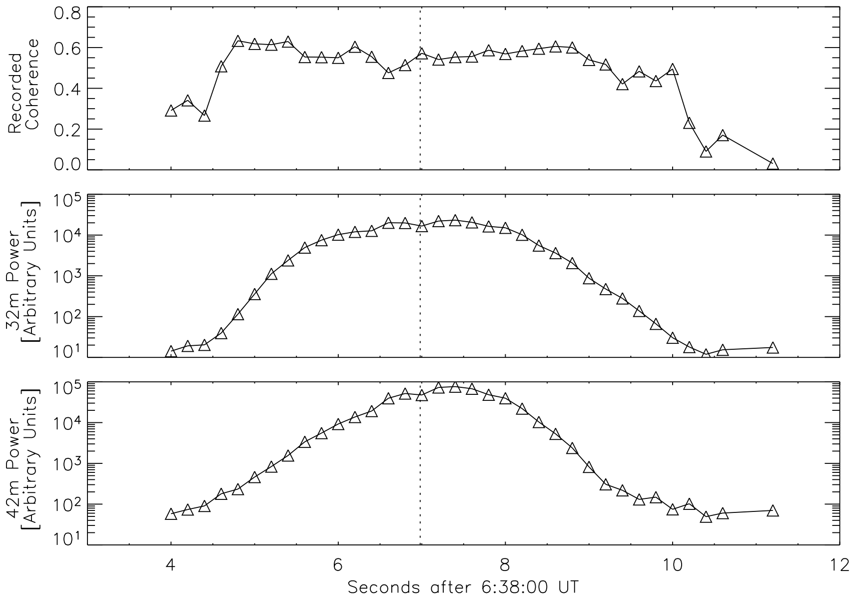

Figure 6.3: Panels from top to bottom: a) Observed coherence at central range and frequency of the satellite echo in ESR spectra, b) Observed power of satellite echo in the ESR 32 m antenna, c) Observed power of satellite echo in the ESR 42 m antenna.

The satellite was identified in radar power spectra of 0.2 s integration between 06:38:04 and 06:38:11 UT, at the corresponding range and displaying similar intensity variations as predicted using the optical track. Figure 6.3 shows the time series of the recorded coherence and power in the 32 m and 42 m antennae, recorded for the satellite signal in the radar data, as shown previously in Figure 6.1. It can be seen that high coherences and intensities in both antennae are recorded for a prolonged period of around 5 s as the satellite passes. The vertical dotted line is the time of maximum power as predicted from the satellite trace in the Odin optics, using a theoretical incoherent scatter antenna pattern. It can be seen that the radar signal matches the optical path of the satellite well, although there is an indication of an offset of about 0.25 s between the times of maximum power, mostly clearly seen in the 42 m antenna.

One possible explanation is that the ESR and Odin GPS time were not exactly synchronised for this campaign season, which will make some contribution to the phase offset between observed phase and optically predicted phase. The observed angular velocity of 0.774 degrees per second, and the phase fringe spacing of 0.26 degrees implies that the satellite phase varies by 2π in just over a third of a second. Timing discrepancies of even small fractions of seconds could therefore contribute significantly to the phase offset. The apparent time offset could also be related to the slight asymmetry present in the 42 m beam power plot. This asymmetry could be caused by slight modification of the antenna pattern by the position of the sub-reflector used to

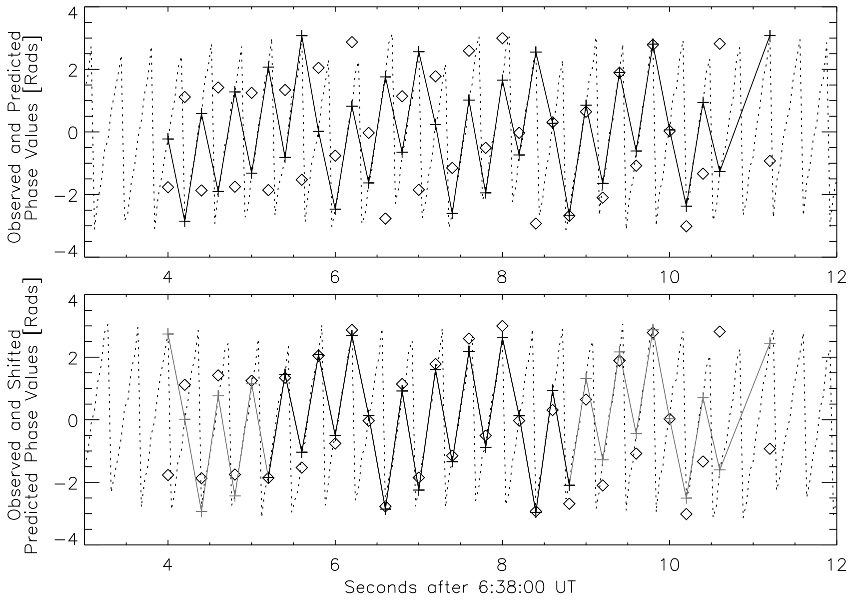

Figure 6.4: Observed and optically predicted phase values. The diamonds mark the observed phase values taken directly from the ESR spectra. The dotted line shows the predicted phase values as taken from the optical satellite trace at 0.04 s resolution and the crosses, joined by the solid line, mark the interpolated phase value on this predicted trace, taken at the same time as the radar measurement. The first panel shows raw ESR and optically predicted phase values. The second panel shows the best match that can be obtained (by varying the baseline and the constant phase offset) between the central radar and optical points for which the power received by the 32 m antenna exceeded 1000 (arbitrary units, see Fig. 6.3), which are joined by the solid black line. Data points with an associated power in the 32 m antenna below the chosen threshold of 1000 are joined by a grey line and are not taken into account in the fitting.

adjust the 42 m field-aligned look-direction, or a build-up of snow inside the dish. A satellite rapidly changing in altitude as it crosses the ESR beam could also result in an asymmetric power plot similar to that observed in the bottom panel of Figure 6.3, although from the constant range of the radar echoes, this was not the case for the satellite pass used here.

The top panel of Figure 6.4 shows the recorded phase values from the ESR spectra (which vary between $-\pi$ and $+\pi$), overlaid onto the theoretical phase values. The second panel of Figure 6.4 shows the best match that can be obtained between the observed and predicted phase if the baseline is varied about its nominal value, which introduces a phase drift of δ_0. In this case, the observed and predicted values follow each other well for the majority of the satellite pass, and then deviate at the edges where the recorded coherence and the power falls off.

To obtain this best match, the optical predictions were corrected in two ways. First, the rate of change of phase was adjusted, thereby effectively varying the baseline, to

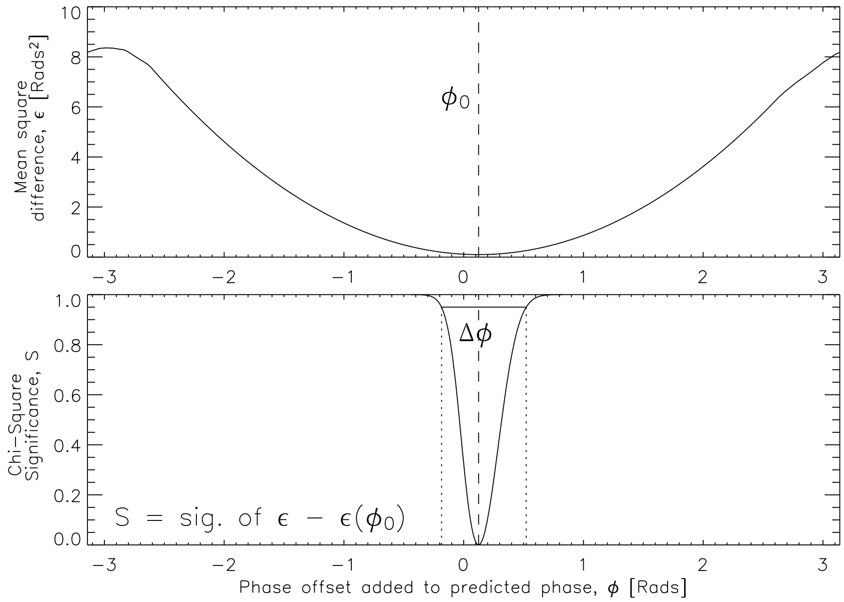

Figure 6.5: Top panel : Plot of mean square difference between observed and optically-predicted phase values, as a function of phase offset added to the predicted phase. Bottom panel : Plot of significance of the phase offset relative to the best offset found, ϕ_0: $\Delta\phi$ is the confidence interval in ϕ_0 for the 95% level.

give the lowest mean square difference between observed and predicted phase values. In reality the radar baseline is not perfectly horizontal, with the antennae being situated on uneven ground and having collecting feeds at different heights. To replicate exactly the observed rate of phase change, the baseline length used should be the distance between the actual focusing points of the antennae, which is not directly measurable by a geometric survey. A method for accurate determination of the baseline will be discussed in Section 6.5.2. Secondly, the optical predictions were shifted by a certain constant phase, which represents the best estimate of phase offset due to the ESR receiver system and timing synchronisation errors between ESR and Odin for this campaign. This was again found by minimising the mean square difference between observed and predicted phases.

The top panel in Figure 6.5 shows the mean square difference between observed phase and predicted phase, against phase offset, once the predicted phase has been adjusted for the best rate of phase change found. A clear minimum in the mean square difference can be seen, which corresponds to an ESR system phase offset of just over 0.1 radians. The second panel of Figure 6.5 shows a Chi-square null hypothesis test on these data, with $\Delta\phi$ representing the range of values within the 95% confidence level. This range can be treated as the uncertainty in the best phase offset found. It can be seen that for only one satellite pass the final uncertainty in the phase offset is

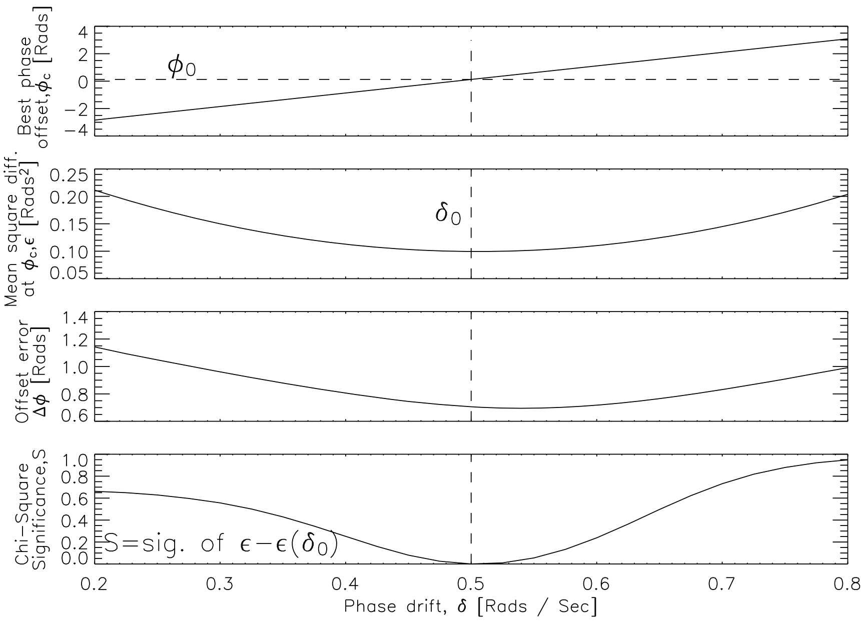

Figure 6.6: From top to bottom : The effect of applied phase drift, δ, to the optically predicted phase values on a) The phase offset found b) the mean square difference between observed phase and predicted phase with this offset c) The width of the 95% confidence interval around the best phase offset found, and d) the Chi-square significance of the best applied phase drift found, δ_0. Only phase values with an associated power in the 32 m antenna of over a chosen threshold of 1000 [arbitrary units] were used for this analysis.

very large at ± 0.4 radians. To reduce this to a usable accuracy more satellite passes are needed that give extended periods of consistent recorded phase values (see Section 6.5.2).

Figure 6.6 shows how the best rate of phase change, used to produce Figure 6.5, was determined. Applied phase drift is here taken to mean the extra phase change added to the rate calculated using the nominal baseline. The effect of varying the applied phase drift is shown for the best phase offset found, the mean square difference between predicted and observed for all data points at best phase offset, and the width of the 95% confidence level for this offset. A drift of an extra 0.5 radians per second, resulting in the lowest mean square difference at best phase offset, was used to produce the plots shown previously in Figure 6.5. It can be seen that despite a clear minimum being evident, the best phase drift found with this limited number of data points during a single satellite pass, is not statistically significant at the 84% (1 sigma) confidence level.

Even with adjusting the optically predicted data for the best phase drift and best phase offset, there is still some deviation from observations with the minimum of the mean square difference curve never reaching zero, especially evident at the edges of

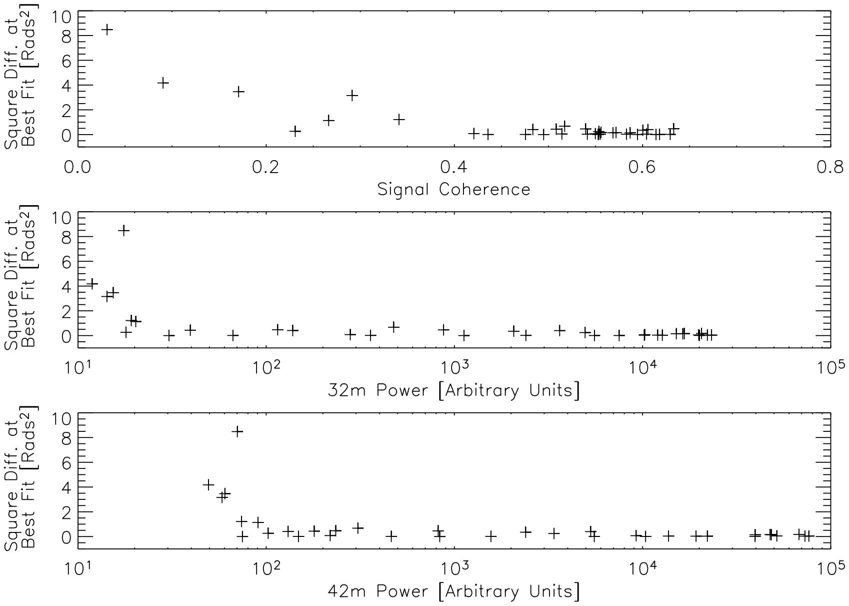

Figure 6.7: Square difference between observed and best-match predicted phase value (i.e adjusted for the best phase drift and phase offset) for each data point, as a function of a) recorded coherence of that data point, b) recorded power in the 32 m antenna for that data point and c) associated recorded power in the 42 m antenna.

the satellite pass. Figure 6.7 shows the square difference at best δ_0 and ϕ_0 for each phase data point against its corresponding antenna intensities and coherence value. It can be seen that at low intensities and low coherences below a certain threshold, the phase values recorded are not consistent with the best-fit predictions and are unreliable for use in phase calibration. Power recorded is shown to be a better measure of the quality of the data and its use for phase calibration than recorded coherence, which has a less clearly defined threshold.

The consistent fit of radar phases to optical data relies on having high enough signal power in both the 32 m and 42 m dishes. If the signal level in either one of the receivers drops below a certain level relative to the noise, the resulting phase values will no longer be reliable. As shown in Figure 6.3, the received power in the 42 m antenna is around 4 times that in the 32m antenna, for the central section of the satellite pass. Hence, at the threshold level where the consistent fit starts to fail, we would expect the 42 m power to be roughly 4 times the 32 m power. This is consistent with the results shown in the bottom two panels of Figure 6.7. In order to obtain consistent phase values, a good estimate for the threshold power required in the 32 m antenna is seen to be 100 [arbitrary units], i.e. lower than the more restrictive power threshold of 1000 [arbitrary units] that was used earlier in determination of the calibration values.

Figure 6.8 shows the same analysis as that of Figure 6.6, but with the lower power

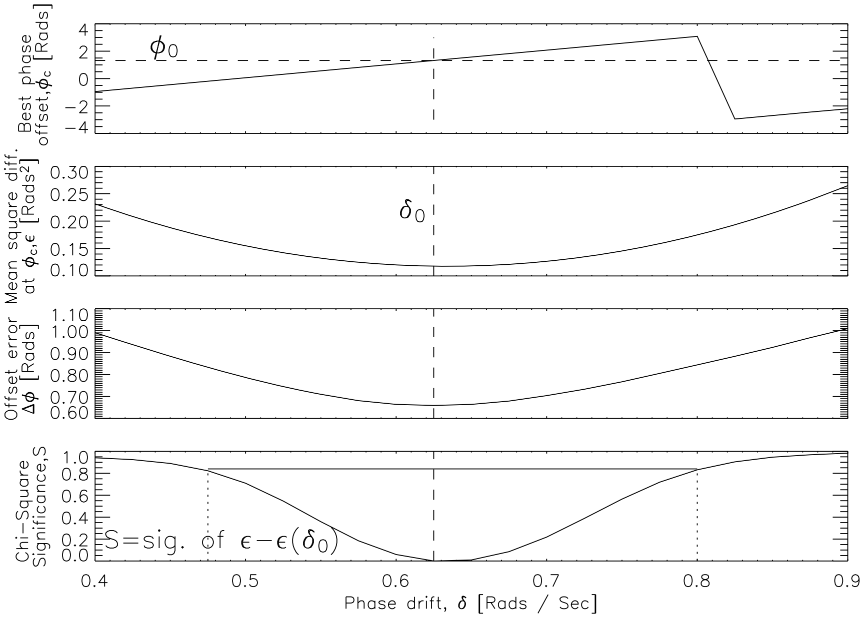

Figure 6.8: .
Phase drift analysis as described in Figure 6.6, but with a lower cut-off threshold power in the 32 m antenna of 100 [arbitrary units].

threshold employed to allow the use of more data points. It can be seen that this increased number of samples results in a statistically significant best phase drift at the 84% (1σ) level. Allowing the use of more data points at lower intensities results in a slightly different best drift rate, but both values lie within the 84% interval shown.

Figure 6.9 shows the corresponding analysis for the satellite signal traced in the SIF imager. The satellite track as seen in SIF in α and ϕ coordinates is adjusted for the parallax to produce theoretical values of the track as it would appear in the Odin field of view. The ϕ values are identical as seen from each station over time but the α values are corrected using the range of the satellite as seen in the radar power spectra. This theoretical Odin track was used to assess the feasibility of using a remote site camera for satellite tracking if a radar co-aligned imager is unavailable or obscured by localized cloud. The drift required for the best match was found to be the same δ_0 = 0.5 radians per second as was found using the trace of the satellite directly in Odin, with the original threshold 32 m power of 1000 [arbitrary units]. This corroborates the interpretation that this drift is due to errors in the defined radar baseline and not errors in the optics. It can be seen that the best phase offset found when using the drift-adjusted SIF trace is 0.5 radians lower than the corresponding analysis. Taking into account the velocity at which the satellite is seen to cross the phase fringes in the radar, this corresponds to a timing error of 0.03 s between SIF and Odin. As the bi-static satellite tracking technique used to synchronise the two optical stations tim-

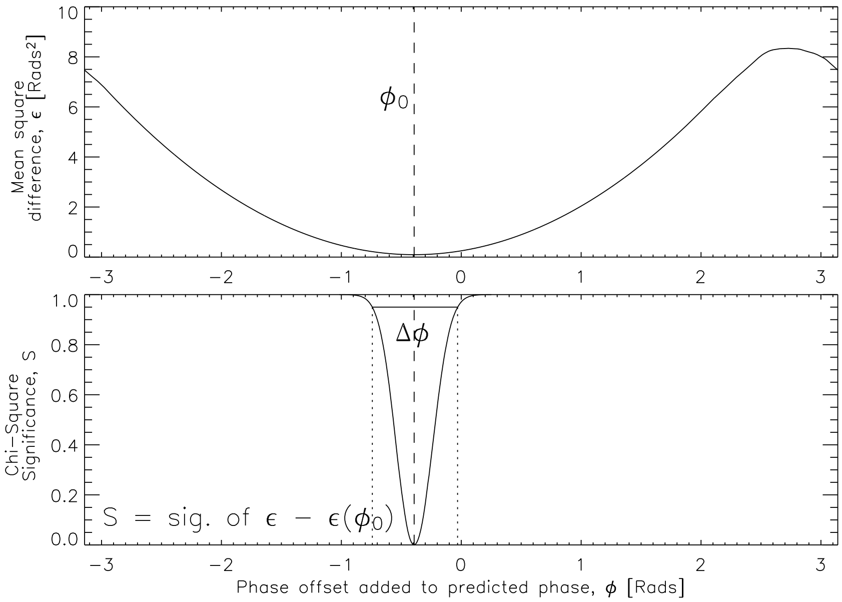

Figure 6.9: Phase offset analysis as described in Fig. 6.5 but using the satellite position as traced from the remote camera on the SIF platform.

ing has an associated uncertainty of ± 0.02 s, this is consistent within the expected bounds of uncertainty.

6.5 Discussion

Feeding an additional calibration signal into the ESR system at the local oscillator stage would be an alternative way of quantifying the phase changes introduced by the interferometry technique. Whilst the introduction of a signal of known phase would be a means of calibrating one part of the phase processing system, i.e. from the local oscillator stage to the phase interferometric data product, the use of satellites described in this chapter allows us to perform an ‘end to end’ calibration of the entire optical and radar interferometry system. The satellite method directly relates phase to optical location in the sky, with any errors in time synchronisation between cameras and radar automatically taken into account. With the high frequency of satellite passes over Svalbard, this technique provides a means of routinely calibrating the phase for any interferometric data run during clear skies, without the need for extra calibration radar time or equipment setup.

6.5.1 Atmospheric effects

In using radar signal phases, it is important to consider whether ionospheric scintillation may have a significant effect on the observed phase of a satellite echo, and hence introduce a source of error into the calibration procedure described here. The interferometry technique is only sensitive to differences in phase at the two antennae, so to have a significant effect would require ionospheric density irregularities, as described in Tereshchenko et al. (1998), with a field-perpendicular wavelength less than the beam separation at the height of the peak effect on the phase path. For a simple order of magnitude calculation we assume this to be at the F-region peak, at an altitude of 300 km. From similar triangles, and for the height of the satellite detected here (determined from the range of the echoes to be 500 km), we find that irregularities of wavelength less than d(500-300) / 500 $\approx$ 50 m are needed to induce a significant phase path difference to the two antenna (where the antenna separation d $\approx$ 130 m). If we assume that the irregularities are moving with a typical F-region convection speed of 1 kms^{-1}, these will give phase path differences that vary with periods of 0.05 s.

Each interferometric data point, integrated over 0.2 s, therefore covers at least 4 such irregularity cycles. This is not enough to average out the variations and implies a possible source of phase error due to scintillation in each data point. However our method relies on minimising the difference for the time series as a whole, rather than fitting each observed phase value individually to its optically predicted counterpart. If we use the power threshold of 100 [arbitrary units] in the 32m dish, as employed for Figure 6.8, we obtain a time series used for the fitting of approximately 5 s in length. This therefore covers more than 100 effective scintillation cycles. The resulting phase differences will average out and have negligible effect on the overall fit. This applies even if the F-region peak was at lower altitudes than assumed here, i.e. down to 200 km.

6.5.2 Method for accurate estimation of interferometer baseline

In order to infer location from phase difference correctly, the interferometer baseline (between the foci of the two antennae) must be known with an accuracy much smaller than the wavelength of the radar signal. For the ESR λ is 0.6 m, meaning that the baseline must be known on centimeter scales and in three dimensions. Rather than trying to make this measurement directly, which would rely on theoretical coordinates of the antenna foci, we here describe a technique that allows us to use the satellite measurements. To make a first fit, we use a nominal baseline vector, $\overline{N}$, which is not

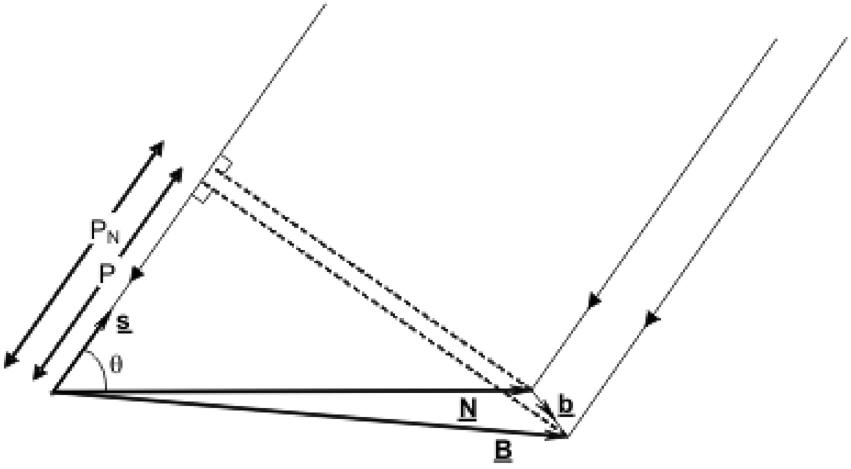

Figure 6.10: Observations geometry. $\bar{N}$ is the nominal (horizontal) baseline between the foci of the 42 m and 32 m antennae, $\bar{B}$ is the true baseline and $\bar{b}$ is the vector difference between the two. $\bar{s}$ is a unit vector pointing at the satellite. The actual phase path difference is P, but that calculated assuming the nominal baseline is P_N.

to the above accuracy (and is assumed to be horizontal, which is not valid because the antennae foci are at slightly different heights) and then correct to the true baseline $\bar{B}$ (the vector difference between $\bar{N}$ and $\bar{B}$ being $\bar{b}$). This geometry is shown in Figure 6.10. Described here is a method by which $\bar{b}$ will be determined by future observations.

The nominal phase path difference, calculated using the nominal (assumed horizontal) baseline $\bar{N}$ is:

$$P_N = Ncos\theta = \bar{N}.\bar{s} \tag{6.5}$$

Similarly the real phase path difference is:

$$P = \bar{B}.\bar{s} = (\bar{N} + \bar{b}).\bar{s} = \bar{N}.\bar{s} + \bar{b}.\bar{s} = P_N + \bar{b}.\bar{s} \tag{6.6}$$

where $\bar{s}$ is a unit vector pointing towards the satellite. The rate of change of the observed phase is therefore:

$$\frac{d\phi}{dt} = \left(\frac{2\pi}{\lambda}\right)\frac{dP}{dt} = \left(\frac{2\pi}{\lambda}\right)\frac{dP_N}{dt} + \left(\frac{2\pi}{\lambda}\right)\frac{d(\bar{b}.\bar{s})}{dt} \tag{6.7}$$

The first term on the right hand side of Equation 6.7 is the rate of change of phase predicted using the nominal baseline and the second term is the ‘drift’ correction (δ_0)

required because the true baseline differs from the nominal one.

$$\delta_0 = \left(\frac{2\pi}{\lambda}\right)\frac{d(\overline{b}.\overline{s})}{dt} = \left(\frac{2\pi}{\lambda}\right)\left(b_x\frac{ds_x}{dt} + b_y\frac{ds_y}{dt} + b_z\frac{ds_z}{dt}\right) \tag{6.8}$$

where the three components of the unit vector $\overline{s}$ obey

$s_x{}^2 + s_y{}^2 + s_z{}^2 = 1$, so:

$$s_x\frac{ds_x}{dt} + s_y\frac{ds_y}{dt} + s_z\frac{ds_z}{dt} = 0 \tag{6.9}$$

From Equations 6.8 and 6.9:

$$\delta_0 = \left(\frac{2\pi}{\lambda}\right)\left(b_x - b_z\frac{s_x}{s_z}\right)\frac{ds_x}{dt} + \left(b_y - b_z\frac{s_y}{s_z}\right)\frac{ds_y}{dt} \tag{6.10}$$

The z-direction of the coordinate system is defined to be in the field aligned direction and because all measurements are taken with the satellite within about 5°of this direction $s_z \approx 1$ and $s_x \approx s_y \approx 0$. Equation 6.10 can then be approximated as:

$$\delta_0 = (\frac{2\pi}{\lambda})(b_x\frac{ds_x}{dt} + b_y\frac{ds_y}{dt}) \tag{6.11}$$

Therefore to calculate δ_0 requires knowledge of b_x and b_y and the satellite pass orientation and speed. If satellite passes that move through the centre of the beam are selected, the x-direction can be defined to be that of the satellite pass, so $\frac{ds_y}{dt} = 0$, and Equation 6.11 reduces to:

$$b_x = \frac{(\lambda\delta_0)}{2\pi(\frac{ds_x}{dt})} \tag{6.12}$$

from which the component of the correction vector $\overline{b}$, in the direction of satellite motion, can be calculated from the best fit drift δ_0, given that $\frac{ds_x}{dt}$ is known. Using several passes of different orientations, $\overline{b}$ will be estimated.

To assess the accuracy of using this method, the fractional uncertainty ε_x in the component b_x is:

$$\varepsilon_x = (\varepsilon_\delta{}^2 + \varepsilon_s{}^2)^{\frac{1}{2}} \tag{6.13}$$

where ε_δ is the fractional uncertainty in the determination of δ_0 and ε_s is the fractional uncertainty in $\frac{ds_x}{dt}$. If the (small) angle between the z-axis and $\overline{s}$ is θ, $s_x = \sin\theta$ and so:

$$\frac{ds_x}{dt} = \cos\theta\frac{d\theta}{dt} \approx \frac{d\theta}{dt} \tag{6.14}$$

i.e. the fractional uncertainty in $\frac{ds_x}{dt}$ is the same as that in $\frac{d\theta}{dt}$.

Using the example presented in this chapter, the satellite moves across the Odin field of view through an angle η of 12.35°, and the uncertainty in this angle ε_η is one camera pixel width (± 0.02°). It moves across this angle in 15.96 s at an average angular speed of $\frac{d\eta}{dt} = 0.774 \pm 0.001$ degrees per second. Thus the fractional uncertainty in the angular speed of the satellite is 0.16%. The angle η in this case is not quite the same as θ because the satellite did not pass through the exact centre of the beam. Nevertheless, η and θ are sufficiently similar that the fractional uncertainty in η is typical of that in θ also (in fact because $\varepsilon_\delta \gg \varepsilon_s$, the difference between η and θ is of no significance in this context). Hence the uncertainty ε_s is taken as 0.0016.

The error ε_δ can be estimated from Figure 6.8, which shows that best-fit drift δ_0 = 0.625 rad s^{-1} with an uncertainty at the 1σ level (84%) of between 0.46 and 0.82, giving an average uncertainty of ±0.18, i.e. a fractional uncertainty of 0.29. From Equation 6.13, ε_s is clearly negligible and $\varepsilon_x = \varepsilon_\delta$ = 0.29.

To estimate the absolute magnitude of this uncertainty, we note that Equation 6.12 gives b_x of 4.42 m (although note that this satellite pass does not go through the centre of the beam and so Equation 6.12 is only approximately valid in this case), and thus a fractional error of ε_x = 0.29 corresponds to an uncertainty of 1.27 m = 2.12 λ. If the measurement is repeated for another pass in the same direction, the estimate and its uncertainty would be independent of the first measurement. Thus, with a set of, for example, n = 16 such passes, the uncertainty in b_x could be reduced by $n^{\frac{1}{2}}$ to 0.53 λ. The key requirement is that no change is made to the radar transmit/receive hardware while the calibration passes are accumulated.

6.5.3 Radar time resolution

With the phase fringes at approximately 0.26°apart, the angular speed of the satellite shown here highlights the need for radar data at sub-second time resolution. With an angular velocity of 0.774 degrees per second this satellite was one of the slowest observed, with most other crossings displaying angular speeds of around 1 degree per second or more. Even so, it can be seen that at 0.2 s resolution the satellite shown here is passing through the phase fringes so quickly that only around 2 data points per phase loop are recorded.

One other satellite passing through the centre of the radar beam was found within the interval of clear sky, but produced no regular phase structures that could be fitted reliably to optical data. The angular velocity here was recorded at 0.93 degrees per second. Within the 0.2 second interval this satellite would have crossed an angular width far greater than the phase fringe half-width, causing aliasing effects. This point can be illustrated by considering the interpretation of Figure 6.4 if every other data point were missing. Radar data at a time resolution of 0.1 seconds or shorter, would increase the number of satellite passes usable for this technique, assuming that the observed signal power still exceeds the threshold for a reliable calibration to be obtained.

6.6 Summary

This chapter presents an interferometry phase calibration technique, used for the first time at the ESR, and shows some initial results of its application. It has been shown that it is possible to recreate observed phase values of a satellite passing through the ESR main dual-beam, using phase values predicted from optical satellite traces. In order to achieve a series of predicted phase values following recorded observations to the highest degree, it is necessary to apply:

[1] a phase offset representing phase added due to components in the ESR receiver system and due to timing synchronisation errors between ESR and Odin.

[2] an added rate of phase change, arising from inaccuracies in the measurement of the interferometric baseline.

A technique has been demonstrated, using the results obtained for one satellite pass, to quantify these effects on the recorded phase values produced by the ESR. In order to calibrate recorded phase values with the position of coherent signals along the baseline, many satellite passes exhibiting high received coherences and power at the radar for several seconds will be needed, in order to obtain phase offset and drift values to usable accuracies. It has been shown that it is possible to use optical satellite traces from a remote-site camera to perform phase calibration, if the ESR co-aligned imager is obscured by localised cloud, to within the accuracy of the current technique. Images from the narrow view imager located at the Auroral Station as part of the Spectrographic Imaging Facility, can therefore be used to extend the database of satellites available for this technique in future campaigns.

For the satellite pass observed here, a phase offset of 0.1 radians to within a statistical accuracy of 0.4 radians has been shown, corresponding to an error in horizontal distance of approximately 400 m at 300 km altitude. With, for example, a collection of n = 16 such satellite passes with similar number of consistent recorded phase values, future work should allow this error to be reduced by $n^{\frac{1}{2}}$, i.e. to within 0.1 radians and to within 100 m horizontally at 300 km altitude. Future extensions of this work will be to apply this technique to a large set of satellite passes observed both in ESR interferometric data of high enough time resolution and in the Odin and SIF fields of view. The next steps will be to see whether an effective phase calibration can be obtained, in order to build up a self-consistent map of the phase fringes throughout an ESR interferometry run. The stability of the phase calibration over time and the effect of temperature changes can then be investigated. In this thesis, mainly manual procedures were used to achieve the calibration. As many such calibrations will be required it will be important to automate the procedure as far as possible, so that sufficient satellite passes can be readily included.

7

Conclusions and Future Work

7.1 New Results

This thesis has demonstrated the value of a new optical instrument, the ASK imager, to studies of the differences in energy distribution for various small-scale auroral forms. Emissions in dynamic rayed aurora, of the type associated with NEIAL signatures in the dayside cusp, have been shown to originate from a broad range of precipitation energies. The use of imaging within a narrow-passband, centred on emission caused by the low-energy component of precipitation, has revealed a direct relationship between small-scale O^+ emission in rays and NEIAL enhancements. Multiple NEIAL signatures have been shown to correspond to spatial auroral features drifting through the radar beam. For the ionospheric parameters and precipitation characteristics observed, numerical simulations have shown that the generation of ion-acoustic turbulence is consistent with wave-wave interactions, driven by the beam instability.

For the NEIAL events observed, the close proximity of a northward IMF lobe reconnection X-line suggests the possibility of the X-line itself being the source region for the persistent low-energy electron streams which repeatedly intersected the ESR beam. More generally, precipitating electron distributions with a prominent low-energy component are linked with Alfvénic acceleration mechanisms, producing an accelerated population with a broader range of energies than in ‘inverted-V’ type acceleration. Studies of auroral morphology with the ASK imager have shown that purely low-energy electrons can be found in quiet and diffuse auroral arcs, not associated with NEIAL activity. Numerical simulations of beam-driven parametric decay predict ion-acoustic enhancements over an increasing range of wave vectors for increasing spread in beam energy. It is suggested that low-energy precipitation alone could be sufficient to drive ion-acoustic wave enhancements, but the addition of a high-energy component increases the likelihood of enhancements being detected at a particular IS radar wavevector. This may therefore explain the relationship between NEIALs and dynamic rayed aurora.

To further the understanding of plasma processes operating on the small scales of NEIALs and related aurora, it is essential to resolve the location of enhanced IS structures within the radar beam. This thesis presents a new technique to calibrate the phase of signals received by both ESR dishes used as an interferometer, with respect to the position of a target which is known from optical methods. This calibration technique demonstrates how coordinated optical and radar observations of NEIALs at high temporal and spatial resolution can be used to study the evolution of NEIALs and their position relative to small-scale auroral features.

7.2 Open science questions and future studies

It is not yet clear whether the NEIALs observed in the nightside ionosphere are commonly generated by the same mechanisms as on the dayside, or if two entirely different mechanisms are at work, producing similar signatures in the radar spectra. Nightside observations have indicated a relation between NEIALs and the dark regions at the edges of large scale auroral arcs (Michell, 2007; Michell et al., 2008). Studies using high temporal resolution radar data with narrow field imaging at the EISCAT Tromsø site are needed to investigate further this apparent difference in behaviour. The mainland EISCAT radars differ considerably in frequency from the ESR (224 and 931 MHz for the VHF and UHF respectively, compared to 500 MHz for the ESR), raising the possibility that different instability processes may be operating, producing enhancements over different frequency ranges. Alternatively small-scale filaments of low-energy precipitation may still be present on short time scales, but are either not as prominent amongst the large scale high-energy morphology of aurora commonly seen on the nightside, or are not easily linked with enhancements in radar data integrated over several seconds. It has been demonstrated that between 25% and 40% of the total energy from electrons deposited into the ionosphere may be attributed to dispersive Alfvén wave activity (Chaston et al., 2007), linked with small-scale aurora and electron populations of broad energy range. Alfvénic acceleration may be the dominant mechanism for auroral particle acceleration during active intervals, both in the dayside cusp region and in the nightside auroral oval.

NEIAL signatures in radar spectra rely on the combination of two different factors: firstly, some plasma turbulence mechanism producing wave enhancements, and secondly, appropriate plasma conditions for the enhancements to be detected at the particular wavevector of the sampling radar. Studies of NEIALs and auroral precipitation characteristics at a wide range of radar frequencies and locations can help to differentiate these factors and advance understanding of plasma turbulence as a whole. Further studies involving the input of data to theoretical simulations can greatly advance the field of plasma theory, by allowing direct comparisons with observations in the natural plasma environment.

The link revealed here for the first time between NEIALs and specific auroral emissions means that optical data can now be used to ‘image’ NEIAL behaviour, using modern camera technology with high temporal and spatial resolution. After being transferred to the EISCAT Tromsø site for the 2006/2007 observing season, the ASK imager has now been returned to Svalbard. Unfortunately during the lifetime of this PhD project, for NEIAL events during periods in which ASK was operating, observations were obscured by cloud cover. In the future, the multi-spectral imaging capability of ASK and its co-location with the ESR beam will allow the mapping of small-scale structure and motions of the spatial precipitation features for periods where large numbers of NEIALs are recorded. The transferral of optical facilities from the auroral station in Adventdalen to the KHO site has reduced the problems of parallax effects caused by separation from the radar beam. However, auroral imagers at multiple locations allow the calculation of range for auroral structures and satellites, providing height information for the emissions and for identification of satellite signatures to use in phase calibration. The possibility of installing another separate imager away from the ESR will therefore be investigated in the future.

In terms of the radar data, direct observations of wave enhancements at high spatial resolution are essential to follow the evolving instability for individual NEIALs. Strømme et al. (2007) have presented NEIAL observations from the new Advanced Modular Incoherent Scatter Radar (AMISR) in Alaska, which is a phased array IS radar with several almost simultaneous look-directions. Such a system can begin to resolve some of the temporal and spatial development of NEIAL signatures as they move through the magnetic zenith, which can then be compared with the intensity and

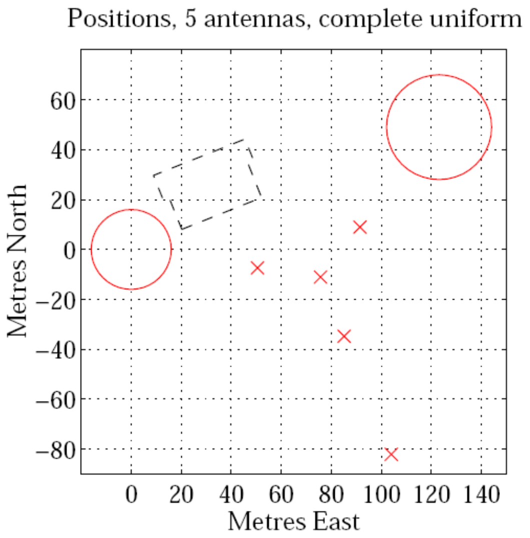

Figure 7.1: Example configuration of 5 passive receiving antennae for the ESR system, in addition to the existing 32 m and 42 m dishes (shown by the red circles). Figure taken from Grydeland et al. (2005).

motions of auroral rays. Interferometric techniques are now being developed for the ESR, which provide far greater angular resolution than individual antennae.

7.2.1 Small-scale radar studies: Interferometry

With the two dishes that form the current ESR system, only one interferometric baseline can be obtained, which allows positioning in one horizontal direction only. The location is also ambiguous, with the relatively long baseline leading to several 2π cycles in phase occurring within the main lobe of the radar beam. A full imaging interferometry capability, i.e. an ability to construct true images of the radar targets being illuminated within the transmitted radar beam, is now being planned for the ESR (Grydeland et al., 2005). Although statistical arguments in previous studies have indicated up and down shifted NEIALs present in the same volume using single-baseline interferometry, multiple baselines would fully resolve this ambiguity. Imaging interferometry can also be used to study other coherent structures in the ionosphere, including artificial radar enhancements generated by active high frequency heating experiments, polar mesospheric summer echoes (thin layers of enhanced scattering generated at altitudes of around 80-90 km altitude) and meteor trails. The emphasis of planned interferometric studies is on powerful coherent echoes (such as NEIALs), because of the relatively small and simple antennae which can be used to detect them.

Simulations have shown that the addition of 5 extra receivers in a configuration shown in Figure 7.1 gives a good visibility coverage, providing baselines with a range of lengths and orientation (Grydeland et al., 2005). The ESR was successfully run with one extra 4 m x 4 m receiver antenna for selected times during the 2005/2006 season. Preliminary results showed that satellite signals could be detected in the processed data. The antenna was not designed to withstand extreme storms over the Svalbard winter, with the intention of being partially disassembled for periods of predicted bad weather and minor parts replaced as required. However, unfortunately the antenna was left fully constructed during unforeseen strong winds, which led to damage to some components which were harder to replace than the antennas themselves.

Four new receiver antennae are now planned in a slightly modified configuration pattern, providing the optimum configuration of baselines. The new receivers are panel-antenna arrays, consisting of metal frames each mounted with 16 panel-antenna boxes, as shown in Figure 7.2. Four of the frames are now populated, the first two being constructed by Tom Grydeland with the help of Martin Langteigen and Paul Gallop, and the most recent two set up by Rico Behlke, Dan Whiter and the author in November 2007. Over the coming 2008/2009 season, the completed arrays will be connected by cable runs to the main building. The next stage will be the addition of extra hardware and software drivers to deal with the collection and processing of the multiple receiver data, which should be ready for testing next year. Interferometric studies together with a network of auroral imagers will allow high resolution imaging of both NEIALs and their optical counterparts. Observations of the evolution of the patterns of precipitation and instability growth are needed to resolve the remaining uncertainties about the mechanisms involved.

Figure 7.2: Photograph of one of the new panel-antenna arrays, with the ESR 42 m dish in the background, taken by the author during the construction of the interferometry receivers in November 2007

A

Coordinate systems

The following section defines the coordinate systems for space plasma physics that have been used to describe data presented in this thesis. This appendix is based on material drawn from Hapgood (1992, 1997).

A.1 Geographic Coordinates

The geographic coordinate system is geocentric (having the origin at the centre of the Earth), fixed with respect to the Earth's rotation and aligned with the rotational axis. The mapped position of any point on the Earth's surface can be described by the spherical coordinates of Geographic Latitude (GLAT) and Geographic Longitude (GLONG). The latitude of any point is the angle in degrees between it and the equatorial plane. The equator is defined at 0°GLAT, while the north and south geographic poles, are at 90° N and 90° S respectively. The longitude for an arbitrary point is the angle between a reference meridian through the two geographical poles to the meridian that passes through that point. The reference meridian of 0°GLONG passes through Greenwich, London, with the 180°E or 180°W meridian on the opposite side of the earth. In the equivalent cartesian geographic frame the Z-axis is parallel to the Earth's rotation axis (positive to the North) and the X-axis points towards the intersection of the Equator and the Greenwich Meridian.

A.1.1 Local geographic coordinates

Local coordinates are used to express vector directions, with respect to the horizontal plane at a particular ground station. The IMAGE magnetometer data uses local cartesian coordinates to describe the components of magnetic field. The local vectors are defined using directions in the geographic frame from the magnetometer station. For the IMAGE data coordinate system, X is North, Y East and Z is vertically downwards.

A.2 Geomagnetic coordinates

The geomagnetic spherical coordinate system rotates with the Earth and describes points in terms of angles, Magnetic Latitude (MLAT) and Magnetic Longitude (MLONG). However, rather than being aligned with the rotational axis, the cartesian Z-axis is the magnetic axis of the Earth's field (positive northwards). The Y-axis of this system is defined as the cross product of the rotational and magnetic axes poles, with the X-axis completing the right-handed set.

The system is set up such that points on the same geomagnetic field line have the same geomagnetic coordinates, mapped out from the ionosphere up into the magnetosphere. The geomagnetic configuration can be described using a variety of models, from a simple dipole approximation to more complex field configurations varying with time epoch. Geomagnetic coordinates therefore vary according to the magnetic field model used.

A.3 Magnetic local time

The Magnetic Local Time (MLT) system describes longitudinal coordinates but differs from magnetic longitude in that it uses hours rather than degrees, where 1 hour is equivalent to 15°. MLT coordinates are derived from mapping magnetic field lines out to the ecliptic plane. The hour angle of the Sun at the mapped location gives the MLT for the origin of the field line at the Earth's surface. Note this system also depends on the magnetic model used to describe the field line mapping; in most cases a simple dipole field is used. MLT coordinates are not fixed with relation to the Earth;

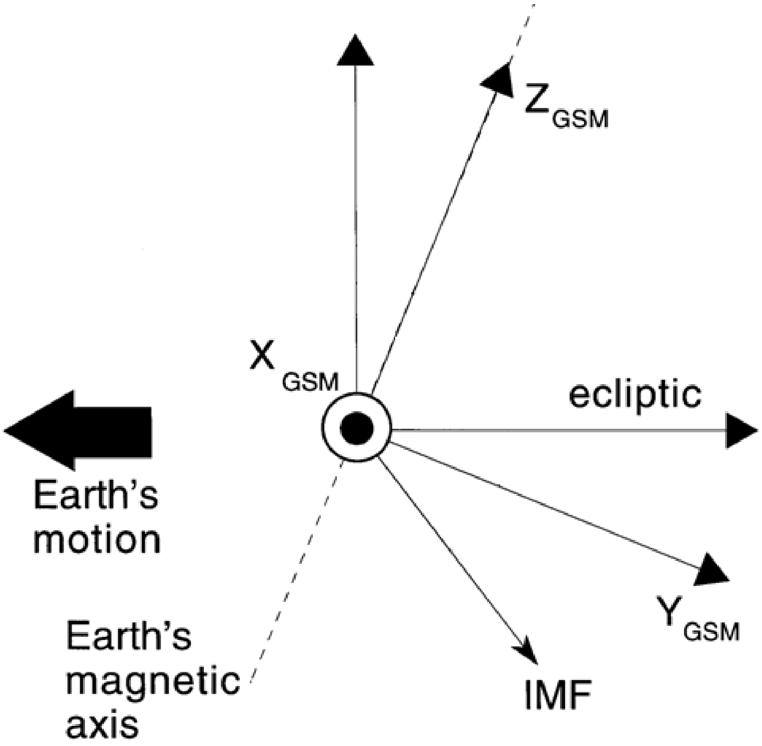

Figure A.1: Geocentric Solar Magnetospheric (GSM) coordinate system, as viewed from the Sun.

the coordinate system is set with 12 MLT (magnetic noon) pointing towards the Sun, and the Earth rotates beneath the coordinate frame.

A.4 Geocentric Solar Magnetospheric (GSM) coordinates

The Geocentric Solar Magnetospheric System (GSM) is a cartesian coordinate system based on the Sun-Earth line. The X-axis points from the Earth to the Sun and the Z-axis is the projection of the Earth's magnetic axis (positive North) on to the plane perpendicular to the X axis, as shown in Figure A.1. The Y-axis completes the right-hand set, pointing approximately from dawn to dusk. With the anti-parallel requirement for interaction between the terrestrial and solar wind magnetic field, this is considered the best system to use in studying the influence of the IMF direction on reconnection processes.

BIBLIOGRAPHY

Alfvén, H.: Existence of electromagnetic-hydrodynamic waves, Nature, 150, 405–406, doi: 10.1038/150405d0, 1942.

Allen, C. W.: Astrophysical quantities, London: University of London, Athlone Press, |c1973, 3rd ed., 1973.

Andersson, L., Ivchenko, N., Clemmons, J., Namgaladze, A. A., Gustavsson, B., Wahlund, J.-E., Eliasson, L., and Yurik, R. Y.: Electron signatures and Alfvén waves, J. Geophys. Res., 107, 1244, doi: 10.1029/2001JA900096, 2002.

Baumjohann, W. and Treumann, R. A.: Basic space plasma physics, London: Imperial College Press, |c1996, 1996.

Blixt, E. M., Grydeland, T., Ivchenko, N., Hagfors, T., La Hoz, C., Lanchester, B. S., Løvhaug, U. P., and Trondsen, T. S.: Dynamic rayed aurora and enhanced ion-acoustic radar echoes, Ann. Geophys., 23, 3–11, 2005.

Buchert, S. C., van Eyken, A. P., Ogawa, T., and Watanabe, S.: Naturally enhanced ion-acoustic lines seen with the EISCAT Svalbard Radar, Adv. Space Res., 23, 1699–1704, doi: 10.1016/S0273-1177(99)00382-8, 1999.

Cabrit, B., Opgenoorth, H., and Kofman, W.: Comparison between EISCAT UHF and VHF backscattering cross section, J. Geophys. Res., 101, 2369–2376, doi: 10.1029/95JA02175, 1996.

Chakrabarti, S., Pallamraju, D., Baumgardner, J., and Vaillancourt, J.: HiTIES: A high throughput imaging echelle spectrograph for ground-based visible airglow and auroral studies, J. Geophys. Res., 106, 30 337–30 348, doi: 10.1029/2001JA001105, 2001.

Chaston, C. C., Carlson, C. W., Peria, W. J., Ergun, R. E., and McFadden, J. P.: FAST observations of inertial Alfvén waves in the dayside aurora, Geophys. Res. Lett., 26, 647–650, doi: 10.1029/1998GL900246, 1999.

Chaston, C. C., Peticolas, L. M., Bonnell, J. W., Carlson, C. W., Ergun, R. E., McFadden, J. P., and Strangeway, R. J.: Width and brightness of auroral arcs driven by inertial Alfvén waves, J. Geophys. Res., 108, 1091, doi: 10.1029/2001JA007537, 2003.

Chaston, C. C., Carlson, C. W., McFadden, J. P., Ergun, R. E., and Strangeway, R. J.: How important are dispersive Alfvén waves for auroral particle acceleration?, Geophys. Res. Lett., 34, L07 101, doi: 10.1029/2006GL029144, 2007.

Chen, J.-S., Röttger, J., and Chu, Y.-H.: System phase calibration of VHF spaced antennas using the echoes of aircraft and incorporating the frequency domain interferometry technique, Radio Sci., 37, 1080, doi: 10.1029/2002RS002604, 2002.

Collis, P. N., Häggström, I., Kaila, K., and Rietveld, M. T.: EISCAT radar observations of enhanced incoherent scatter spectra; their relation to red aurora and field-aligned currents, Geophys. Res. Lett., 18, 1031–1034, 1991.

Cowley, S. W. H.: Magnetic Reconnection, in: Solar System Magnetic Fields, edited by Priest, E. R., p. 125, D. Reidel Publishing Co., Dordrecht, Holland, 1985.

Cowley, S. W. H. and Lockwood, M.: Excitation and decay of solar wind-driven flows in the magnetosphere-ionosphere system, Ann. Geophys., 10, 103–115, 1992.

Crooker, N. U. and Rich, F. J.: Lobe cell convection as a summer phenomenon, J. Geophys. Res., 98, 13 403–13 407, 1993.

Dahlgren, H., Ivchenko, N., Lanchester, B. S., Sullivan, J., Whiter, D., Marklund, G., and Strømme, A.: Using spectral characteristics to interpret auroral imaging in the 732.0 nm O^+ line, Ann. Geophys., 26, 1905–1917, 2008a.

Dahlgren, H., Ivchenko, N., Sullivan, J., Lanchester, B., Marklund, G., and Whiter, D.: Morphology and dynamics of aurora at fine scale: first results from the ASK instrument, Ann. Geophys., 26, 1041–1048, 2008b.

Daldorff, L. K. S., Pécseli, H. L., and Trulsen, J.: Nonlinearly generated plasma waves as a model for enhanced ion acoustic lines in the ionosphere, Geophys. Res. Lett., 34, L18 101, doi: 10.1029/2007GL031513, 2007.

Davis, T. N.: Observed characteristics of auroral forms, Space Science Reviews, 22, 77–113, 1978.

Ergun, R. E., Carlson, C. W., McFadden, J. P., Clemmons, J. H., and Boehm, M. H.: Langmuir wave growth and electron bunching - Results from a wave-particle correlator, J. Geophys. Res., 96, 225–238, 1991.

Forme, F. R. E.: A new interpretation on the origin of enhanced ion acoustic fluctuations in the upper ionosphere, Geophys. Res. Lett., 20, 2347–2350, 1993.

Forme, F. R. E.: Parametric decay of beam-driven Langmuir waves and enhanced ion-acoustic fluctuations in the ionosphere: a weak turbulence approach, Ann. Geophys., 17, 1172–1181, doi: 10.1007/s005850050842, 1999.

Forme, F. R. E. and Fontaine, D.: Enhanced ion acoustic fluctuations and ion outflows, Ann. Geophys., 17, 182–189, doi: 10.1007/s005850050749, 1999.

Forme, F. R. E., Ogawa, Y., and Buchert, S. C.: Naturally enhanced ion acoustic fluctuations seen at different wavelengths, J. Geophys. Res., 106, 21 503–21 515, doi: 10.1029/2000JA900164, 2001.

Foster, J. C., del Pozo, C., Groves, K., and St. Maurice, J.-P.: Radar observations of the onset of current driven instabilities in the topside ionosphere, Geophys. Res. Lett., 15, 160–163, 1988.

Frederick-Frost, K. M., Lynch, K. A., Kintner, P. M., Klatt, E., Lorentzen, D., Moen, J., Ogawa, Y., and Widholm, M.: SERSIO: Svalbard EISCAT Rocket Study of Ion Outflows, J. Geophys. Res., 112, A08 307, doi: 10.1029/2006JA011942, 2007.

Fuselier, S. A., Anderson, B. J., and Onsager, T. G.: Particle signatures of magnetic topology at the magnetopause: AMPTE/CCE observations, J. Geophys. Res., 100, 11 805–11 821, 1995.

Gattinger, R. L. and Vallance-Jones, A.: Quantitative spectroscopy of the aurora - II. The spectrum of medium intensity aurora between 4500 and 8900 Å, Can. J. Phys., 52, 2343–2356, 1974.

Grydeland, T., La Hoz, C., Hagfors, T., Blixt, E. M., Saito, S., Strømme, A., and Brekke, A.: Interferometric observations of filamentary structures associated with plasma instability in the auroral ionosphere, Geophys. Res. Lett., 30, 1338, doi: 10.1029/2002GL016362, 2003.

Grydeland, T., Blixt, E. M., Løvhaug, U. P., Hagfors, T., La Hoz, C., and Trondsen, T. S.: Interferometric radar observations of filamented structures due to plasma instabilities and their relation to dynamic auroral rays, Ann. Geophys., 22, 1115–1132, 2004.

Grydeland, T., Chau, J. L., La Hoz, C., Hagfors, T., and Brekke, A.: An imaging interferometry capability for the EISCAT Svalbard Radar, Ann. Geophys., 23, 221–230, 2005.

Guio, P. and Forme, F.: Zakharov simulations of Langmuir turbulence: effects on the ion-acoustic waves in incoherent scattering, Phys. Plasmas, 13, 122 902, doi: 10.1063/1.2402145, 2006.

Haerendel, G.: Origin and dynamics of thin auroral arcs, Adv. Space Res., 23, 1637–1645, 1999.

Hallinan, T. J., Kimball, J., Stenbaek-Nielsen, H. C., Lynch, K., Arnoldy, R., Bonnell, J., and Kintner, P.: Relation between optical emissions, particles, electric fields, and Alfvén waves in a multiple rayed arc, J. Geophys. Res., 106, 15 445–15 454, doi: 10.1029/2000JA000321, 2001.

Hapgood, M. A.: Space physics coordinate transformations - A user guide, Planet. Space Sci., 40, 711–717, doi: 10.1016/0032-0633(92)90012-D, 1992.

Hapgood, M. A.: Corrigendum to Space physics coordinate transformations: a user guide, Planet. Space Sci., 45, 1047, 1997.

Hasegawa, H., Retinò, A., Vaivads, A., Khotyaintsev, Y., Nakamura, R., Takada, T., Miyashita, Y., Rème, H., and Lucek, E. A.: Retreat and reformation of X-line during quasi-continuous tailward-of-the-cusp reconnection under northward IMF, Geophys. Res. Lett., 35, L15 104, doi: 10.1029/2008GL034767, 2008.

Holt, J. M., Erickson, P. J., Gorczyca, A. M., and Grydeland, T.: MIDAS-W: a workstation-based incoherent scatter radar data acquisition system, Ann. Geophys., 18, 1231–1241, doi: 10.1007/s005850000271, 2000.

Ivchenko, N., Rees, M. H., Lanchester, B. S., Lummerzheim, D., Galand, M., Throp, K., and Furniss, I.: Observation of O^+ (^4P-$^4D^0$) lines in electron aurora over Svalbard, Ann. Geophys., 22, 2805–2817, 2004.

Ivchenko, N., Blixt, E. M., and Lanchester, B. S.: Multispectral observations of auroral rays and curls, Geophys. Res. Lett., 32, L18 106, doi: 10.1029/2005GL022650, 2005.

Ivchenko, N., Lanchester, B. S., Höök, J., Bampton, M., Dahlgren, H., Whiter, D., Strømme, A., and Ivanov, Y.: Auroral Structure and Kinetics - a new optical instrument for auroral studies, Journal of Applied Remote Sensing, in preparation, 2008.

Kaila, K. U.: Determination of the energy of auroral electrons by the measurements of the emission ratio and altitude of aurorae, Planet. Space Sci., 37, 341–349, doi: 10.1016/0032-0633(89)90031-7, 1989.

Knudsen, D. J., Donovan, E. F., Cogger, L. L., Jackel, B., and Shaw, W. D.: Width and structure of mesoscale optical auroral arcs, Geophys. Res. Lett., 28, 705–708, doi: 10.1029/2000GL011969, 2001.

Kontar, E. P. and Pécseli, H. L.: Nonlinear development of electron-beam-driven weak turbulence in an inhomogeneous plasma, Phys. Rev. E, 65, 066 408, doi: 10.1103/PhysRevE.65.066408, 2002.

Kontar, E. P. and Pécseli, H. L.: Nonlinear wave interactions as a model for naturally enhanced ion acoustic lines in the ionosphere, Geophys. Res. Lett., 32, L05 110, doi: 10.1029/2004GL022182, 2005.

Kosch, M. J., Pedersen, T., Rietveld, M. T., Gustavsson, B., Grach, S. M., and Hagfors, T.: Artificial optical emissions in the high-latitude thermosphere induced by powerful radio waves: An observational review, Adv. Space Res., 40, 365–376, doi: 10.1016/j.asr.2007.02.061, 2007.

Lanchester, B. S.: Mapping of Auroral Forms from an All-Sky Coordinate Grid, in: European Rocket Balloon Program, p. 313, 1980.

Lanchester, B. S., Rees, M. H., Lummerzheim, D., Otto, A., Frey, H. U., and Kaila, K. U.: Large fluxes of auroral electrons in filaments of 100 m width, J. Geophys. Res., 102, 9741–9748, doi: 10.1029/97JA00231, 1997.

Lanchester, B. S., Rees, M. H., Robertson, S., Galand, D. L. M., Mendillo, M., Baumgardner, J., Furniss, I., and Aylward, A. D.: Proton and electron precipitation over Svalbard -first results from a new Imaging Spectrograph (HiTIES), in Proc. of Atmos. Studies by Optical Methods, SGO Pubs 92, 33–36, 2003.

Lavraud, B., Thomsen, M. F., Lefebvre, B., Schwartz, S. J., Seki, K., Phan, T. D., Wang, Y. L., Fazakerley, A., Rème, H., and Balogh, A.: Evidence for newly closed magnetosheath field lines at the dayside magnetopause under northward IMF, J. Geophys. Res., 111, A05 211, doi: 10.1029/2005JA011266, 2006.

Lehtinen, M. S., Markkanen, J., Väänänen, A., and Huuskonen, A.: Using EISCAT radars for space debris detection, in: Space Debris, edited by Sawaya-Lacoste, H., vol. 473 of ESA Special Publication, pp. 67–71, 2001.

Lockwood, M. and Hapgood, M. A.: On the cause of a magnetospheric flux transfer event, J. Geophys. Res., 103, 26 453–26 478, doi: 10.1029/98JA02244, 1998.

Lockwood, M. and Moen, J.: Reconfiguration and closure of lobe flux by reconnection during northward IMF: possible evidence for signatures in cusp/cleft auroral emissions, Ann. Geophys., 17, 996–1011, 1999.

Lockwood, M., Bromage, B. J. I., Willis, D. M., Horne, R. B., and St-Maurice, J.-P.: Non-Maxwellian ion velocity distributions observed using EISCAT, Geophys. Res. Lett., 14, 111–114, 1987.

Lorentzen, D. A., Kintner, P. M., Moen, J., Sigernes, F., Oksavik, K., Ogawa, Y., and Holmes, J.: Pulsating dayside aurora in relation to ion upflow events during a northward interplanetary magnetic field (IMF) dominated by a strongly negative IMF B_Y, J. Geophys. Res., 112, A03 301, doi: 10.1029/2006JA011757, 2007.

Lummerzheim, D. and Lilensten, J.: Electron transport and energy degradation in the ionosphere: evaluation of the numerical solution, comparison with laboratory experiments, auroral observations, Ann. Geophys., 12, 1039–1051, doi: 10.1007/s005850050127, 1994.

Lunde, J., Gustavsson, B., Løvhaug, U. P., Lorentzen, D. A., and Ogawa, Y.: Particle precipitations during NEIAL events: simultaneous ground based observations at Svalbard, Ann. Geophys., 25, 1323–1336, 2007.

Lyons, L. R.: Generation of large-scale regions of auroral currents, electric potentials, and precipitation by the divergence of the convection electric field, J. Geophys. Res., 85, 17–24, 1980.

Maggs, J. E. and Davis, T. N.: Measurements of the thicknesses of auroral structures, Planet. Space Sci., 16, 205, 1968.

McComas, D. J., Bame, S. J., Barker, P., Feldman, W. C., Phillips, J. L., Riley, P., and Griffee, J. W.: Solar Wind Electron Proton Alpha Monitor (SWEPAM) for the Advanced Composition Explorer, Space Science Reviews, 86, 563–612, doi: 10.1023/A:1005040232597, 1998.

McWhirter, I., Furniss, I., Aylward, A. D., Lanchester, B. S., Rees, M. H., Robertson, S. C., Baumgardner, J., and Mendillo, M.: A new spectrographic platform for auroral studies in Svalbard, Sodankylä Geophysical Observatory Publications, 92, 73–76, 2003.

Michell, R.: Examining auroral downward current region processes using ground based data, Doctor of Philosophy thesis, Dartmouth College, Hanover, New Hampshire, 2007.

Michell, R. G., Lynch, K. A., Heinselman, C. J., and Stenbaek-Nielsen, H. C.: PFISR nightside observations of naturally enhanced ion acoustic lines, and their relation to boundary auroral features, Ann. Geophys., 26, 3623–3639, 2008.

Nygrén, T.: Introduction to incoherent scatter measurements, Invers Publications, Sodankylä, Finland, 1996.

Ogawa, Y., Forme, F., and Buchert, S. C.: Frequency dependent power fluctuations: a feature of the ESR system or physical?, Ann. Geophys., 18, 1224–1230, 2000.

Ogawa, Y., Buchert, S. C., Fujii, R., Nozawa, S., and Forme, F.: Naturally enhanced ion-acoustic lines at high altitudes, Ann. Geophys., 24, 3351–3364, 2006.

Pallamraju, D. and Chakrabarti, S.: First ground-based measurements of OI 6300 Å daytime aurora over Boston in response to the 30 October 2003 geomagnetic storm, Geophys. Res. Lett., 32, L03S10, doi: 10.1029/2004GL021417, 2005.

Rees, M. H.: Physics and chemistry of the upper atmosphere, Cambridge atmospheric and space science series, Cambridge University Press, Cambridge, 1989.

Reiff, P. H. and Burch, J. L.: IMF B_Y-dependent plasma flow and Birkeland currents in the dayside magnetosphere. II - A global model for northward and southward IMF, J. Geophys. Res., 90, 1595–1609, 1985.

Rietveld, M. T., Collis, P. N., and St.-Maurice, J.-P.: Naturally Enhanced Ion Acoustic Waves in the Auroral Ionosphere Observed With the EISCAT 933-MHz Radar, J. Geophys. Res., 96, 19 291–19 305, 1991.

Rietveld, M. T., Collis, P. N., van Eyken, A. P., and Løvhaug, U. P.: Coherent echoes during EISCAT UHF Common Programmes, J. Atmos. Terr. Phys., 58, 161–174, doi: 10.1016/0021-9169(95)00027-5, 1996.

Rietveld, M. T., Isham, B., Grydeland, T., La Hoz, C., Leyser, T. B., Honary, F., Ueda, H., Kosch, M., and Hagfors, T.: HF-Pump-induced parametric instabilities in the auroral E-region, Adv. Space Res., 29, 1363–1368, doi: 10.1016/S0273-1177(02)00186-2, 2002.

Robertson, S. C., Lanchester, B. S., Galand, M., Lummerzheim, D., Stockton-Chalk, A. B., Aylward, A. D., Furniss, I., and Baumgardner, J.: First ground-based optical analysis of H_β Doppler profiles close to local noon in the cusp, Ann. Geophys., 24, 2543–2552, 2006.

Roble, R. G. and Rees, M. H.: Time-dependent studies of the aurora: Effects of particle precipitation on the dynamic morphology of ionospheric and atmospheric properties, Planet. Space Sci., 25, 991–1010, doi: 10.1016/0032-0633(77)90146-5, 1977.

Ruohoniemi, J. M. and Greenwald, R. A.: Statistical patterns of high-latitude convection obtained from Goose Bay HF radar observations, J. Geophys. Res., 101, 21 743–21 764, doi: 10.1029/96JA01584, 1996.

Sedgemore-Schulthess, K. J. F. and St.-Maurice, J.-P.: Naturally enhanced ion-acoustic spectra and their interpretation, Surv. Geophys., 22, 55–92, doi: 10.1023/A:1010691026863, 2001.

Sedgemore-Schulthess, K. J. F., Lockwood, M., Trondsen, T. S., Lanchester, B. S., Rees, M. H., Lorentzen, D. A., and Moen, J.: Coherent EISCAT Svalbard Radar spectra from the dayside cusp/cleft and their implication for transient field-aligned currents, J. Geophys. Res., 104, 24 613–24 624, doi: 10.1029/1999JA900276, 1999.

Semeter, J.: Critical comparison of OII(732-733 nm), OI(630 nm), and N_2(1PG) emissions in auroral rays, Geophys. Res. Lett., 30, 1225, doi: 10.1029/2002GL015828, 2003.

Semeter, J. and Blixt, E. M.: Evidence for Alfvén wave dispersion identified in high-resolution auroral imagery, Geophys. Res. Lett., 33, 10.1029/2002GL015 828, doi: 10.1029/2006GL026274, 2006.

Semeter, J., Lummerzheim, D., and Haerendel, G.: Simultaneous multispectral imaging of the discrete aurora, J. Atmos. Sol. Terr. Phys., 63, 1981–1992, 2001.

Sigernes, F., Svenøe, T., and Deehr, C. S.: The Auroral Station in Adventdalen, Svalbard, Chinese J. Pol. Sci., 13, 67–74, 2002.

Sigernes, F., Holmes, J. M., Dyrland, M., and Lorentzen, D. A.: Absolute calibration of optical devices with a small field of view, Journal of Optical Technology, 74, 669–674, 2007.

Smart, W. M. and Green, R. M.: Textbook on Spherical Astronomy, Textbook on Spherical Astronomy, by William Marshall Smart and Edited by Robin Michael Green, pp. 446. ISBN 0521291801. Cambridge, UK: Cambridge University Press, July 1977., 1977.

Smith, C. W., L'Heureux, J., Ness, N. F., Acuña, M. H., Burlaga, L. F., and Scheifele, J.: The ACE Magnetic Fields Experiment, Space Sci. Rev., 86, 613–632, doi: 10.1023/A:1005092216668, 1998.

Stasiewicz, K., Bellan, P., Chaston, C., Kletzing, C., Lysak, R., Maggs, J., Pokhotelov, O., Seyler, C., Shukla, P., Stenflo, L., Streltsov, A., and Wahlund, J.-E.: Small Scale Alfvénic Structure in the Aurora, Space Sci. Rev., 92, 423–533, 2000.

Strømme, A., Belyey, V., Grydeland, T., La Hoz, C., Løvhaug, U. P., and Isham, B.: Evidence of Naturally Occurring Wave-Wave Interactions in the Polar Ionosphere and its Relation to Naturally Enhanced Ion Acoustic Lines, Geophys. Res. Lett., 32, L05 103, doi: 10.1029/2004GL020239, 2005.

Strømme, A., Semeter, J., and Zettergren, M.: Naturally Enhanced Ion Acoustic Lines with the Poker Flat AMISR radar., AGU Fall Meeting Abstracts, p. A6, 2007.

Stubbs, T. J., Lockwood, M., Cargill, P., Fennell, J., Grande, M., Kellett, B., Perry, C., and Rees, A.: Dawn-dusk asymmetry in particles of solar wind origin within the magnetosphere, Ann. Geophys., 19, 1–9, 2001.

Sullivan, J. M., Ivchenko, N., Lockwood, M., Grydeland, T., Blixt, E. M., and Lanchester, B. S.: Phase calibration of the EISCAT Svalbard interferometer using optical satellite signatures, Ann. Geophys., 24, 2419–2427, 2006.

Sullivan, J. M., Lockwood, M., Lanchester, B., Kontar, E. P., Ivchenko, N., Dahlgren, H., and Whiter, D.: An optical study of multiple NEIAL events driven by low energy electron precipitation, Ann. Geophys., 26, 2435–2447, 2008.

Tereshchenko, E. D., Khudukon, B. Z., Rietveld, M. T., and Brekke, A.: Spatial structure of auroral day-time ionospheric electron density irregularities generated by a powerful HF-wave, Ann. Geophys., 16, 812–820, doi: 10.1007/s005850050650, 1998.

Trondsen, T. S. and Cogger, L. L.: A survey of small-scale spatially periodic distortions of auroral forms, J. Geophys. Res., 103, 9405–9416, doi: 10.1029/98JA00619, 1998.

Vedenov, A. A., Velikhov, E. P., and Sagdeev, R. Z.: Quasi-linear theory of plasma oscillations, Nuclear Fusion Supplement, Part 2., 465–475, 1962.

Viljanen, A. and Häkkinen, L.: Image Magnetometer Network, in: Satellite-Ground Based Coordination Sourcebook, edited by Lockwood, M., Wild, M. N., and Opgenoorth, H. J., vol. 1198 of ESA Special Publication, pp. 111–118, 1997.

Vogt, J., Frey, H. U., Haerendel, G., Höfner, H., and Semeter, J. L.: Shear velocity profiles associated with auroral curls, J. Geophys. Res., 104, 17 277–17 288, doi: 10.1029/1999JA900148, 1999.

Wagner, J. S., Sydora, R. D., Tajima, T., Hallinan, T., Lee, L. C., and Akasofu, S.-I.: Small-scale auroral arc deformations, J. Geophys. Res., 88, 8013–8019, 1983.

Wahlund, J.-E., Forme, F. R. E., Opgenoorth, H. J., Persson, M. A. L., Mishin, E. V., and Volokitin, A. S.: Scattering of electromagnetic waves from a plasma: enhanced ion acoustic fluctuations due to ion-ion two-stream instabilities, Geophys. Res. Lett., 19, 1919–1922, 1992a.

Wahlund, J.-E., Opgenoorth, H. J., Häggström, I., Winser, K. J., and Jones, G. O. L.: EISCAT Observations of Topside Ionospheric Ion Outflows During Auroral Activity: Revisited, J. Geophys. Res., 97, 3019–3037, 1992b.

Wahlund, J.-E., Opgenoorth, H. J., Forme, F. R. E., Persson, M. A. L., Häggström, I., and Lilensten, J.: Electron energization in the topside auroral ionosphere: on the importance of ion-acoustic turbulence, J. Atmos. Terr. Phys., 55, 623–645, 1993.

Whiter, D.: A study of auroral fine structure in the magnetic zenith, Master of Philosophy thesis, University of Southampton, 2008.

Winser, K. J., Lockwood, M., and Jones, G. O. L.: Non-thermal plasma observations using EISCAT - Aspect angle dependence, Geophys. Res. Lett., 14, 957–960, 1987.